

Environmental Sustainability in the Synthesis and Characterization of Hybrid/Composite Nanomaterials

Lead Guest Editor: Maria Giulia Faga

Guest Editors: Roberto Nisticò, Jana Kukutschova, Giuliana Magnacca,
and Luciano Carlos





Environmental Sustainability in the Synthesis and Characterization of Hybrid/Composite Nanomaterials

**Environmental Sustainability in the
Synthesis and Characterization of
Hybrid/Composite Nanomaterials**

Lead Guest Editor: Maria Giulia Faga

Guest Editors: Roberto Nisticò, Jana Kukutschova,
Giuliana Magnacca, and Luciano Carlos



Copyright © 2018 Hindawi. All rights reserved.

This is a special issue published in "Journal of Nanomaterials." All articles are open access articles distributed under the Creative Commons Attribution License, which permits unrestricted use, distribution, and reproduction in any medium, provided the original work is properly cited.

Editorial Board

- Domenico Acierno, Italy
Katerina Aifantis, USA
Nageh K. Allam, USA
Margarida Amaral, Portugal
Martin Andersson, Sweden
Raul Arenal, Spain
Ilaria Armentano, Italy
Vincenzo Baglio, Italy
Lavinia Balan, France
Thierry Baron, France
Andrew R. Barron, USA
Hongbin Bei, USA
Stefano Bellucci, Italy
Enrico Bergamaschi, Italy
D. Bhattacharyya, New Zealand
Sergio Bietti, Italy
Giovanni Bongiovanni, Italy
Mohamed Bououdina, Bahrain
Victor M. Castaño, Mexico
Albano Cavaleiro, Portugal
Bhanu P. S. Chauhan, USA
Shafiq Chowdhury, USA
Yu-Lun Chueh, Taiwan
Elisabetta Comini, Italy
Giuseppe Compagnini, Italy
David Cornu, France
Miguel A. Correa-Duarte, Spain
P. Davide Cozzoli, Italy
Anuja Datta, USA
Loretta L. Del Mercato, Italy
Yong Ding, USA
Yu Dong, Australia
Zehra Durmus, Turkey
Joydeep Dutta, Oman
Ovidiu Ersen, France
Ana Espinosa, France
Claude Estournès, France
Andrea Falqui, Saudi Arabia
Matteo Ferroni, Italy
Ilaria Fratoddi, Italy
Siddhartha Ghosh, Singapore
Filippo Giubileo, Italy
Fabien Gasset, Japan
Jean M. Greneche, France
- Kimberly Hamad-Schifferli, USA
Simo-Pekka Hannula, Finland
Michael Harris, USA
Yasuhiko Hayashi, Japan
Michael Z. Hu, USA
Nay Ming Huang, Malaysia
Zafar Iqbal, USA
Balachandran Jeyadevan, Japan
J.-w. Kang, Republic of Korea
Hassan Karimi-Maleh, Iran
Antonios Kelarakis, UK
Alireza Khataee, Iran
Ali Khorsand Zak, Iran
Philippe Knauth, France
Prashant Kumar, UK
Eric Le Bourhis, France
Jun Li, Singapore
Meiyong Liao, Japan
Shijun Liao, China
Silvia Licoccia, Italy
Nathan C. Lindquist, USA
Zainovia Lockman, Malaysia
Jim Low, Australia
Gaurav Mago, USA
Muhamamd A. Malik, UK
Francesco Marotti de Sciarra, Italy
Ivan Marri, Italy
Laura Martinez Maestro, UK
Sanjay R. Mathur, Germany
Tony McNally, UK
Yogendra Mishra, Germany
Paulo Cesar Morais, Brazil
Paul Munroe, Australia
J.-M. Myoung, Republic of Korea
Rajesh R. Naik, USA
Albert Nasibulin, Russia
Toshiaki Natsuki, Japan
Hiromasa Nishikiori, Japan
Natalia Noginova, USA
Sherine Obare, USA
Won-Chun Oh, Republic of Korea
Abdelwahab Omri, Canada
Ungyu Paik, Republic of Korea
Edward A. Payzant, USA
- Alessandro Pegoretti, Italy
Oscar Perales-Pérez, Puerto Rico
Jorge Pérez-Juste, Spain
Alexey P. Popov, Finland
Thathan Premkumar, Republic of Korea
Helena Prima-García, Spain
Alexander Pyatenko, Japan
Haisheng Qian, China
You Qiang, USA
Philip D. Rack, USA
Peter Reiss, France
Ilker S. Bayer, Italy
Lucien Saviot, France
Sudipta Seal, USA
Shu Seki, Japan
Donglu Shi, USA
Bhanu P. Singh, India
Surinder Singh, USA
Vladimir Sivakov, Germany
Adolfo Speghini, Italy
Marinella Striccoli, Italy
Fengqiang Sun, China
Xuping Sun, Saudi Arabia
Ashok K. Sundramoorthy, India
Angelo Taglietti, Italy
Bo Tan, Canada
Leander Tapfer, Italy
Valeri P. Tolstoy, Russia
Muhammet S. Toprak, Sweden
R. Torrecillas, Spain
Achim Trampert, Germany
Takuya Tsuzuki, Australia
Tamer Uyar, Turkey
Luca Valentini, Italy
Antonio Vassallo, Italy
Ester Vazquez, Spain
Ajayan Vinu, Australia
Ruibing Wang, Macau
Shiren Wang, USA
Yong Wang, USA
Magnus Willander, Sweden
Ping Xiao, UK
Zhi Li Xiao, USA
Yingchao Yang, USA



Yoke K. Yap, USA
Dong Kee Yi, Republic of Korea

Jianbo Yin, China
William Yu, USA

Michele Zappalorto, Italy
Renyun Zhang, Sweden

Contents

Environmental Sustainability in the Synthesis and Characterization of Hybrid/Composite Nanomaterials

Maria Giulia Faga , Roberto Nisticò , Jana Kukutschova, Giuliana Magnacca , and Luciano Carlos 
Editorial (2 pages), Article ID 7131325, Volume 2018 (2018)

Nanocomposite Kaolin/TiO₂ as a Possible Functional Filler in Automotive Brake Pads

Kateřina Dědková , Marcus Morbach, Jakub Výravský, Kateřina Mamulová Kutláková, Kristina Čabanová , Miroslav Vaculík, and Jana Kukutschová
Research Article (14 pages), Article ID 9780894, Volume 2018 (2018)

Synthesis and Characterization of Ti-Fe Oxide Nanomaterials for Lead Removal

Buzuayehu Abebe  and H. C. Ananda Murthy
Research Article (10 pages), Article ID 9651039, Volume 2018 (2018)

Microstructural Analysis and Magnetic Characterization of Native and Magnetically Modified Montmorillonite and Vermiculite

Yvonna Jiraskova , Jiri Bursik , Jana Seidlerova, Katerina Mamulova Kutlakova, Ivo Safarik, Mirka Safarikova, Kristyna Pospiskova, and Ondrej Zivotsky 
Research Article (14 pages), Article ID 3738106, Volume 2018 (2018)

Possible Monitoring and Removal of As(III) by an Integrated System of Electrochemical Sensor and Nanocomposite Materials

Xuan T. Chu, Quan V. V. Trieu, Thinh Q. Tran, Thanh D. Pham, Trung Q. Vu, Thuy H. Tran, and Tuan A. Mai 
Research Article (9 pages), Article ID 9250463, Volume 2018 (2018)

Mechanical and Optical Properties of Polylactic Acid Films Containing Surfactant-Modified Cellulose Nanocrystals

Jose Luis Orellana, Derek Wichhart, and Christopher L. Kitchens 
Research Article (12 pages), Article ID 7124260, Volume 2018 (2018)

Structural, Optical, and Photocatalytic Activities of Ag-Doped and Mn-Doped ZnO Nanoparticles

Mengstu Etay Ashebir , Gebrekidan Mebrahtu Tesfamariam, Gebretinsae Yeabyo Nigussie , and Tesfakiros Woldu Gebreab
Research Article (9 pages), Article ID 9425938, Volume 2018 (2018)

Fabrication of Bifunctional TiO₂/POM Microspheres Using a Layer-by-Layer Method and Photocatalytic Activity for Methyl Orange Degradation

Ping Niu , Dunqing Wang, Aili Wang, Yuhua Liang, and Xinfang Wang
Research Article (8 pages), Article ID 4212187, Volume 2018 (2018)

Editorial

Environmental Sustainability in the Synthesis and Characterization of Hybrid/Composite Nanomaterials

Maria Giulia Faga ¹, **Roberto Nisticò** ², **Jana Kukutschova**,³ **Giuliana Magnacca** ⁴,
and Luciano Carlos ⁵

¹CNR-IMAMOTER, Torino, Italy

²Politecnico di Torino, Torino, Italy

³VSB-Technical University of Ostrava, Ostrava, Czech Republic

⁴Università degli Studi di Torino, Torino, Italy

⁵Instituto de Investigación y Desarrollo en Ingeniería de Procesos, Biotecnología y Energías Alternativas, PROBIEN (CONICET-UNCo), Neuquén, Argentina

Correspondence should be addressed to Maria Giulia Faga; m.faga@imamoter.cnr.it

Received 27 November 2018; Accepted 27 November 2018; Published 9 December 2018

Copyright © 2018 Maria Giulia Faga et al. This is an open access article distributed under the Creative Commons Attribution License, which permits unrestricted use, distribution, and reproduction in any medium, provided the original work is properly cited.

The guest editors for this special issue are pleased to welcome contributions from researchers studying hybrid/composite nanomaterials reporting significant advancements in terms of environmental friendliness and sustainability in their preparation and characterization methods. Manuscripts selected for this special issue deal with the development of alternative/innovative synthetic routes for the production of nanocomposites and/or hybrid materials, with proven or expected reduction of the overall environmental impact as well as the production of biocompatible components or showing improved sustainability.

Four articles focused on the use of (eventually magnetic) nanomaterials for the remediation of contaminated media via either photocatalysis or adsorption mechanisms. M. Etay et al. evaluated the photocatalytic properties of bare, Ag-doped, and Mn-doped ZnO nanoparticles prepared via a coprecipitation method by monitoring the light-induced decolorization of methyl violet aqueous solutions. P. Niu et al. synthesized bifunctional films of Keggin-type polyoxometalates and TiO₂ onto Fe₃O₄@SiO₂ microspheres using a layer-by-layer method and tested their photocatalytic efficiencies in the photo-induced degradation of methyl orange. X. T. Chu et al. studied the performances of magnetic nanocomposites made by polyaniline-coated magnetite

nanoparticles for the removal of As(III) from simulated contaminated aqueous medium via adsorption. Lastly, B. Abebe and H. C. Ananda Murthy reported the production of magnetic TiO₂-Fe₂O₃ binary oxides and their adsorption performances against Pb(II) ions from aqueous solution.

The production and testing of magnetic materials for other purposes were also evaluated by Y. Jiraskova et al., who analyzed the structural and magnetic properties of magnetically modified clays (i.e., Fe₃O₄ introduction into both montmorillonite and vermiculite) and compared to the unmodified clay minerals.

The other two articles devoted to the improvement of mechanical properties of nanomaterials. J. L. Orellana et al. evaluated the effect of introducing surfactants as compatibilizers in blends of surface-modified cellulose nanocrystals with a polylactic acid (PLA) matrix produced via film extrusion. K. Dedkova et al. introduced ad hoc prepared kaolin/TiO₂ nanocomposites in a commercially available automotive low-steel brake pad, observing an improvement in the wear resistance (and consequently a reduction in both wear rate and particulate emission).

In our opinion, the seven articles forming this special issue are good examples on how the development of advanced nanocomposites is able to both directly and

indirectly improve the environmental sustainability of products and processes. The editors hope that these scientific contributions will positively stimulate the creativity of researchers to focus their efforts on this very intriguing research field.

Conflicts of Interest

The editors declare that they have no conflicts of interest regarding the publication of this special issue.

Acknowledgments

The editors would like to thank all authors for having submitted their manuscripts to this special issue, the editors for having spent their time selecting reviewers and making editorial decisions, and of course the reviewers for providing their expert opinions.

*Maria Giulia Faga
Roberto Nisticò
Jana Kukutschova
Giuliana Magnacca
Luciano Carlos*

Research Article

Nanocomposite Kaolin/TiO₂ as a Possible Functional Filler in Automotive Brake Pads

Kateřina Dědková ^{1,2}, **Marcus Morbach**,³ **Jakub Výravský**,⁴
Kateřina Mamulová Kutláková,⁵ **Kristina Čabanová** ^{1,2}, **Miroslav Vaculík**,^{1,2}
and **Jana Kukutschová**^{1,2}

¹Center of Advanced Innovation Technologies, VŠB-Technical University of Ostrava, 708 00 Ostrava-Poruba, Czech Republic

²Regional Materials Science and Technology Centre, VŠB-Technical University of Ostrava, 708 33 Ostrava-Poruba, Czech Republic

³Federal-Mogul Friction Products GmbH, 65520 Bad Camberg, Germany

⁴TESCAN Brno, s.r.o, 623 00 Brno, Czech Republic

⁵Nanotechnology Centre, VŠB-Technical University of Ostrava, 70800 Ostrava-Poruba, Czech Republic

Correspondence should be addressed to Kateřina Dědková; katerina.dedkova@vsb.cz

Received 20 May 2018; Revised 28 August 2018; Accepted 5 September 2018; Published 21 November 2018

Academic Editor: Albano Cavaleiro

Copyright © 2018 Kateřina Dědková et al. This is an open access article distributed under the Creative Commons Attribution License, which permits unrestricted use, distribution, and reproduction in any medium, provided the original work is properly cited.

An automotive friction brake pad is a complex system consisting of several components with unique and balanced properties related to operation conditions. There are efforts to develop brake pads with longer lifetime and better friction performance and wear properties. Those properties are related to composition of the pads, and therefore, new materials are being evolved. Tuning the friction and wear properties can be achieved with the selection of a functional filler and optimizing its amount in a formulation of friction brake pad. Laboratory-developed and laboratory-prepared nanocomposite material kaolin/TiO₂ (KATI) has been introduced to formulation of the commercially available automotive low-steel brake pad. Kaolin was utilized as a matrix for anchoring TiO₂ nanoparticles. New unused pads and pads after AK master, a standard dynamometer testing procedure of friction performance, were investigated using light and scanning electron microscopy providing information on the structure and its changes after the friction processes. Moreover, MTK wear test was used to compare wear rate of the newly developed pad with the reference low-steel pad. Improved durability of the brake pad formulation has been observed together with sufficient friction performance. Microscopic analysis shown homogenous distribution of the KATI nanocomposite in the friction layer. From the obtained results, it can be assumed that the new formulation is promising regarding to the life cycle of the pads and reduction of wear rate and thus potential production of wear particulate emissions.

1. Introduction

Typically, a brake pad is a multicomponent composite material characteristically consisting of more than 10 constituents. Phenolic resin usually serves as a matrix, and several forms of metals, ceramics, minerals, polymers, and carbonaceous ingredients are present in a typical brake pad. Due to significantly different material properties of single components, the resulting friction layer established on the surface of friction composites is strongly heterogeneous and also its surface is rough with many asperities across it [1, 2]. Friction materials have to be durable, mechanically and thermally stable, provide

a consistent friction force, be tribologically compatible with the other part of friction pair, have balanced vibration and noise, be environmentally acceptable, and last but not the least have to be cost-effective in design, manufacturing, and usage [3].

Significant phase transformations of brake pad material occur during friction processes. These transformations lead to origination of newly formed friction layer and have a great effect on the friction efficiency of brake pads as well as an effect on wear debris formation and its properties. While braking, both parts of braking couple in the disc brake system (i.e., pads and rotating disc) are worn and thus wear debris is generated. It is well known that the wear debris may have a

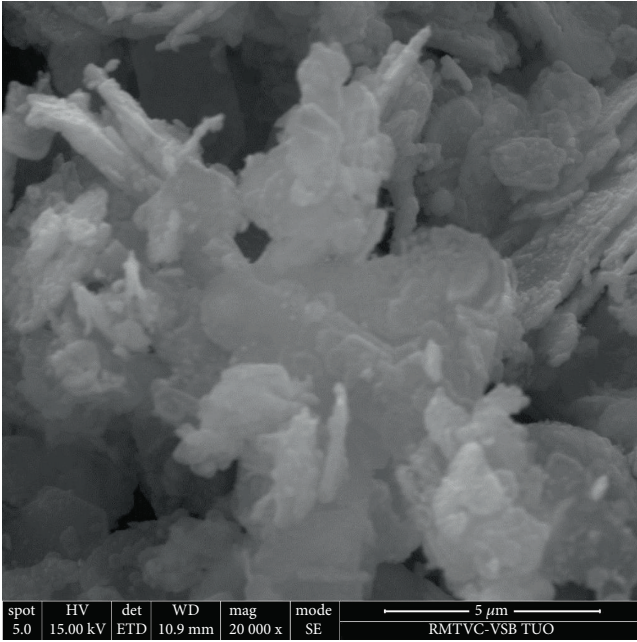


FIGURE 1: SEM image of KATI [15].

negative impact on the environment and human health [4]. Heat created during friction is dissipated through exchange mainly with the environment and rise tremendously in the contact regions.

Nowadays, environmental issues are being discussed due to the potential influence of wear products on the air quality in urban areas. It has been proved that the nonexhaust emission comes also from the wear of the pads and rotors [5]. Therefore, there are enormous efforts to develop new brake pad formulations with lower particulate emissions and stable friction performance. In connection with the development of new formulations for automotive brake pads, new raw materials are being investigated. The influence of nanopotassium titanate filler on the performance of nonasbestos organic brake pads has been already studied. It has been shown that nanopotassium titanate has improved friction performance and wear resistance compared to bulk potassium titanate [6]. Moreover, potential new abrasives in nanometer size have been studied. It has been revealed that all the friction and wear parameters were significantly and beneficially influenced due to the nanosize of the tested abrasives. Nanosilica increased wear resistance as well as nano-SiC and alumina [7]. Recent work [8] has also shown the significant influence of the particle size of SiO₂ on the transformation of friction mechanisms.

Therefore, nanostructured composite material kaolin/TiO₂ could be one of the suitable candidates and thus the aim of the study was the introduction of this nanomaterial into the brake pad formulation together with subsequent detailed characterization of friction surfaces of tested brake pads and their chemical and phase composition as well as evaluation of their changes during the friction process.

TABLE 1: Description of brake pad composition in volume%.

| | Reference pad | Pad with KATI |
|-------------------------|---------------|---------------|
| Abrasives | 12.5 | 4.9 |
| Organic binder | 23.0 | 22.0 |
| Metals | 17.0 | 17.4 |
| Organic fiber | 3.5 | 3.7 |
| Carbon | 25.0 | 22.0 |
| Lubricants | 7.0 | 7.0 |
| Filler | 12.0 | 9.0 |
| Kaolin/TiO ₂ | 0 | 14 |

2. Materials and Methods

2.1. Brake Pad Samples. Federal-Mogul Motorparts (Germany) provided reference commercial brake pads and manufactured the brake pads with modified composition used in this study. The composition of the reference commercially available low-steel brake pad was adjusted, and nanocomposite kaolin/TiO₂ (KATI) (Figure 1) was introduced to the formulation as a new possible functional filler. Detailed description of laboratory procedure for preparation of KATI is presented in the study [9]. The prepared KATI contained about 60 wt% of TiO₂ nanoparticles with crystallite size of 18 nm.

Hence, the phase composition of the pads is confidential; therefore, Table 1 shows only content of the groups of ingredients in volume% without detailed specification.

AK Master and MTK wear test with both samples were performed using full-scale dynamometer at Federal-Mogul Motorparts, Germany. These procedures simulate various braking scenarios with various brake pressures and speed, and thus, these studied materials were exposed to different conditions, which may occur during usage of automotive friction brakes. The dynamometer program AK Master describes the friction value behavior of a friction material with regard to the influences of pressure, temperature, and speed. Its main purpose is to compare friction materials under the most equal conditions possible. To take account of the different cooling behavior of the different test stands, the fading series are temperature-controlled. Project-related brakes and brake discs must be used. Test conditions are defined by inertia, press rate increase, sampling frequencies, temperature measurement, and cooling conditions. The friction performance is tested under various braking conditions, such as speed, pressure, and disc temperature representing different situations during vehicle driving. Firstly, pads and rotor go through a friction check in new conditions (30 brake applications), followed by a bedding section to get pad and rotor surface adapted (62 Ba). After that, a characterization of the friction value at standard pressure, speed, and initial temperature is measured (6 Ba). Next point is speed/pressure sensitivity of the friction coefficient (5 × 8 Ba). Again, a characterization as before is added (6 Ba). A cold temperature check followed by a highway simulation with elevated speed is next (3 Ba). This section is closed by a newly conducted characterization (18 Ba). The fade characteristic is tested by

TABLE 2: AK Master braking procedure.

| | Unit | Reference pad | Pad with KATI |
|--------------------------|------|---------------|---------------|
| μ nom | (1) | 0.44 | 0.44 |
| μ min | (1) | 0.34 | 0.37 |
| μ char. value | (1) | 0.48 | 0.50 |
| μ speed/pressure | (1) | 0.42 | 0.44 |
| μ char. value | (1) | 0.41 | 0.42 |
| μ 40°C brake appl. 2 | (1) | 0.40 | 0.34 |
| μ motorway appl. 2 | (1) | 0.45 | 0.43 |
| μ char. value | (1) | 0.43 | 0.41 |
| μ min fade 1 | (1) | 0.34 | 0.37 |
| μ char. value | (1) | 0.46 | 0.43 |
| μ min. temp. | (1) | 0.35 | 0.37 |
| μ char. value | (1) | 0.45 | 0.46 |
| μ min fade 2 | (1) | 0.46 | 0.38 |
| μ char. value | (1) | 0.40 | 0.41 |
| Average pad wear | (mm) | 0.92 | 0.41 |
| Disc wear | (g) | 11.6 | 11.6 |

continuously increasing disc temperature up to 550°C initial temperature by executing 15 brake applications. The next characterization (18 Ba) is followed by pressure lines. This means 8 Ba with increasing pressure at 100°C initial temperature, an increase of disc temperature up to 500°C by 9 Ba, and again a pressure line at 500°C starting temperature (8 Ba). Next sections are again a characterization (18 Ba), followed by a second fade (15 Ba), and finally a characterization (18 Ba \geq total 274 Ba).

Friction values are determined by the following formula. Efficiency factor η is determined as 100%. The brake torque is measured during the brake application, and an arithmetic average is calculated to each of them. The μ value is calculated as follows:

$$\mu = \frac{Md_{\text{brake}}}{2(p - p_{\text{threshold}}) \cdot A_{\text{piston}} \cdot r_{\text{eff}} \cdot \eta} \quad (1)$$

Evaluation of wear behavior of pad material in Main-Taunus endurance course based on vehicle data was done. The course is a driving cycle containing 240 brake applications each, depending on the driving conditions tracked from the vehicle driving. 20 test cycles are run during the MTK test, which means 4800 brake applications in total. The wear of friction pads is determined by thickness measurement before and after the test at four defined positions.

The inner brake pad (placed in the inner side of the disc) was selected for further experiments due to higher pressures and temperatures achieved during braking. For better manipulation with the studied samples, back plates were removed from the pads. Since friction composites could be considered as homogenous material on the macro level, randomly selected area of 25 mm² of the initial sample surface was labelled and the rest of the sample was covered with aluminum foil to ensure that the same one will be analyzed by all

TABLE 3: MTK wear braking procedure.

| | Unit | Reference pad | Pad with KATI |
|--------------------------------|------|---------------|---------------|
| Circuit 3–20 average pad life | (km) | 27,367 | 57,665 |
| Circuit 3–20 average disc life | (km) | 181,154 | 279,380 |
| MTK—inner pad wear (mean) | (mm) | 1.22 | 0.56 |
| MTK—outer pad wear (mean) | (mm) | 1.11 | 0.56 |
| MTK—disc wear | (g) | 9.2 | 8.0 |
| Pad condition MPU (min) | (1) | 9 | 10 |
| Disc scoring/grooving (min) | (1) | 10 | 8 |

of the techniques used. Since the friction layer formation depends on many factors and varies at the sample surface, two spots (called site 1 and site 2) of 25 mm² from different areas of the tested sample surface were labelled. Rest of the sample was covered with aluminum foil. The samples prepared this way were analyzed using a combination of selected analytical methods.

2.2. Material Characterization Techniques. Light digital microscope VHX-500 (Keyence Corporation, Japan) was used for macroscale characterization of the friction surface of the studied samples together with surface roughness.

The EDS mapping of the selected (400 \times 400 μ m) areas from both new and tested samples was performed using TESCAN S8252G microscope equipped with field emission electron gun and Oxford Peltier-cooled SDD detector with 150 mm² active area. The following analytical conditions were used: analytical working distance 6 mm, acc. voltage 20 kV, probe current 3 nA, mapping resolution of 1024 \times 1024 pixels, and 10 accumulations. The experimental data were collected, and maps were obtained using the Aztec software.

The samples of the tested brake pads were also measured using TESCAN TIMA (TESCAN Integrated Mineral Analyzer) equipped with tungsten emitter at the following working conditions: acc. voltage 25 kV, working distance 15 mm, and probe current 7 nA. The EDAX Element 30 detectors were used for collecting the characteristic X-rays. The detectors are Peltier-cooled SDD (silicon drift detectors) with 30 mm² active area. Two areas of CCA 5 \times 5 mm were measured from each sample. Liberation analysis with high-resolution mapping mode was used. Pixel spacing was 1 μ m/pixel, and 1000 X-ray counts and BSE intensity were collected from each pixel. Combination of BSE intensity and X-ray spectra was used for distinguishing the phase boundaries. The data were interpreted, and reports were processed by the TIMA 1.5.49 software.

3. Results and Discussion

Table 2 lists parameters of friction performance evaluation including the average friction coefficient dimensionless values (ranging between 0 and 1) in the individual sections

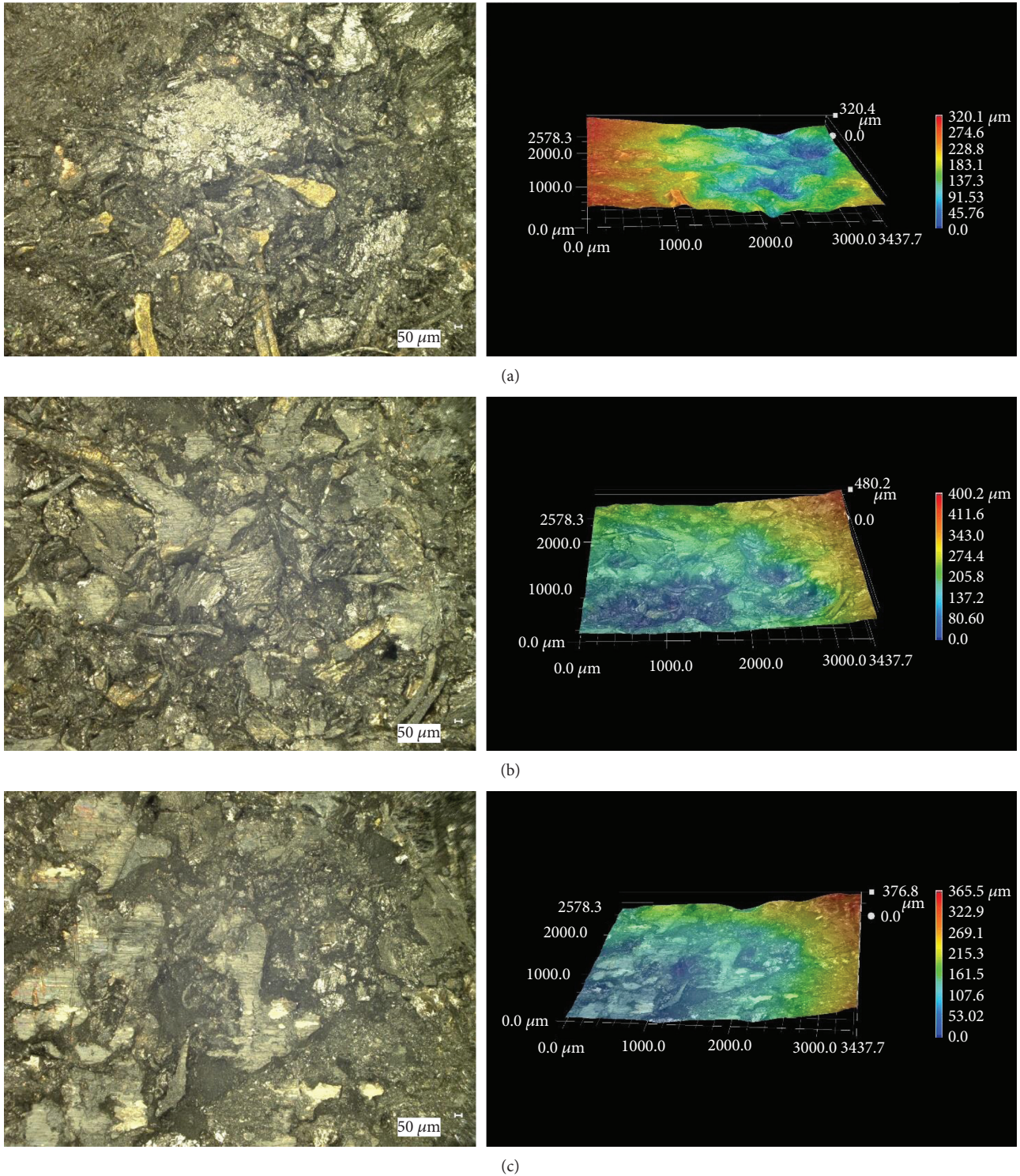


FIGURE 2: Selected area of the reference low-steel brake pad surface with its corresponding 3D reconstruction (a), site 1 (b), and site 2 (c) of the tested reference pad.

of the AK Master test. The average and minimum values of the entire AK Master test are also presented. For friction composites with organic polymer matrix, the optimum friction coefficient is around 0.4. Both composites achieved very similar friction efficiency in the standard AK Master sections.

In sections with high heat load (fade 1 and fade 2), the composite with KATI addition achieves higher average friction coefficient values which is a desirable feature, since other similar materials have the opposite tendency in this AK Master section. Both composites had a comparable weight loss of

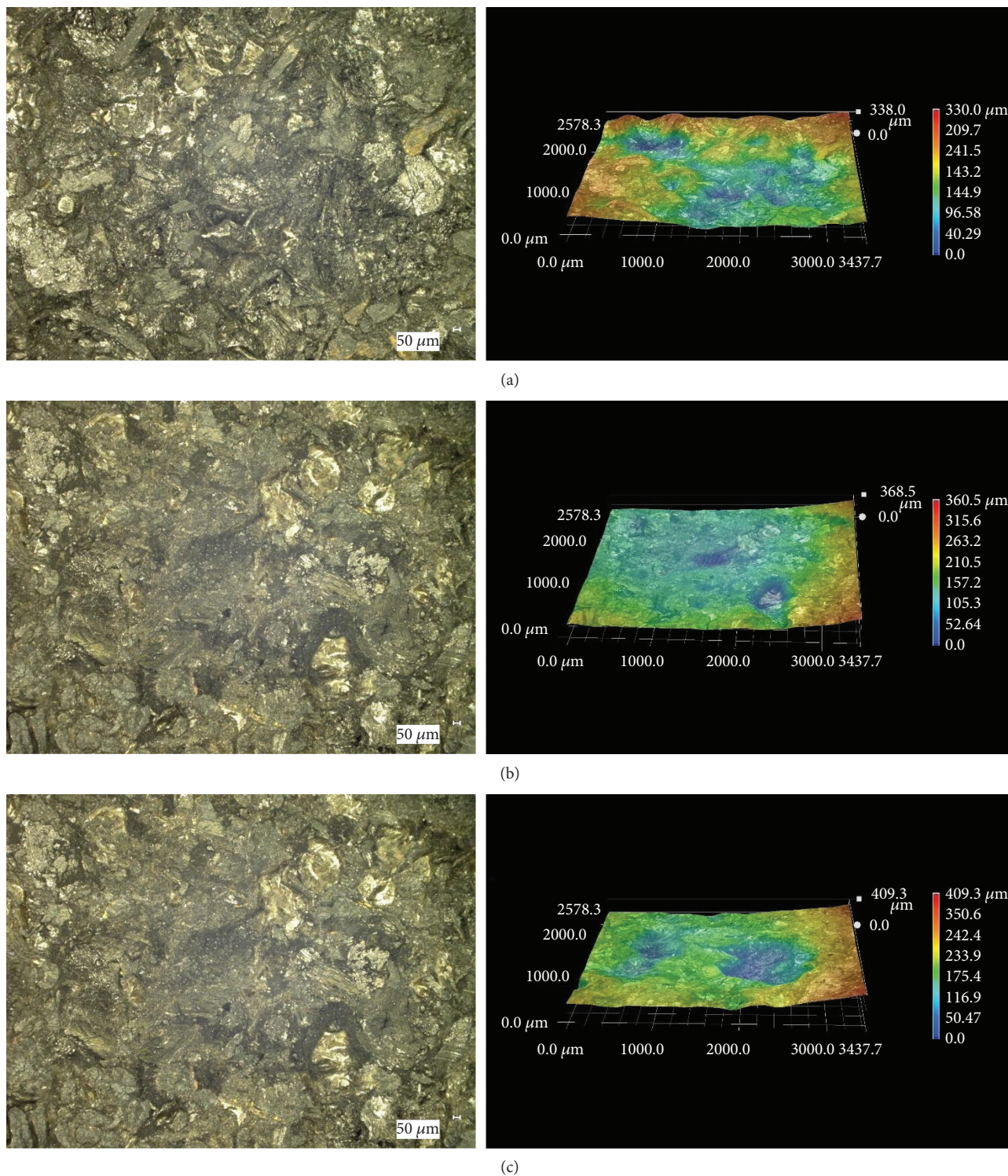


FIGURE 3: Selected area of the surface of the brake pad containing KATI nanocomposite with its corresponding 3D reconstruction (a), site 1 (b), and site 2 (c) of the tested pad containing KATI.

the disc after the test, while pad wear was reduced by 44.6% after KATI addition.

Table 3 presents results from MTK wear test and shows significant reduction of pad wear which leads to increased lifetime of the pad with KATI nanocomposite compared to the reference pad. It is worth mentioning that mean wear of

inner and outer pad is the same. Commercial cast iron disc was used for both dynamometer tests and its wear rate is comparable for all tested pads.

Light digital microscopy is a useful technique for studying sample surface in the macroscale. It enables to image the surface in real colors, which may help to identify some

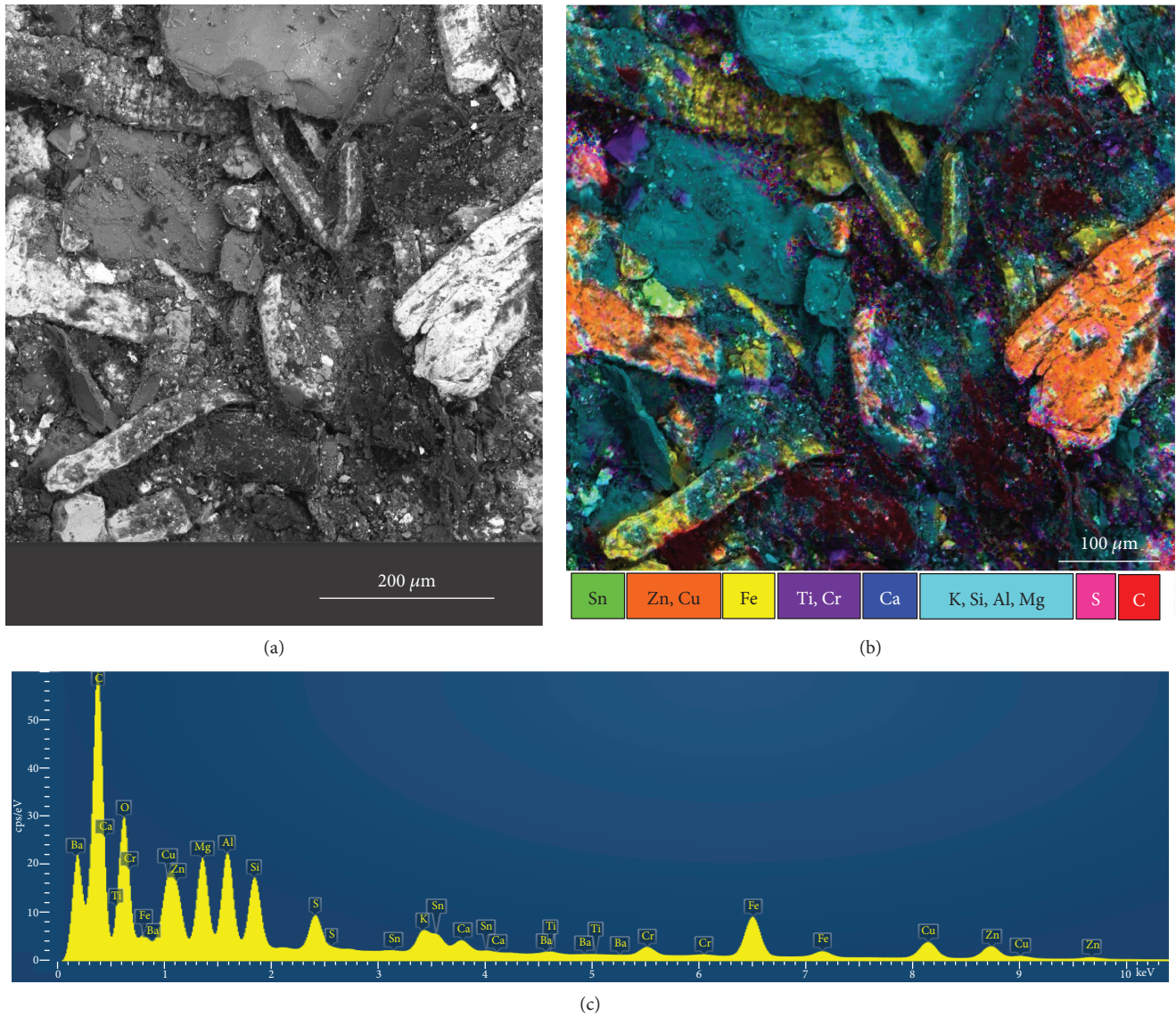


FIGURE 4: Selected magnified area of the reference pad before testing (a), EDS spectral map overlapped with electron image (b), and its corresponding spectrum (c).

of the present structures. For instance, in the case of the reference pad, it can be presumed that shiny gold-like features could be brass fibers (Figure 2(a)). Nevertheless, it might not be helpful in the cases without high color contrast samples or without having knowledge about the studied sample. 3D reconstruction of the surface shows the roughness and profile of the surface; however, the scale should not be considered as absolute values due to the influence of the sample placement in the microscope. Therefore, the 3D reconstruction of the surface should be used only for theoretical comparison of each point or area at one image instead of comparing among images.

The surface of the reference pad is quite rough with remarkable fibrous structures. The surface of two selected areas after the dynamometer testing is more flat, but still exhibits notable roughness and contains cavities. The first area (Figure 2(b)) contains some fibers, but the second area

(Figure 2(c)) contains no visible fibers. Contact plateaus (fractions of the pad surface that mediate direct contact with a disc) are clearly visible at both areas.

The surface of the initial pad containing KATI nanocomposite is less rough. Some fibers can be seen, but they are not made of brass as in the reference pad. Some cavities can be seen at the surface of the tested pad (Figures 3(b) and 3(c)). Contact plateaus are not clearly visible in both cases of the tested samples.

Combination of electron image with EDS mapping enables visualization of elemental composition of each component of pad surface. Due to the lack of colors in the software, several elements, which were presented at the same areas of the sample (most probably create together a compound), have the same color (e.g., Cu and Zn—brass or K, Si, Al, and Mg—clay minerals). Oxygen is not included in these maps because it was present almost in every point,

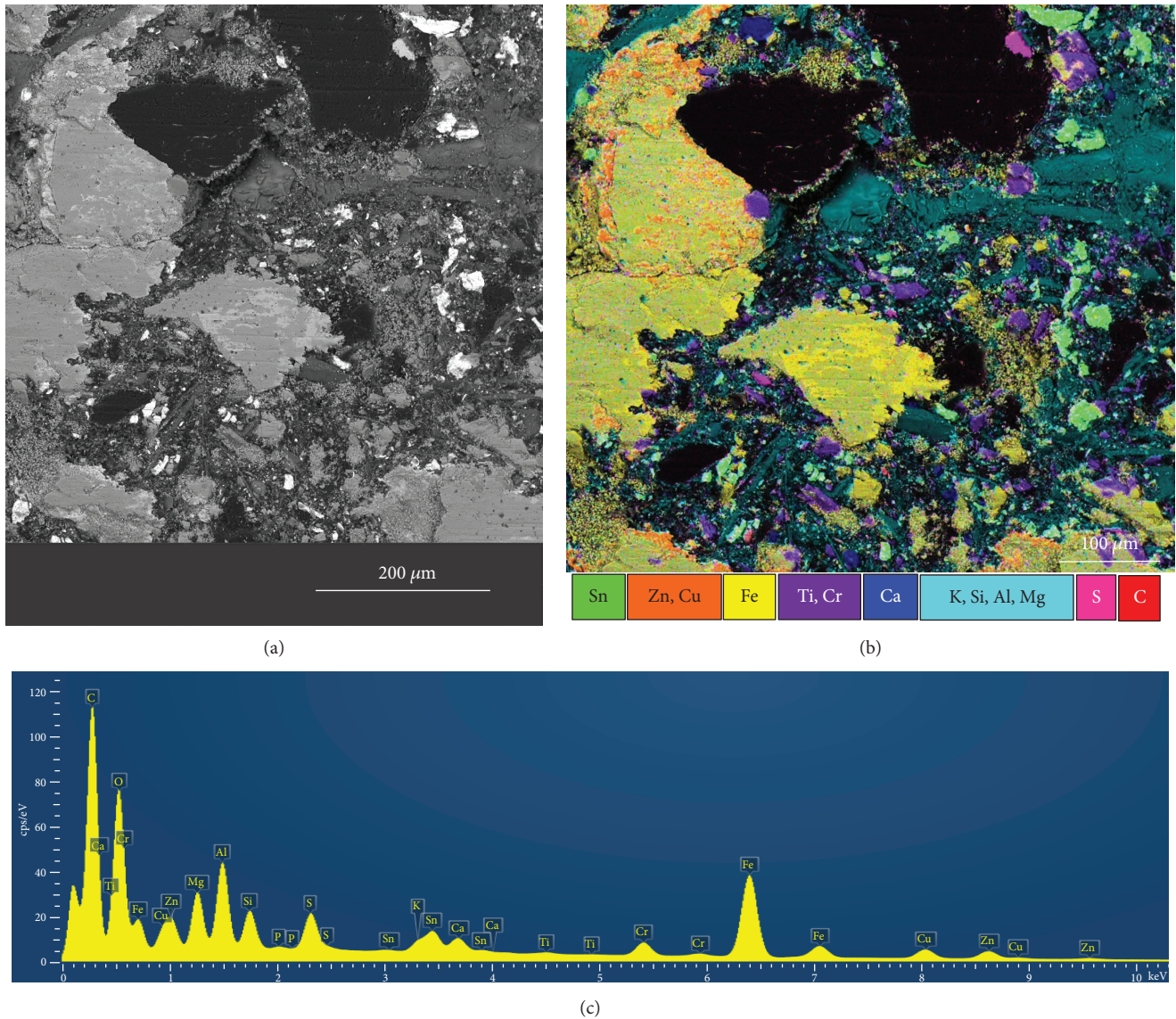


FIGURE 5: Selected magnified area of site 1 of the reference pad after dynamometer testing (a), EDS spectral map overlapped with electron image (b), and its corresponding spectrum (c).

and thus, such map including oxygen would be useless. Figure 4 confirms the presumption that some fibers are made of brass and some are made of steel. Layered structure of clay minerals is also clearly visible.

Contact plateaus based on iron visible in Figure 5, together with high amount of fine wear particles based on chromium, tin, or barium, and some residues of layered structure of clay minerals, are also visible. Brass fibers create contact plateaus together with steel fibers but are in minority. Phase contrast in the contact plateaus together with different intensity of yellow color in the EDS map indicates that part of the surface of the plateaus consists of elemental iron and other parts are created by iron oxide, which is consistent with finding of Österle et al. [10].

The larger part of the surface of site 2 of the reference pad (Figure 6) is created by contact plateaus than in site 1 of the same pad (Figure 5). Therefore, the content of iron and also

copper and zinc in the analyzed area is significantly higher. Other difference is in the presence of wear particles based on chromium and titanium, which are not clearly visible in Figure 5. Finally, this friction surface contains larger carbon-based structures than site 1; nevertheless, weight percentage of carbon is slightly lower.

The surface of the selected area of the pad with KATI nanocomposite (Figure 7) contains steel fibers, layered structure of clay minerals quite high number of fine particles based on titanium and chromium, where titanium is in significantly higher amount according to EDS, because of the addition of kaolinite/TiO₂ filler. There are also some areas rich in carbon particles composed of sulfur as well. Iron layer evidently covers a large particle of brass.

The surface of site 1 pad with KATI nanocomposite (Figure 8) is partly created by contact plateaus and partly by wear particles. Some of the contact plateaus are composed

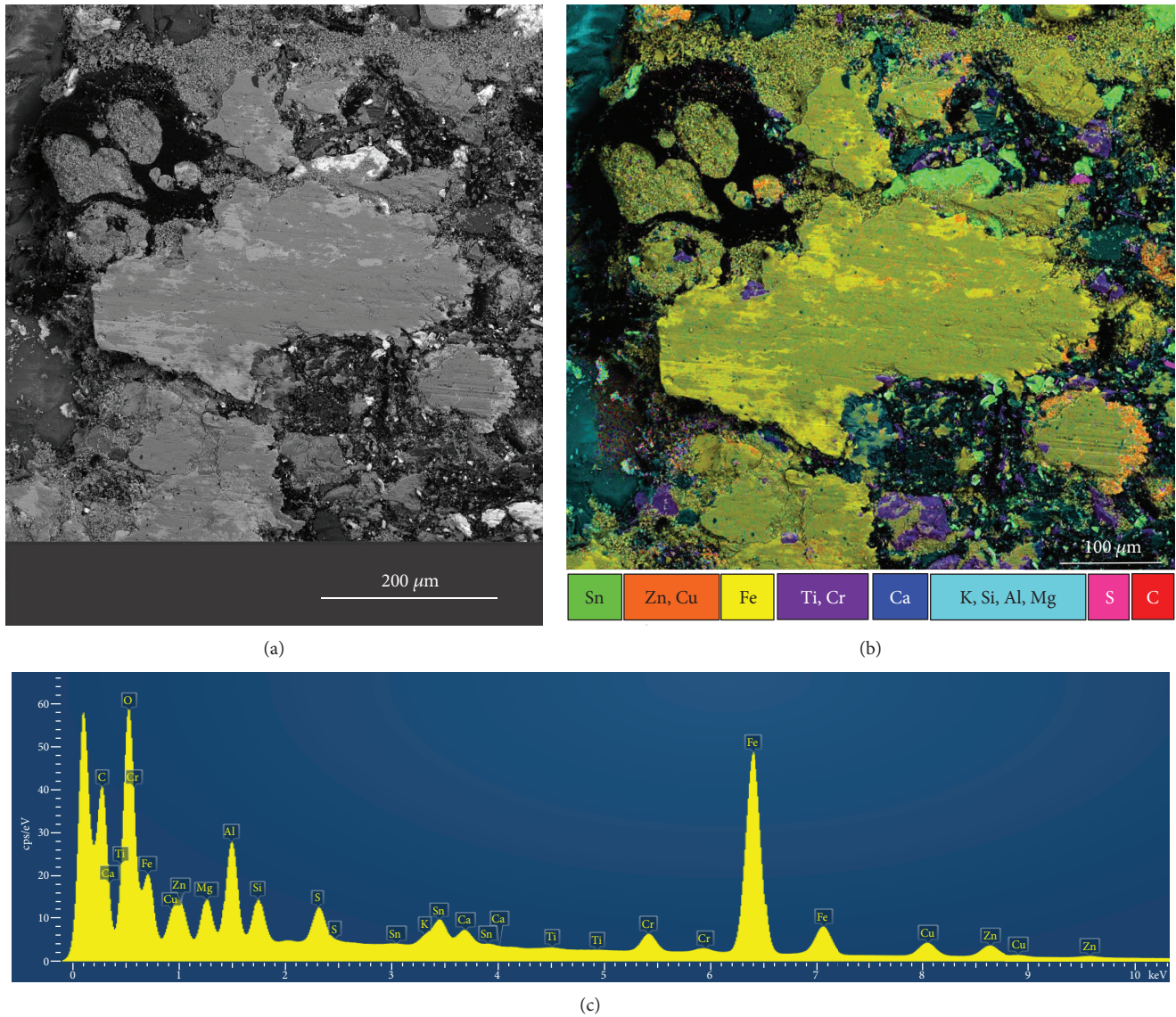


FIGURE 6: Selected magnified area of site 2 of the reference pad after dynamometer testing (a), EDS spectral map overlapped with electron image (b), and its corresponding spectrum (c).

of iron or iron oxides and some of brass. There are only few clay minerals structures visible in the image. Contrary to the reference pad, it is evident that there is significantly higher number of very fine wear particles on the surface composed of carbon, titanium, chromium, iron, and tin. As in the previous sample, there are bright blue-green particles with unknown elemental composition.

The surface of site 2 pad with KATI nanocomposite (Figure 9) is different from the surface of site 1 of the same pad. The contact plateaus are mainly created by iron and iron oxides, and only minority of them are created by brass. Layered structure of clay minerals is more visible in this site, and fine wear particles do not cover the top of contact plateaus, but they are trapped around them. Carbon-rich areas can be distinguished.

EDS mapping is a useful technique, which provides information about the distribution of single elements; however,

multicomponent samples such as brake pads are hitting limits of this technique and even knowledge and experience with this kind of samples cannot guarantee a good result. Thus, there are tendencies to find other complementary techniques to obtain results with limited misinterpretations. Therefore, TESCAN TIMA microscope was used in this pilot study, and based on the published research paper available, it was the first time when it was used for this kind of sample.

Since initial pads have some defined composition (even industrially protected) and significant chemical and morphological changes could not be expected, only pads after dynamometer testing were further examined. Additionally, phase mapping provided by TIMA was also very time-consuming (approx. 12–15 hours). Signal from backscattered electrons and X-ray was collected to create a map of phase composition as can be seen in the following images.

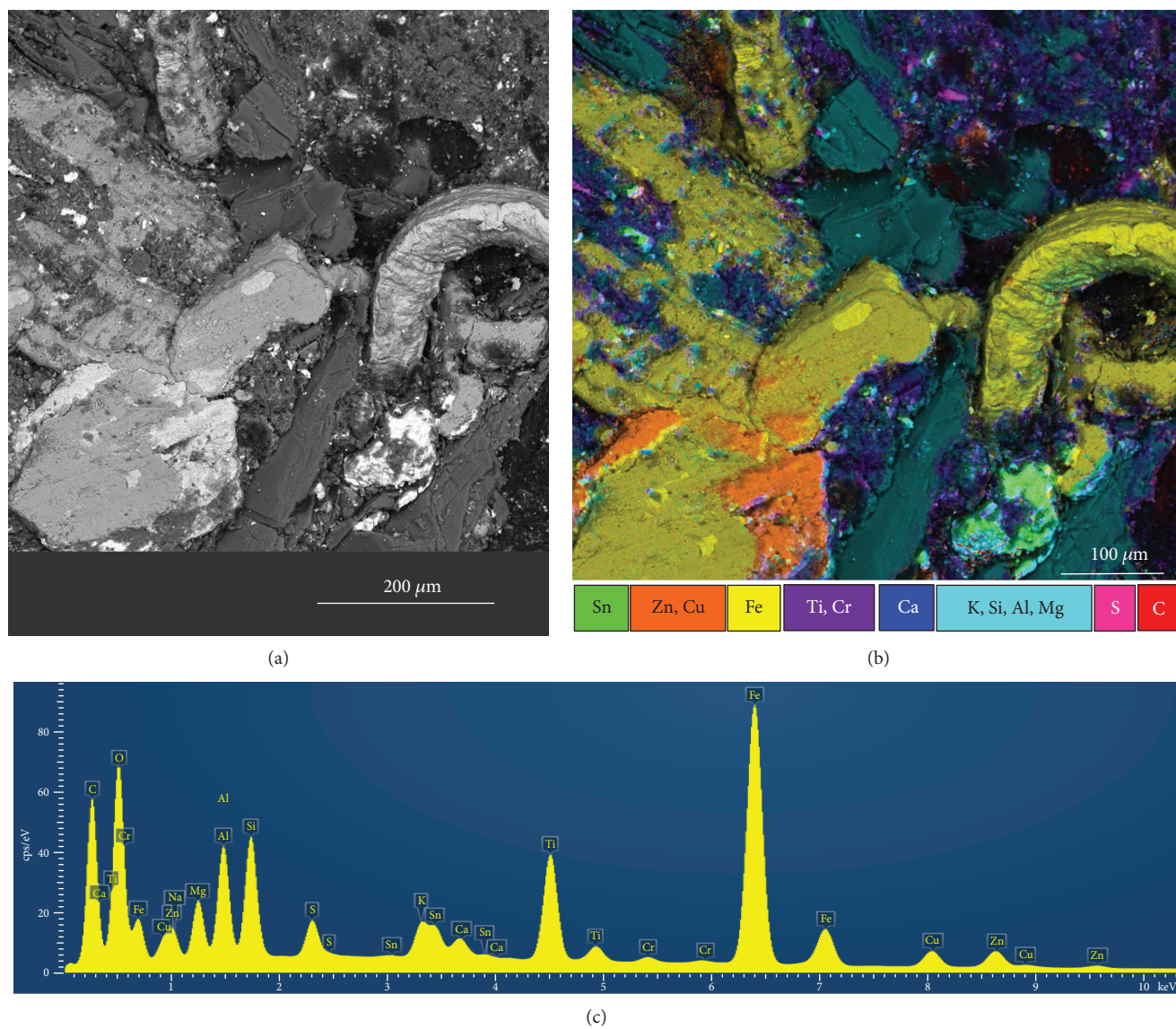


FIGURE 7: Selected magnified area of the pad with KATI nanocomposite before testing (a), EDS spectral map overlapped with electron image (b), and its corresponding spectrum (c).

The phase composition of site 1 (25 mm²) of the reference pad after dynamometer testing is shown in Figure 10. Most of the presented phases were identified via software. Due to difficulties with the detection limit and for certain level of simplification, carbon-S-rich was stated. Fe-Cu oxide was revealed to be the major phase at the surface. Since there are no well-defined phases with corresponding composition, it can be assumed that it can have intermetallic character and originated due to the local high temperatures, when melting of metals or their oxides can occur and subsequently those melted metals are mixed due to the kinetic force. The blue frame is a signal from the background (Al foil). Some pixels have not been classified (below 0.5% of the surface).

The phase composition of site 2 of the reference pad is given in Figure 11. Fe-Cu oxide is dominant at the surface of this area as well; however, significant part is created also by fine grained particles based on corundum, Ca oxide, Sn

sulfide, and others. The surface of this sample appears to be more fragmented into contact plateaus and agglomerated particles, as well as in site 1 of the reference pad, intermetallic compounds can be found. Contrary to site 1, there is a higher incidence of iron pure and Fe oxide phases.

The surface of site 1 of the pad with KATI nanocomposite (Figure 12) contains Al-Si titanates, carbon-S-rich, and Fe-Cu oxide as the dominant phases. It can be assumed that Al-Si titanates represent the added KATI nanocomposite. Interestingly, Al-Si titanates are accompanied with clays as another phase. Noticeable amount of Fe oxide can be also seen. Generally, distribution of KATI nanocomposite among the surface is quite homogenous, which is desired for better friction performance of the pad.

The last examined surface is site 2 of the pad with addition of KATI nanocomposite (Figure 13). It can be stated that the surface of sites 1 and 2 is nearly similar with Al-Si titanates homogeneously dispersed and accompanied with

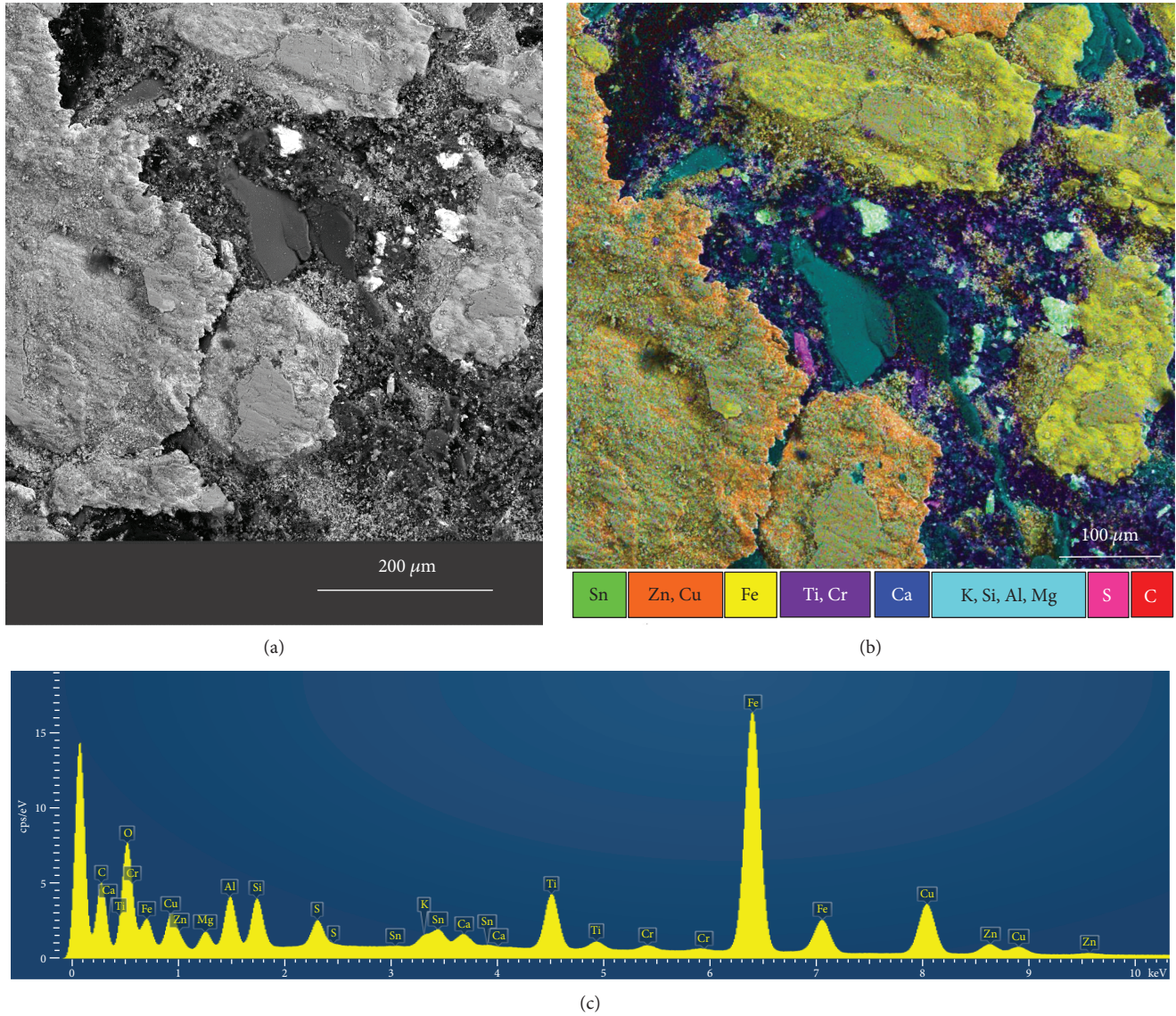


FIGURE 8: Selected magnified area of site 1 of the pad with KATI nanocomposite after dynamometer testing (a), EDS spectral map overlapped with electron image (b), and its corresponding spectrum (c).

clays. Site 2 contains approximately more Fe oxide and carbon phases. The incidence of other phases is nearly similar.

Exported elemental maps and cumulative spectra of individual grains (the cumulative spectra are summed from all analyzed pixels comprising the grain Figure 14) support the idea of glassy-like nature of the mixed intermetallic phases (the Fe-Cu oxide and Fe-Cu-Zn oxide). The elemental maps of a representative grain (Figure 15) show that both Fe (Figure 15(c)) and Cu (Figure 15(a)) are homogeneously distributed within the grain (Figure 15(b)). The same applies for other elements present in these phases in smaller amounts (Si, S, Sn, and others (see Table 4)). Since the material appears to be chemically homogeneous at least on the microscale level (spatial resolution of EDS), it would suggest involvement of at least some degree of melting and not only mechanical mixing caused by friction process. The presence of Sn and S in the spectra of the intermetallic phases may

point to melting of the grains of Sn sulfides which can occur around 880°C [11].

It can be said that addition of TiO_2 to the brake pad formulations is still not frequently studied, and this study with KATI nanocomposite is one of the first in this field; however, there are some studies with titanates. Mahale et al. [6] studied the influence of nanopotassium particles on the friction performance of nonasbestos organic brake pad. Addition of nanopotassium titanates improved performance and wear resistance of the tested pad formulation compared to the one with potassium titanates with micron-sized particles due to its lubricating character that led to the reduction of friction coefficient fluctuations. This finding is in accordance with the study of Kim et al. [12] describing the positive impact of potassium titanate on fluctuation of friction coefficient. It has been also reported that potassium titanate has a positive impact on friction coefficient at higher temperatures [13, 14].

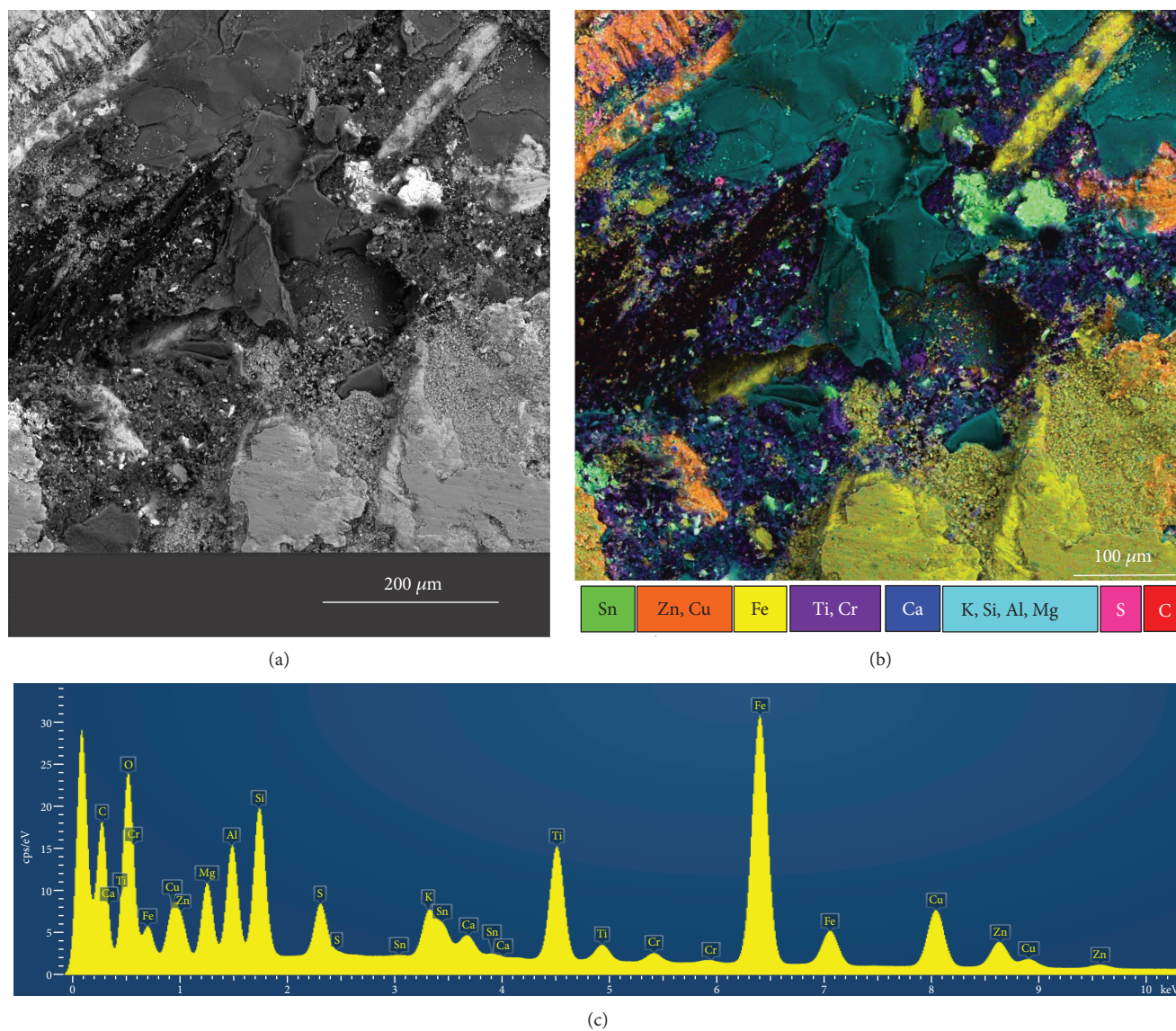


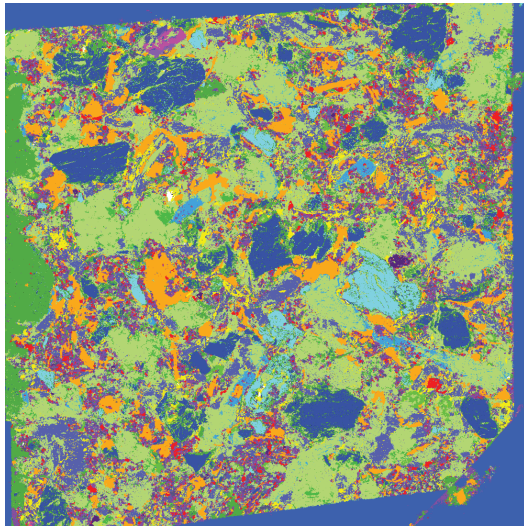
FIGURE 9: Selected magnified area of site 2 of the pad with KATI nanocomposite after dynamometer testing (a), EDS spectral map overlapped with electron image (b), and its corresponding spectrum (c).

Based on these findings, we assume the KATI nanocomposite can stabilize friction coefficient at higher temperatures and then has a positive impact on the wear of brake pads. An original idea was to introduce KATI to the brake pad formula as a new functional filler; nevertheless, this material has probably lubricating properties, which contribute to reduction of wear and thus could increase of the lifetime of the pad.

4. Conclusions

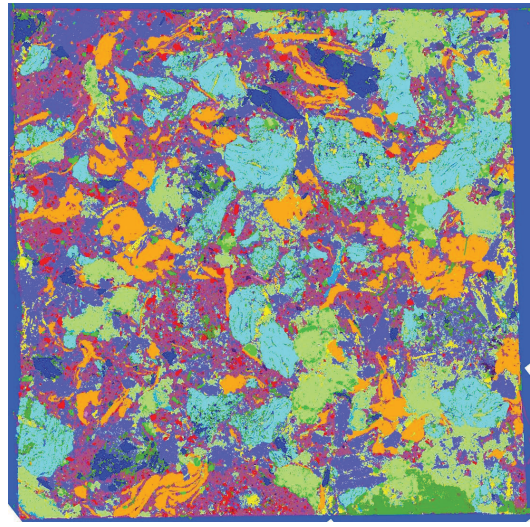
Nanostructured composite material kaolin/TiO₂ (KATI) has been successfully introduced to the existing automotive brake pad formulation. This pad with modified formulation has been tested together with commercially available low-steel pad on full-scale brake dynamometer to determine its friction performance and wear properties. It has been found that friction performance of the pad with KATI nanocomposite is comparable with the commercial low-steel pad;

however, the average pad durability was significantly higher expressed by pad thickness loss which was about 50% lower compared to the reference pad formulation. Microscopic techniques revealed structures of the friction surface where some intermetallic phases have been found, what indicates occurrence of local high temperatures. The nanocomposite KATI was homogeneously distributed on the surface of the pad before and also after the dynamometer testing which indicates good thermal stability of the modified composite. This modified brake pad formulation may be promising regarding the durability of pads and the needs to control wear and reduce particulate emissions. Most expected phases of the initial compounds were determined; however, some of the detected phases do not correspond to possible initial components. It can be interpreted as a result of phase transformation. When selecting a suitable nanomaterial for application in automotive friction composites, nanocomposite materials appear to be suitable candidates due to decrease



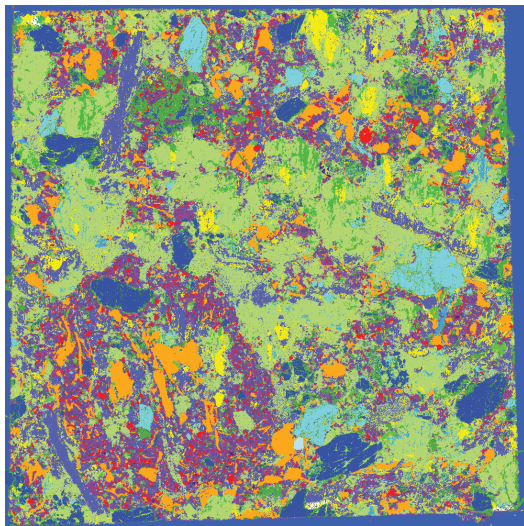
- | | |
|------------------------|------------------------|
| ■ Feoxide | ■ Fe-Cu-Znoxide |
| ■ Al-Sittitanates | ■ Cu-Zn alloy |
| ■ Fe-Cuoxide | ■ MgO |
| ■ Carbon-S-rich | ■ Ca-Al-Siglass fibers |
| ■ Clays | ■ Cu sulfide |
| ■ Carbon-rich mixtures | ■ Quartz |
| ■ Carbon | ■ Molybdenite |
| ■ Ironpure | ■ Ca oxide |
| ■ Snsulfide | ■ Muscovite |
| ■ Corundum | ■ Flourite |
| ■ Native zinc | ■ Unclassified |
| ■ Chromite | ■ Kaolinite |
| ■ Cuoxide | |

FIGURE 10: Panorama map of phase composition of site 1 of the reference pad after dynamometer testing.



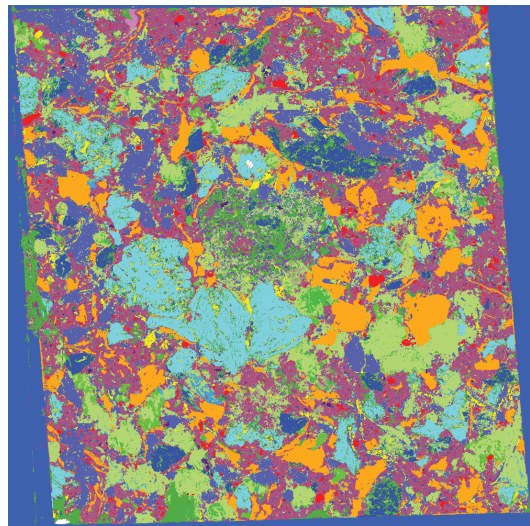
- | | |
|------------------------|------------------------|
| ■ Feoxide | ■ Fe-Cu-Znoxide |
| ■ Al-Sittitanates | ■ Cu-Zn alloy |
| ■ Fe-Cuoxide | ■ MgO |
| ■ Carbon-S-rich | ■ Ca-Al-Siglass fibers |
| ■ Clays | ■ Cusulfide |
| ■ Carbon-rich mixtures | ■ Quartz |
| ■ Carbon | ■ Molybdenite |
| ■ Ironpure | ■ Caoxide |
| ■ Snsulfide | ■ Muscovite |
| ■ Corundum | ■ Flourite |
| ■ Native zinc | ■ Unclassified |
| ■ Chromite | ■ Kaolinite |
| ■ Cuoxide | |

FIGURE 12: Panorama map of phase composition of site 1 of the pad with KATI nanocomposite after dynamometer testing.



- | | |
|------------------------|------------------------|
| ■ Feoxide | ■ Fe-Cu-Znoxide |
| ■ Al-Sittitanates | ■ Cu-Zn alloy |
| ■ Fe-Cuoxide | ■ MgO |
| ■ Carbon-S-rich | ■ Ca-Al-Siglass fibers |
| ■ Clays | ■ Cusulphide |
| ■ Carbon-rich mixtures | ■ Quartz |
| ■ Carbon | ■ Molybdenite |
| ■ Ironpure | ■ Caoxide |
| ■ Snsulfide | ■ Muscovite |
| ■ Corundum | ■ Flourite |
| ■ Native zinc | ■ Unclassified |
| ■ Chromite | ■ Kaolinite |
| ■ Cuoxide | |

FIGURE 11: Panorama map of phase composition of site 2 of the reference pad after dynamometer testing.



- | | |
|------------------------|------------------------|
| ■ Feoxide | ■ Fe-Cu-Znoxide |
| ■ Al-Sittitanates | ■ Cu-Zn alloy |
| ■ Fe-Cuoxide | ■ MgO |
| ■ Carbon-S-rich | ■ Ca-Al-Siglass fibers |
| ■ Clays | ■ Cusulfide |
| ■ Carbon-rich mixtures | ■ Quartz |
| ■ Carbon | ■ Molybdenite |
| ■ Ironpure | ■ Caoxide |
| ■ Snsulfide | ■ Muscovite |
| ■ Corundum | ■ Flourite |
| ■ Native zinc | ■ Unclassified |
| ■ Chromite | ■ Kaolinite |
| ■ Cuoxide | |

FIGURE 13: Panorama map of phase composition of site 2 of the pad with KATI nanocomposite after dynamometer testing.

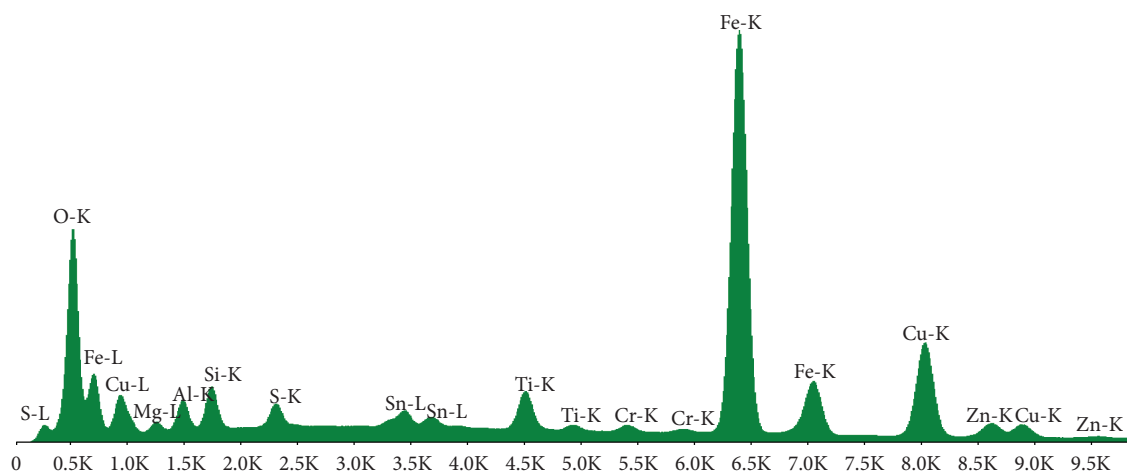


FIGURE 14: Representative spectrum of a grain of Fe-Cu oxide from site 1 of the pad with KATI nanocomposite after dynamometer testing.

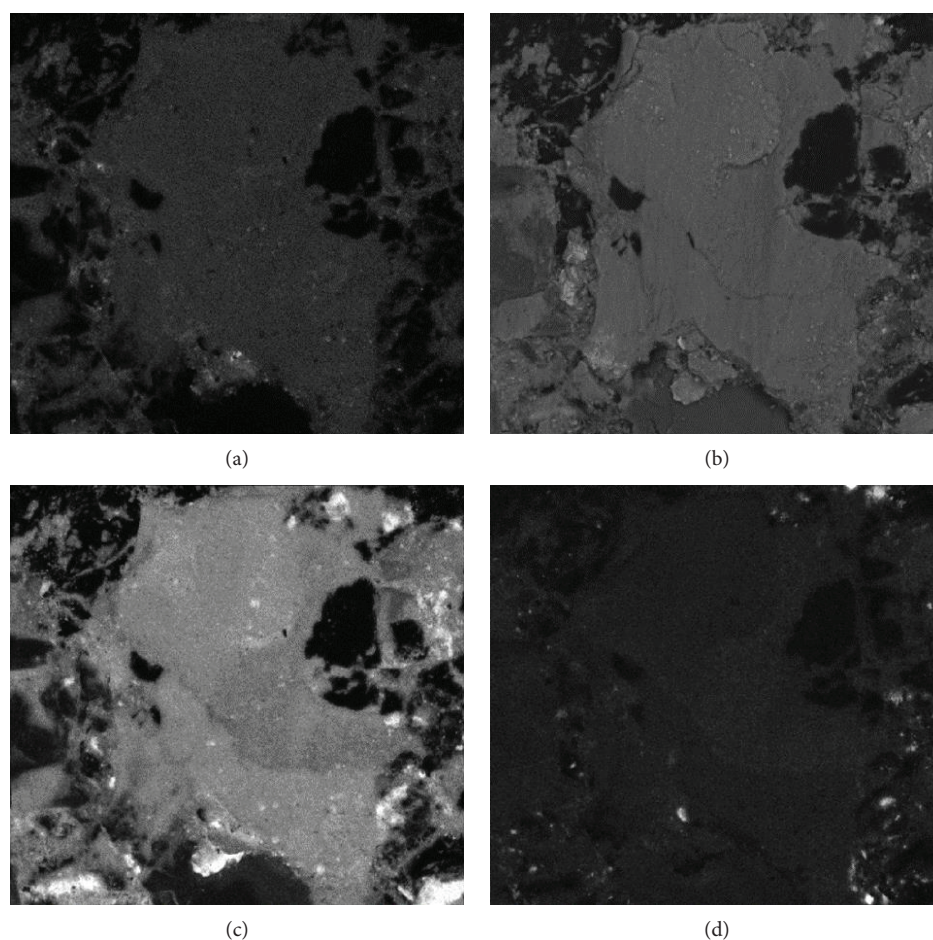


FIGURE 15: Image of a representative grain of Fe-Cu oxide: (a) Cu-K elemental map, (b) BSE image, (c) Fe-K, and (d) Sn-L.

TABLE 4: The average composition of 100 largest grains of Fe-Cu oxides from all samples.

| Spectra of 100 grains | O | Mg | Al | Si | S | K | Ti | Cr | Fe | Cu | Zn | Sn |
|-----------------------|-------|------|------|------|------|------|------|------|-------|-------|------|------|
| Average content wt% | 26.55 | 2.04 | 3.74 | 2.50 | 1.38 | 0.49 | 0.50 | 1.23 | 34.87 | 16.99 | 4.67 | 4.71 |

of potential environmental risk, because of anchoring of nanoparticles in a matrix. New useful properties of the friction composite can also be achieved by using a lower amount of suitable nanomaterial than conventional bulk material.

Data Availability

No data were used to support this study.

Conflicts of Interest

The authors of the paper certify that they have no affiliations with or involvement in any organization or entity with any financial interest.

Acknowledgments

This study was supported by the project no. LO1203 “Regional Materials Science and Technology Centre - Feasibility Program” funded by the Ministry of Education, Youth and Sports of the Czech Republic and by the European Union’s Horizon 2020 research and innovation programme under grant agreement no. 636592.

References

- [1] M. Eriksson, F. Bergman, and S. Jacobson, “On the nature of tribological contact in automotive brakes,” *Wear*, vol. 252, no. 1-2, pp. 26–36, 2002.
- [2] P. Filip, L. Kovařík, and M. Wright, “Automotive brake lining characterization,” in *Proceedings of the 15th Annual SAE Brake Colloquium*, pp. 41–61, Phoenix, Arizona, 1997.
- [3] A. Day, *Braking of Road Vehicles*, Elsevier Inc., Oxford, 2014.
- [4] K. Malachova, J. Kukutschova, Z. Rybkova et al., “Toxicity and mutagenicity of low-metallic automotive brake pad materials,” *Ecotoxicology and Environmental Safety*, vol. 131, pp. 37–44, 2016.
- [5] F. Amato, *Non-Exhaust Emission: An Urban Air Quality Problem for Public Health Impact and Mitigation Measures*, Academic Press, 2018.
- [6] V. Mahale, J. Bijwe, and S. Sinha, “Influence of nanopotassium titanate particles on the performance of NAO brake-pads,” *Wear*, vol. 376-377, pp. 727–737, 2017.
- [7] J. Bijwe, N. Aranganathan, S. Sharma, N. Dureja, and R. Kumar, “Nano-abrasives in friction materials-influence on tribological properties,” *Wear*, vol. 296, no. 1-2, pp. 693–701, 2012.
- [8] W. Sun, W. Zhou, J. Liu, X. Fu, G. Chen, and S. Yao, “The size effect of SiO₂ particles on friction mechanisms of a composite friction material,” *Tribology Letters*, vol. 66, no. 1, 2018.
- [9] K. Mamulová Kutláková, J. Tokarský, P. Kovář et al., “Preparation and characterization of photoactive composite kaolinite/TiO₂,” *Journal of Hazardous Materials*, vol. 188, no. 1–3, pp. 212–220, 2011.
- [10] W. Österle, C. Deutsch, T. Gradt, G. Orts-Gil, T. Schneider, and A. I. Dmitriev, “Tribological screening tests for the selection of raw materials for automotive brake pad formulations,” *Tribology International*, vol. 73, pp. 148–155, 2014.
- [11] R. C. Sharma and Y. A. Chang, “The S-Sn (sulfur-tin) system,” *Bulletin of Alloy Phase Diagrams*, vol. 7, no. 3, pp. 269–273, 1986.
- [12] S. J. Kim, M. H. Cho, R. H. Basch, J. W. Fash, and H. Jang, “Tribological properties of polymer composites containing barite (BaSO₄) or potassium titanate (K₂O₆(TiO₂)),” *Tribology Letters*, vol. 17, no. 3, pp. 655–661, 2004.
- [13] K. H. Cho, M. H. Cho, S. J. Kim, and H. Jang, “Tribological properties of potassium titanate in the brake friction material; morphological effects,” *Tribology Letters*, vol. 32, no. 1, pp. 59–66, 2008.
- [14] M. L. Halberstadt, S. K. Rhee, and J. A. Mansfield, “Effects of potassium titanate fiber on the wear of automotive brake linings,” *Wear*, vol. 46, no. 1, pp. 109–126, 1978.
- [15] K. Dědková, K. Matějová, J. Lang et al., “Antibacterial activity of kaolinite/nanoTiO₂ composites in relation to irradiation time,” *Journal of Photochemistry and Photobiology B: Biology*, vol. 135, pp. 17–22, 2014.

Research Article

Synthesis and Characterization of Ti-Fe Oxide Nanomaterials for Lead Removal

Buzuayehu Abebe  and H. C. Ananda Murthy

Department of Applied Chemistry, School of Applied Natural Sciences, Adama Science and Technology University, P.O. Box 1888, Adama, Ethiopia

Correspondence should be addressed to Buzuayehu Abebe; buzea8@gmail.com

Received 25 May 2018; Revised 16 August 2018; Accepted 9 September 2018; Published 7 November 2018

Guest Editor: Maria Giulia Faga

Copyright © 2018 Buzuayehu Abebe and H. C. Ananda Murthy. This is an open access article distributed under the Creative Commons Attribution License, which permits unrestricted use, distribution, and reproduction in any medium, provided the original work is properly cited.

TiO₂-Fe₂O₃ binary oxides containing different percentage of Fe₂O₃ were synthesized using impregnation method. The Fourier transform infrared spectroscopy (FT-IR), X-ray diffraction (XRD), scanning electron microscopy with energy-dispersive X-ray spectroscopy (SEM-EDX), and thermogravimetric with differential thermal analyzer (TG-DTA) analytical techniques were used for understanding of the physicochemical properties and well impregnation of Fe₂O₃ in TiO₂ lattice. During adsorption study, pH of the solution, adsorbent dosage, time of contact, agitation speed, and concentration of adsorbate were optimized. From Langmuir, Freundlich, FG, D-RK, Temkin, and FH adsorption isotherm models, relatively, Langmuir isotherm model fits well. For adsorption-reaction kinetic model, pseudo-first order (PFO), pseudo-second order (PSO), and Elovich were tested and intraparticle diffusion (IPD) for adsorption-diffusion kinetic models. Out of those, the PSO fits well; this indicates that the mechanism of adsorption is under control of adsorption-reaction. The mean adsorption energy, spontaneity, and reproducibility of the adsorbent were also conducted, and all of those studies support the domination of physical adsorption mechanism.

1. Introduction

Heavy metals are toxic pollutants which are not degradable biologically. The consumption of those heavy metals, even at trace level, has a risk for human beings. Therefore, removing of those metals is important [1]. Materials in nanosize range exhibit distinct properties and effective process parameters for removing pollutants. This is because of the small particle size (high surface area to volume ratio), specificity for pollutants, magnetic separation properties, surface chemistry, and surface interactions. In recent years, the use of semiconductor metal oxides for the removal of pollutants has gained more attention in the scientific community. Those oxide nanoparticles have been widely studied due to their new optical, magnetic, electronic, thermal, and mechanical behaviors and their roles in pollutant removal, catalyst, gas sensors, and photoelectronic device applications [2].

Liquid-solid translation synthesis methods of metal oxide nanomaterial are largely used in order to regulate the

shape, size, and structural features of the nanomaterials. Among many synthesis routes, frequently applied methods are sol-gel [3], coprecipitation [4], micelle and inverse micelle [5], hydrothermal method [6], mesoporous/nanoporous [7], sonochemical [8], and impregnation [9, 10]. The most common techniques used for heavy metal treatment include reduction and precipitation [11], coagulation-flocculation [12], electrocoagulation [13], adsorption [14], and membrane and ultramembrane filtration [15]. Among those different techniques, adsorption is the most common and popular method used to reduce pollutants that enter into water bodies.

Current studies have confirmed that nanosized titanium oxide has a number of unique properties (e.g., it is cheap, has high surface area, highly porous, nontoxic, high degree of contact, and hydrophilic in nature). It is also the most appropriate semiconductor for remediation of heavy metals and degradation of different dyes from aqueous solution. Even if this metal oxide has several positive key properties related to removal of pollutants, the agglomeration between its particles is the main problem. To overcome this challenge,

which makes it useless for pollutant remediation after, many researchers had tried in the past to develop TiO₂-based mixed oxide materials that can give large number of adsorptive sites without agglomeration. Among different types of metal oxides, iron oxide is found to be the best choice. And the most common iron oxides are γ -Fe₂O₃, α -Fe₂O₃, and Fe₃O₄ [4].

In this study, Ti-Fe binary oxides were synthesized by impregnation of iron oxide into titanium oxide using impregnation method. The as-synthesized material was characterized by TG-DTA (DTG-60H), FT-IR (Bruker IFS120 M PerkinElmer), and XRD and SEM/EDXS (ZEISS EVO 18) analytical techniques. And its adsorption capacity has been tested by removing the lead ion from aqueous solution. The explanation of adsorption isotherms about homogeneity, heterogeneity, fractional coverage, mean adsorption energy, energy of adsorbate-adsorbate interaction, and spontaneity was tested by Langmuir, Freundlich, FG, D-RK, Temkin, FH models, respectively. For adsorption-reaction kinetic study, PFO, PSO, and Elovich models were used, and for adsorption-diffusion kinetic studies, the IPD model was used. The effect of temperature and desorption experiments were also done.

2. Methodology

2.1. Synthesis. Impregnation method was used to synthesize nanosized TiO₂-Fe₂O₃ binary oxides [9, 10]. To prepare a 0.1 M solution, initially, iron (III) nitrate nonahydrate [(Fe(NO₃)₃·9H₂O) (99.95%) as precursor salt was dissolved in deionized water, and in this solution, the powder TiO₂ was added. The temperature of the solution was adjusted to 80°C on hotplate with constant stirring magnetic stirrer. Dilute NaOH was added dropwise to increase the pH of the solution from 3 to 8 and aged with stirring continuously for one hour for oxidation of Fe₃O₄ to Fe₂O₃. The precipitate was centrifuged and washed repeatedly with alcohol and water. Finally, it was calcined for 2 hours at 450°C after drying it in an oven at 110°C overnight. All chemicals/reagents used for this study have analytical grade purity.

2.2. Batch Adsorption Experiments. The adsorption experiment was carried out in 50 mL Erlenmeyer flasks having Ti-Fe oxide to lead ion aqueous solution ratio of 1:300 [0.1 g of iron oxides: 30 mL of 35 mg/L of Pb(NO₃)₂]. Equilibration of the experiments was done on a rotary shaker. Then, the obtained solution was filtered to separate the residue from the solution. The amount of lead ion deposited on adsorbent was obtained with the help of atomic adsorption spectroscopy (AAS). During the sorption experiments, the pH of the solution, dosage, speed of agitation, time of contact, and initial lead ion concentration were optimized. From the mass balance for the adsorbate in the glassware, the equation becomes

$$m(q_o - q_e) = (C_o - C_e)v. \quad (1)$$

To determine the equilibrium relationship at $q_o = 0$, the relation becomes

$$q_e = \frac{v}{m} \times (C_o - C_e). \quad (2)$$

The percent of sorption (%) was calculated using equation

$$\% = \left(\frac{C_o - C_e}{C_o} \right) * 100, \quad (3)$$

where C_o is the initial concentration (mg/L) and C_e is the equilibrium concentration (mg/L) of lead ion, q_e is the adsorption capacity of adsorbent (mg/g), v is the volume of reaction mixture (L), and m is the mass of adsorbent used (g).

2.2.1. Optimization of Parameters. To optimize the effect of pH on lead ion sorption, 0.1 g of the sorbent was taken into 50 mL of Erlenmeyer flask containing 30 mL of 40 mg/L lead ions and varying the pH of the solutions as 2, 4, 6, 8, 10, and 12. To optimize the amounts of loaded powder, 0.05, 0.10, 0.15, 0.20, 0.25, 0.30, and 0.35 g of sorbent were taken. The effect of speed of agitation was optimized by adjusting the speed of the shaker as 40, 70, 100, 130, 160, and 190 rpm. During optimization, the first optimized parameters are kept at the optimized value and those that are not optimized are kept at constant value.

2.2.2. Adsorption Isotherms. Sorption isotherm experiment was done by taking all the optimized values of parameters and varying the lead ion concentration as 15, 25, 35, 45, 55, 65, and 75 mg/L in a separate 50 mL Erlenmeyer flask.

2.2.3. Kinetics of Sorption. The study of kinetics was conducted by taking various contact time (10, 40, 70, 100, 130, and 160 min), and all the optimized values of parameters were used.

2.3. Temperature Effect. In order to determine the effect of temperature on sorption phenomenon, all predetermined and optimized values of parameters were used and the temperature was established at 25, 35, 45, and 55°C.

2.4. Desorption Study. Reproducibility study was done using lead ion-loaded powder obtained after sorption experiment and using optimized values. 0.1 g of lead ion-loaded binary oxide powder was added into six 50 mL of Erlenmeyer flasks having approximately 30 mL of distilled water, and the pH of the solution was adjusted to 2, 4, 6, 8, 10, and 12 using acid and base.

3. Result and Discussions

3.1. XRD. Figure 1(a) shows the XRD diffraction spectra of TiO₂, TiO₂-Fe₂O₃, and Fe₂O₃. The sharpness of the peak on TiO₂ and TiO₂-Fe₂O₃ shows its crystallinity. The particle size was calculated using Debye-Scherrer equation, $D = K\lambda/\beta \cos \theta$, where d is the mean size, K is a constant (0.9), λ is the wavelength of X-ray (0.15506 nm), β is the line of broadening (in radian), and θ is the Bragg angle; $\beta = G - g$, where G is the line width (in radians) and g is the instrument line broadening (in radians) [16]. Among the various percentages of Fe₂O₃ impregnated into TiO₂ lattice, the optimized particle size value was

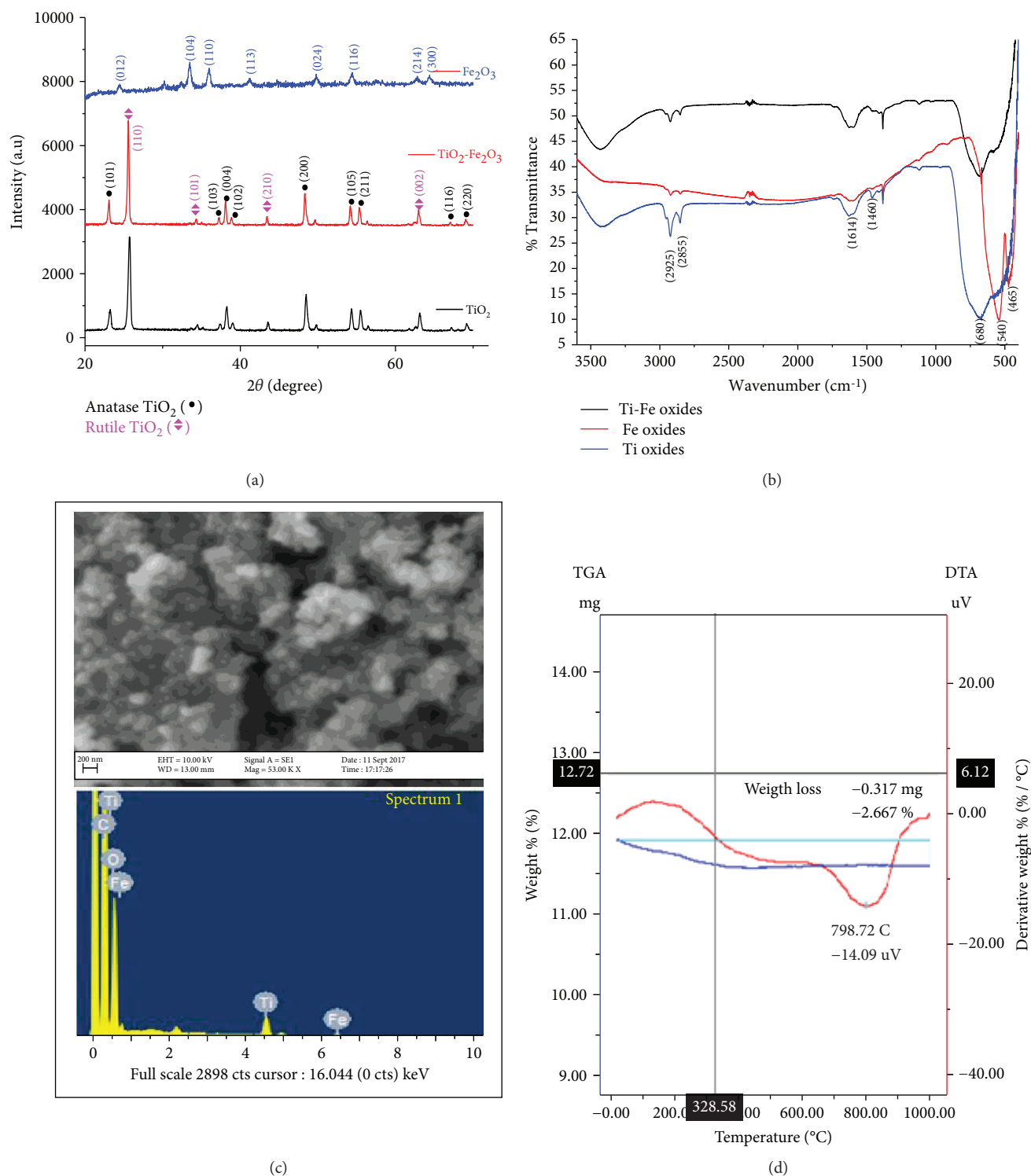


FIGURE 1: (a) XRD. (b) FT-IR. (c) SEM-EDX ($\text{TiO}_2\text{-Fe}_2\text{O}_3$). (d) TG-DTA spectra of nanosized metal oxides.

approximately found to be 31 nm (Table 1). The effects of Fe_2O_3 loading were investigated as shown in Table 1. The outcome revealed that the increase in loading of Fe_2O_3 causes increase in the particle size and then it further decreases as the percentage of iron oxide increases to 8.

In comparison with the separate titanium oxide peak and the reported result of pure titania spectra, 2θ

corresponding to 23.5(101), 37.1(103), 38.2(004), 38.8(102), 48.4(200), 54.40(105), 55.5(211), 67.1(116), and 69.1(220) was for anatase and the other 26.0(110), 34.2(101), 43.4(210), and 63.2 (002) are for rutile [17, 18]. No matching iron oxide peaks appeared in $\text{TiO}_2\text{-Fe}_2\text{O}_3$ diffraction spectrum. This indicates the total impregnation of small percentage of iron oxide in the

TABLE 1: Description of percentage composition and XRD results of the as-synthesized powders.

| TiO ₂ (%) | Fe ₂ O ₃ (%) | 2θ (degree) | β (degree) | θ (radian) | D (nm) |
|----------------------|------------------------------------|----------------|------------|------------|--------|
| 100 | 0 | 25.713 | 0.3542 | 0.2244 | 24.05 |
| 96 | 4 | 25.567 | 0.2509 | 0.2237 | 33.93 |
| 92 | 8 | 25.598 | 0.2758 | 0.2240 | 30.87 |
| 88 | 12 | 25.607 | 0.2520 | 0.2241 | 33.79 |
| 0 | 100 | 33.476 | 0.5237 | 0.2921 | 16.56 |

lattice of titanium oxides. As suggested by Jamalluddin and Abdullah [19], the absence of appearance of peaks for Fe₂O₃ may be due to the close similarities in radii of titanium and iron ion which were 0.68 and 0.64 Å, respectively; these similarities may cause substitution of one ion by the other. The other reason for the absence of iron peak may be due to its small percentage relative to titanium oxides [20].

3.2. *FT-IR*. From FT-IR spectra (Figure 1(b)), the band appeared at 680 cm⁻¹ was due to bending vibration of Ti-O and the broadband stretched from 500–700 cm⁻¹ was due to Ti-O-Ti and Ti-O bending vibration, and on the pure iron oxide FR-IR spectra, the two sharp band appeared at 540(α-Fe₂O₃) and 465(γ-Fe₂O₃) was due to bending vibrations of Fe-O bond. Except for some small shifts and decreasing of bands on the spectra of TiO₂-Fe₂O₃, both TiO₂ and TiO₂-Fe₂O₃ spectra are almost similar; this indicates the well impregnation of Fe₂O₃ in TiO₂ lattice. In fact, the linking of those two oxides was well confirmed by SEM-EDX analysis. The broad and strong absorption band appeared around 3426 cm⁻¹ and medium band at 1613 cm⁻¹ are attributed to the stretching vibration of hydroxyl (O-H) and water (H-O-H) groups absorbed on the adsorbent surface, respectively. Those bands are common on metal oxides and very essential for adsorption process [21, 22].

3.3. *SEM-EDX*. From the SEM-EDX spectrum of Ti-Fe oxide (Figure 1(c)), a spherical shape of nearly equal size was observed. The EDXS spectrum confirms only the presence of Fe, Ti, C, and O. The appearance of carbon (C) is from the standard used during analysis. The appearance of only the three elements without any other elements indicates the purity of the powder.

3.4. *TG-DTA*. From TG-DTA graph (Figure 1(d)) initially due to the removal of the surface deposited moisture or solvent molecules on the powder, a little weight loss was observed in between 0 and 110°C. The other weight loss occurred in between 200 and 250°C is probably due to the breakdown of metal hydroxide bonds of Fe(OH)₂. Out of 11.886 mg total weight, the loss is only 0.317 mg (2.667%). Above the temperature of 380°C, no weight loss occurred; this indicates that the thermal stability of the metal oxides is quite stable up to 1000°C [23]. In fact, oxides may undergo phase transitions which are not simply seen by TGA.

3.5. *Parameter Optimization*. The effects of solution pH, dose, agitation speed, and time of contact for sorption of lead ion were conducted (Figure 2). During pH optimization, the greatest sorption was observed under alkaline pH range (Figure 2(a)). Due to H⁺, the acidic pH makes the surface of metal oxides to be more positive, so repulsive interaction exists between the iron oxides and lead cation. Above seven pH value, the presence of OH⁻ assists the surface to be more negatively charged; therefore, the interactions become attractive [24]. On dosage optimization (Figure 2(b)), up to optimum point (0.1 g), the sorption efficiency was found to be high which is due to the availabilities of high sorption sites [25]. But, further increasing adsorbent dosage, it does not shows significant change, because the total number of the adsorbate becomes negligible. From Figure 2(c), as the speed of agitation increases, diffusion of lead ion towards the adsorbent surface also increases. After the optima (100 rpm), as the rate of agitation speed further increases, the adsorbate starts to desorb from the surface. And on contact time optimization (Figure 2(d)), after reaching optimum point 130 min, sorption capacity becomes constant since the sorbent sites were almost occupied.

3.6. *Adsorption Isotherms*. The experimental data conducted by taking different initial concentrations (Figure 2(e)) were fitted by Langmuir, Freundlich, Fowler-Guggenheim (FG), Flory-Huggins (FH), Temkin, and Dubinin-Radushkevich (D-RK) isotherm models. The linear equations for all isotherm models are given as follows:

$$\text{Langmuir : } \left(\frac{C_o}{q_e}\right) = \frac{1}{bq_{\max}} + \frac{C_e}{q_{\max}},$$

$$R_L = \frac{1}{(1 + bC_o)},$$

$$\text{Freundlich : } \log q_e = \log k_f + \left(\frac{1}{n}\right) \log C_e,$$

$$\text{Fowler-Guggenheim : } \frac{C_e(1-\theta)}{\theta} = \left(\frac{2w}{RT}\right)\theta - \ln k_{FG},$$

$$\text{Dubinin-Radushkevich : } \ln q_e = \ln q_s - \beta \varepsilon^2,$$

$$\varepsilon = RT \ln \left(1 + \frac{1}{C_e}\right),$$

$$E = \frac{1}{\sqrt{2\beta}},$$

$$\text{Temkin : } q_e = \left(\frac{RT}{b}\right) \ln k_T + \left(\frac{RT}{b}\right) \ln C_e,$$

$$\text{Flory-Huggins : } \ln \left(\frac{\theta}{C_o}\right) = \ln k_{FH} + n \ln (1-\theta),$$

$$\Delta G^o = -RT \ln (k_{FH}),$$

(4)

where C_o is the initial lead ion (adsorbate) concentration in solution (mg/L), C_e is the adsorbate equilibrium

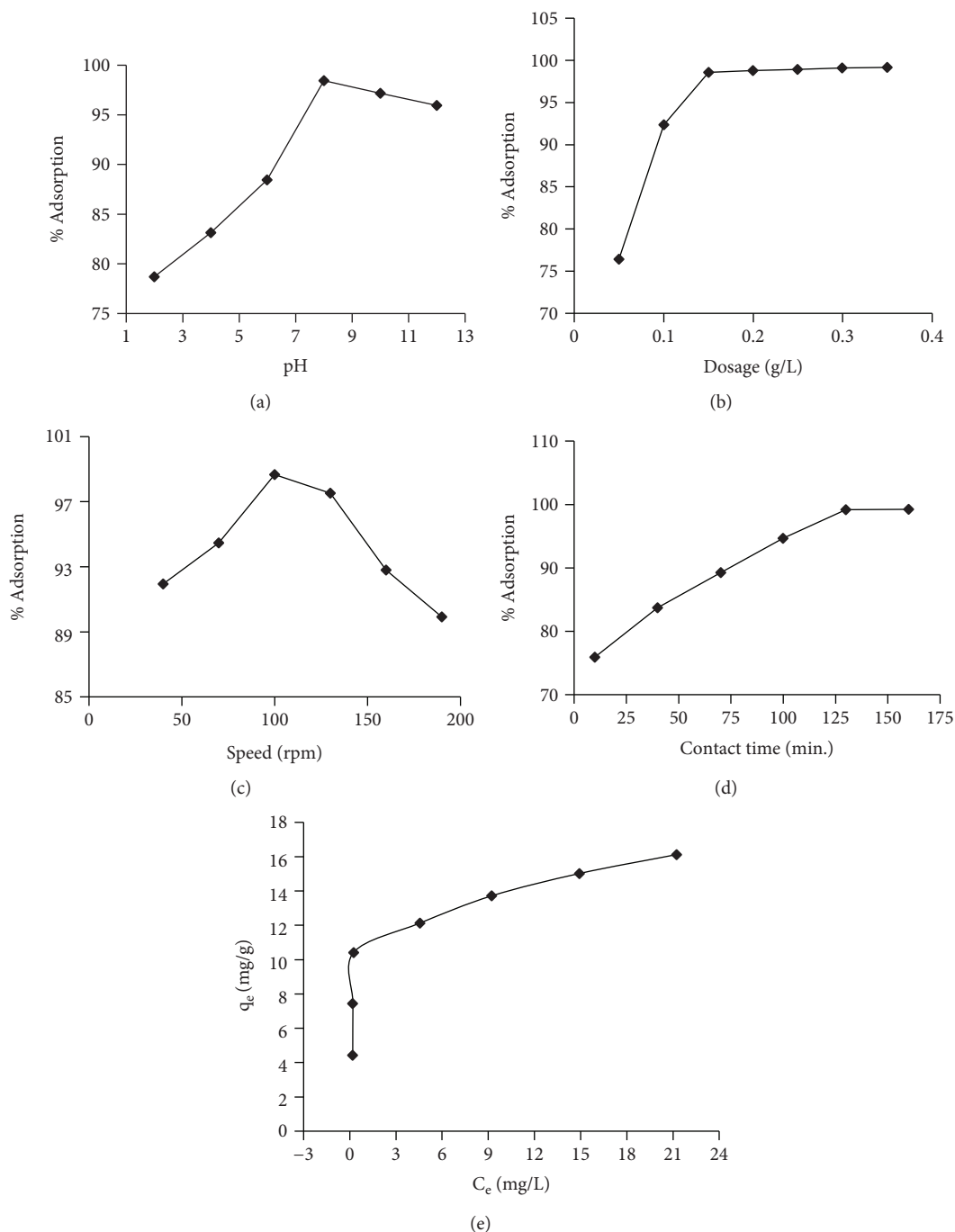


FIGURE 2: Effect of (a) pH, (b) adsorbent dose, (c) agitation speed, (d) contact time, and (e) adsorption isotherm for lead ion adsorption onto Ti-Fe oxide.

concentration in solution, q_e is the amount of adsorbate accumulated per gram of the adsorbent, q_{\max} is the maximum uptake corresponding to the site saturation, b is the ratio of adsorption and desorption rates, k_f is the distribution coefficient and represents the quantity of adsorbate adsorbed onto adsorbent for unit equilibrium concentration, $1/n$ is an empirical constant related to the magnitude of the adsorption or surface heterogeneity, $\theta = [1 - (C_e/C_o)]$ is

the fractional coverage, w is the interaction energy, ϵ is the Dubinin-Radushkevich isotherm constant, q_s is the saturation capacity (mg/g), β is the constant related to free energy, k_T is the Temkin isotherm equilibrium binding constant (L/g), b is the Temkin adsorption constant (J/molK), n is the number of ions occupying adsorption sites, T is the absolute temperature (K), and R is the universal gas constant (8.314 J/molK).

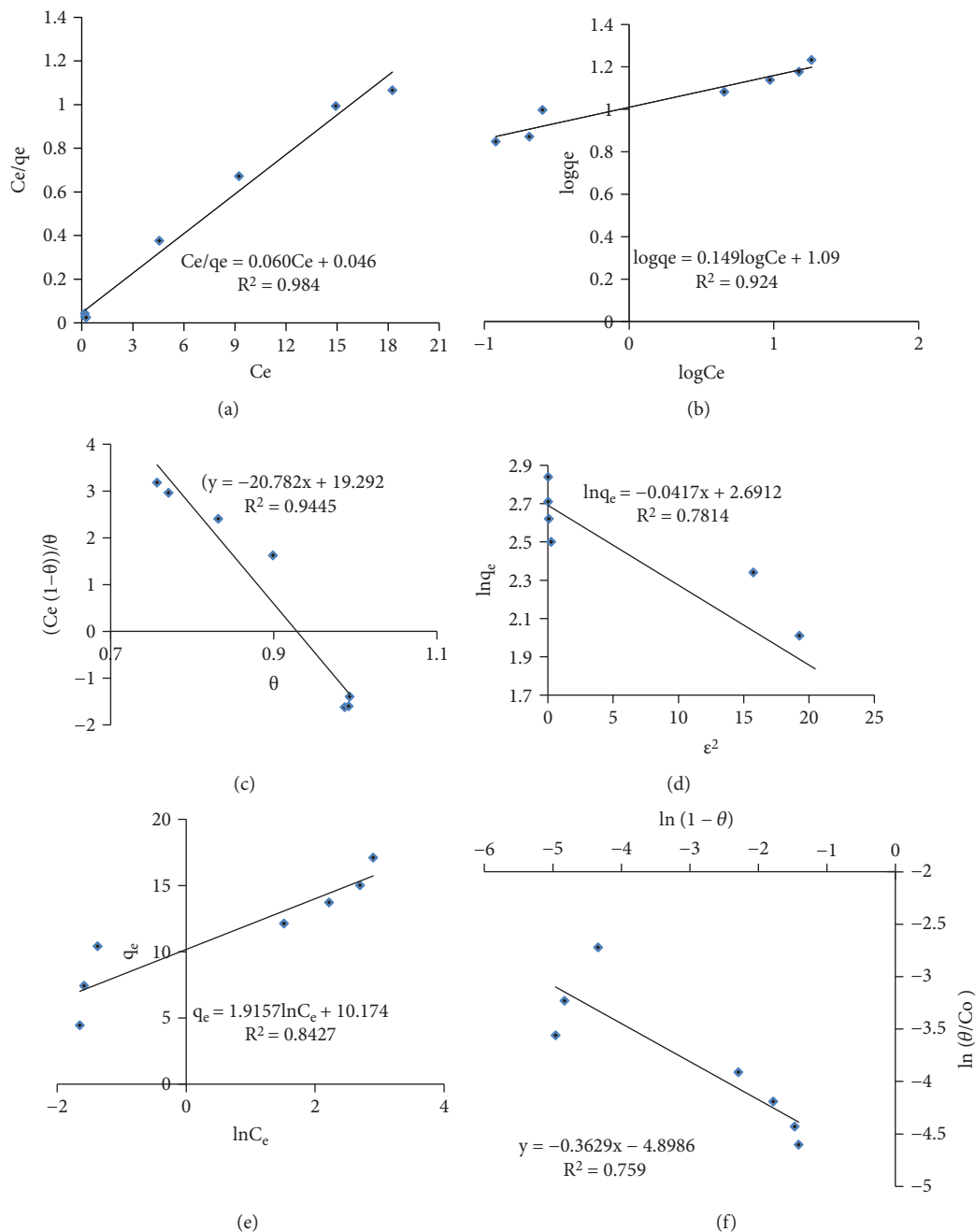


FIGURE 3: (a) Langmuir, (b) Freundlich, (c) Fowler-Guggenheim, (d) Dubinin-Radushkevich, (e) Temkin, and (f) Flory-Huggins adsorption isotherm.

TABLE 2: Kinetic constants for sorption of lead ion on binary oxide.

| q_{\max} | Langmuir | | Freundlich | | Fowler-Guggenheim | | Dubinin-Radushkevich | | Temkin | | Flory-Huggins | |
|------------|----------|-------|------------|------|-------------------|--------------|----------------------|---------|-------------|-------|---------------|---------------------|
| | b | R_L | k_f | n | k_{FG} | w (kJ/mol) | E (kJ/mol) | β | b (J/mol) | k_T | n | ΔG (kJ/mol) |
| 16.67 | 1.3 | 0.02 | 10.21 | 6.71 | $4.2 * 10^{-9}$ | -25.7 | 3.45 | -0.042 | 1293 | 202.5 | -0.363 | -12.137 |

Figures 3(a)–3(f) explain the sorption isothermal behavior based on concentration optimization results. The extracted sorption constant values are given in Table 2. Depending on R^2 values (given on each graph), Langmuir

sorption isotherm model (Figure 3(a)) fits the sorption data relatively better than other models. The R_L value tells the type of isotherm to be unfavorable ($R_L > 1$), linear ($=1$), irreversible ($=0$), and favorable (<1).

The R_L values in this study were in between 0 and 1 indicating that the adsorption is favorable. The Freundlich isotherm model (Figure 3(b)), which is responsible for the heterogeneity of the adsorbent sites. Generally, if the value of constant n is in between 1 and 10, the adsorption process becomes acceptable; when the value of n is greater than one, physical adsorption process occurs; and if it is less than one, the adsorption process becomes chemically driven. The value of n obtained for this study was 6.71, which shows the domination of physical adsorption process and also indicates the presence of high affinity between adsorbate and adsorbent.

From FG (Figure 3(c)) model which accounts the surface characteristics of adsorbate adsorbed on adsorbent, the value of heat of adsorption (w) being negative (-25.7 kJ/mol) indicates the presence of repulsive interaction between adsorbed molecules. D-RK (Figure 3(d)) and FH (Figure 3(e)) models fit relatively less; this may be because those models are suitable for only intermediate adsorbate concentration range. In D-RK isotherm model, the mean free energy, $E < 8$ kJ/mol, indicates the domination of physical adsorption, 8–16 kJ/mol (ion exchange) and 20–40 kJ/mol (chemical adsorption). The obtained mean free energy, E value for this study, was 3.45 kJ/mol, and this indicates that the physical adsorption is the controlling mechanism. The Temkin model (Figure 3(e)) is valid only for an intermediate range of adsorbate concentrations and gives information for adsorbate/adsorbate interactions. The constant k_T (202.5 L/g) on Temkin is an equilibrium binding constant which is related to maximum bonding energy. The FH model (Figure 3(f)) is responsible for the characteristic surface coverage of the adsorbate adsorbed on the adsorbent and responsible for suggesting the spontaneity of the reaction. The obtained value of standard free energy (ΔG°) from FH model was -12.14 kJ/mol; this value indicates that the reaction was spontaneous. The obtained maximum uptake corresponding to the site saturation (q_{\max}) for the adsorbent is 16.67 mg/g.

3.7. Kinetics of Adsorption. To interpret time-dependent experimental data, the linear equations of the PFO, PSO, Elovich, and IPD were given as follows:

$$\text{Pseudo-first order : } \log(q_e - q_t) = -\left(\frac{K_1}{2.303}\right)t + \log q_e,$$

$$\text{Pseudo-second order : } \frac{t}{q_t} = \left(\frac{1}{q_e}\right)t + \frac{1}{K_2 q_e^2},$$

$$\text{Elovich : } q_t = \left(\frac{1}{\beta}\right) \ln(\alpha\beta) + \left(\frac{1}{\beta}\right) \ln t,$$

$$\text{Weber-Morris IPD model : } q_t = k_i \sqrt{t} + C,$$

(5)

where q_e and q_t are the amounts of adsorbate adsorbed on the adsorbent at equilibrium and at various times, t (mg/g), respectively; K_1 is the rate constant of the PFO model for

the adsorption process (1/min); K_2 is the rate constant for the PSO model (g/gmin); α is the initial sorption rate (mol/gmin); β is the desorption constant (g/mol); k_i is the IPD constant (mg/gmin^{0.5}); and C (mg/g) is the intercept that gives an idea about boundary layer thickness—the larger the intercept is equal to the greater value of boundary layer effect.

The results of kinetics of sorption study obtained after optimization of all parameters are shown in Figure 4. From adsorption-reaction models, PFO (Figure 4(a)), PSO (Figure 4(b)), and Elovich (Figure 4(c)) were tested. Depending on R^2 values, PSO model relatively fits well than PFO and Elovich and its theoretical equilibrium capacity values (10.41 mg/g) also fit well with the experimental data values (10.87 mg/g). But there is great variation between experimental (3.133 mg/g) and theoretical (10.41 mg/g) values for PFO. Often, the calculated q_e value is less than the experimental value, but it should be close to each other to say the model is fitted well [26].

The calculated results and different constants for kinetic model are presented in Table 3. From adsorption-diffusion model which helps to check whether the reaction mechanism is under control of adsorption-diffusion in addition to surface reaction, the intraparticle diffusion (IPD) model was tested. Being the R^2 values for IPD is relatively less than other adsorption-reaction models, which suggests that the mechanism is not under control of adsorption-diffusion kinetics; actually, to say the reaction is under the control of diffusion kinetics, the IPD linear line should pass through the origin ($C = 0$), unlike that of obtained result in this paper. Therefore, it is possible to deduce that the reaction is totally under control of surface/adsorption-reaction [27].

3.8. Thermodynamics Study. The effect of temperature on lead ion sorption is shown in Figure 5(a). The values of ΔG° being negative and the values of ΔH° being positive indicate the respective spontaneous and an endothermic reaction of sorption (Table 4). As temperature increases, the ΔG° values decrease, which shows that the sorption process of lead ion is high at high temperature. The thermodynamic parameters (ΔG , ΔH , and ΔS) can be calculated using the following equation:

$$\Delta G = -RT \ln K_c,$$

$$\ln K_c = -\left(\frac{\Delta H^\circ}{RT}\right) + \frac{\Delta S^\circ}{R}, \quad (6)$$

$$\Delta G^\circ = \Delta H^\circ - T\Delta S^\circ,$$

where R (8.314 J/molK) is the universal gas constant, T is the absolute temperature, and K_c is the standard thermodynamic equilibrium constant defined by q_e/C_e . By plotting the graph of $\ln K_c$ versus $1/T$, the value of ΔH° and ΔS° can be estimated from the slopes and intercept values. The decrease in ΔG° with increasing of temperature indicates more efficient sorption at higher temperature [28].

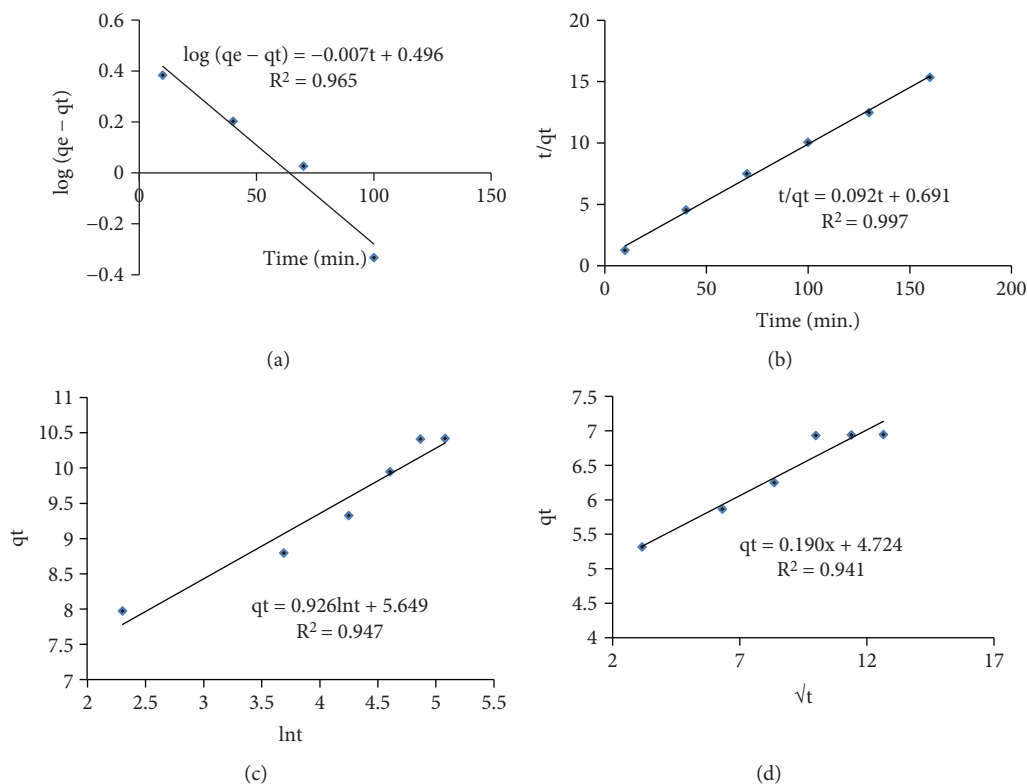


FIGURE 4: Plot of (a) pseudo-first order, (b) pseudo-second order, (c) Elovich, and (d) intraparticle diffusion model.

TABLE 3: Kinetic constants and coefficient values of lead sorption on binary metal oxides.

| Metal | q_e * | K_1 | Pseudo-first | | Pseudo-second | | | k_{dif} | IPD | | Elovich model | | |
|--------|---------|-------|--------------|-------|---------------|--------------|-------|-----------|-------|------|---------------|----------|-------|
| | | | q_e (mg/g) | R^2 | K_2 | q_e (mg/g) | R^2 | | R^2 | C | β | α | R^2 |
| Pb(II) | 10.41 | 0.016 | 3.133 | 0.965 | 0.012 | 10.87 | 0.997 | 0.19 | 0.947 | 4.72 | 1.08 | 173 | 0.941 |

*Represents calculated q_e values.

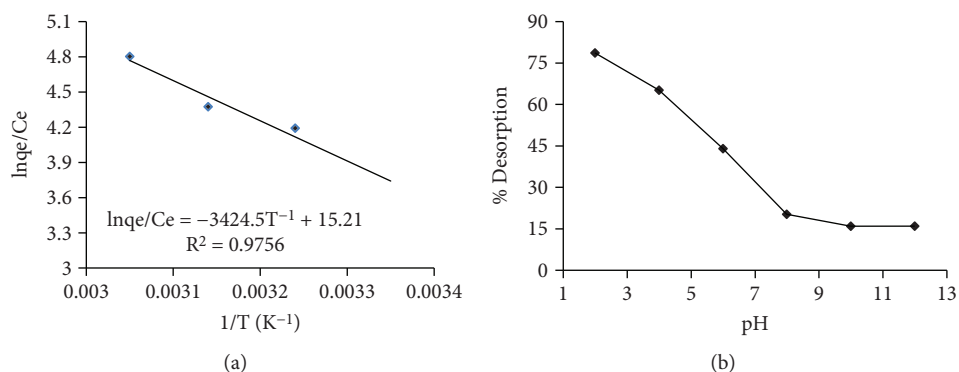


FIGURE 5: (a) Plot of thermodynamic study and (b) effect of pH on desorption of lead ion at various pH values.

3.9. Desorption Study. From the reproducibility/desorption studies (Figure 5(b)), as pH increases, the amount of desorption of lead ion decreases. About 79% of adsorbed lead ions were desorbed. Desorption efficiency was calculated using the equation as given below:

$$\% \text{ desorption efficiency} = \frac{\text{desorbed}}{\text{adsorbed}} * 100, \quad (7)$$

where desorbed is the amount of the lead ion that was removed from the loaded powder after desorption study and adsorbed is $C_o - C_e$ for each recovery process.

4. Conclusion

TiO₂-Fe₂O₃ oxides nanocomposite containing different percentage of iron oxide was successfully synthesized using

TABLE 4: Values of thermodynamic parameters for lead ion sorption.

| T (K) | ΔG (kJ/mol) | ΔH (kJ/mol) | ΔS (J/molK) |
|-------|---------------------|---------------------|---------------------|
| 298 | -9.219 | 28.471.3 | 126.48 |
| 308 | -10.48 | | |
| 318 | -11.75 | | |
| 328 | -13.01 | | |

impregnation method. The well impregnation of iron oxides on titanium oxides was confirmed by FTIR, XRD, and SEM-EDX (morphology-composition) analysis. FTIR and XRD analytical techniques confirm the appearance of crystalline binary metal oxide. The obtained approximate particle size for impregnated binary oxide was 31 nm. The superior stability of $\text{TiO}_2\text{-Fe}_2\text{O}_3$ oxide was revealed by TG-DTA analysis. Factors affecting sorption experiment (pH, adsorbent dose, speed of agitation, time of contact, and initial lead ion concentration) were optimized. Langmuir adsorption isotherm fits well than other isotherms models. From PFO, FSO, Elovich, and adsorption-reaction kinetic models, PSO fits the adsorption mechanism well. The IPD adsorption-diffusion model fails to fit well, and its line did also not pass through the origin. Therefore, the adsorption kinetics is under control of adsorption-reaction mechanism. The assistance of temperature increment for adsorption of lead ion on the adsorbent and spontaneity of the reaction was proofed by thermodynamics study.

Data Availability

The [Excel] data used to support the findings of this study are available from the corresponding author upon request.

Conflicts of Interest

The authors declare that they have no conflicts of interest.

Authors' Contributions

The study and the first draft writing were conducted by Buzuayehu Abebe, and the supervision and edition were done by Dr. H C. Ananda Murthy. Both authors participated in drafting the manuscript.

Acknowledgments

The authors are grateful to the management of Adama Science and Technology University for providing the financial support towards this research work. The authors acknowledge Mr. Yilkal Dessie for the software support, Dr. Senthilkumar Subramanian for the characterization support, and Guta Amanu for his assistance in the laboratory.

References

- [1] J. M. Rivera, S. Rincón, C. Ben Youssef, and A. Zepeda, "Highly efficient adsorption of aqueous Pb(II) with mesoporous metal-organic framework-5: an equilibrium and kinetic study," *Journal of Nanomaterials*, vol. 2016, 9 pages, 2016.
- [2] D. Mehta, S. Mazumdar, and S. K. Singh, "Magnetic adsorbents for the treatment of water/wastewater—a review," *Journal of Water Process Engineering*, vol. 7, pp. 244–265, 2015.
- [3] L. Durães, O. Oliveira, L. Benedini, B. F. O. Costa, A. Matos Beja, and A. Portugal, "Sol-gel synthesis of iron(III) oxyhydroxide nanostructured monoliths using $\text{Fe}(\text{NO}_3)_3 \cdot 9\text{H}_2\text{O}/\text{CH}_3\text{CH}_2\text{OH}/\text{NH}_4\text{OH}$ ternary system," *Journal of Physics and Chemistry of Solids*, vol. 72, no. 6, pp. 678–684, 2011.
- [4] I. J. Porter, S. K. Cushing, L. M. Carneiro et al., "Photoexcited small polaron formation in goethite ($\alpha\text{-FeOOH}$) nanorods probed by transient extreme ultraviolet spectroscopy," *The Journal of Physical Chemistry Letters*, vol. 9, no. 14, pp. 4120–4124, 2018.
- [5] Y. A. Gromova, V. G. Maslov, M. A. Baranov et al., "Magnetic and optical properties of isolated and aggregated CoFe_2O_4 superparamagnetic nanoparticles studied by MCD spectroscopy," *Journal of Physical Chemistry*, vol. 122, no. 21, pp. 11491–11497, 2018.
- [6] K. Nguyen, N. D. Hoa, C. M. Hung, D. T. Thanh Le, N. Van Duy, and N. Van Hieu, "A comparative study on the electrochemical properties of nanoporous nickel oxide nanowires and nanosheets prepared by a hydrothermal method," *RSC Advances*, vol. 8, no. 35, pp. 19449–19455, 2018.
- [7] X. Huang, G. Zhao, G. Wang, and J. T. S. Irvine, "Synthesis and applications of nanoporous perovskite metal oxides," *Chemical Science*, vol. 9, no. 15, pp. 3623–3637, 2018.
- [8] M. Rostami, M. Aghajanzadeh, M. Zamani, H. K. Manjili, and H. Danafar, "Sono-chemical synthesis and characterization of $\text{Fe}_3\text{O}_4@\text{mTiO}_2\text{-GO}$ nanocarriers for dual-targeted colon drug delivery," *Research on Chemical Intermediates*, vol. 44, no. 3, pp. 1889–1904, 2017.
- [9] X.-F. Dong, H.-B. Zou, and W.-M. Lin, "Effect of preparation conditions of $\text{CuO-CeO}_2\text{-ZrO}_2$ catalyst on CO removal from hydrogen-rich gas," *International Journal of Hydrogen Energy*, vol. 31, no. 15, pp. 2337–2344, 2006.
- [10] B. Abebe, A. M. Taddesse, T. Kebede, E. Teju, and I. Diaz, "Fe-Al-Mn ternary oxide nanosorbent: synthesis, characterization and phosphate sorption property," *Journal of Environmental Chemical Engineering*, vol. 5, no. 2, pp. 1330–1340, 2017.
- [11] E. Katsou, S. Malamis, and K. J. Haralambous, "Industrial wastewater pre-treatment for heavy metal reduction by employing a sorbent-assisted ultrafiltration system," *Chemosphere*, vol. 82, no. 4, pp. 557–564, 2011.
- [12] X. Tang, H. Zheng, H. Teng et al., "Chemical coagulation process for the removal of heavy metals from water: a review," *Desalination and Water Treatment*, vol. 57, no. 4, pp. 1733–1748, 2016.
- [13] J. Ding, L. Wei, H. Huang et al., "Tertiary treatment of landfill leachate by an integrated electro-oxidation/electro-coagulation/electro-reduction process: performance and mechanism," *Journal of Hazardous Materials*, vol. 351, pp. 90–97, 2018.
- [14] B. E. Monárrez-Cordero, P. Amézaga-Madrid, A. Sáenz-Trevizo, P. Pizá-Ruiz, W. Antúnez-Flores, and M. Miki-Yoshida, "Synthesis and characterization of composite Fe-Ti oxides nanoparticles with high surface area obtained via AACVD," *Ceramics International*, vol. 44, no. 6, pp. 6990–6996, 2018.
- [15] S. Malamis, E. Katsou, M. Stylianiou, K. J. Haralambous, and M. Loizidou, "Copper removal from sludge permeate with ultrafiltration membranes using zeolite, bentonite and

- vermiculite as adsorbents,” *Water Science and Technology*, vol. 61, no. 3, pp. 581–589, 2010.
- [16] R. Saravanan, J. Aviles, F. Gracia, E. Mosquera, and V. K. Gupta, “Crystallinity and lowering band gap induced visible light photocatalytic activity of TiO₂/CS (Chitosan) nanocomposites,” *International Journal of Biological Macromolecules*, vol. 109, pp. 1239–1245, 2018.
- [17] Y. Wang, L. Li, X. Huang, Q. Li, and G. Li, “New insights into fluorinated TiO₂ (brookite, anatase and rutile) nanoparticles as efficient photocatalytic redox catalysts,” *RSC Advances*, vol. 5, no. 43, pp. 34302–34313, 2015.
- [18] A. S. Zhao, S. Zhou, Y. Wang, J. Chen, C. R. Ye, and N. Huang, “Molecular interaction of fibrinogen with thermally modified titanium dioxide nanoparticles,” *RSC Advances*, vol. 4, no. 76, pp. 40428–40434, 2014.
- [19] N. A. Jamalluddin and A. Z. Abdullah, “Reactive dye degradation by combined Fe(III)/TiO₂ catalyst and ultrasonic irradiation: effect of Fe(III) loading and calcination temperature,” *Ultrasonics Sonochemistry*, vol. 18, no. 2, pp. 669–678, 2011.
- [20] M. A. Ahmed, E. E. El-Katori, and Z. H. Gharni, “Photocatalytic degradation of methylene blue dye using Fe₂O₃/TiO₂ nanoparticles prepared by sol-gel method,” *Journal of Alloys and Compounds*, vol. 553, pp. 19–29, 2013.
- [21] N. Abbas, G. N. Shao, M. S. Haider, S. M. Imran, S. S. Park, and H. T. Kim, “Sol-gel synthesis of TiO₂-Fe₂O₃ systems: effects of Fe₂O₃ content and their photocatalytic properties,” *Journal of Industrial and Engineering Chemistry*, vol. 39, pp. 112–120, 2016.
- [22] W. Subramonian, T. Y. Wu, and S.-P. Chai, “Photocatalytic degradation of industrial pulp and paper mill effluent using synthesized magnetic Fe₂O₃-TiO₂: treatment efficiency and characterizations of reused photocatalyst,” *Journal of Environmental Management*, vol. 187, pp. 298–310, 2017.
- [23] N. M. Al-Hada, E. Saion, H. M. Kamari et al., “Structural, morphological and optical behaviour of PVP capped binary (ZnO)_{0.4}(CdO)_{0.6} nanoparticles synthesised by a facile thermal route,” *Materials Science in Semiconductor Processing*, vol. 53, pp. 56–65, 2016.
- [24] A. E. Ofomaja, E. I. Unuabonah, and N. A. Oladoja, “Competitive modeling for the biosorptive removal of copper and lead ions from aqueous solution by *Mansonia* wood sawdust,” *Bioresource Technology*, vol. 101, no. 11, pp. 3844–3852, 2010.
- [25] Y. Liu, C. Luo, J. Sun, H. Li, Z. Sun, and S. Yan, “Enhanced adsorption removal of methyl orange from aqueous solution by nanostructured proton-containing δ-MnO₂,” *Journal of Materials Chemistry A*, vol. 3, no. 10, pp. 5674–5682, 2015.
- [26] K. L. Tan and B. H. Hameed, “Insight into the adsorption kinetics models for the removal of contaminants from aqueous solutions,” *Journal of the Taiwan Institute of Chemical Engineers*, vol. 74, pp. 25–48, 2017.
- [27] H. Yang, S. Masse, M. Rouelle et al., “Magnetically recoverable iron oxide-hydroxyapatite nanocomposites for lead removal,” *International journal of Environmental Science and Technology*, vol. 12, no. 4, pp. 1173–1182, 2015.
- [28] R. Alfaro-Cuevas-Villanueva, A. R. Hidalgo-Vazquez, C. D. J. Cortes Penagos, and R. Cortes-Martinez, “Thermodynamic, kinetic, and equilibrium parameters for the removal of lead and cadmium from aqueous solutions with calcium alginate beads,” *The Scientific World Journal*, vol. 2014, 9 pages, 2014.

Research Article

Microstructural Analysis and Magnetic Characterization of Native and Magnetically Modified Montmorillonite and Vermiculite

Yvonna Jiraskova ¹, Jiri Bursik ¹, Jana Seidlerova,² Katerina Mamulova Kutlakova,² Ivo Safarik,^{3,4} Mirka Safarikova,³ Kristyna Pospiskova,⁴ and Ondrej Zivotsky ^{5,6}

¹CEITEC IPM, Institute of Physics of Materials, Academy of Sciences of the Czech Republic, Zizkova 22, 616 00 Brno, Czech Republic

²Nanotechnology Centre, VSB–Technical University of Ostrava, 17. listopadu 15/2172, 708 33 Ostrava-Poruba, Czech Republic

³Department of Nanobiotechnology, Biology Centre, ISB, CAS, Na Sadkach 7, 370 05 Ceske Budejovice, Czech Republic

⁴Regional Centre of Advanced Technologies and Materials, Palacky University, Slechtitelu 27, 783 71 Olomouc, Czech Republic

⁵Department of Physics, VSB–Technical University of Ostrava, 17. listopadu 15/2172, 708 33 Ostrava-Poruba, Czech Republic

⁶Boris Yeltzin Ural Federal University, 620002 Ekaterinburg, Russia

Correspondence should be addressed to Yvonna Jiraskova; jirasko@ipm.cz

Received 16 May 2018; Revised 3 August 2018; Accepted 19 August 2018; Published 10 October 2018

Academic Editor: Luciano Carlos

Copyright © 2018 Yvonna Jiraskova et al. This is an open access article distributed under the Creative Commons Attribution License, which permits unrestricted use, distribution, and reproduction in any medium, provided the original work is properly cited.

Two clay minerals of the similar 2:1 layer structure and chemical composition, vermiculite and montmorillonite, were studied using a wide spectrum of experimental methods in their original states and the magnetically modified states after mixing with microwave-synthesized iron oxide particles. This magnetic modification led to different microstructural morphology influencing magnetic behaviour at room and more pronounced at low temperatures.

1. Introduction

The clay minerals, defined as a class of hydrated phyllosilicates [1], are the primary products of chemical weathering and the more abundant constituents of sedimentary rocks. From this viewpoint, their investigation is of high importance as it follows from many studies over the world, e.g., [2–4].

The basic unit of phyllosilicates (including clay minerals) is based on interconnected rings of SiO_4^{4-} tetrahedron that extend in infinite sheets [5]. Three apical oxygen atoms from each tetrahedron are shared with other tetrahedron, and the fourth apical oxygen points vertically upon the sheet. In such a way, a basic structural unit $\text{Si}_2\text{O}_5^{2-}$ is formed, and in an ideal case, the sheet yields a hexagonal symmetry, see Figure 1. Nevertheless, the tetrahedral position can be occupied also by Al atoms, and in such a way, the tetrahedral sheet is deformed, and its symmetry is lower than hexagonal.

An integral part forms the sheets of octahedrons $\text{X}(\text{O}, \text{OH})_6$ which share not only vertexes but also a half of edges. Octahedrons are tagged together by the octahedron plane perpendicularly to [001] so that three anions (O^- or OH^-) form a lower layer, three anions are in the upper layer and in between the octahedral cations (X), mostly Al, Fe, and Mg, are present. The occupation of the structural positions in the octahedral sheet generates trioctahedral sheet silicates where each O or OH is surrounded by 3 divalent cations, like Fe(II) or Mg(II), and dioctahedral sheet silicates where each O or OH ion is surrounded by 2 trivalent cations, mostly Al(III) [5].

The individual sheets can be variously connected. If the tetrahedral and octahedral sheets have one shared plane of oxygen atoms, the phyllosilicates are of type 1:1 (layers t-o). The type 2:1 (layers t-o-t) means that one octahedral sheet shares two tetrahedral sheets of opposite polarity. Then each tetrahedral sheet joins the octahedral sheet from one side with its apical oxygen atoms. A space

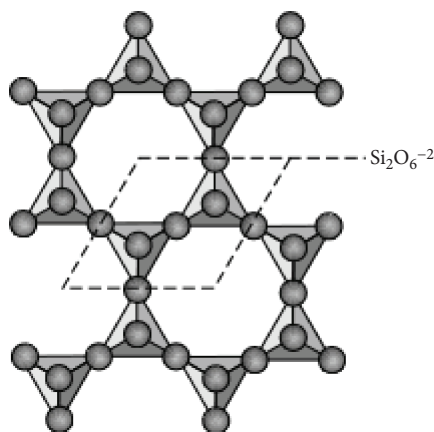


FIGURE 1: The basic structural unit of phyllosilicates.

between layers is denoted as interlayer, and one layer with interlayer forms a basic structural unit of phyllosilicates. The layers can be combined regularly or irregularly and can be electrically neutral or they can carry a certain negative charge due to substitutions. A charge size determines a mechanism of a mutual bond between layers in a structure [5]. Clay minerals are classified pursuant to several mentioned criteria: (i) layer type (1:1, 2:1), (ii) type of interlayer (water or interlayer cation), (iii) charge of layer, (iv) type of octahedral sheets (di- or trioctahedral), and (v) chemical composition. In accordance with these criteria, they are divided into a few groups [1, 6]. The clay minerals chosen for the present studies were montmorillonite from the group of smectites and vermiculite from the group of vermiculites.

Montmorillonite (Mt) is a member of the smectite group containing the layer of the 2:1 type. It means that it has two tetrahedral sheets of silica SiO_4 sandwiching a central octahedral sheet of one AlO_6 (Figure 2(a), [7]). The particles are plate-shaped with an average diameter lower than $2\ \mu\text{m}$ and a thickness of about 10 nm. Water molecules and cations occupy the space between the 2:1 layers. Generally, the crystalchemical formula is $(\text{Si}_4)^{\text{IV}}(\text{Al}_2 - y\text{Mg}_y)^{\text{VI}}\text{O}_{10}(\text{OH})_2 x\text{X}^+ \cdot n\text{H}_2\text{O}$, where X represents mono- (e.g., Na(I), K(I)) or divalent interlayer cations (Ca(II), Fe(II)). These mono- or divalent cations balance the negative charge of montmorillonite layers [8]. Essentially, the clay mineral can be modified in two ways: in the interlayer space in pursuance of swelling and cation exchange and on the surface due to an adsorption process.

Vermiculite (Ver) is also a layered clay mineral composed of two sheets of SiO_4 [9]; tetrahedra coupled symmetrically to another sheet of MgO_6^{4-} octahedral in a tetrahedral-octahedral-tetrahedral layer lattice (Figure 2(b), [7]). The basic characteristics can be found in [10]. The theoretical formula is $(\text{X}_v \cdot n\text{H}_2\text{O})(\text{R}_z^{2+}\text{R}_y^{3+})(\text{Al}, \text{Fe}^{3+})(\text{Si}_4\text{O}_{10})(\text{OH})_2$, where X represents mono- or divalent cations located primarily in the interlayer. The natural vermiculite contains usually the hydrated Mg(II) cations located

at the surface. They balance the negative charge of the SiO_4^- anions. In accordance with a structural analysis of Shirozu and Bailey [11], the Mg interlayer is octahedral coordinated with water molecules forming a mono-octahedral sheet.

The abovementioned clay minerals are widely used in the building and foundry industries, as a part of the thin layers and composites in modern technologies. They are also used in acoustics and in agriculture as fireproof insulators, fertilizer carriers, etc. [1]. For their high specific surface area, chemical and mechanical stabilities, variety of structural and surface properties, and high values of cation exchange capacities, they are an excellent group of adsorbents [12, 13]. Montmorillonite and vermiculite are used as effective sorbents for removing toxic ions [14–18], toxic molecules from waste water [19–21], dyes [22–25], or other compounds [26, 27].

In the last years, new materials are designed to improve sorption efficiency, decrease the price of purification technology, and enhance the functionality of a material. In order to improve the sorption properties of clay minerals, different acid activation and other chemical procedure modification were developed [28–31]. Most of the papers are devoted to the improvements of clay minerals from the viewpoint of their applications [32, 33]. Clay minerals modified by metal oxides in their interlayer space are known as pillared clays. The oxide particles act as pillars and keep silicate layers apart and form two-dimensional molecular sieves. Compared to original clay minerals, they have a higher fraction of the surface area.

In present study, the main attention is devoted to analysis of the complex structural and magnetic properties of the magnetically modified montmorillonite (MMt) and vermiculite (MVer) using the iron oxide particles and of the original, unmodified clay minerals (Mt, Ver). The structural properties, morphology and chemical composition, are determined by X-ray fluorescence spectroscopy (XRFS), scanning electron microscopy (SEM), transmission electron microscopy (TEM), and X-ray diffraction (XRD). The macro- and micromagnetic characterizations of samples are achieved by the magnetic and Mössbauer measurements at room and elevated temperatures completed by the low-temperature measurements.

2. Experiment

2.1. Sample Preparation. Two different types of clay minerals were used in present studies: montmorillonite (Mt) and vermiculite (Ver). Montmorillonite consists of a double aluminium and magnesium silicates. It was obtained from a product of the Beaufour Ipsen Industrie (France) which is used in medicine as diosmecticum containing besides montmorillonite also glucose, saccharine, and vanilla. These three components had to be removed by water leaching to obtain pure montmorillonite. Vermiculite was obtained from the Paraíba region of Brazil occurring in Santa Luzia [34].

The newly developed, relatively simple, procedure was applied for magnetic modification of both studied clay

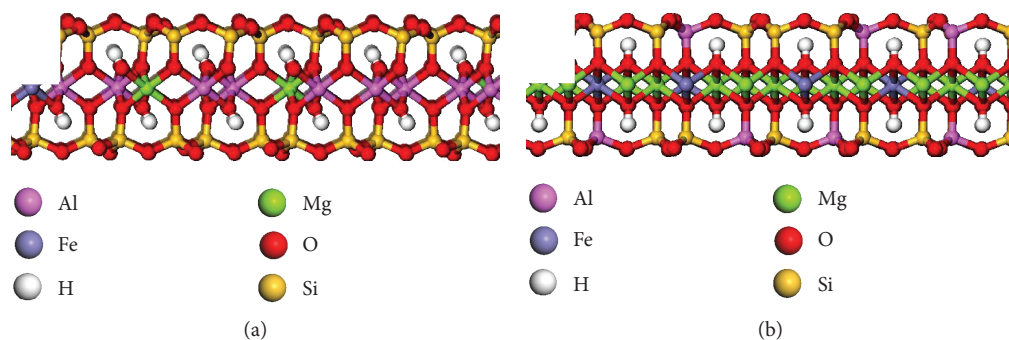


FIGURE 2: Chemical structure of montmorillonite (a) and vermiculite (b) [7].

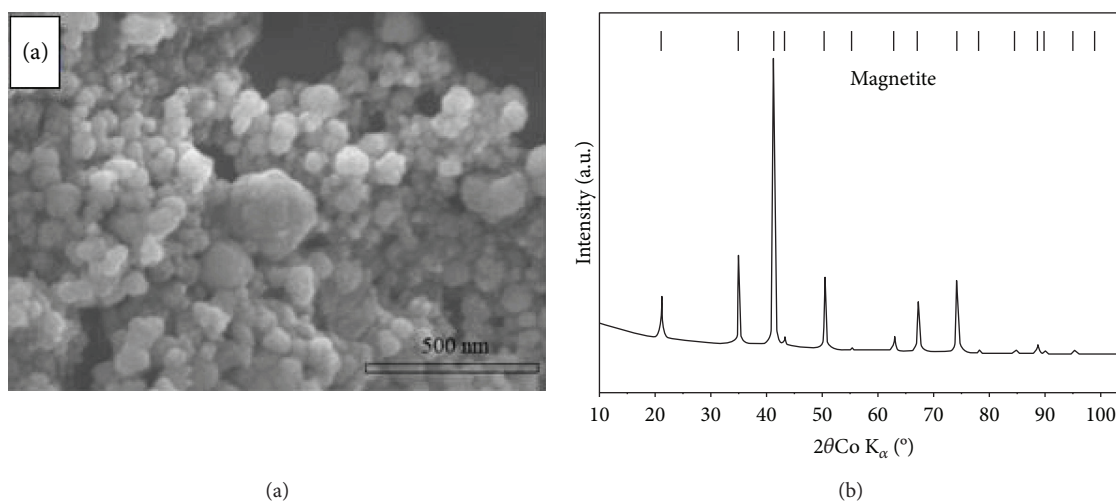


FIGURE 3: SEM micrograph (a) and X-ray powder diffraction pattern (b) of iron oxide nanoparticles prepared by microwave-assisted synthesis.

minerals. Initially, the magnetic iron oxide nanoparticles were prepared from a single Fe^{2+} salt—ferrous sulfate, employing a microwave irradiation according to the following procedure: 2 g $FeSO_4 \cdot 7H_2O$ was dissolved in 100 ml of water in an 800 ml beaker. Subsequently, NaOH solution (1 mol l^{-1}) was slowly added under stirring whereas the iron hydroxide precipitates were formed by monitoring pH. At pH 11–12, the beaker with suspension was filled with water to amount of 250 ml and inserted into a standard domestic microwave oven (700 W, 2.45 GHz) for 10 min. This resulted in the suspension containing magnetic iron oxide particles which were repeatedly washed with water to remove completely the rest of NaOH [35, 36]. The morphology of the final iron oxide powder is shown in Figure 3(a). An analysis of particle dimensions from the SEM images has yielded their mean size ranging between 25 nm and 100 nm. Sporadically, particles below 25 nm were also present. The analysis of the X-ray pattern in Figure 3(b) yielded the presence of pure magnetite with the lattice parameter $a = 0.8396(3) \text{ nm}$, in good agreement with literature data, e.g., [37]. The mean crystallite size was determined to be 43 nm.

In the next step, 10 ml suspension of iron oxide particles and water in ratio 1:4 (v/v ; magnetic particles sedimented overnight at 1 g) was mixed with 5 g of dried clay mineral Mt and/or Ver and stirred using a laboratory spoon as long as a homogeneous distribution of iron oxide particles in the clay mineral was obtained. Finally, the mixture was dried completely at 40°C .

2.2. Experimental Methods

2.2.1. Scanning Electron Microscopy (SEM). The morphology of iron oxide nanoparticles was analyzed by SEM 120 Hitachi SU6600 (Hitachi, Tokyo, Japan) with accelerating voltage 5 kV and by TESCAN LYRA 3XMU FEG/SEM scanning electron microscope working at accelerating voltage of 20 kV. The second microscope equipped with an XMax80 Oxford Instrument detector for EDX was used for the chemical composition of powdered samples pressed into a small disc of 3 mm in diameter.

2.2.2. X-Ray Fluorescence Spectroscopy (XRFS). The XRFS was performed using an energy dispersive spectrometer

equipped by Pd X-ray tube with Be window, 50 W/50 kV, targets HOPG, Mo, Al₂O₃, Xflash drift chamber, Si detector with Pelletier's cooling and resolution of 170 eV on line Mn K α at 10000 pulse/s (XEPOS, Spectro Al, Germany).

2.2.3. Transmission Electron Microscopy (TEM). A Jeol 2010 HC (resolution limit—0.19 nm) with a LaB₆ crystal cathode operating at 200 kV was used to study the microstructure of powders. Samples for TEM study were treated ultrasonically in an ethanol bath for 5 minutes and then placed on holey carbon copper grids for observations in an electron microscope.

2.2.4. X-Ray Powder Diffraction (XRD). X-ray powder diffraction measurements were done at room temperature (RT) using X'PERT PRO diffractometer by Panalytical. The samples were measured in a form of a small disc about 2 mm in diameter and approximately 500 μ m thick prepared by powder pressing and used subsequently for thermomagnetic measurements. The patterns were taken in a reflection mode using CoK α irradiation ($\lambda = 0.1789$ nm), Bragg-Brentano geometry, 2θ range 10°–100°, with 0.008° step and time per step 250 s.

2.2.5. Mössbauer Spectrometry. Mössbauer measurements were carried out at room and low (7 K) temperatures in standard transmission geometry using a ⁵⁷Co(Rh) source. The calibration of the velocity scale was performed with α -Fe, and the isomer shifts are given with respect to the RT Mössbauer spectrum of α -Fe. All spectra were evaluated within the transmission integral approach using the program CONFIT [38]. In the measured Mössbauer spectrum, the ferromagnetic (fm) phases are represented by sextuplets while the paramagnetic (pm) phase by singlets and/or doublets of Lorentzian lines. The phases can be characterized by either one or more subspectra depending on the atom ordering in the structure. All subspectra are characterized by discrete values of hyperfine parameters: isomer shift (δ), quadrupole splitting (ΔEQ) for pm, fm phase(s), and hyperfine induction (B) for fm phase(s). A weakly resolved atom ordering and/or highly defected region are represented by a distribution of hyperfine induction. The relative representation of phases is denoted by A.

2.2.6. Magnetic Measurements. The magnetic properties were studied using the vibration sample magnetometers (VSM) Microsense EV9 and Physical Property Measurement System (PPMS) Quantum Design Inc. Hysteresis curves describing the dependence of the mass magnetization on the applied magnetic field H were measured at room temperature (RT \approx 300 K) in an external field up to ± 1600 kA/m (2 T) and at low temperature (LT \approx 2 K) up to ± 4000 kA/m (5 T). The magnetic parameters, mass magnetization at 2 T and 5 T, remnant magnetization, and coercivity, were determined from the hysteresis curves with an accuracy $\pm 1\%$ [39]. To analyze the magnetic interactions among particles, the Henkel plot was constructed. It represents a relation between the initial (virgin) curve, $M_{\text{vir}}(H)$, and magnetizations at

increasing (M_{UP}) and decreasing (M_{DOWN}) positive magnetic fields [40]:

$$\Delta M(H) = M_{\text{VIR}}(H) - \frac{M_{\text{UP}}(H) + M_{\text{DOWN}}(H)}{2}. \quad (1)$$

The zero-field-cooled (ZFC) and field-cooled (FC) curves were measured between 2 K and 300 K in a magnetic field of 8 kA/m. The thermomagnetic curves (TMC) representing magnetic behaviour of samples at elevated temperatures were obtained in an external magnetic field of 8 kA/m, temperature increase of 4 K/min up to 1073 K, and vacuum to prevent oxidation. The transition from the magnetic to nonmagnetic state is characterized by a decrease in magnetization to zero value at Curie temperature. It was determined from the TMC with accuracy of about ± 5 K.

3. Results and Discussion

3.1. Chemical Composition and Morphology. The results of chemical analysis of the original (Mt, Ver) and magnetically modified (MMt, MVer) samples using XRFS and EDX are summarized in Table 1. An increase in content of the iron oxides after magnetic modification is evident at both samples. Besides Fe₂O₃, a small amount of wüstite Fe_{1-x}O was detected. A total content of iron oxides 8.38 wt% was slightly higher in vermiculite (MVer) compared to 5.62 wt% in montmorillonite (MMt).

SEM observations of both Mt and Ver samples have yielded similar morphology as seen in Figure 4. To obtain information about the chemical homogeneity, the Mt sample was chosen as an example for the local-dot and large area EDX chemical analyses summarized in Figure 5. The table corresponding to SEM image demonstrates that both large area (a) and local-dot analyse (b) show a dispersion smaller than 1% and thereby prove a high homogeneity of powder up to 1 micrometer level. The EDX analyses in Figure 5 were quantified and normalized without oxygen due to generally lower sensitivity of EDX for light elements. The results of elements were further recalculated with respect to oxygen stoichiometry of constituent phases, and the obtained values are given in Table 1 where they are compared with normalized data obtained by chemical analysis and recalculated without loss on ignition (LOI). A good agreement in obtained data is seen for all samples.

The more detail morphology of the vermiculite and montmorillonite samples in their original (Ver, Mt) and modified (MVer, MMt) states is seen in the TEM micrographs in Figure 6. They document that the submicron iron oxide nanoparticles occur at the surface and intergrain of the MVer and MMt samples and that their size is surprisingly larger at the MVer sample though the preparation procedure was the same for both clay minerals. This corresponds with a difference in XRD patterns of the magnetically modified samples in the next subsection.

TABLE 1: Chemical composition in wt% of the montmorillonite and vermiculite in their original states (Mt, Ver) and after the magnetic modification (MMt, MVer). LOI is loss on ignition; Mt_n , MMt_n , Ver_n , and $MVer_n$ denote normalized contents without LOI. Mt_{EDX} , MMt_{EDX} , Ver_{EDX} , and $MVer_{EDX}$ are the values obtained by EDX analysis and recalculated with respect to oxygen.

| | Mt | Mt_n | Mt_{EDX} | MMt | MMt_n | MMt_{EDX} | Ver | Ver_n | Ver_{EDX} | MVer | $MVer_n$ | $MVer_{EDX}$ |
|-----------|------------------|--------|------------|------------------|---------|-------------|------------------|---------|-------------|------------------|----------|--------------|
| Al_2O_3 | 14.4 ± 1.1 | 17.28 | 17.28 | 14.1 ± 1.2 | 18.23 | 16.68 | 10.5 ± 0.8 | 12.62 | 12.60 | 10.4 ± 0.8 | 12.32 | 14.18 |
| SiO_2 | 55.5 ± 2.3 | 70.28 | 73.56 | 54.1 ± 2.2 | 70.28 | 69.85 | 39.6 ± 1.6 | 67.46 | 51.63 | 39.2 ± 1.6 | 46.42 | 51.37 |
| TiO_2 | 0.17 ± 0.02 | 0.22 | 0.23 | 0.17 ± 0.02 | 0.22 | 0.25 | 1.03 ± 0.12 | 1.24 | 1.40 | 1.02 ± 0.12 | 1.21 | 0.34 |
| Na_2O | 0.20 ± 0.02 | 0.25 | 0.26 | 0.20 ± 0.02 | 0.25 | 0.16 | 0.50 ± 0.05 | 0.60 | 0.54 | 0.50 ± 0.05 | 0.59 | 0.07 |
| K_2O | 0.16 ± 0.0 | 0.20 | 0.14 | 0.16 ± 0.01 | 0.20 | 0.16 | 2.20 ± 0.14 | 2.64 | 3.74 | 2.18 ± 0.03 | 2.58 | 0.03 |
| MgO | 4.13 ± 0.25 | 5.23 | 4.54 | 4.03 ± 0.25 | 5.03 | 4.06 | 21.1 ± 1.28 | 25.37 | 18.28 | 20.9 ± 1.25 | 24.75 | 22.72 |
| CaO | 1.85 ± 0.12 | 2.34 | 2.14 | 1.81 ± 0.11 | 2.26 | 2.25 | 1.88 ± 0.13 | 2.26 | 2.20 | 1.86 ± 0.12 | 2.20 | 0.17 |
| Fe_2O_3 | 2.56 ± 0.10 | 3.24 | 1.87 | 4.69 ± 0.09 | 3.24 | 6.58 | 6.37 ± 0.25 | 7.66 | 9.61 | 7.54 ± 0.15 | 8.93 | 11.11 |
| FeO | — | — | — | 0.93 ± 0.08 | 1.16 | — | — | — | — | 0.84 ± 0.08 | 0.99 | — |
| LOI | 21.30 ± 0.30 | — | — | 20.30 ± 0.40 | — | — | 19.44 ± 0.02 | — | — | 19.60 ± 0.40 | — | — |

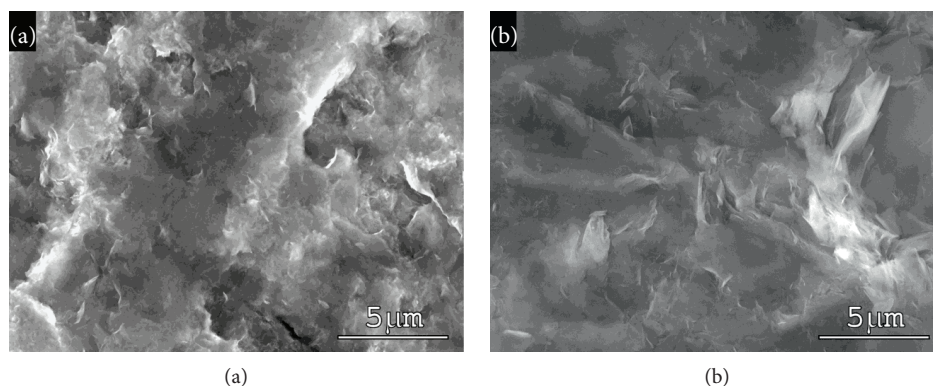
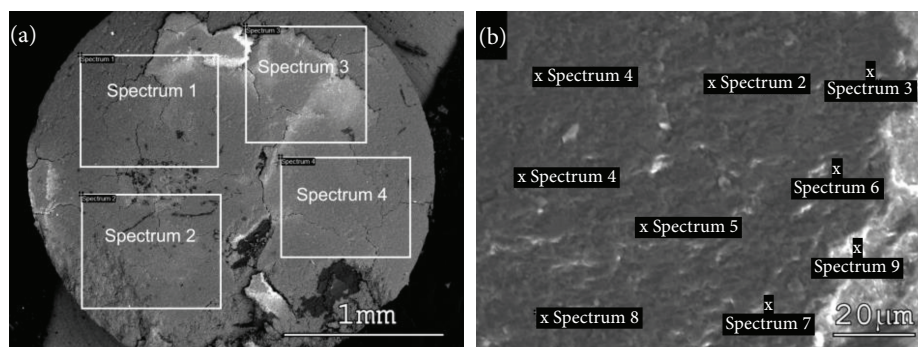


FIGURE 4: Morphology of the original (a) montmorillonite (Mt) and (b) vermiculite (Ver) samples obtained by SEM in the secondary electron mode.

3.2. *X-Ray Diffraction.* The X-ray diffraction patterns in Figure 7 represent the vermiculite (a) and montmorillonite (b) in their original (Ver, Mt) and magnetically modified (MVer, MMt) states. The diffraction patterns of both clay minerals are highly sensitive to chemical composition and to a strong texture consequently the layered nature as it follow from more detail studies of the vermiculite and/or montmorillonite taken from various geographic regions (e.g., [41–43]). The analysis of both magnetically modified samples did not yield any input of iron oxide nanoparticles into interlayers. The complicated composition of both clay samples was a reason why more detailed analysis of all patterns has remained out of the present study. The X-ray patterns in Figure 7 have only to document a difference between the original and the magnetically modified states. This difference is remarkably higher in the low-angle region for 2θ between 10° and 40° (upper panels), namely, at vermiculite. The outstanding peaks in both vermiculite samples (Ver, MVer) at $2\theta = 21.79^\circ - 29.07^\circ - 36.48^\circ - 44.27^\circ - 52.07^\circ$ yield nearly the same positions. At present, it can be only speculated that the magnetic modification did not affect the

structure of the sample. From the structural viewpoint, more detailed studies of both modified clay minerals should be done.

3.3. *Mössbauer Spectrometry.* The Mössbauer spectra of the original (Mt, Ver) and magnetically modified (MMt, MVer) montmorillonite and vermiculite samples recorded at room and low (7 K) temperatures are depicted in Figure 8. While the X-ray diffraction yields information on the major minerals in clays, Mössbauer spectroscopy looks selectively at the iron-containing compounds that are often difficult to detect by X-ray diffraction due to their low concentration, small particle size, or poor crystallinity. Nevertheless, also a unique interpretation of Mössbauer spectra can be sometimes difficult or impossible, either because the spectrum cannot be decomposed in a unique shape into individual components, or because different iron-based components have very similar Mössbauer patterns. Sometimes, it is helpful to supplement the measurements at ambient temperature by measurements at liquid nitrogen or helium temperatures.



| Spect. | Na | Mg | Al | Si | K | Ca | Ti | Fe |
|--------|------|------|-------|-------|------|------|------|------|
| (a) 1 | 0.48 | 5.54 | 18.36 | 69.50 | 0.17 | 3.02 | 0.20 | 2.72 |
| 2 | 0.34 | 5.39 | 18.05 | 68.87 | 0.19 | 3.76 | 0.34 | 3.06 |
| 3 | 0.38 | 5.62 | 18.83 | 69.90 | 0.16 | 2.75 | 0.30 | 2.07 |
| 4 | 0.32 | 5.43 | 18.32 | 69.08 | 0.34 | 3.14 | 0.39 | 2.97 |
| Mean | 0.38 | 5.49 | 18.39 | 69.34 | 0.22 | 3.17 | 0.31 | 2.71 |
| Stdv. | 0.07 | 0.11 | 0.32 | 0.46 | 0.09 | 0.43 | 0.08 | 0.42 |
| (b) 1 | 0.44 | 6.23 | 18.59 | 71.09 | 0.01 | 2.46 | 0 | 1.21 |
| 2 | 0.33 | 5.97 | 19.14 | 69.72 | 0.25 | 2.09 | 0.64 | 1.86 |
| 3 | 0.23 | 6.97 | 19.09 | 69.71 | 0.24 | 2.37 | 0.02 | 1.36 |
| 4 | 0.38 | 6.64 | 18.23 | 70.99 | 0.08 | 2.43 | 0.11 | 1.14 |
| 5 | 0.39 | 5.50 | 20.03 | 70.48 | 0.13 | 2.11 | 0.04 | 1.32 |
| 6 | 0.48 | 6.55 | 18.30 | 70.41 | 0.16 | 2.47 | 0.11 | 1.52 |
| 7 | 0.22 | 5.65 | 19.48 | 70.00 | 0.36 | 2.37 | 0.24 | 1.67 |
| 8 | 0.45 | 5.49 | 20.04 | 70.59 | 0 | 2.17 | 0.10 | 1.18 |
| 9 | 0.62 | 6.03 | 18.11 | 70.91 | 0.24 | 2.37 | 0.28 | 1.45 |
| Mean | 0.39 | 6.12 | 19.00 | 70.43 | 0.16 | 2.32 | 0.17 | 1.41 |
| Stdv. | 0.12 | 0.53 | 0.74 | 0.53 | 0.12 | 0.15 | 0.20 | 0.24 |

FIGURE 5: SEM micrographs of sample Mt with marked large area (a) and point (b) EDX analyses.

Iron may be present in both minerals as Fe(II) and Fe(III) and on positions with a tetrahedral or octahedral oxygen environment. They can be distinguished by hyperfine parameters, namely, isomer shift and quadrupole splitting.

The Mössbauer spectra for the Ver sample in its original state collected at 295 K and at 7 K are shown in Figure 8(a)—upper panel. The low-temperature spectrum yields a weak magnetically broadened six-line component with relative area of 3.6% pointed up in black color in the same way as in other spectra. Its hyperfine induction 51 T is slightly lower as obtained by other authors [40, 43]. The small relative area as well as isomer shift ($\delta = 0.37$ mm/s) and quadrupole splitting ($\Delta EQ = -0.45$ mm/s) make difficult an assignment to a specific oxide or oxyhydroxide. The magnetic modification of vermiculite (MVer) has contributed to an increase in relative area of magnetic component to 9.8% at RT and to 18.2% at 7 K. The hyperfine parameters obtained by analysis of the RT Mössbauer spectrum, $B = 46.82(33)$ T, $\delta = 0.55(5)$ mm/s, $\Delta EQ = -0.26(10)$ mm/s, and of the low-temperature spectrum, $B = 51.70(16)$ T, $\delta = 0.42(2)$ mm/s, $\Delta EQ = -0.06(4)$ mm/s, reflect rather a

complex iron (oxide, hydroxide, and oxyhydroxide) due to the presence of Al, Fe, and Ti cations and the anionic part either of oxygen ($-O$) and of the hydroxyl group ($-OH$ or $-OOH$). These results are supported also by the fact that the low-temperature spectrum consists of not only single sextuplets but also the hyperfine induction representing the mean value of the Gaussian hyperfine distribution with a width of 4.9(6) T. A more detail assignment to a certain component is also difficult because of variations in crystallinity.

The dominant paramagnetic fraction of all spectra has been fitted by four symmetric doublets whose parameters are listed in Table 2 for vermiculite samples and both temperatures. The doublets with isomer shift of ca. 1 mm/s can be assigned to Fe(II) ions and with smaller one around to Fe(III) in agreement with other authors [44–46].

The amount of iron-based compounds is in original montmorillonite (Mt) sample low as it results from the chemical analysis. The Mössbauer spectra are presented in Figure 8(b), upper panel. The parameters of doublets are summarized for both RT and low temperature in Table 3. The magnetic six-line components are seen in

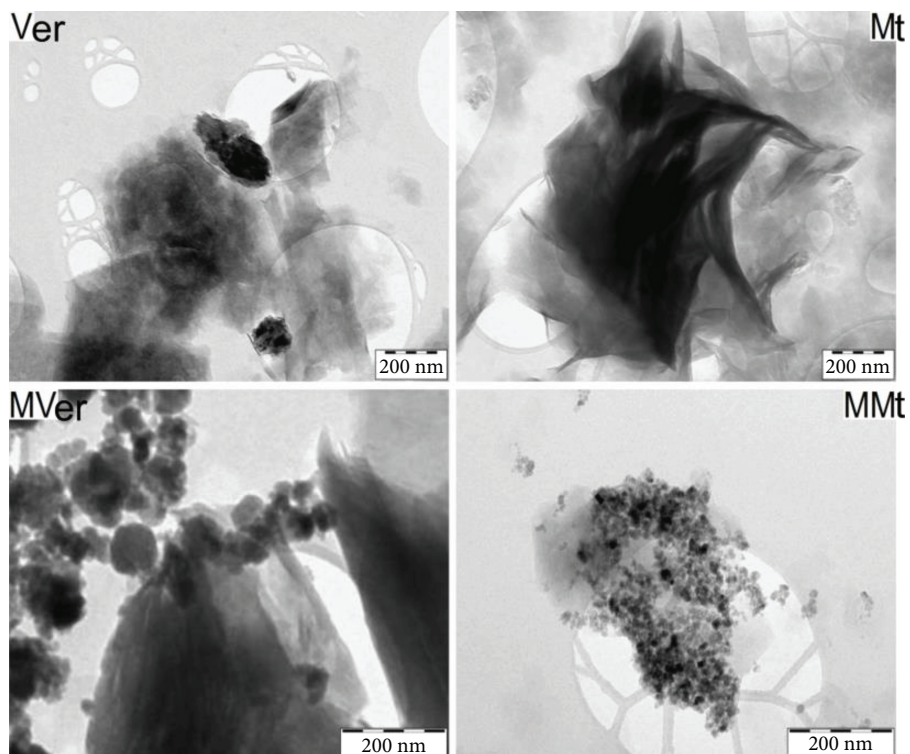


FIGURE 6: TEM micrographs of the original (Ver, Mt) and magnetically modified (MVer, MMt) clay minerals.

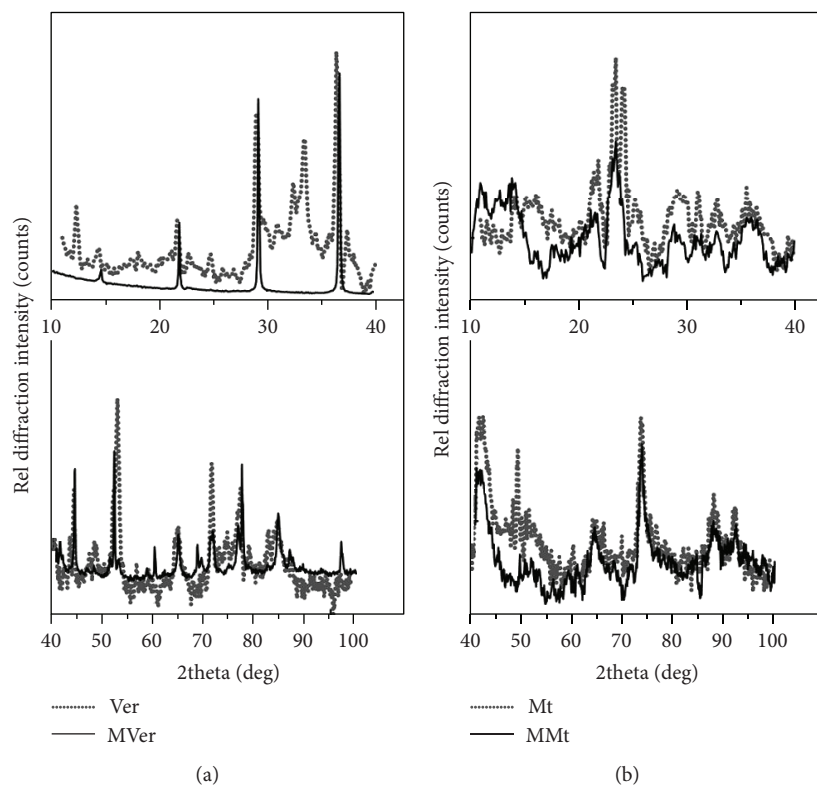


FIGURE 7: Room temperature reflection X-ray powder diffraction patterns of vermiculite (a) and montmorillonite (b) in the original (Ver, Mt) and magnetically modified (MVer, MMt) states.

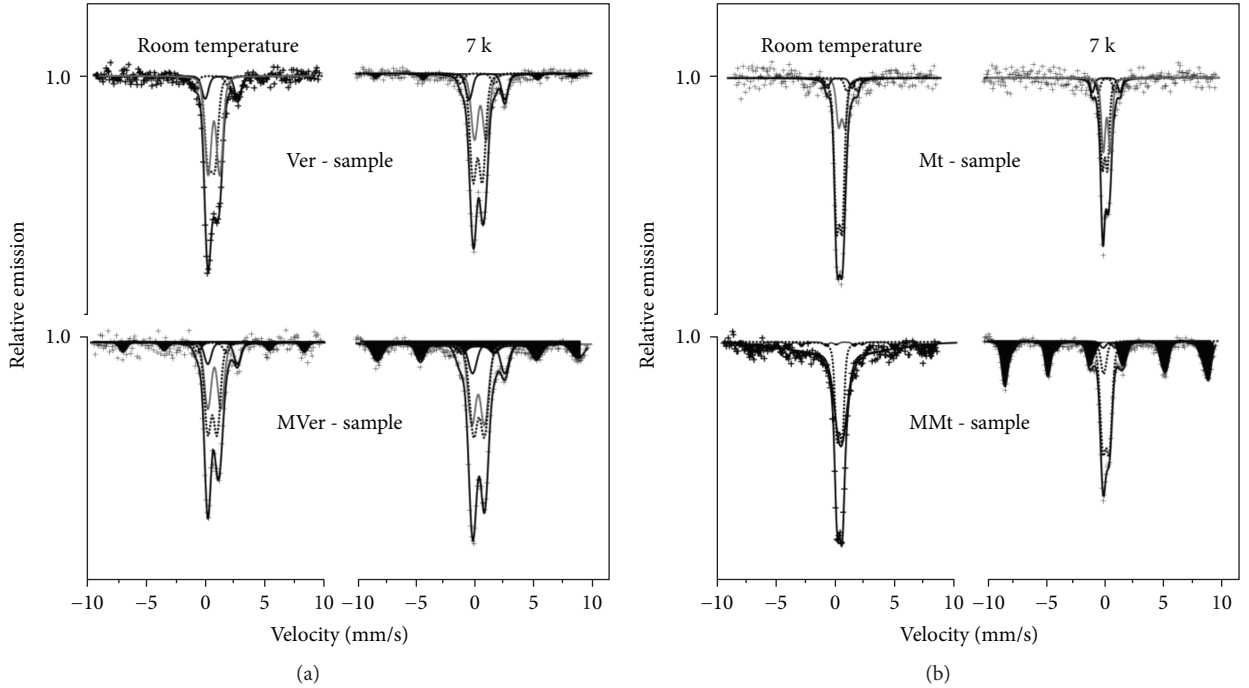


FIGURE 8: Mössbauer spectra of the original (Ver, Mt) and magnetically modified (MVer, MMt) vermiculite (a) and montmorillonite (b) samples measured at room and low temperatures.

TABLE 2: Mössbauer parameters of paramagnetic fraction in the vermiculite samples; original (Ver) and magnetically modified (MVer) state; T (K): temperature of measurement.

| T (K) | 295 | | 7 | |
|----------------------|-----------|-----------|----------|-----------|
| | Ver | MVer | Ver | MVer |
| δ_1 (mm/s) | 0.44 (1) | 0.48 (3) | 0.61 (2) | 0.43 (3) |
| δ_2 (mm/s) | 0.24 (1) | 0.32 (2) | 0.39 (1) | 0.48 (3) |
| δ_3 (mm/s) | 0.22 (1) | 0.28 (7) | 0.39 (4) | 0.30 (5) |
| δ_4 (mm/s) | 1.07 (4) | 1.17 (2) | 1.16 (2) | 1.37 (2) |
| ΔEQ_1 (mm/s) | 0.97 (2) | 1.09 (6) | 0.97 (4) | 1.05 (7) |
| ΔEQ_2 (mm/s) | 0.57 (2) | 0.76 (4) | 0.76 (2) | 0.95 (5) |
| ΔEQ_3 (mm/s) | 2.74 (12) | 2.40 (16) | 2.81 (8) | 2.92 (10) |
| ΔEQ_4 (mm/s) | 2.71 (9) | 2.46 (4) | 2.96 (4) | 2.55 (4) |

TABLE 3: Mössbauer parameters of paramagnetic fraction in the montmorillonite samples; original (Mt) and magnetically modified (MMt) state; T (K): temperature of measurement.

| T (K) | 295 | | 7 | |
|----------------------|-----------|----------|-----------|----------|
| | Mt | MMt | Mt | MMt |
| δ_1 (mm/s) | 0.41 (6) | 0.22 (1) | 0.48 (3) | 0.42 (1) |
| δ_2 (mm/s) | 0.20 (3) | 0.31 (1) | 0.32 (3) | 0.22 (1) |
| δ_3 (mm/s) | 1.26 (3) | — | 0.46 (4) | 0.67 (1) |
| δ_4 (mm/s) | 0.22 (6) | — | 0.42 (4) | — |
| ΔEQ_1 (mm/s) | 0.52 (7) | 0.42 (1) | 0.58 (5) | 0.54 (1) |
| ΔEQ_2 (mm/s) | 0.46 (1) | 0.04 (1) | 0.42 (3) | 0.00 (1) |
| ΔEQ_3 (mm/s) | 0.84 (10) | — | 1.36 (13) | 1.02 (1) |
| ΔEQ_4 (mm/s) | 2.06 (14) | — | 2.30 (7) | — |

the magnetically modified montmorillonite (MMt) occupying relative area of about 11% at RT and 51% at low temperature. The hyperfine parameters obtained for the MMt sample at RT, $B = 44.9$ T, $\delta = 0.46$ mm/s, $\Delta EQ = -0.02$ mm/s, and at 7 K, $B = 51.5$ T, $\delta = 0.45$ mm/s, $\Delta EQ = -0.06$ mm/s, are typical for nanocrystalline γ -Fe₂O₃ particles [47–49]. Similar to the MVer sample, the assignment of obtained values of the hyperfine parameters accurately to the specific iron oxide or oxyhydroxide is again difficult and not unique.

3.4. Magnetic Properties. The RT hysteresis curves, Henkel plots, and corresponding magnetic parameters of samples are depicted in Figure 9 and in Table 4, respectively. Montmorillonite (Mt) and vermiculite (Ver) in the original state own the coercive field of about 2.44 kA/m and 0.945 kA/m

and nearly the same low values of remanent magnetization. The magnetization at 2 T is higher at the Ver sample ($0.275 \text{ Am}^2\text{kg}^{-1}$) compared to $0.057 \text{ Am}^2\text{kg}^{-1}$ at the Mt sample that corresponds with higher iron oxide compounds found out by the chemical analysis (see Table 1). The magnetic field of 1.6 MA/m (2 T) is sufficient to saturate only the montmorillonite while at the vermiculite, the magnetization increase linearly above 100 kA/m of applied field and a substantial field is required to saturate it entirely. The magnetic modification leads to visible change in magnetization curves of both samples that are nearly saturated above 800 kA/m. The modified montmorillonite (MMt) exhibits higher saturation magnetization and markedly lower values of the remanent magnetization and coercivity (Table 4). It relates with higher relative area of the ferromagnetic

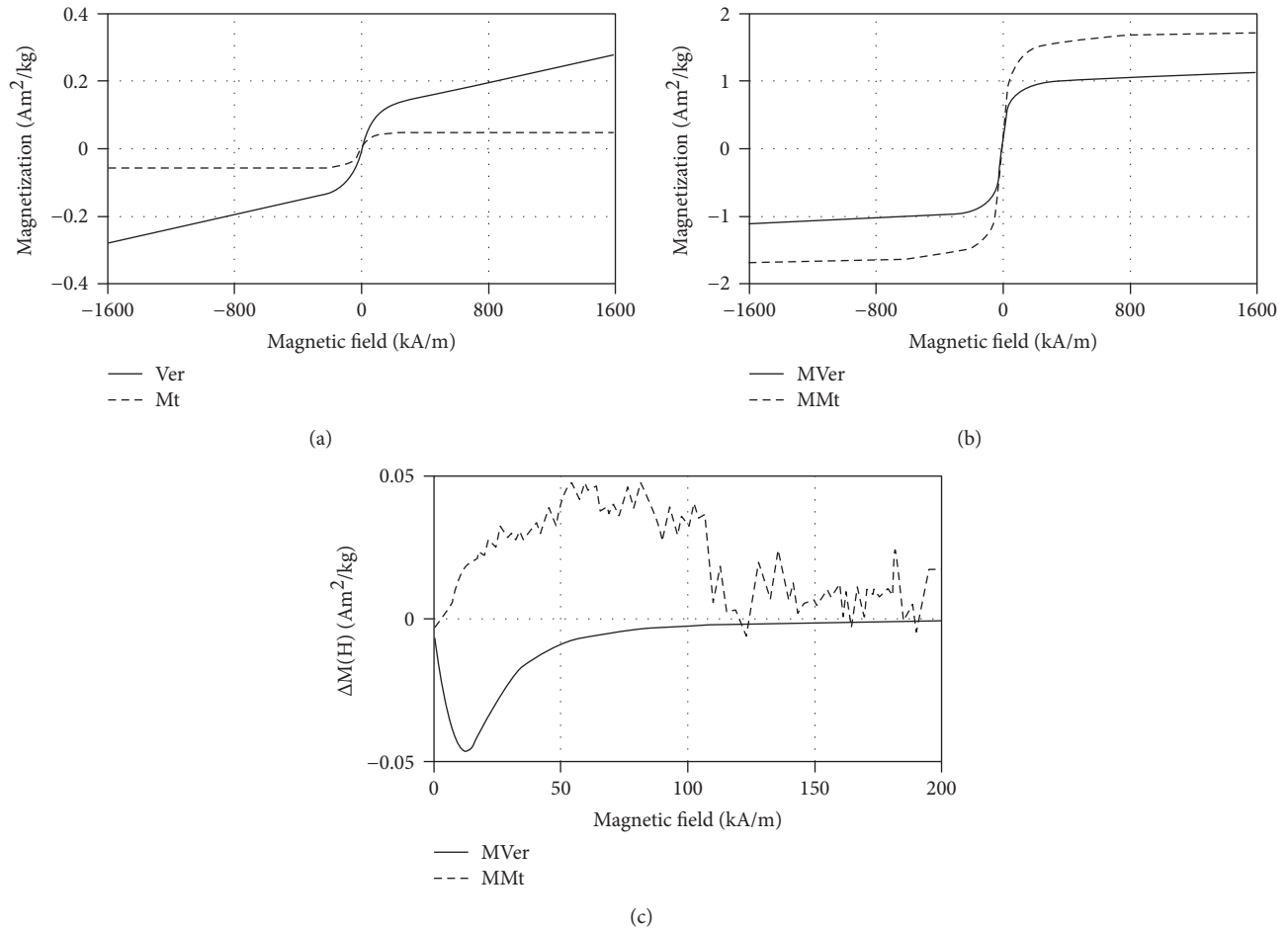


FIGURE 9: Room temperature magnetization curves of original samples (a), magnetically modified samples (b), and Henkel plots of MVer and MMt samples (c).

TABLE 4: Room temperature (RT \approx 300 K) and low-temperature (LT \approx 2 K) magnetic parameters of the original (Mt, Ver) and magnetically modified (MVer, MMt) vermiculite and montmorillonite samples; M : magnetization; M_r : remanent magnetization; H_c : coercivity.

| Sample | RT | | | LT | | |
|--------|--|---|--------------|--|---|--------------|
| | M at 2 T (Am ² kg ⁻¹) | M_r (Am ² kg ⁻¹) | H_c (kA/m) | M at 5 T (Am ² kg ⁻¹) | M_r (Am ² kg ⁻¹) | H_c (kA/m) |
| Mt | 0.057 | 0.003 | 2.440 | 6.554 | 0.017 | 3.065 |
| MMt | 1.695 | 0.004 | 0.018 | 9.116 | 0.790 | 26.502 |
| Ver | 0.275 | 0.004 | 0.945 | 14.383 | 0.031 | 2.378 |
| MVer | 1.113 | 0.146 | 6.066 | 13.912 | 0.414 | 18.503 |

component obtained by analysis of the Mössbauer spectrum at RT and more outstanding at the 7 K spectrum. A positive contribution to good magnetic parameters is also a visibly smaller particle size as it follows from TEM in Figure 6 (right panel bottom). It is supported by a well-known dependence of coercivity on the grain size presented by Herzer in [50]. Moreover, the particles in MMt are not agglomerated as it is at modified vermiculite, and therefore, the MVer sample embodies higher coercivity and remnant magnetization. The influence of particle agglomeration refer to the prevailing contributions of anisotropic energy reducing the magnetization at 1.6 MA/m (2 T) compared to the MMt sample.

The interparticle magnetic interactions were analyzed by Henkel plots using (1). While the original samples behave practically as noninteracting systems with very low negative magnetic dipole interactions (not presented), several times stronger interactions are observed for magnetically modified samples (Figure 9(c)). Positive exchange interactions dominate in the MMt sample due to low distances among separated very small nanoparticles. Interaction maximum is detected at magnetic fields about 60–80 kA/m. Contrarily, in the modified vermiculite the large objects of the small but agglomerated particles contribute to a visibly higher distances among them. Consequently, the negative dipole

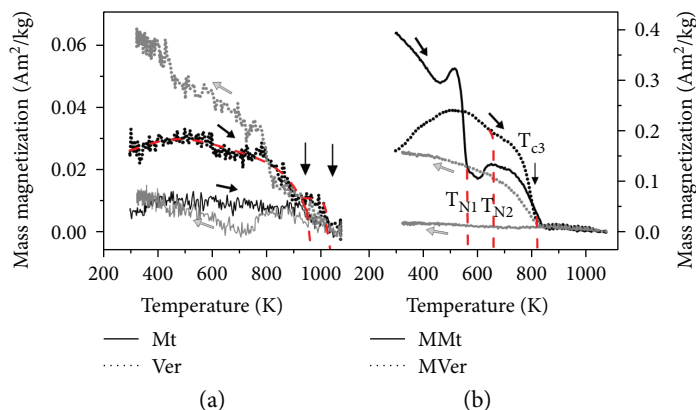


FIGURE 10: Thermomagnetic curves of the original (Ver, Mt) (a) and magnetically modified (MVer, MMt) samples (b) measured in an external magnetic field of 8 kA/m.

interactions with maximum at the lower magnetic field 11 kA/m prevail. It means that particles interact mainly through their total magnetic moments.

The thermomagnetic curves of samples in the original and magnetically modified states are presented in Figure 10. The measurements were done in an external magnetic field of 8 kA/m, and due to small magnetic moments of both samples in the original states (Ver, Mt), the curves are not smooth and the measurements reach a limit of equipment sensitivity. Magnetization curves at increasing temperature (Figure 10(a)) consist of two parts (red dashed lines), better resolved at the Ver sample. The first part decreases to zero at $T_{C1} \sim 950$ K corresponding to the Curie temperature of the α - Fe_2O_3 phase [46] and the second one at $T_{C2} \sim 1040$ K agrees with the Curie temperature of α -Fe.

The TMC curves in Figure 10(b) are visibly different due to the magnetic modification reflecting changes in Fe-based compounds. The Curie temperature $T_{C3} \sim 820$ K for MVer and MMt samples corresponds to a ferromagnetic-paramagnetic transition of maghemite, γ - Fe_2O_3 , [47] and thereby supports the Mössbauer results. The other two temperatures, Néel temperatures T_{N1} and T_{N2} , are very probably antiferromagnetic-paramagnetic transitions of the odd iron oxide and/or oxyhydroxide compounds.

The cooling of all samples back to room temperature returns them into a weak ferromagnetic and/or antiferromagnetic state with different magnetizations indicating the irreversible changes in the magnetic behaviour of powders treated up to 1073 K.

The behaviour of all samples below RT is documented by the FC/ZFC curves and hysteresis loops at 2 K shown in Figure 11 (Ver, Mt) and Figure 12 (MVer, MMt). The shape of FC/ZFC curves of Ver and Mt samples is practically identical showing slow changes of magnetization from 300 K to 25 K followed by its sharp increase from 25 K to 2 K. Such phenomenon was already observed, e.g., in hematite nanorods [51] or in CeO_2/α , γ - Fe_2O_3 nanocomposites [52], and could be ascribed to the magnetic phase transformation coming from ordering of surface spins at low temperatures and resulting in prevailing

exchange interactions among iron oxide particles and increase of magnetization.

The LT loops of samples in both original and magnetically modified states document that their saturation is not achieved even in the applied external field of 5 T (4 MA/m). The main reason could be in the presence of metal and ionic compounds, in different influences of ferrous and/or ferric iron, in very small grains, and also in a direction of the applied field with regard to direction of the sheets [53]. All magnetic parameters determined from the LT loops of the original and magnetically modified samples yield higher values compared to RT parameters (see Table 4).

The ZFC curves for MVer and MMt samples differ. The ZFC curve of the MVer sample shows an atypical behaviour when it decreases nearly linearly with decreasing temperature and at about 25 K an inexpressive maximum denoted as blocking temperature T_B can be seen at this curve (inset in Figure 12—upper right panel). This T_B temperature separates the high-temperature superparamagnetic state from the low-temperature blocked state of magnetic moment of nanoparticles. Another characteristic value is irreversible temperature T_{irr} defining a point at which the ZFC and FC curves separate. It corresponds to blocking temperature of the largest nanoparticles in the system and achieves here 300 K. Minimum at the ZFC curve and subsequent increase in magnetization below about 10 K is related again to the surface spins of particles, effect observed already at original samples.

The magnetically modified montmorillonite (MMt) exhibits contrary to the MVer sample superparamagnetic behaviour at RT with nearly zero coercive field and remnant magnetization. It means that temperature fluctuations of nanoparticles easily overcome the barrier consisting of their anisotropic energy. However, marked increase of H_c up to 26.5 kA/m at 2 K confirms that during cooling of the MMt sample, magnetic nanoparticles attract the properties typical for magnetically ordered materials and pass into the blocking state at $T_B \approx 150$ K (see Figure 12).

The difference between blocking T_B (150 K) and irreversible T_{irr} (~ 200 K) temperatures is relatively small and reflects a narrow size distribution of particles. Moreover,

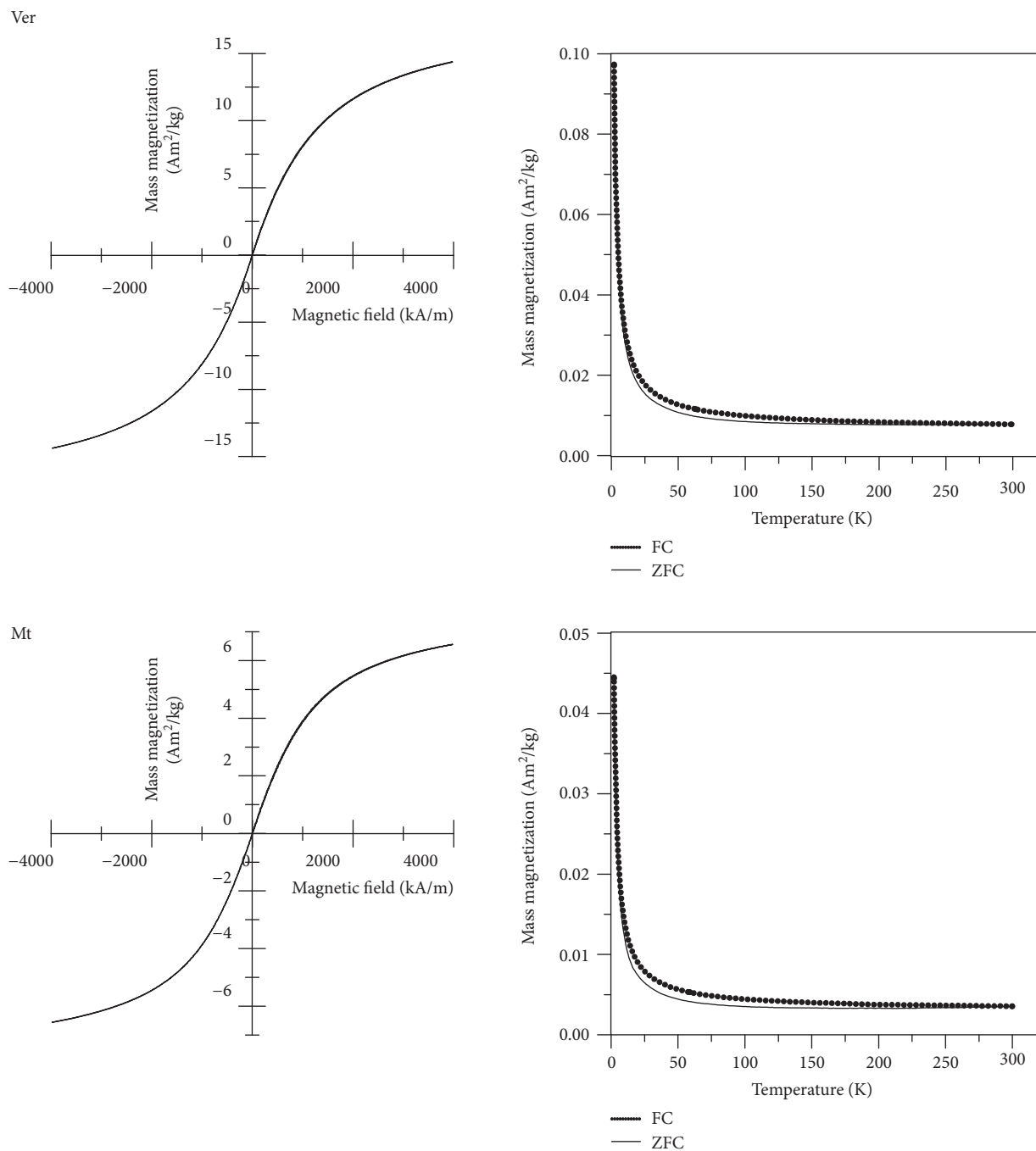


FIGURE 11: Low-temperature magnetization curves of original (Ver, Mt) samples measured at 2 K supplemented by the ZFC/FC curves.

the FC curve below T_B is nearly constant which is typical for the system yielding strong interparticle interactions. The ZFC curve below about 10 K increases in a similar way as was observed at all previous samples reflecting an influence of the spins.

4. Conclusions

Montmorillonite from the smectite group and vermiculite from the vermiculite group were magnetically modified by mixing the original clay minerals with iron oxide particles

prepared using a microwave irradiation procedure. The complex structural and magnetic studies of the original and magnetically modified powders were performed using scanning and transmission electron microscopy, X-ray fluorescence spectroscopy, X-ray diffraction, Mössbauer spectrometry, and magnetic methods at room temperature. Most of the results is supported also by low-temperature measurements. Both clay minerals are of the 2:1 layer type, and SEM observations yield similar morphology and large-area as local-dot chemical homogeneity of all studied samples. Nevertheless, the TEM micrographs clearly show

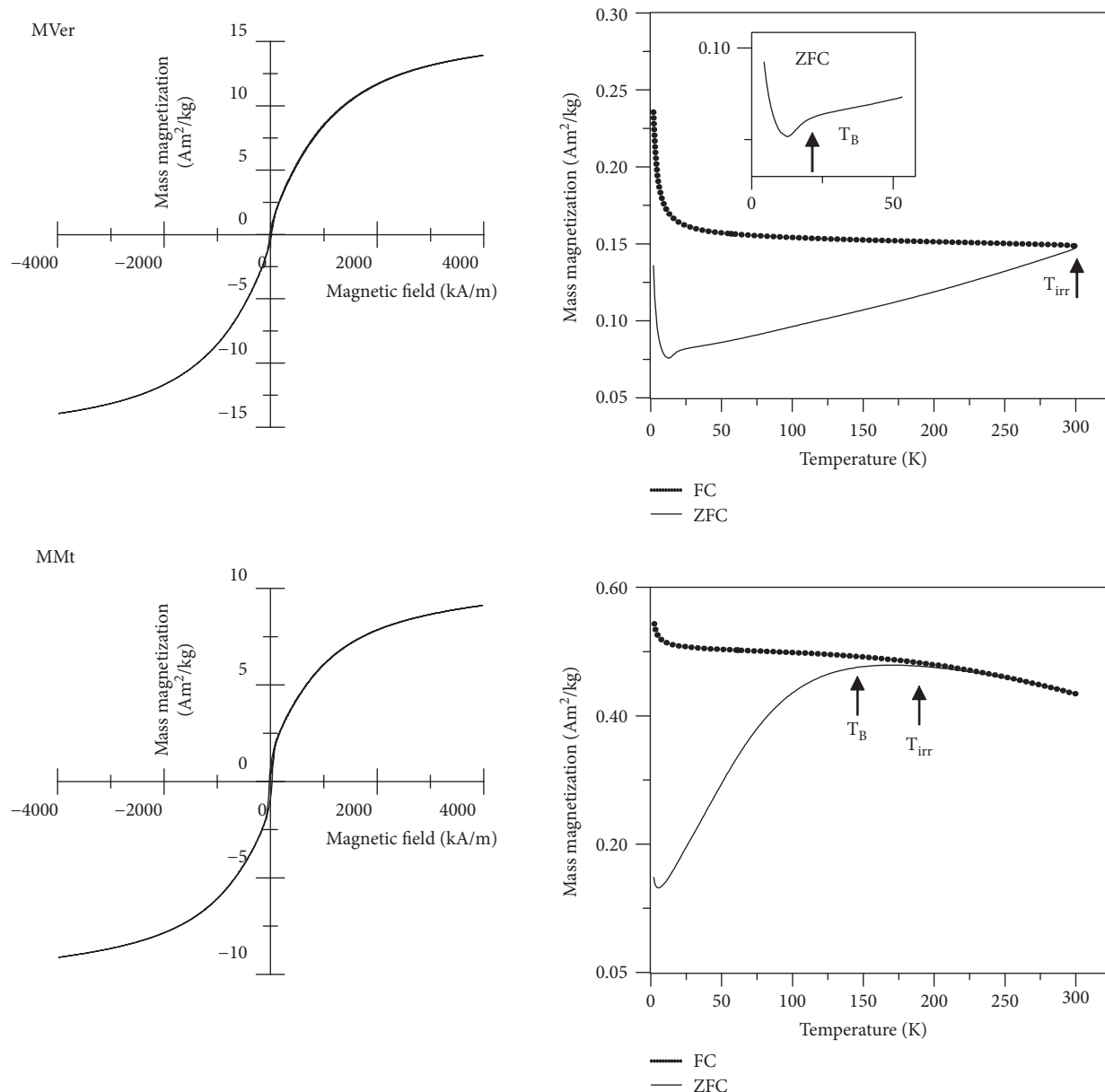


FIGURE 12: Low-temperature magnetic properties of magnetically modified (MVer, MMt) samples.

larger particle agglomerates at the vermiculite sample contrary to montmorillonite consisting of very small separated nanoparticles. The original clay minerals behave in a way corresponding to their composition; vermiculite with higher content of the iron-based compounds yields slightly softer magnetic properties and the presence of magnetic component at low temperature while montmorillonite is paramagnetic and/or superparamagnetic at both room and low temperatures. The magnetic modification changes the magnetic properties of both samples in different ways. The particle agglomerates in vermiculite cause magnetic hardening and prevailing dipolar interaction or dipolar coupling which refers to the direct magnetostatic interaction between two magnetic dipoles (moments). Contrary, the magnetically modified montmorillonite exhibits superparamagnetic behaviour at RT with nearly zero coercive field and remnant

magnetization. It means that temperature fluctuations of nanoparticles easily overcome the barrier consisting of their anisotropic energy. Marked increase of H_c at 2 K confirms that during cooling, the magnetic nanoparticles attract the properties typical for magnetically ordered materials and pass into the blocking state at $T_B \approx 150$ K.

Data Availability

The experimental data used to support the findings of this study are included within the article.

Conflicts of Interest

The authors declare that they have no conflicts of interest.

Acknowledgments

This work was financially supported by the project SP2018/43 from ERDF/ESF New Composite Materials for Environmental Applications (No. CZ.02.1.01/0.0/0.0/17_048/0007399), by the CEITEC 2020 National Sustainability Programme II (No. LQ1601) and the project LO1305 both funded by Ministry of Education, Youth and Sports of the Czech Republic, by the Grant Agency of the Czech Republic (No. 13-13709S), and by the scientific researchers of higher education institutions within the State Task of the Russian Federation No. 2014/236.

References

- [1] F. Bergaya, B. K. G. Theng, and G. Lagaly, Eds., *Handbook of Clay Science*, vol. 1, Elsevier, Developments of Clay Science, Amsterdam, Netherlands, 2006.
- [2] T. B. Musso, K. E. Roehl, G. Pettinari, and J. M. Vallés, "Assessment of smectite-rich claystones from Northpatagonia for their use as liner materials in landfills," *Applied Clay Science*, vol. 48, no. 3, pp. 438–445, 2010.
- [3] X. Zheng, J. Dou, J. Yuan, W. Qin, X. Hong, and A. Ding, "Removal of Cs⁺ from water and soil by ammonium-pillared montmorillonite/Fe₃O₄ composite," *Journal of Environmental Sciences*, vol. 56, pp. 12–24, 2017.
- [4] J. Wang, Y. Chen, G. Liu, and Y. Cao, "Synthesis, characterization and photocatalytic activity of inexpensive and non-toxic Fe₂O₃-Fe₃O₄ nano-composites supported by montmorillonite and modified by graphene," *Composites Part B: Engineering*, vol. 114, pp. 211–222, 2017.
- [5] S. Mukherjee, *The Sciences of Clays—Applications in Industry, Engineering and Environment*, vol. 1, Capital Publishing Company and Springer, New Delhi, India, 2013.
- [6] Z. Weiss and M. Kužvart, *Clay Minerals: Their Nanostructure and Utilization*, Karolinum, Prague, Czech Republic, 2005.
- [7] J. Tokarsky, *Prepared Figures by Molecular Modelling Using Accelrys Materials Studio, (Software, unpublished)*, 2016.
- [8] R. T. Martin, "Report of the clay minerals society nomenclature committee: revised classification of clay materials," *Clays and Clay Minerals*, vol. 39, no. 3, pp. 333–335, 1991.
- [9] G. Lagaly, "Layer charge heterogeneity in vermiculites," *Clays and Clay Minerals*, vol. 30, no. 3, pp. 215–222, 1982.
- [10] J. W. Gruner, "The structures of vermiculites and their collapse by dehydration," *American Mineralogist*, vol. 19, no. 12, pp. 557–575, 1934.
- [11] H. Shirozu and S. W. Bailey, "Crystal structure of A2-layer Mg-vermiculite," *American Mineralogist*, vol. 51, pp. 1124–1143, 1966.
- [12] J. Wang, G. Liu, C. Zhou, T. Li, and J. Liu, "Synthesis, characterization and aging study of kaolinite-supported zero-valent iron nanoparticles and its application for Ni(II) adsorption," *Materials Research Bulletin*, vol. 60, pp. 421–432, 2014.
- [13] T. B. Musso, F. M. Francisca, G. Pettinari, and K. E. Roehl, "Suitability of a cretaceous natural Na-bentonite as construction material for landfill liners," *Environmental Engineering and Management Journal*, vol. 15, no. 11, pp. 2519–2528, 2016.
- [14] T. S. Anirudhan, C. D. Bringle, and P. G. Radhakrishnan, "Heavy metal interactions with phosphatic clay: kinetic and equilibrium studies," *Chemical Engineering Journal*, vol. 200–202, pp. 149–157, 2012.
- [15] T. B. Musso, M. E. Parolo, G. Pettinari, and F. M. Francisca, "Cu(II) and Zn(II) adsorption capacity of three different clay liner materials," *Journal of Environmental Management*, vol. 146, pp. 50–58, 2014.
- [16] S. Shahmohammadi-Kalalagh, "Isotherm and kinetic studies on adsorption of Pb, Zn and Cu by kaolinite," *Journal of Environmental Sciences*, vol. 9, no. 2, pp. 243–255, 2011.
- [17] H. Sis and T. Uysal, "Removal of heavy metal ions from aqueous medium using Kuluncak (Malatya) vermiculites and effect of precipitation on removal," *Applied Clay Science*, vol. 95, pp. 1–8, 2014.
- [18] J. Zhao and M.-C. He, "Theoretical study of heavy metal Cd, Cu, Hg, and Ni(II) adsorption on the kaolinite(0 0 1) surface," *Applied Surface Science*, vol. 317, pp. 718–723, 2014.
- [19] C. Blachier, L. Michot, I. Bihannic, O. Barres, A. Jacquet, and M. Mosquet, "Adsorption of polyamine on clay minerals," *Journal of Colloid and Interface Science*, vol. 336, no. 2, pp. 599–606, 2009.
- [20] L. Zhang, L. Luo, and S. Zhang, "Adsorption of phenanthrene and 1,3-dinitrobenzene on cation-modified clay minerals," *Colloids and Surfaces A: Physicochemical and Engineering Aspects*, vol. 377, no. 1–3, pp. 278–283, 2011.
- [21] R. Zhang, W. Yan, and C. Jing, "Mechanistic study of PFOS adsorption on kaolinite and montmorillonite," *Colloids and Surfaces A: Physicochemical and Engineering Aspects*, vol. 462, pp. 252–258, 2014.
- [22] A. S. Elsherbiny, "Adsorption kinetics and mechanism of acid dye onto montmorillonite from aqueous solutions: stopped-flow measurements," *Applied Clay Science*, vol. 83–84, pp. 56–62, 2013.
- [23] L. Guz, G. Curutchet, R. M. Torres Sanchez, and R. Candal, "Adsorption of crystal violet on montmorillonite (or iron modified montmorillonite) followed by degradation through Fenton or photo-Fenton type reactions," *Journal of Environmental Chemical Engineering*, vol. 2, no. 4, pp. 2344–2351, 2014.
- [24] K. A. Selim, M. A. Youssef, F. H. Abd El-Rahiem, and M. S. Hassan, "Dye removal using some surface modified silicate minerals," *International Journal of Mining Science and Technology*, vol. 24, no. 2, pp. 183–189, 2014.
- [25] M. T. Yagub, T. K. Sen, S. Afroz, and H. M. Ang, "Dye and its removal from aqueous solution by adsorption: a review," *Advances in Colloid and Interface Science*, vol. 209, pp. 172–184, 2014.
- [26] J. L. Marco-Brown, M. M. Areco, R. M. Torres Sanchez, and M. dos Santos Afonso, "Adsorption of picloram herbicide on montmorillonite: kinetic and equilibrium studies," *Colloids and Surfaces A: Physicochemical and Engineering Aspects*, vol. 449, pp. 121–128, 2014.
- [27] A. Parbhakar, J. Cuadros, M. A. Sephton, W. Dubbin, B. J. Coles, and D. Weiss, "Adsorption of L-lysine on montmorillonite," *Colloids and Surfaces A: Physicochemical and Engineering Aspects*, vol. 307, no. 1–3, pp. 142–149, 2007.
- [28] W. Y. Hernandez, M. A. Centeno, J. A. Odriozola, S. Moreno, and R. Molina, "Acidity characterization of a titanium and sulfate modified vermiculite," *Materials Research Bulletin*, vol. 43, no. 7, pp. 1630–1640, 2008.
- [29] H. Long, P. Wu, and N. Zhu, "Evaluation of Cs⁺ removal from aqueous solution by adsorption on ethylamine-modified

- montmorillonite,” *Chemical Engineering Journal*, vol. 225, pp. 237–244, 2013.
- [30] A. G. San Cristóbal, R. Castelló, M. A. Martín Luengo, and C. Vizcayno, “Acid activation of mechanically and thermally modified kaolins,” *Materials Research Bulletin*, vol. 44, no. 11, pp. 2103–2111, 2009.
- [31] S. Yang, M. Gao, Z. Luo, and Q. Yang, “The characterization of organo-montmorillonite modified with a novel aromatic-containing gemini surfactant and its comparative adsorption for 2-naphthol and phenol,” *Chemical Engineering Journal*, vol. 268, pp. 125–134, 2015.
- [32] L. Chen, C. H. Zhou, S. Fiore et al., “Functional magnetic nanoparticle/clay mineral nanocomposites: preparation, magnetism and versatile applications,” *Applied Clay Science*, vol. 127–128, pp. 143–163, 2016.
- [33] J. Yao, Y. Chen, H. Yu et al., “Efficient and fast removal of Pb(II) by facile prepared magnetic vermiculite from aqueous solution,” *RSC Advances*, vol. 6, no. 103, pp. 101353–101360, 2016.
- [34] A. P. M. Alves, M. G. Fonseca, and A. F. Wanderley, “Inorganic-organic hybrids originating from organosilane anchored onto leached vermiculite,” *Materials Research*, vol. 16, no. 4, pp. 891–897, 2013.
- [35] K. Pospiskova and I. Safarik, “Low-temperature magnetic modification of sensitive biological materials,” *Materials Letters*, vol. 142, pp. 184–188, 2015.
- [36] I. Safarik and M. Safarikova, “One-step magnetic modification of non-magnetic solid materials,” *International Journal of Materials Research*, vol. 105, no. 1, pp. 104–107, 2014.
- [37] D. Levy, R. Giustetto, and A. Hoser, “Structure of magnetite (Fe_3O_4) above the curie temperature: a cation ordering study,” *Physics and Chemistry of Minerals*, vol. 39, no. 2, pp. 169–176, 2012.
- [38] T. Zak and Y. Jiraskova, “CONFIT: Mössbauer spectra fitting program,” *Surface and Interface Analysis*, vol. 38, no. 4, pp. 710–714, 2006.
- [39] Y. Jiraskova, J. Bursik, O. Zivotsky, and J. Cuda, “Influence of Fe_2O_3 on alloying and magnetic properties of Fe–Al,” *Materials Science and Engineering: B*, vol. 186, pp. 73–78, 2014.
- [40] S. Thamm and J. Hesse, “A simple plot indicating interactions between single-domain particles,” *Journal of Magnetism and Magnetic Materials*, vol. 154, no. 2, pp. 254–262, 1996.
- [41] A. Argüelles, S. A. Khainakov, J. Rodríguez-Fernández, M. Leoni, J. A. Blanco, and C. Marcos, “Chemical and physical characterization of iron-intercalated vermiculite compounds,” *Physics and Chemistry of Minerals*, vol. 38, no. 7, pp. 569–580, 2011.
- [42] A. Campos, S. Moreno, and R. Molina, “Characterization of vermiculite by XRD and spectroscopic techniques,” *Earth Sciences Research Journal*, vol. 13, no. 2, pp. 108–118, 2009.
- [43] A. Wiewióra, J. L. Pérez-Rodríguez, L. A. Perez-Maqueda, and J. Drapala, “Particle size distribution in sonicated high- and low-charge vermiculites,” *Applied Clay Science*, vol. 24, no. 1–2, pp. 51–58, 2003.
- [44] A. Lerf, F. E. Wagner, and J. Poyato, “Mössbauer spectroscopic investigation of redox reactions in vermiculites from Santa Olalla (Huelva, Spain),” *Solid State Ionics*, vol. 141–142, pp. 479–486, 2001.
- [45] J. M. D. Coey, “Mössbauer spectroscopy of silicate minerals,” in *Mössbauer Spectroscopy Applied to Inorganic Chemistry*, G. J. Long, Ed., vol. 1 of Modern Inorganic Chemistry, pp. 443–509, Springer, Boston, MA, USA, 1984.
- [46] F. E. Wagner and U. Wagner, “Mössbauer spectra of clays and ceramics,” *Hyperfine Interactions*, vol. 154, no. 1–4, pp. 35–82, 2004.
- [47] R. M. Cornel and U. Schwertmann, *Iron oxides—structure, properties, reactions, occurrences and uses*, WILEY-VCH Verlag, Weinheim, Germany, 2013.
- [48] P. M. A. de Bakker, E. de Grave, R. E. Vandenberghe, and L. H. Bowen, “Mössbauer study of small-particle maghemite,” *Hyperfine Interactions*, vol. 54, no. 1–4, pp. 493–498, 1990.
- [49] R. Zboril, M. Mashlan, and D. Petridis, “Iron(III) oxides from thermal processes synthesis, structural and magnetic properties, Mössbauer spectroscopy characterization, and applications,” *Chemistry of Materials*, vol. 14, no. 3, pp. 969–982, 2002.
- [50] G. Herzer, “Nanocrystalline soft magnetic alloys,” in *Handbook of Magnetic Materials*, K. H. J. Buschow, Ed., p. 4178, Elsevier Science B.V., 1997.
- [51] Y. Zhao, C. W. Dunnill, Y. Zhu et al., “Low-temperature magnetic properties of hematite nanorods,” *Chemistry of Materials*, vol. 19, no. 4, pp. 916–921, 2007.
- [52] J. Luňáček, O. Životský, Y. Jirásková, J. Buršík, and P. Janoš, “Thermally stimulated iron oxide transformations and magnetic behaviour of cerium dioxide/iron oxide reactive sorbents,” *Materials Characterization*, vol. 120, pp. 295–303, 2016.
- [53] O. Ballet and J. M. D. Coey, “Magnetic properties of sheet silicates; 2:1 layer minerals,” *Physics and Chemistry of Minerals*, vol. 8, no. 5, pp. 218–229, 1982.

Research Article

Possible Monitoring and Removal of As(III) by an Integrated System of Electrochemical Sensor and Nanocomposite Materials

Xuan T. Chu,¹ Quan V. V. Trieu,^{1,2} Thanh Q. Tran,^{1,2} Thanh D. Pham,¹ Trung Q. Vu,³ Thuy H. Tran,¹ and Tuan A. Mai^{1,2} 

¹Hanoi University of Science and Technology, No. 1, Dai Co Viet Road, Hanoi, Vietnam

²National Center for Technological Progress, 25 Le Thanh Tong, Hanoi, Vietnam

³Hanoi National University of Education, 136 Xuan Thuy Road, Hanoi, Vietnam

Correspondence should be addressed to Tuan A. Mai; mtuan@itims.edu.vn

Received 23 May 2018; Accepted 19 August 2018; Published 9 October 2018

Academic Editor: Jana Kukutschova

Copyright © 2018 Xuan T. Chu et al. This is an open access article distributed under the Creative Commons Attribution License, which permits unrestricted use, distribution, and reproduction in any medium, provided the original work is properly cited.

In this study, nanocomposites composed of magnetite nanoparticles (MNPs) coated with polyaniline fabricated by in situ polymerization were prepared for arsenic adsorption. Properties of particular MNPs and their nanocomposites were characterized with scanning electron microscopy, X-ray diffraction spectroscopy, and Fourier transform infrared spectroscopy. The As(III) concentration before and after adsorption on nanocomposites was detected by atomic absorption spectroscopy method and then compared with the results measured by a self-developed potentiostat system with anodic stripping voltammetry method. The polyaniline coating resulted in an improvement for As(III) adsorption ability of magnetite nanoparticles, and among the three compositions of PANi/MNP nanocomposites, the 5 wt% PANi showed the highest capability of As(III) adsorption (or removal) of 50 mg/g. Performing pH investigation, the concentration of remaining As decreased when pH increased from 2 to 5 and reached saturation value at higher pH. Above all, the electronic device can be integrated with As(III) removal system using PANi/MNP nanocomposites, proving to act as an independent monitoring system, and even more the adsorbent on the composites could be removed and the recyclability of the material was also investigated.

1. Introduction

Arsenite (As III) and arsenate (As V) are arsenic (As) compounds in water which are recognized globally by their extreme health hazards. The acute exposures to arsenic compounds may cause many organ malfunctions (especially the kidney) and several types of cancers [1]. A dose of arsenic which may induce fatal effects for matures is 120–200 mg per kg body weight (MPBW) and 20 MPBW for infants [2, 3]. The inorganic As(III) compounds in water are reported to have higher toxicity than the organic ones [4, 5]. Because arsenic is an ubiquitous element of the outer rock layer, it may naturally contaminate at high levels the groundwater elsewhere [6, 7]. In 2010, the World Health Organization (WHO) recommended a maximum contaminant level (MCL) for arsenic in drinking water at 10 ppb.

A trace of As(III) in water can be detected by several methods, such as the inductively coupled plasma mass spectroscopy (ICP-MS) or atomic absorption spectroscopy (AAS). However, those instruments are expensive and complicated with long-time sample preparation [8]. Recently, electrochemical method has attracted a large attention of researchers thanks to its sensibility, low cost, and ability to detect very low concentration of analytes [8, 9]. Electrochemical sensors found its application in DNA identification [10], glucose measurement [11], and environmental monitoring [12]. As for example, As(III) ions were detected by anodic stripping voltammetry (ASV) method with a low limit of detection [13, 14]. The researchers have kept studying to develop a cost-effective device for on-site heavy metal ion detection in water. Besides, the price of a commercial electrochemical instrument can be up to \$10,000 or higher and it is

not suitable for field measurement. In this work, we present a self-developed system on chip- (SOC-) based potentiostat for signal processing of sensors. The circuit was then used to measure As(III) concentration.

Besides, arsenic treatment is highly motivated. Among the materials used for arsenic adsorbents, magnetite nanoparticles (MNPs) provide various possibilities of cost per value reduction as well as removal efficiency. Such material is easily attracted by low magnetization field [15–17] and obtained in a massive amount through some hydrothermal synthesis. In addition, the desorption processes to recycle these MNP adsorbents are possible for several times of use [17]. Therefore, many researchers have focused on MNPs for arsenic adsorbent. However, the problem of using nano-sized magnetite for adsorbent is generally laid on their ease of oxidation-induced transformation to maghemite (γ - Fe_2O_3) and hematite (α - Fe_2O_3). Oxidation together with agglomeration of MNPs often elevates when the size of particles decreases. In addition, the strong magnetic dipole–dipole interaction and Vander Waals attractive forces among the nanoparticles also cause the particles to aggregate [18]. These problems reduce not only the magnetization degree but also the affinity of magnetite toward arsenic [19, 20]. To maintain adsorptive functionality of MNPs under a corrosive condition, numerous manipulation methods have been proposed, including surfactant-supported nanosuspension and polymer coating [21, 22]. Among those, nanocomposite of MNPs with polyaniline (emeraldine base coating) has been extensively studied in syntheses and applications for medical and environment purposes. Compared to many coating polymers, polyaniline (PAni) is highly compatible in bio- and environment applications due to its good environment stability, low monomer cost, ease of syntheses and purification, and convenient degrading process [23, 24]. The PAni/MNP nanocomposite can also be mixed with other polymer substrates such as poly(p-hydroxyaniline) and polyacrylonitrile to increase hydrophilicity of materials in aqueous media and mechanical strength of materials in product processing [24, 25]. Nevertheless, it is noticeably remarked that there has been no study informing PAni-coated MNPs to be an As(III) adsorbent as well as performing recyclability of this material in metal ion adsorption.

In this study, we focused on synthesis of PAni-coated MNPs for As(III) adsorption. The morphology and recyclability of nanocomposites were evaluated. The detection of As(III) was conducted with the ASV method using a self-developed potentiostat and paired with AAS methods.

2. Materials and Methods

2.1. Chemicals. Iron(II) chloride tetrahydrate ($\text{FeCl}_2 \cdot 4\text{H}_2\text{O}$), iron(III) chloride hexahydrate ($\text{FeCl}_3 \cdot 6\text{H}_2\text{O}$), sodium arsenite (NaAsO_2) as an As(III) compound, aniline, isopropanol, HCl solution, phosphate-buffered saline (PBS, pH = 7.4), and ammonium persulfate were purchased from Sigma-Aldrich (Missouri, USA). Ammonium hydroxide solution (25% NH_3 in H_2O) was purchased from Kanto (Shanghai, China). Deionized (DI) water was produced by deionizer system EW-01503-20, Cole Parmer (Illinois, USA), with a resistivity of

17 M Ω -cm. Solutions of 1 ppm As(III) were prepared as stock solutions. DI water, prepared solutions, and solid materials were kept in nitrogen gas atmosphere before use. HCl and PBS solutions were prepared to control the pH of tested solutions in the range of 2–8 at room temperature.

2.2. Preparation of Polyaniline/MNP Nanocomposites and Magnetite Nanoparticles (MNPs). 5 ml of 0.4 M FeCl_3 and 10 ml of 0.3 M FeCl_2 aqueous solutions were mixed in the rubber-plugged flask with nitrogen gas flow. The mixing solution was agitated for 10 minutes at 70°C. After that, an excessive amount of ammonia for the final pH of 13 was quickly dropped into the flask to get black precipitated MNP product. Reaction solution was centrifuged to obtain the deposition; the supernatant was discarded. The final deposition part was rinsed 6 times by DI water, being centrifuged and kept in deoxygenated DI water.

A predetermined amount of MNPs was mixed with DI water (100 weight equivalent amount) and isopropanol (20 weight equivalent amount) and then kept in a sonicator at room temperature for 1 hour to homogeneously disperse the MNPs. A predetermined amount of aniline hydrochloride was added into the prepared suspension and magnetically stirred for 1 hour. Three different weight equivalences of aniline monomer (5%, 10%, and 15% versus MNPs) were used for coating. The oxidant $(\text{NH}_4)_2\text{S}_2\text{O}_8$ and HCl were added into the reaction flask with a molar ratio equivalent to 1.25 and 0.25 of aniline monomer. All solutions were cooled down to 4°C in an ice bath and kept under deoxygenated atmosphere. The reaction was carried out for 20 hours in nitrogen gas flow. After the reaction, the mixture was centrifuged and rinsed 5 times by DI water then rinsed in acetone for 2 times to remove water. Finally, the obtained greenish black powders were dried in a vacuum at 40°C for 2 hours.

2.3. Characterization of MNPs and Polyaniline/MNP Nanocomposites. The shape and size distribution of MNPs as well as the nanocomposites were observed by scanning electron microscopy (SEM) (GeminiSEM, ZEISS Germany). The magnetic property was measured by a vibrating-sample magnetometer DMS 880 (ADE Technologies, USA). The standard crystal structure of Fe_3O_4 was confirmed by X-ray diffraction spectroscopy (XRD) (D2 PHASER 2nd, Bruker Singapore Pte. Ltd.). The formation of PAni and nanocomposites was investigated by Fourier transform infrared spectroscopy (FTIR) (Spectrum One, PerkinElmer, Massachusetts, USA). The ions compositions of resulted solutions were confirmed by AAS (iCE 3400 AA, Thermo Fisher Scientific, Massachusetts, USA).

2.4. Arsenic Adsorption Ability and Recyclability Evaluation. Adsorption experiments were performed under deoxygenated atmosphere. 1 mg of each adsorbent was stuffed into a glass tube container (2 cm in length, 0.5 cm in diameter). 1 ml arsenite solutions (As III) of different concentrations were injected into the containers for immersion. The pH range in this study for arsenic adsorption test was investigated from 2 to 8, and the adsorption time was from 10 to 60 minutes. Adsorbent containers were sealed by rubber

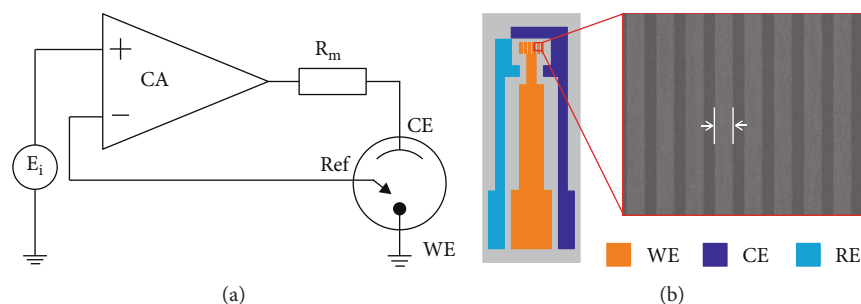


FIGURE 1: (a) Concept of 3-electrode measurement sensor; (b) electrode configuration and the inset showing the SEM image of WE.

plugs and shaken horizontally by an autosshaker. After immersion time, a cotton fiber was used to replace rubber plugs and the resulted As solutions were moved out by nitrogen gas flow through adsorbent containers. The resulted solution samples were filtered through a $0.22\ \mu\text{m}$ syringe filter with mixed cellulose ester membrane (Millipore, USA), and then the final As(III) concentrations in the filtrates were determined by AAS analyses. To perform a desorption experiment, the adsorbent container was washed by 1 ml acetone and immersed in free-arsenite aliquot (pH=3). The containers were sealed by rubber plugs and shaken for 12 hours. Released As solutions were filtered with the above-mentioned procedure and taken into AAS analyses. To evaluate the maximum adsorption ability of materials, each 1 g adsorbent was immersed in a 1 l aqueous solution of 1 ppm As(III) for 20 minutes.

2.5. Detection of Arsenic Ions Using ASV and Electrochemical Sensor. The electrochemical sensor was designed in triple-electrode configuration: working electrode (WE), reference electrode (RE), and counter electrode (CE) (Figure 1). During the data acquisition, the voltage between the WE and RE was kept stable and the current generated at the WE was measured. The self-fabricated sensor is illustrated in Figure 1(b), in which all three electrodes were made of gold and the working area of the WE is parallel assembled wires of $2\ \mu\text{m} \times 400\ \mu\text{m} \times 0.1\ \mu\text{m}$ each.

The ASV has a great advantage in heavy metal detection because of its specificity and high sensibility. Apart from arsenic, this method can also be used to detect copper ion (Cu^{2+}) or antimony ion (Sb^{3+}) [26]. Anodic stripping voltammetry (ASV) measurement includes accumulation and stripping phases. In a sample solution containing As(III), at the accumulation step, the As(III) deposited on the WE under the attractive force due to applied negative voltage and reduced to As(0). In a latter stripping phase, all accumulated metals will be stripped off the surface of the WE and oxidized, resulting in an electrochemical current peak which is proportional to the amount of adsorbed metal ions on the WE under the accumulation phase as well as the concentration of ions in the solution.

Firmware for programed measurement was written in C for Cypress CY8C27443. The integrated chip can provide a digital-to-analog converter (DAC) up to 9 bits and analog-to-digital converter (ADC) up to 14 bits. Text liquid crystal digit (LCD) screen and buttons were used for user interface.

The DAC signal was provided for the electrochemical reaction, then the generated signal was processed and came back to the microcontroller via ADC. The raw signal was then converted into digital and transmitted to a computer via the universal asynchronous receiver/transmitter (UART) protocol.

The hardware is the heart of the design. The circuit diagram of the system was shown in Figure 2. For simplicity, it was built from instrumentation amplifiers (INA) combined with operation amplifiers (OPA). The power is supplied from a linear regulator or USB port. The circuit uses an instrumentation amplifier to measure the current produced at the WE via a sensing resistor. The value of the sensing resistor as well as the gain of instrumentation amplifier can be adjusted so that the measured current range can be changed. High-quality instrumentation amplifier is advantageous over OPA transimpedance amplifier due to low DC offset, low drift, low noise, and high common mode rejection ratio which are suitable for high-precision applications. By using INA and careful processing, the resultant current in nA range can be measured. The voltage applied in the accumulation stage at the WE is negative referred to RE, so that the DAC signal must go through a negative shift and then the processed signal must be leveled up to match with the allowed input range of ADC. The offset voltage was also provided by a channel of microcontroller. The connection of operational amplifier (OA) to the RE was to ensure that there is no current that comes in or out of the electrode which will make the electrochemical system unstable [27, 28]. The excitation signal from the OA will be injected to the CE; the inverted form of applied voltage will appear at the WE due to the negative feedback loop between electrodes [29]. To avoid the noises from the environment and inside of the system's setup, some low-pass filter (LPF) had been used to decrease the influence of unwanted signal.

Raw ADC signal was transmitted directly to the computer via the UART protocol. The program was written in LabVIEW (National Instruments Corporation, Austin, Texas, USA) which shows the responding current vs. time in seconds.

3. Results and Discussion

3.1. Characterization of Adsorbents. SEM images of bare MNPs and of PANi/MNPs with 5%, 10%, and 15% aniline monomer are shown in Figure 3. Magnetite was formed in a coprecipitation with increasing temperature under

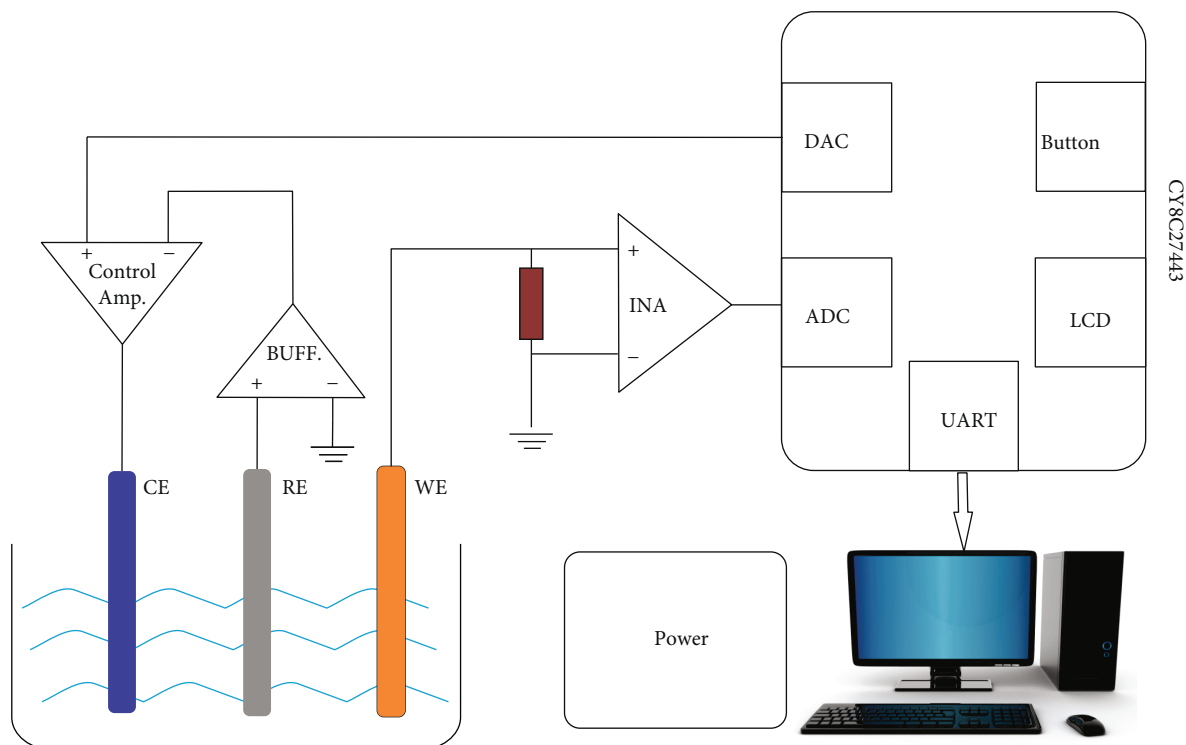


FIGURE 2: Block diagram of potentiostat.

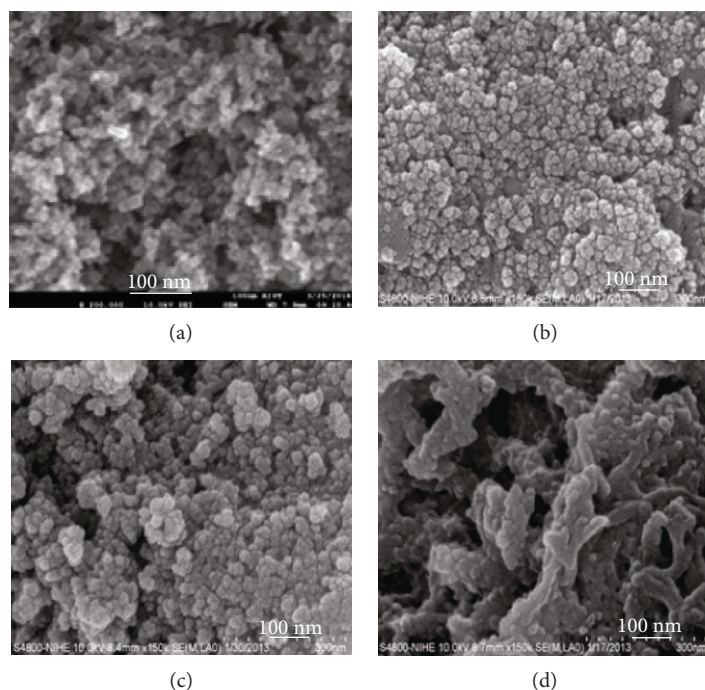


FIGURE 3: SEM images of (a) bare MNPs, (b) 5% PAni/MNPs, (c) 10% PAni/MNPs, and (d) 15% PAni/MNP nanocomposites.

aggressive agitation, then followed by sonication resulting in nanoparticles with diameter from 8 to 12 nm (Figure 3(a)). MNPs were routinely stored in deoxygenated DI water before each characterization and syntheses, to maintain the dispersion and minimize the prospect of being oxidized. The

morphologies of nanocomposites were differentiated by the feeding ratios of aniline salt monomer versus MNPs. The particles of nanocomposite with 5% of aniline monomer were formed in round shape with a diameter range of 15–30 nm (Figure 3(b)); meanwhile, with 10% aniline monomer,

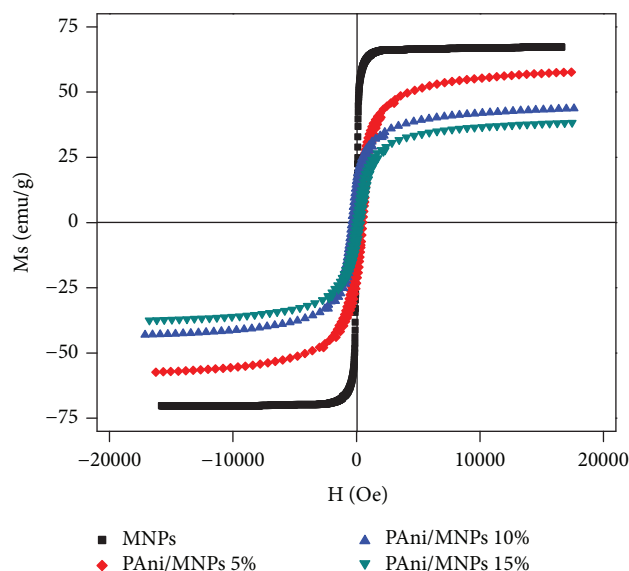


FIGURE 4: Magnetization momenta of MNPs and PANi/MNPs with deferent weight equivalences of aniline monomer.

the nanoparticles were bonded to form a building-flock shape (Figure 3(c)). In a nanocomposite with 15% aniline monomer feed, it is difficult to see the separation of particles because the nanoparticles, nanoflocks, and short nanofibers are located in a thick polymer matrix (Figure 3(d)).

Together with morphology, the magnetic property of PANi/MNPs was also investigated in order to reveal the relation between nanocomposites' structure and their adsorption ability. As shown in Figure 4, the magnetization momenta of nanocomposites decreased as the composition of coating PANi increased. The reduction of magnetization momenta corresponds to larger radii of nanounits in nanocomposite materials, which was caused by the coverage of PANi layer, while the size of magnetization centers (MNPs) was not changed. Due to higher magnetic field dwelling, the SEM image contrast of bare MNPs (Figure 3(a)) was lower than that of PANi/MNPs (Figures 3(b)–3(d)). By coating with PANi, the agglomerations of particles were supposed to declined, leading to higher surface area ratio of nanocomposites. The magnetization reduction at a particle surface as well as charge elevation at the surface of nanocomposites may lead to an antiagglomeration effect of the PANi layer [30, 31].

Figure 5 shows the XRD patterns of MNPs and PANi/MNPs showing 7 peaks which characterized for magnetite crystal of 111, 220, 311, 400, 422, 511, and 440 planes. No peak of hematite was observed in the XRD spectrum [32] meaning that the obtained nanoparticles contain maghemite or magnetite.

Direct oxidative polymerization of PANi had been performed with three aniline monomer compositions. The FT-IR spectra (Figure 6) of PANi, bare MNPs, and PANi/MNP nanocomposites were shown in Figure 6. In the case of PANi, the peaks at 1600, 1480, 1300, and 1172 cm^{-1} are attributed to C=C stretching of the quinoid ring, C=C stretching of the benzenoid ring, C–N stretching of the benzenoid unit, and N=quinoid=N vibration [33], respectively. The spectrum of

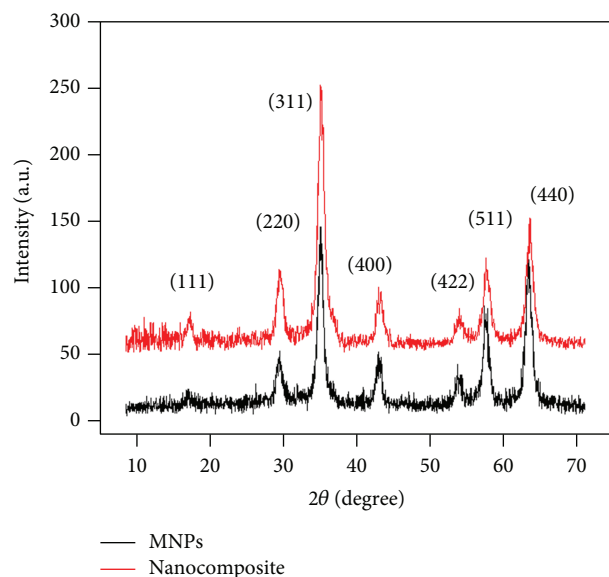


FIGURE 5: XRD patterns of bare MNPs and 5% PANi/MNP nanocomposite.

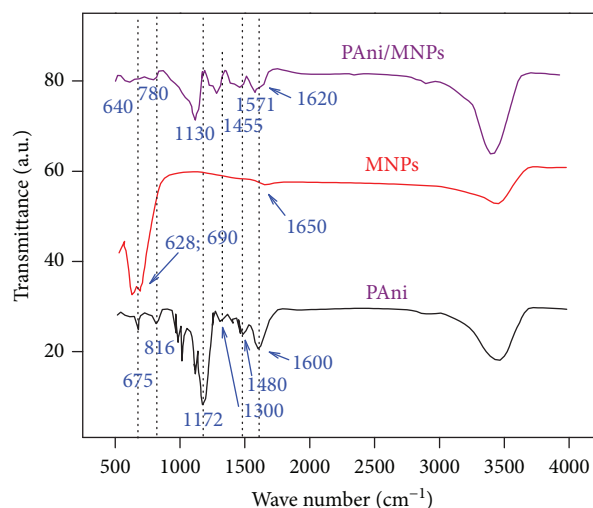


FIGURE 6: FTIR spectra of PANi, bare MNPs, and 5% PANi/MNP nanocomposites.

bare MNPs exhibits characteristic peaks at 3450 and 1650 cm^{-1} , which can be assigned, respectively, to O–H stretching and O–H bending vibration of water molecule existing in the physical adsorption or ferrofluid [30]. The strong peaks at 690 and 628 cm^{-1} are attributed to the stretching vibration mode of Fe–O bonds in the crystalline lattice of Fe_3O_4 . The spectrum of PANi/MNP composite exhibits almost the same vibrational bands as pure PANi, but characteristic peaks shifted to lower wave number, e.g., from 1600 to 1571 cm^{-1} with C=C stretching of the quinoid ring. The shifting of the peaks can be attributed to the interaction of 3d orbit of ferrite with nitrogen atoms in PANi to form coordinate bonds [30], which is similar to the band shift on the FTIR spectrum of metal-ligand complexes [34]. Therefore, the shoulder peak around 1620 cm^{-1} on the

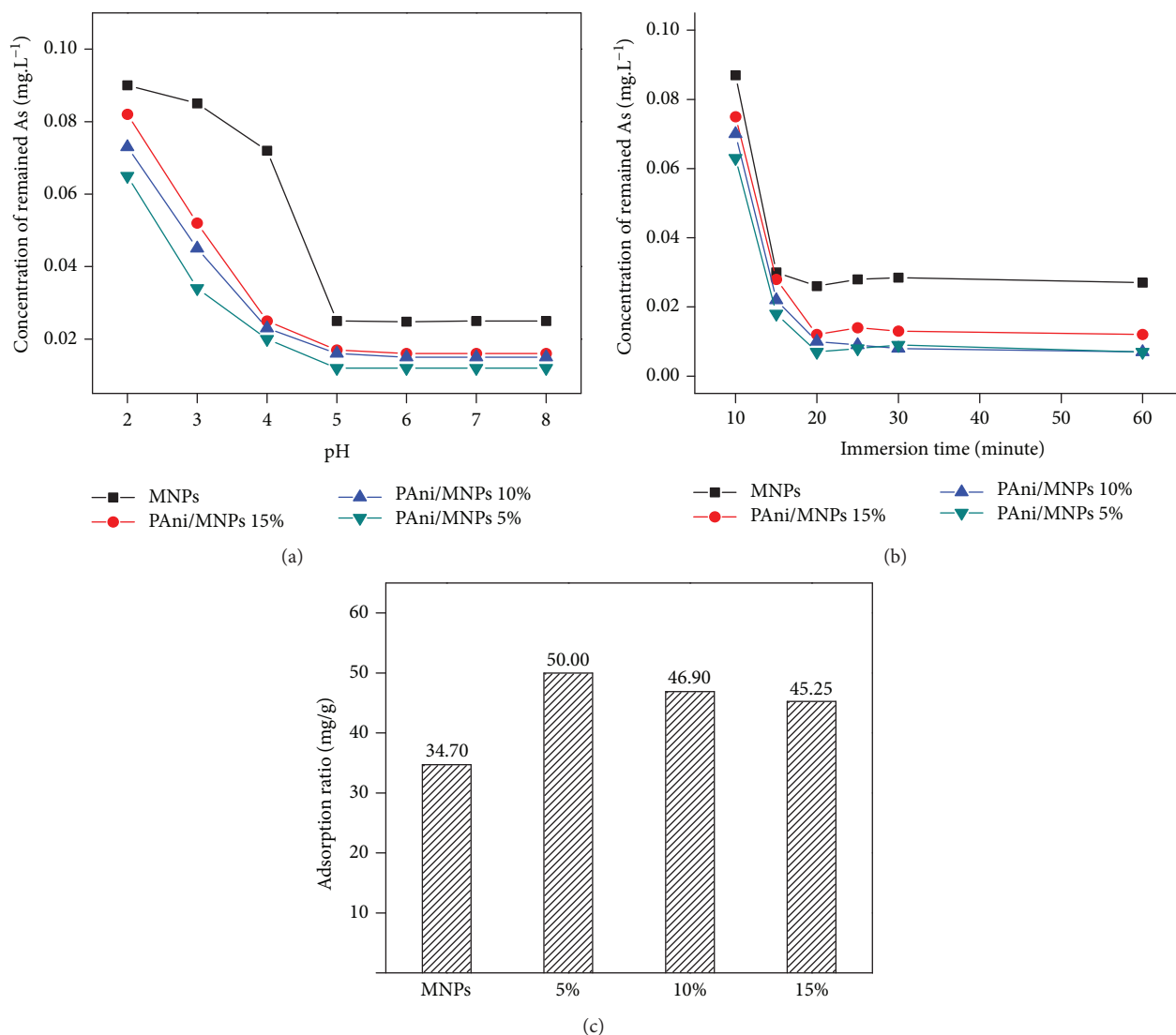


FIGURE 7: Adsorption behavior of PANi/MNPs over (a) pH in 20 mins and (b) immersion time at pH 5; (c) histogram presents maximum As(III) adsorption ratios of MNPs and PANi/MNP nanocomposite at an optimized condition.

spectrum of the composite is attributed to O-H vibration of water molecules that exists in hydrogen bonding with N-H groups of PANi. The characterization peak can be explained by two reasons. Firstly, the hydrogen bonding interaction leads to the slight shift of O-H vibration to a lower wave number. Secondly, hydrogen-bonded OH groups also have broader adsorption bands [34]. These results also demonstrate that the coating of PANi to the surface of the magnetic particles occurs through the hydrogen bonding between N-H groups in the PANi and OH group of bonded water molecules in the ferrofluid, leading to the encapsulation of magnetic particles by PANi [30].

3.2. Adsorption Ability of PANi/MNP Nanocomposites. Maximum adsorption values of the adsorbent were examined by immersing each adsorbent in excessive 1 ppm As(III) solution and followed by the previously described immersing steps. As shown in Figure 7(a), the concentration of the remaining As(III) decreased when the pH increased from 2

to 5 and reached a saturation value at higher pH. In investigating the pH range, the 5% PANi composite showed the highest adsorption ability toward As compared to 10% and 15% PANi ones and MNPs, too. The similar result was found when varying adsorption time (Figure 7(b)), and the As(III) adsorption reached saturation state after 20 minutes. A histogram of As(III) adsorption ratios of MNPs and PANi/MNPs nanocomposite at optimized condition was illustrated in Figure 7(c), in which the maximum adsorption ratio was attained with the sample of 5% PANi/MNP composite. The adsorption was improved because of the tolerating effect of electron-rich phenyl rings on the side chain of PANi, which enhanced the affinity of Fe(II) in MNPs [30]. It is supposed that PANi may interact with MNPs in a dynamic model, by which the polymer layer partly covers the MNP surface, allowing a slight planar movement of some fragments on each other. Diffusion of As(III) to the MNP surface could be available with suitable distances between MNP and PANi. According to the reports of Liu et al. [35] and Yang et al. [36],

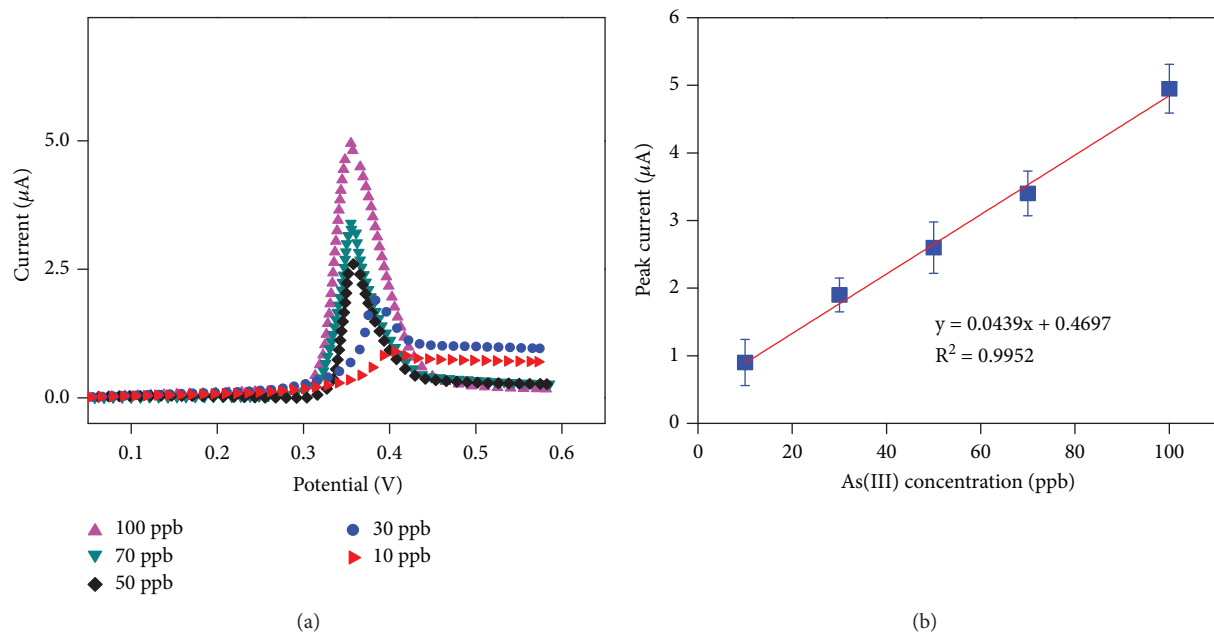


FIGURE 8: (a) ASV curves of different As(III) concentrations; (b) dependence of peak current versus As(III) concentration in ASV measurement.

the oxidation of MNPs might also be suppressed by the interaction of electron-rich PANi layer on the MNP surface. Besides, in an acidic medium, the amine ($-\text{NH}_2$) units of PANi might act as competitive factors to attract the protonated species from MNPs' surfaces [30].

3.3. Operation of Developed Potentiostat Circuit in As(III) Measurement. A portable potentiostat circuit along with the electrode system was used to determine As(III) concentration in the solution as follows: (1) stripping stage at -0.45 V for 100 s; (2) stability stage at -0.3 V for 10 s, and (3) applied potential then jump to stripping voltage at 0.6 V at the rate of 1 V/s . The mentioned potential is between the WE and RE. The results measured with our potentiostat are shown in Figure 8. The portable potentiostat can measure the trace of As(III) at the concentration of 10 ppb, which is the critical level suggested by the WHO. The corresponding peak current and measured concentration of As(III) are a first order and linear function (Figure 8(b)). For each As(III) concentration, three ASV measurements were performed similarly using three separate sensors. Using the developed calibration curve, As(III) concentrations of posttreatment as well as desorption were evaluated during real-time operations of adsorbents.

3.4. Evaluation for Adsorbent's Adsorption, Desorption, and Corrosion. Resulted As solutions after adsorption at $\text{pH}=2$ and $\text{pH}=5$ were used as samples for simple measurement by developed ASV sensing system; the second batch of each solution was separated for confirmation by AAS measurement. Quantitative results of measurements were compared in Table 1. At a higher As(III) concentration from 70 to 100 ppb, the ASV sensing system showed high accuracy with

TABLE 1: Adsorption behavior of MNPs and PANi/MNPs after 20 minutes. The analysis results obtained by developed ASV sensing system and AAS.

| Adsorbent | Remained As conc. by ASV (mg/l) ^a | | Remained As conc. by AAS (mg/l) ^b | | Difference |
|-----------|--|--------|--|--------|------------|
| | pH = 2 | pH = 5 | pH = 2 | pH = 5 | |
| MNPs | 0.094 | 0.025 | 0.091 | 0.028 | 3.2–10.7% |
| 5% PANi | 0.085 | 0.010 | 0.082 | 0.009 | 3.6–10.0% |
| 10% PANi | 0.074 | 0.012 | 0.076 | 0.013 | 1.3–7.6% |
| 15% PANi | 0.066 | 0.019 | 0.071 | 0.022 | 4.6–13.6% |

^aASV measurement by developed sensor; ^busing AAS method for confirmation.

a deviation of 3–5%. In a smaller and narrower range, 10–20 ppb, the accuracy was lowered but the deviations of about 10% are acceptable.

Along with the observation for adsorption ability, the desorption behavior of 5% PANi/MNP nanocomposite was also evaluated. Each desorption step was performed in 24 hours in a free-arsenite aqueous solution of $\text{pH}=3$. After 4 times of desorption, the 5%-PANi/MNP nanocomposite remained its high adsorption ability of 82.74% As(III) ions uptaken. Desorption ratios of 50% experienced 5 times of operation (Table 2).

With the result, this PANi/MNP nanocomposite can be recycled for at least 4 times in reality. Additionally, the released Fe concentration after each adsorption/desorption step was compared between 5% PANi/MNPs and bare MNPs as corrosion indicator. In the case of nanocomposite, the released amounts of Fe tended to decrease, while those tended to increase in the case of bare MNPs (Table 2). At

TABLE 2: Adsorption/desorption behavior of 5%-PAni/MNPs (1 g) toward the initial 11 As(III) solution 0.1 ppm after adsorbing and washing 5 times, at 25°C and agitation.

| Try | Adsorbed As % ^(a) | Released As % ^(b) | Released Fe (mg/L) ^(c) | |
|-----|------------------------------|------------------------------|-----------------------------------|-----------|
| | | | Bare MNPs | PAni/MNPs |
| 1 | 93.79 | 55.25 | 45.5 | 20.5 |
| 2 | 92.61 | 53.27 | 61.3 | 15.7 |
| 3 | 88.22 | 49.72 | 100.7 | 11.8 |
| 4 | 82.74 | 51.16 | 255.2 | 10.5 |
| 5 | 77.63 | 49.20 | 382.8 | 10.7 |

^(a)Adsorption process in pH = 5; ^(b)desorption process in arsenite-free solution pH = 3; ^(c)measured by AAS.

such a low pH value equal to 3, PAni showed good protection for MNPs as expected. The released amount of Fe from the nanocomposite might closely correspond to the physically adsorbed Fe during synthesis. In the acidic medium, MNPs were degraded; therefore, irons were found to be easily released (Table 2, (c)). In the nanocomposite forms, MNPs were covered by PAni, the solving process of iron by acidic medium was declined, and as a result, the released amounts of iron approached the constant after several recycle times (Table 2, (c)).

4. Conclusions

The adsorbent material was a nanocomposite prepared by coating of nanosized magnetite (MNPs) with polyaniline (PAni) in direct oxidative polymerization. The PAni/MNP nanocomposite exhibited better ability in arsenite removal than the bare magnetite. The polyaniline coating showed advantages in reducing not only agglomeration but also corrosion of MNPs and accordingly helped the adsorbent to maintain its adsorbing ability over several recycling times. The maximum adsorption ratio of the nanocomposite was obtained at 50 mg/g with aniline composition of 5 wt%. A compact ASV-based sensing system was developed to directly evaluate the performance of adsorbent versus arsenite concentration. Using a self-fabricated triple-gold electrode, a calibration curve was built with limit-of-detection (LOD) as low as 10 ppb As(III). The design of this study can provide a real-time/rapid treatment and observation for highly toxic As(III) contamination in water resources following the recommended standard of the World Health Organization (WHO).

Data Availability

The data used to support the findings of this study are included within the article.

Conflicts of Interest

The authors declare that there is no conflict of interest regarding the publication of this paper.

Acknowledgments

This research is funded by Vietnam National Foundation for Science and Technology Development (NAFOSTED) under grant number 103.02-2015.44. This research is supported by The World Academy of Sciences (TWAS) under Grant no. (16-169 RG/PHYS/AS_I-FR3240293345).

References

- [1] A. H. Smith, C. Hopenhayn-Rich, M. N. Bates et al., "Cancer risks from arsenic in drinking water," *Environmental Health Perspectives*, vol. 97, pp. 259–267, 1992.
- [2] J. B. Mowry, D. A. Spyker, D. E. Brooks, N. McMillan, and J. L. Schauben, "2014 annual report of the American Association of Poison Control Centers' National Poison Data System (NPDS): 32nd annual report," *Clinical Toxicology*, vol. 53, no. 10, pp. 962–1147, 2015.
- [3] M. F. Hughes, B. D. Beck, Y. Chen, A. S. Lewis, and D. J. Thomas, "Arsenic exposure and toxicology: a historical perspective," *Toxicological Sciences*, vol. 123, no. 2, pp. 305–332, 2011.
- [4] R. L. Kingston, S. Hall, and L. Sioris, "Clinical observations and medical outcome in 149 cases of arsenate ant killer ingestion," *Journal of Toxicology Clinical Toxicology*, vol. 31, no. 4, pp. 581–591, 1993.
- [5] R. C. Dart, *Medical Toxicology*, Lippincott, Williams & Wilkins, 3rd edition, 2004.
- [6] D. Postma, F. Larsen, N. T. Thai et al., "Groundwater arsenic concentrations in Vietnam controlled by sediment age," *Nature Geoscience*, vol. 5, no. 9, pp. 656–661, 2012.
- [7] P. L. Smedley, D. G. Kinniburgh, D. M. J. Macdonald et al., "Arsenic associations in sediments from the loess aquifer of La Pampa, Argentina," *Applied Geochemistry*, vol. 20, no. 5, pp. 989–1016, 2005.
- [8] A. K. Sakira, I. T. Somé, E. Ziemons et al., "Determination of arsenic (III) at a nanogold modified solid carbon paste electrode," *Electroanalysis*, vol. 27, no. 2, pp. 309–316, 2015.
- [9] P. Niedzielski and M. Siepak, "Analytical methods for determining arsenic, antimony and selenium in environmental samples," *Polish Journal of Environmental Studies*, vol. 12, no. 6, pp. 653–667, 2003.
- [10] B. D. McKean and D. A. Gough, "A telemetry-instrumentation system for chronically implanted glucose and oxygen sensors," *IEEE Transactions on Biomedical Engineering*, vol. 35, no. 7, pp. 526–532, 1988.
- [11] J. L. Lai, H. N. Wu, H. H. Chang, and R. J. Chen, "Design a portable bio-sensing system for glucose measurement," in *2011 International Conference on Complex, Intelligent, and Software Intensive Systems*, pp. 71–76, Seoul, South Korea, June-July 2011.
- [12] G. Hanrahan, D. G. Patil, and J. Wang, "Electrochemical sensors for environmental monitoring: design, development and applications," *Journal of Environmental Monitoring*, vol. 6, no. 8, p. 657, 2004.
- [13] R. Feeney and S. P. Kounaves, "On-site analysis of arsenic in groundwater using a microfabricated gold ultramicroelectrode array," *Analytical Chemistry*, vol. 72, no. 10, pp. 2222–2228, 2000.
- [14] X. Dai, O. Nekrassova, M. E. Hyde, and R. G. Compton, "Anodic stripping voltammetry of arsenic (III) using gold

- nanoparticle-modified electrodes,” *Analytical Chemistry*, vol. 76, no. 19, pp. 5924–5929, 2004.
- [15] K. Raj, B. Moskowitz, and R. Casciari, “Advances in ferrofluid technology,” *Journal of Magnetism and Magnetic Materials*, vol. 149, no. 1-2, pp. 174–180, 1995.
- [16] J. L. Wilson, P. Poddar, N. A. Frey et al., “Synthesis and magnetic properties of polymer nanocomposites with embedded iron nanoparticles,” *Journal of Applied Physics*, vol. 95, no. 3, pp. 1439–1443, 2004.
- [17] X. Batlle and A. Labarta, “Finite-size effects in fine particles: magnetic and transport properties,” *Journal of Physics D: Applied Physics*, vol. 35, no. 6, pp. R15–R42, 2002.
- [18] A. K. Gupta and M. Gupta, “Synthesis and surface engineering of iron oxide nanoparticles for biomedical applications,” *Biomaterials*, vol. 26, no. 18, pp. 3995–4021, 2005.
- [19] Y. S. Kang, S. Risbud, J. F. Rabolt, and P. Stroeve, “Synthesis and characterization of nanometer-size Fe_3O_4 and $\gamma\text{-Fe}_2\text{O}_3$ particles,” *Chemistry of Materials*, vol. 8, no. 9, pp. 2209–2211, 1996.
- [20] D. K. Kim, Y. Zhang, W. Voit, K. V. Rao, and M. Muhammed, “Synthesis and characterization of surfactant-coated superparamagnetic monodispersed iron oxide nanoparticles,” *Journal of Magnetism and Magnetic Materials*, vol. 225, no. 1-2, pp. 30–36, 2001.
- [21] H. Qiao, F. Chen, X. Xia, Q.-F. Wei, and F.-L. Huang, “Characterization of polyaniline/ Fe_3O_4 -polyacrylonitrile composite nanofibers,” *Journal of Fiber Bioengineering and Informatics*, vol. 2, no. 4, pp. 253–258, 2010.
- [22] M. R. Saboktakin, A. M. Maharramov, and M. A. Ramazanov, “Synthesis and characterization of polyaniline/poly (p-hydroxyaniline)/ Fe_3O_4 magnetic nanocomposite,” *Journal of Non-Oxide Glasses*, vol. 1, no. 3, pp. 211–215, 2009.
- [23] M. R. Patil, S. D. Khairnar, and V. S. Shrivastava, “Synthesis, characterisation of polyaniline- Fe_3O_4 magnetic nanocomposite and its application for removal of an acid violet 19 dye,” *Applied Nanoscience*, vol. 6, no. 4, pp. 495–502, 2016.
- [24] K. Basavaiah, Y. Pavan Kumar, and A. V. Prasada Rao, “A facile one-pot synthesis of polyaniline/magnetite nanocomposites by micelles-assisted method,” *Applied Nanoscience*, vol. 3, no. 5, pp. 409–415, 2013.
- [25] S. A. Baig, T. Sheng, C. Sun, X. Xue, L. Tan, and X. Xu, “Arsenic removal from aqueous solutions using Fe_3O_4 -HBC composite: effect of calcination on adsorbents performance,” *PLoS One*, vol. 9, no. 6, article e100704, 2014.
- [26] J. Raj, A. Raina, Mohineesh, and T. D. Dogra, “Direct determination of zinc, cadmium, lead, copper metal in tap water of Delhi (India) by anodic stripping voltammetry technique,” *E3S Web of Conferences*, vol. 1, article 09009, 2013.
- [27] C.-Y. Huang, M.-J. Syu, Y.-S. Chang, C.-H. Chang, T.-C. Chou, and B.-D. Liu, “A portable potentiostat for the bilirubin-specific sensor prepared from molecular imprinting,” *Biosensors & Bioelectronics*, vol. 22, no. 8, pp. 1694–1699, 2007.
- [28] C.-Y. Huang, “Design of a voltammetry potentiostat for biochemical sensors,” *Analog Integrated Circuits and Signal Processing*, vol. 67, no. 3, pp. 375–381, 2011.
- [29] C. Y. Huang, Y. C. Huang, T. Y. Lin, C. H. Chang, and X. F. Li, “An SOC-based portable cyclic voltammetry potentiostat for micro-albumin biosensors,” in *2007 2nd IEEE Conference on Industrial Electronics and Applications*, pp. 604–609, Harbin, China, May 2007.
- [30] C. Leng, J. Wei, Z. Liu, J. Shi, and C. Pan, “Synthesis of polyaniline- Fe_3O_4 nanocomposites and their conductivity and magnetic properties,” *Journal of Wuhan University of Technology - Materials Science Edition*, vol. 25, no. 5, pp. 760–764, 2010.
- [31] P. Tamilarasan and S. Ramaprabhu, “Polyaniline-magnetite nanocapsules based nanocomposite for carbon dioxide adsorption,” *International Journal of Greenhouse Gas Control*, vol. 10, pp. 486–493, 2012.
- [32] K. Song, S. Lee, C. Y. Suh, W. Kim, K. S. Ko, and D. Shin, “Synthesis and characterization of iron oxide nanoparticles prepared by electrical explosion of Fe wire in Ar- O_2 gas mixtures,” *Materials Transactions*, vol. 53, no. 11, pp. 2056–2059, 2012.
- [33] Y. Dong, Y. Zhou, Y. Ding, X. Chu, and C. Wang, “Sensitive detection of Pb(II) at gold nanoparticle/polyaniline/graphene modified electrode using differential pulse anodic stripping voltammetry,” *Analytical Methods*, vol. 6, no. 23, pp. 9367–9374, 2014.
- [34] K. Nakamoto, *Infrared and Raman Spectra of Inorganic and Coordination Compounds*, John Wiley & Sons, Inc., Hoboken, NJ, USA, 2008.
- [35] C.-H. Liu, Y.-H. Chuang, T.-Y. Chen et al., “Mechanism of arsenic adsorption on magnetite nanoparticles from water: thermodynamic and spectroscopic studies,” *Environmental Science & Technology*, vol. 49, no. 13, pp. 7726–7734, 2015.
- [36] C. Yang, J. Du, Q. Peng et al., “Polyaniline/ Fe_3O_4 nanoparticle composite: synthesis and reaction mechanism,” *The Journal of Physical Chemistry B*, vol. 113, no. 15, pp. 5052–5058, 2009.

Research Article

Mechanical and Optical Properties of Polylactic Acid Films Containing Surfactant-Modified Cellulose Nanocrystals

Jose Luis Orellana, Derek Wichhart, and Christopher L. Kitchens 

Department of Chemical and Biomolecular Engineering, Clemson University, Clemson, South Carolina 29634, USA

Correspondence should be addressed to Christopher L. Kitchens; ckitche@clemson.edu

Received 30 April 2018; Revised 14 August 2018; Accepted 26 August 2018; Published 2 October 2018

Academic Editor: Roberto Nisticò

Copyright © 2018 Jose Luis Orellana et al. This is an open access article distributed under the Creative Commons Attribution License, which permits unrestricted use, distribution, and reproduction in any medium, provided the original work is properly cited.

The addition of surface-modified cellulose nanocrystals (CNCs) to polymeric matrices can lead to an enhancement of the mechanical and optical properties of host polymers. The use of surfactants can provide an easy and effective way to change the CNC functionality and to evaluate the effects of surface chemistry in the reinforcement mechanisms. In this work, CNCs were solution blended with polylactic acid (PLA) and melt extruded into films. The PLA toughness increased from 1.70 MJ/m^3 to 2.74 MJ/m^3 , a 61% increase, with the addition of 1% of decylamine-modified CNCs without a decrease of the tensile strength or modulus. In this work, we investigated the use of two surfactants, decylamine and cetyltrimethylammonium bromide, to enhance CNC compatibility with the hydrophobic PLA matrix. Decylamine at 1.0 wt.% with respect to CNC loading was found to significantly enhance CNC compatibility and property enhancement. The low concentration of surfactant is notable, as other works typically use significantly higher loadings for CNC incorporation and property enhancement. At high CNC concentrations, mechanical properties decreased but the aligned assembly of the CNCs provided intricate colors to the films when observed between crossed polars. The alignment and nanoscale structure of CNCs within the films play an important role in the properties obtained.

1. Introduction

Polylactic acid (PLA) is a well-known biodegradable polymer that has potential to serve as a sustainable alternative to petroleum-derived plastics and is one of the most widely used biopolymers on the market [1]. PLA accounts for nearly 40% of the bioplastic total market, with nearly \$700 million in revenue in 2017 and a projected growth to over \$2 billion and 830,000 metric tons by 2023 [2]. PLA is synthesized from lactic acid made from corn starch or sugar cane [3], and the production requires 25–55% less energy than petroleum-based polymers due to its relatively lower melting point (T_m) [4, 5], thus reducing the net CO_2 emission to the environment [6, 7]. Moreover, PLA has received much research attention in the last two decades due to its high tensile properties, transparency, and low toxicity. The result is an improved material at a competitive cost with emergence in a highly competitive polymer market [8–12]. On the other hand, the brittleness and low vapor and gas barrier properties

of PLA are potential limitations in extending its applications, thus representing areas of current development [1].

One avenue to address these limitations is the reinforcement of PLA with cellulose nanocrystals (CNCs). This nanofiller has attracted much attention as a polymer reinforcement material due to its exceptional mechanical properties, ability for surface functionalization, abundance, and renewability [13–16]. Similar to other nanofillers, CNCs exploit properties not found in macrosized materials, specifically their high surface areas, aspect ratios, and multifunctionalities. These nanocrystals can be isolated from a variety of sources such as cotton, wood pulp, tunicate, or bacteria usually by acid hydrolysis [17]. Through this process, noncrystalline regions of the cellulose are hydrolyzed while the highly crystalline ones resist acid attack, resulting in a crystalline, high-performance material. Crystalline cellulose has been estimated to possess a higher elastic modulus than Kevlar and higher tensile strength than steel wire with 80% less weight than the

latter one [18, 19]. However, to incorporate all of the benefits of CNCs into polymer nanocomposites, the CNC surface needs to be modified to enhance compatibility with the desired polymer matrix.

Surface modifications such as acetylation, silylation, oxidation, polymer grafting, and absorption of surfactants, among others, have been reported in the literature [17]. For example, a single-step method for the acetylation of CNCs, proposed by Braun and Dorgan [20], is one method for successful dispersion of CNCs in organic solvents. Moreover, it is believed that CNC acetylation enhances the absorption of surfactants, promoting a better dispersion of CNCs in an organic matrix without compromising the cellulose degradation temperature. Recent research suggests that the absorption of surfactants and long-chain molecules have shown to be effective in the compatibilization of CNCs with hydrophobic polymers, increasing the toughness of the composites [17]. However, it is usually observed that a high amount of surfactant addition ranging from 0.5:1 to 4:1 molar ratio of surfactant to the CNC hydroxyl group (50 to 200 wt.% surfactant to CNC) is required for compatibilization, thus restricting the nanocomposite properties or performance [21]. For this reason, it is important to explore surfactants having similar effects but at lower proportions. In this study, we explore decylamine (DA) and cetyltrimethylammonium bromide (CTAB) for solution compatibilization within PLA-CNC film nanocomposites.

The reinforcement of polymers varies as a function of the nanocrystal morphology, functionality, polydispersity, and the processing conditions [17]. Therefore, the results reported in literature differ considerably, suggesting that future research is needed to identify the variables and the mechanisms of reinforcement. Past research indicates that good dispersibility of CNCs within the matrix, with minimal aggregation, is important for composite reinforcement [22]. Interestingly, some hydrophobic matrices have been reinforced using hydrophilic CNCs [23], while in other cases, surface-modified CNCs have not exhibited the enhancement in the mechanical properties that would be expected from improved compatibility with rigid fillers [24]. These behaviors can be attributed to different stress transfer mechanisms. A percolating network can be formed at a critical filler concentration, in which stress transfer is facilitated by filler-filler interactions, usually increasing the tensile strength and modulus of the composites [25]. On the other hand, at low filler concentrations, the stress transfer is mainly through filler-matrix interactions, for which good compatibility usually results in increased toughness [17]. Additionally, fillers with larger aspect ratios tend to increase the tensile modulus, while smaller sizes, such as that of the nanocrystals, have been observed to enhance toughness [26].

The aim of this work is to enhance the toughness of PLA by the addition of acetylated CNCs plus the absorption of surfactants. We have previously shown that surfactant introduction improves CNC stability and self-assembly in organic solvents. For this work, PLA-CNC nanocomposite films (0, 1, 3, 5, and 10 wt.% CNCs) were extruded and mechanically tested using an Instron testing machine. An increase in toughness was observed at low CNC concentrations when

using DA surfactant, while the tensile strength and modulus remained constant compared to neat PLA. The CNC orientation and self-assembly were studied using polarized light microscopy, demonstrating significant organization for the toughened composites. Moreover, these organized structures within the composites provided colored properties to the films when observed between crossed polars and which have the potential for advanced applications such as biodegradable security papers and defense applications.

2. Experimental Section

2.1. Materials. PLA was purchased from NatureWorks 2003D (95% L-PLA and 5% D-PLA) and used as received for the polymer matrix. Clippings of ashless filter aid from Whatman™ were used as the CNC starting material. Other reactants for the synthesis (glacial acetic acid and hydrochloric acid 37% w/v) were ACS grade obtained from VWR. Chloroform and decylamine were ACS grade reagents obtained from Sigma-Aldrich. High-purity grade cetyltrimethylammonium bromide (CTAB) was obtained from AMRESCO.

2.2. Synthesis and Characterization of CNCs. CNCs were synthesized according to the method developed by Braun and Dorgan [20] as briefly described here. Cotton cellulose filter aid (10 g) was soaked overnight in 225 mL of acetic acid. Concentrated hydrochloric acid (0.8 mL, 37%) and 24.5 mL of deionized water were added, and the 10 hr reaction time began when a reaction temperature of 105°C was reached. After the reaction, the mixture was cooled in an ice bath and centrifuged to remove the solvent in the supernatant. DI water was added to the precipitated cellulose to the original volume and mixed for 2 minutes with a vortex mixer using a Vortex-Genie 2 (Scientific Industries Inc.). The centrifugation and redispersion were repeated for two additional cycles. The cellulose dispersion was then sonicated using a Fisher Scientific 550 Sonic Dismembrator for 5 cycles of 7 min in an ice bath. The suspension was again centrifuged and redispersed for additional cycles until a cloudy supernatant was observed. The aqueous supernatant of isolated acetylated CNCs was obtained by combining the following 2-3 dispersion supernatants. The nanocrystals were transferred to an organic solvent by dispersion in acetone with two centrifugation and redispersion cycles, with final dispersion in THF. Vigorous mixing was performed with a final 40 min of vortex mixing until minimal agglomeration was visible in the resulting suspension. The desired surfactant (decylamine or CTAB) was subsequently added to the suspension and mixed for 5–10 min.

The CNC dimensions were measured by transmission electron microscopy (TEM) using a Hitachi 7600 TEM with an accelerating voltage of 120 kV. CNC samples were prepared by nebulizing a diluted CNC suspension (~0.01% w/v) onto a formvar carbon-coated copper grid (Ted Pella). Thermal gravimetric analysis (TGA) (TA instruments SDT Q600) was performed to determine the CNC degradation temperature. A sample of CNC organic suspension was dried, and the remaining powder was placed in the TGA

TABLE 1: Nomenclature and composition of PLA-CNC nanocomposites prepared in this work.

| Sample name | CNC (%) | PLA (%) | Surfactant (1 wt.% w.r.t. CNC) |
|------------------|---------|---------|--------------------------------|
| PLA | 0 | 100 | — |
| PLA-CNC(1%)-UM | 1 | 99 | — |
| PLA-CNC(5%)-UM | 5 | 95 | — |
| PLA-CNC(1%)-DA | 1 | 99 | Decylamine |
| PLA-CNC(5%)-DA | 5 | 95 | Decylamine |
| PLA-CNC(1%)-CTAB | 1 | 99 | CTAB |
| PLA-CNC(5%)-CTAB | 5 | 95 | CTAB |

alumina pans. The sample was heated to 110°C for 25 min to remove residual solvent, cooled to 80°C, and then heated at 10°C/min to 650°C. The TGA was carried out under a nitrogen atmosphere (100 mL/min) and then switched to oxygen from 650°C to 800°C.

2.3. Preparation of PLA-CNC Nanocomposites. PLA nanocomposites were made by blending a 5% (w/v) solution of PLA in chloroform with a 1% (w/v) CNC suspension using an overhead stirrer. These PLA-CNC solutions, with CNC contents of 1, 3, 5, and 10 wt.%, were allowed to dry overnight at room conditions in a glass dish. The films were placed under vacuum at 70°C for 12 h and then to 120°C for 1 h to remove any residual solvent. Approximately 15 g of nanocomposite films was cut and compounded in a DSM Xplore corotating twin-screw microcompounding extruder for 10 min at 195°C. The extruder was set to a constant force at the die of 500 N, allowing variable screw rotation to obtain a constant melt flow. The polymer melt was extruded through a rectangular cross-sectional-shaped die, cooled with ambient nitrogen gas, and collected on a chill roll with a take-up speed of 120 rpm. The films were cut into 95 mm × 12.5 mm strips using a hydraulic press and a custom-made metal die for tensile testing. A minimum of 10 samples was prepared for each CNC composite loading and type of surfactant. The thicknesses of the films were taken at 4 different sections of the films, and an average of 0.18 ± 0.02 mm was obtained. Table 1 lists some of the nanocomposites prepared and their respective names in this work.

2.4. Nanocomposite Characterization. Tensile testing of the nanocomposites was performed using an Instron 1125 tensile testing instrument. The initial grip separation was 45 mm and set to a strain rate of 4 mm/min. Information on displacement and force exerted in the stretching of the films was obtained in stress-strain curves shown in supplemental information Figure S1 and used to determine tensile strength, tensile modulus, and toughness (energy at break) of each film.

PerkinElmer Pyris 1 differential scanning calorimetry (DSC) was used to determine the crystallinity of the nanocomposites. Between 5 and 6 mg of the sample was carefully sealed inside an aluminum pan. The samples were heated to 210°C at 20°C/min under nitrogen atmosphere and maintained at a constant temperature for 2 min prior

to cooling at a rate of 20°C/min. The crystallinity of PLA-CNC films was calculated by measuring the area under the melting and crystallization curves and using

$$X_c [\%] = \frac{\Delta H_m - \Delta H_{cc}}{(\Delta H_m^{\infty}) * X_{PLA}} * 100\%, \quad (1)$$

where ΔH_m and ΔH_{cc} are the enthalpies of melting and crystallization, respectively, measured by DSC. X_{PLA} is the fraction of PLA in the composites as described in Table 1 [23]. The theoretical enthalpy of fusion of 100% crystalline PLA, ΔH_m^{∞} , was taken to be 93.0 J/g [27].

The optical properties of the films and orientation of the CNCs in the nanocomposite were investigated by optical polarized light microscopy (Olympus BX60) in transmission mode with the polarizer below the sample and the analyzer rotated 90° above. The films were placed directly on glass slides and analyzed at 10x magnification with the stage being rotated from 0 to 135°. Adobe Photoshop was used to increase the contrast for display purposes and to measure the percentage of colors.

In order to elucidate CNC orientation direction or the sign of birefringence, a first-order red plate was added between the polarizer and analyzer (see orientation of filters in Figure S2). The direction of the slow red axis of the filter is oriented at 135°, and therefore, orientation at 135° appears blue. CNCs oriented in the 45° direction appear yellow due to the lower-interference colors resulting from the slow axes being perpendicular. CNCs oriented at 0° and 90°, as well as nonoriented crystals, will appear magenta. The first-order red plate is designed for low-retardation structures, which appear as a gray scale between crossed polars, which eliminates the ability to properly analyze the 5% and 10% CNC composites since their brightness is too strong.

In order to fully characterize the extent of orientation and directionality, the sample is rotated to discern between non-oriented and parallel or perpendicular orientation. The total extent of orientation is calculated theoretically by adding the colors blue and yellow from the 0° and 45° angle images. Image analysis was performed with Photoshop software to quantify the percentage of colors magenta, blue, and yellow from the entire area of the images.

3. Results and Discussion

3.1. Characterization of Cellulose Nanocrystals. The nanoscale dimension and high aspect ratio of the CNCs are important for polymer property enhancement with particle orientation. The high surface area to volume ratio enables good molecular level interactions with different matrices [20], and a high aspect ratio ensures enhanced stress transfer to the nanocrystals [22]. Figure 1 shows a representative TEM micrograph of CNCs dried from a THF suspension, confirming the successful isolation of the nanocrystals. These nanocrystals are observed to have the tendency to aggregate after drying which is due to the lack of surface charge for the acetylated CNCs [22]. It is expected that the introduction of compatibilized CNCs into an organic media will reduce

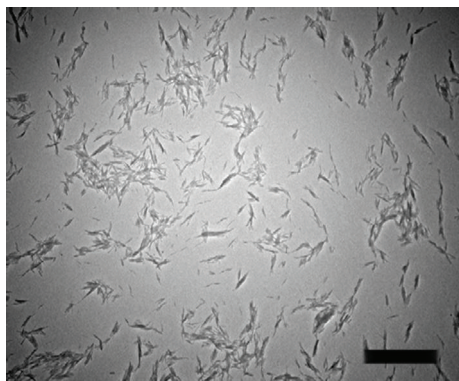


FIGURE 1: TEM image of cellulose nanocrystals synthesized using acetic acid and stabilized with decylamine surfactant. Bar: 2 μm .

the tendency to agglomerate due to enhanced filler-matrix interactions. The CNCs were measured to be 250 nm long and 35 nm wide, which is in agreement with reported literature values [20].

The thermal stability of nanofillers is important for nanocomposite melt processing due to the relatively high melting point and temperatures required for melt compounding. Figure 2 shows the degradation temperatures of CNCs without surfactant and with decylamine (DA), demonstrating the excellent thermal stability of the CNCs. The onset degradation temperature was 331°C for acetylated CNC with and without surfactant, which is well above the processing temperature of the PLA (190°C). This CNC modification, as shown by Braun and Dorgan [20], has the advantage of maintaining the thermal stability of native cellulose, contrary to other common modifications which significantly reduce the degradation temperature of cellulose [28–30].

3.2. Mechanical Properties of the Nanocomposite Films. The mechanical properties of the nanocomposite films from the stress-strain curves are presented in Figure 3. The energy at break or toughness of PLA-CNC nanocomposites exhibited a maximum enhancement at 1% CNC content before decreasing with increasing loading. This maximum enhancement occurred for the nanocomposites with DA surfactant and represented a 61% increase from 1.70 MJ/m³ for neat PLA to 2.74 MJ/m³. For the 3% DA-modified CNC composites, a slight enhancement of 8% was exhibited, while for the 5 and 10% composites, the toughness was decreased with respect to neat PLA. The unmodified (UM) and CTAB-modified nanocomposites exhibited a decreased toughness compared to PLA and PLA-CNC-DA at each CNC concentration. The composites at 10% CNC load were more brittle, demonstrating a reduced toughness of up to 95% less than that for PLA. The decrease in toughness in nanocomposites has been attributed to large agglomerations of nanofillers [22, 31]. These agglomerations can act as stress concentrators, which facilitate the spreading of defects generated at the interface. These defects can grow larger than the critical crack size, resulting in film failure.

In comparison with other literature focused on melt extrusion of CNC reinforcement of PLA with added

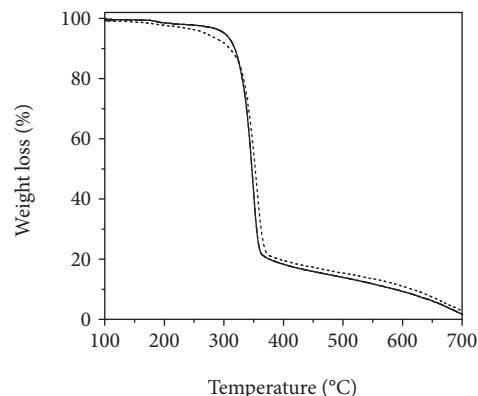


FIGURE 2: TGA weight loss as a function of temperature for the acetylated CNC without surfactant (solid line) and with decylamine surfactant (dotted line).

surfactants, our results show enhancement at lower values of loading. Bondeson and Oksman investigated NaOH-neutralized sulfuric acid-hydrolyzed CNC with the addition of phosphate anionic surfactant with loadings of 5% CNC and surfactant loadings of 5 to 20% [14]. They observed optimal results with an increase in tensile modulus from 2.65 to 3.10 GPa with 5% CNC and 5% surfactant; however, a 16.5% decrease in strength was observed. In all cases, the tensile strength was reduced. These results are not that different from our results with higher CNC loading. Fortunati et al. also investigated NaOH-neutralized sulfuric acid-hydrolyzed CNC with a phosphate ester surfactant and added silver nanoparticles for antimicrobial properties [15]. Their work also observed optimal performance at 5% CNC with surfactant where the modulus was increased from 2.4 to 4.4 GPa and the strength was maintained at 54 MPa. As a result, the percent elongation was decreased. While the strength was maintained for this result, the composite became more brittle, and again, CNC loadings below 5% were not investigated. Muiruri et al. took a different approach where homo- and copolymers of caprolactone and lactic acid were grafted onto the surface of CNC by ring-opening polymerization [16]. The CNC with PDLA grafts at 2.5 and 5.0% loading, the tensile strength, and modulus decreased nominally, and the elongation at break nominally increased. Incorporation of the caprolactone rubber graft also exhibited decreased strength and modulus, but the elongation at break was drastically increased from 8% for neat PLLA to 247% for 10% loading. Along this same line, Dhar et al. covalently grafted PLA onto the CNC surface and observed a 40% increase in tensile strength and 490% increase in modulus but with significantly decreased elongation at break, which is indicative of a brittle material [32]. While surface grafting is a viable alternative, the simplicity of using noncovalent surfactants is an attractive alternative; however, special attention must be paid to the composite toughness for many applications.

In other related works, Hossain et al. observed a 31% increase in modulus and a 34% increase in the strength of solvent cast thin films of PLA with 1% CNC but these

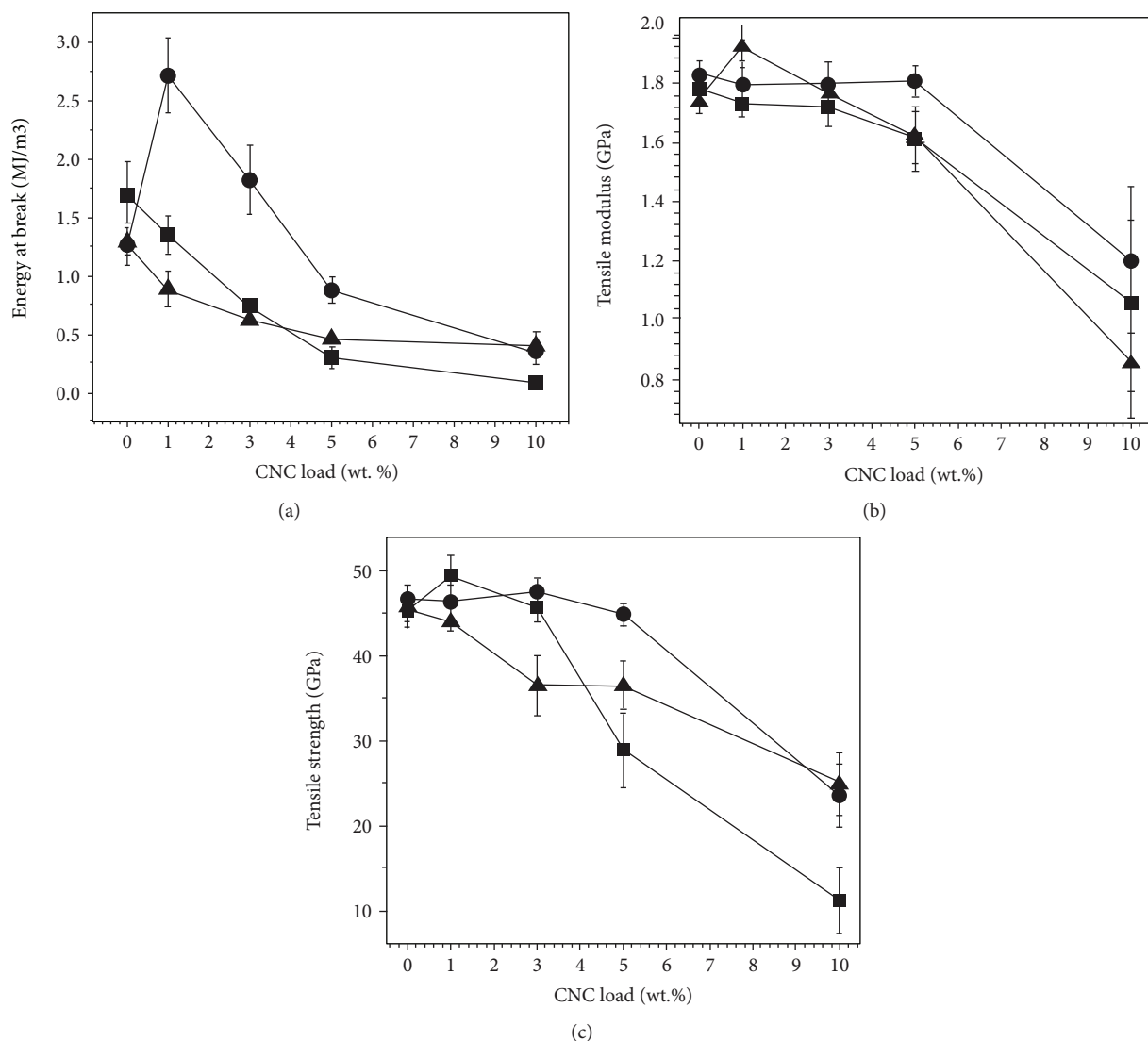


FIGURE 3: Mechanical properties of PLA-CNC composites using different surfactants. ■: UM; ●: DA; ▲: CTAB.

were not extruded into films [31]. Kamal and Khoshkava did not perform tensile tests of their PLA-CNC composites but did determine that the network structure of agglomerates contributes significantly to good dispersion in the PLA matrix [33].

A maximum in the reinforcement of toughness is frequently observed when good dispersions occur at low filler concentrations [34, 35] as observed for the PLA-CNC(1%)-DA composites. This improvement can therefore be the result of favorable dispersions and better interfacial compatibility of CNC-DA with PLA compared to UM- and CTAB-modified CNCs [36, 37]. There are a few toughening mechanisms with rigid fillers discussed in the literature; however, this discussion is inconclusive for CNC nanocomposites. Toughening mechanisms include the formation of microvoids [38], crack bifurcation and crack path alteration [39], interfacial debonding [26], assembly into spiral orientation [40], and shear yielding resulting from the difference on the Young's moduli of the filler and the matrix [41]. In our previous work, the addition of DA improved the CNC

compatibility with aprotic solvents compared to plain CNCs, which agrees with the enhanced mechanical properties obtained when using this surfactant in the present work.

The tensile strength and modulus of the composites followed similar trends as it can be observed in Figures 3(b) and 3(c), remaining fairly constant up to a 3% CNC load but decreasing drastically after 5%. At a 10% load, the mechanical properties were deteriorated obtaining at best a 45% and 32% reduction for the strength and modulus, respectively. This behavior follows the same trend as the energy at break for the 10% films, and it may be indicative of CNC agglomeration.

It has been demonstrated that one mechanism occurring in the reinforcement of the tensile properties of CNC nanocomposites is the formation of a percolating network which transfers the stresses effectively throughout the nanocomposite when high concentrations of filler are added [17, 25]. This mechanism has been often observed with hydrophilic- or surface-charged CNCs when the filler-filler interactions are stronger than the filler-matrix ones and they do not tend to easily aggregate [42, 43].

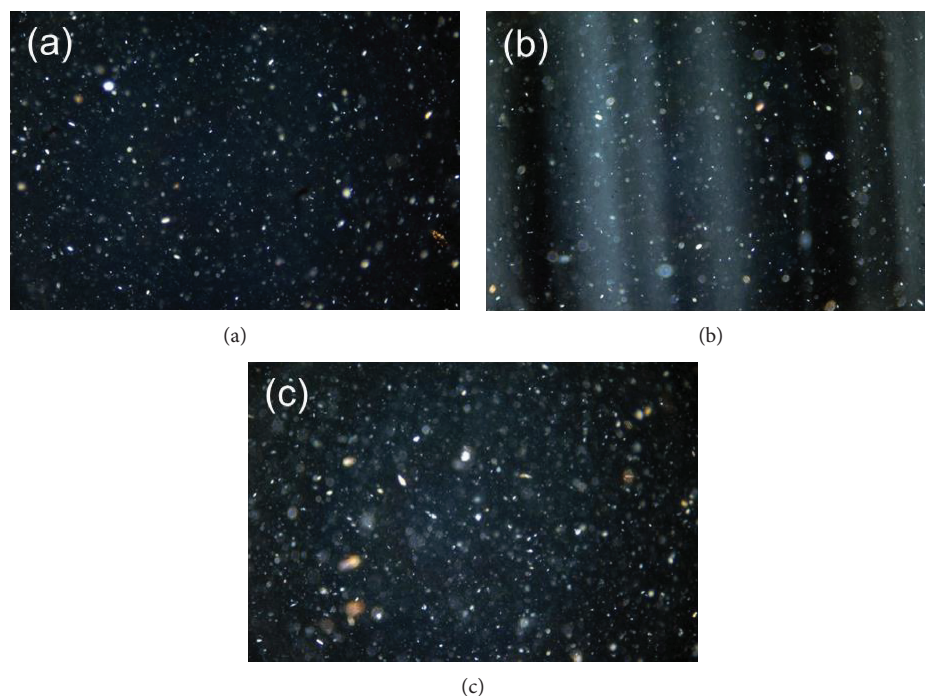


FIGURE 4: Polarized light microscopy images demonstrating the agglomerations on the 3% CNC nanocomposites. (a) UM; (b) DA; (c) CTAB. Length of the longest side of each image: 1.5 mm.

In non-surface-charged nanocrystals, such as the acetylated CNCs in this work, a percolating network is more difficult to form without the formation of agglomerates, introducing defects and thus reducing polymer reinforcement [22]. Therefore, the reinforcement exhibited at low filler concentrations can be attributed to the stress transfer through filler-matrix interactions. However, the relatively low aspect ratios of the CNCs, which are estimated to be approximately 6 to 12, may not enable a perfect transfer of the stresses, possibly reducing the effect of the good compatibility provided by the surfactant [25]. According to the Halpin-Tsai model for short-fiber composites, only nanofillers with aspect ratios larger than 50 can guarantee an efficient reinforcement of the elastic modulus [44].

The addition of surfactants does not seem to significantly affect the tensile strength and modulus of the films as observed in Figures 3(b) and 3(c). However, DA-modified composites possessed overall slightly higher values compared to the other two modified composites, which may also confirm the enhancement of the filler-matrix interactions. Even though these tensile properties were not significantly increased, they were not reduced for the toughened composites (PLA-CNC(1%)-DA), which is frequently a disadvantage in the toughening of polymers. The tensile properties of pure PLA are already comparable to other petroleum-based polymers; therefore, enhancing toughness without compromising other properties becomes an integral step in the reinforcement of PLA.

3.3. Alignment of CNCs and Agglomerations. The CNC agglomeration in all of the 3% CNC nanocomposites was

observed by polarized light microscopy (Figure 4). All composites have relatively large agglomerations; however, the agglomerates in PLA-CNC(3%)-UM (Figure 4(a)) are considerably more than those for DA (Figure 4(b)) and less than those for CTAB composites (Figure 4(c)). This confirms that DA enhances the interfacial interaction and increases CNC compatibility in the composite. Moreover, this also endorses the proposed idea that the detriment of the mechanical properties occurs due to agglomerations forming at high concentrations as a result of insufficient compatibility. PLA-CNC(3%)-DA also displayed white bands under polarized light that can be attributed to ordered assembly resulting from local CNC self-assembly within the composite.

The ordering and self-assembly of the nanocomposite films was studied using polarized light microscopy. Figure 5 shows strong birefringence and anisotropy in the PLA composites at different CNC loads and rotation angles. An ordered anisotropic phase is formed when molecules or particles assemble into a semiorganized structure, changing the refraction of the incident light and allowing the transmission of light between crossed polarized films. The brightness or birefringence observed on the composites in Figure 5, especially at 45° and 135° , increases with CNC concentration, indicating a higher level of crystal organization in the films. In this case, the polarizer and analyzer are fixed at 0° and 90° , respectively. Nonoriented crystals and crystals aligned in the 0° or 90° direction will not diffract light since they possess the same angle of the polarized light. As a result, a bright phase will appear when crystals are oriented at 45° or 135° from the polarizer. For example, at 45° rotation angles in

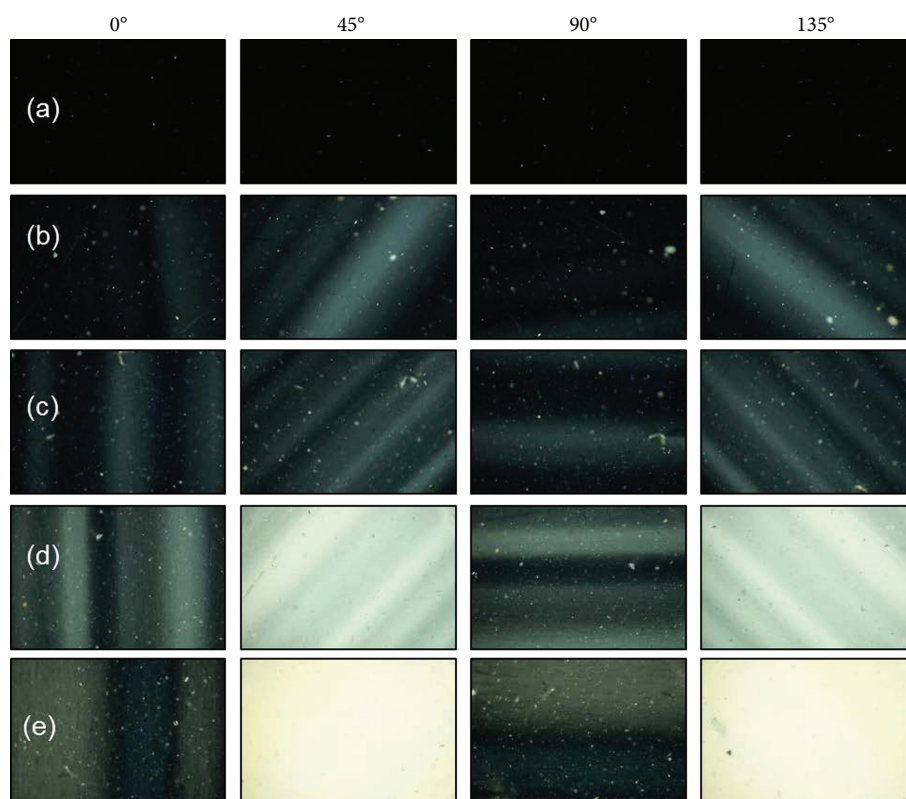


FIGURE 5: Polarized light microscopy images of PLA-CNC-DA composites at different CNC loads: (a) 0, (b) 1, (c) 3, (d) 5, and (e) 10% CNC. At different rotating angles 0° , 45° , 90° , and 135° . Images demonstrate the increasing formation of birefringence in the composites. Length of the longest side of each image: 1.5 mm.

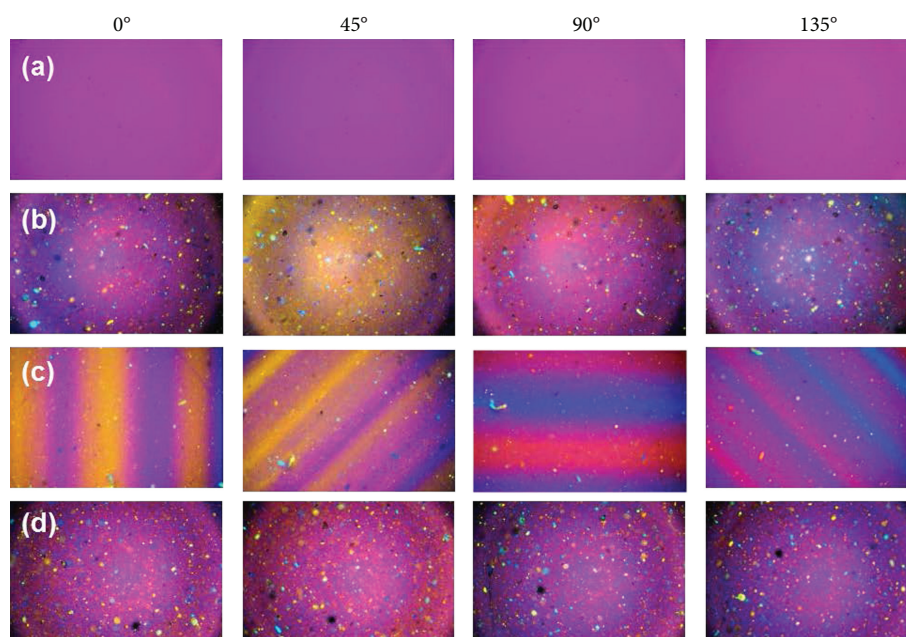


FIGURE 6: Polarized light microscopy images of the 3% CNC-loaded nanocomposites using a first-order red filter: (a) neat PLA; (b) UM; (c) DA; (d) CTAB. At 0° , 45° , 90° , and 135° rotation angles. Length of the longest side of each image: 1.5 mm.

Figure 5, the bright phase indicates that the crystals are oriented either at 45° and 135° , indicating that the crystals are oriented parallel or perpendicular to the film extrusion.

Figure 6 shows the polarized light microscopy images with the red plate for neat PLA and the composites at 3% CNC loading. As discussed above, the levels of agglomeration

TABLE 2: Approximate percentage of colors of PLA-CNC composites observed under polarized light microscopy with a first-order red plate.

| | 0° | 0° | 0° | 45° | 45° | 45° | Estimated oriented area |
|------------------|---------|--------|------|---------|--------|------|-------------------------|
| | Magenta | Yellow | Blue | Magenta | Yellow | Blue | |
| PLA | 100% | 0% | 0% | 100% | 0% | 0% | 0% |
| PLA-CNC(1%)-UM | 53% | 42% | 5% | 77% | 22% | 1% | 70% |
| PLA-CNC(3%)-UM | 92% | 3% | 5% | 0% | 89% | 11% | 108% |
| PLA-CNC(1%)-DA | 43% | 23% | 34% | 59% | 26% | 14% | 97% |
| PLA-CNC(3%)-DA | 40% | 38% | 21% | 60% | 26% | 14% | 100% |
| PLA-CNC(1%)-CTAB | 100% | 0% | 0% | 100% | 0% | 0% | 0% |
| PLA-CNC(3%)-CTAB | 97% | 1% | 2% | 95% | 2% | 3% | 8% |

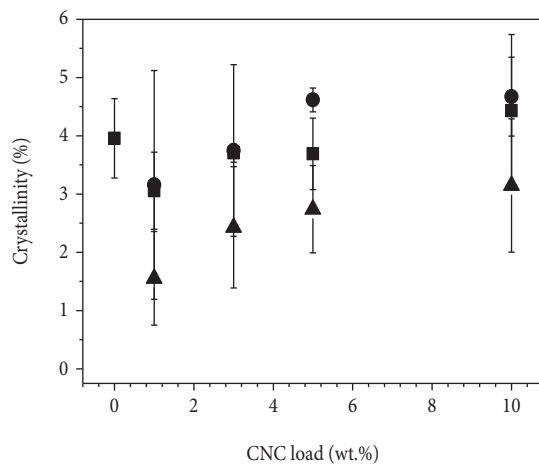


FIGURE 7: Crystallinity of PLA-CNC composites estimated by DSC. ■: UM; ●: DA; ▲: CTAB.

for the UM- and CTAB-modified composites are evident, correlating also with the low degree of CNC orientation in the films. On the other hand, CNC films with DA clearly display a change of color between the angles of rotation, indicating that the crystals are oriented. The total areas occupied by the oriented crystals were quantified by adding the percentage of colors magenta, blue, and yellow from the entire area of the images. The 1 and 3% CNC-loaded composites were analyzed at 0° and 45° angles as observed in Table 2. For neat PLA, the orientation is negligible, resulting in a 0% oriented area. As the CNC load increases, the total calculated oriented area increases in different proportions for each of the composites. The orientation in the CNC-DA composites increases from ~97% to ~100%; while for the UM, it increases from ~70% to ~100% (108% was measured) with an increasing CNC content. Such results indicate a better organization for DA composites at low concentrations as discussed above. The assembly of CNC for the CTAB composites is the lowest among all (0% and 8% for PLA-CNC(1%)-CTAB and PLA-CNC(3%)-CTAB, respectively), correlating with the poor mechanical properties obtained for those composites.

The high level of assembly for the DA composites does not necessarily mean having well-oriented fillers in the direction of the extrusion. Indeed, the DA composites only have ~26% of their organized crystals oriented parallel to the

extrusion of the flow, ~14% is perpendicular, and around 60% is distributed between 45° and 135° with respect to the extrusion direction. In the case of UM composites, an unexpected high orientation of the crystals was observed in the direction of extrusion (~89% for PLA-CNC(3%)-UM). Poorly oriented crystals cannot necessarily be translated to poor mechanical properties. It has been suggested in the literature that a lower degree of CNC orientation may enhance the nanocomposite toughness, although a reduced tensile modulus is accompanied [40]. Therefore, it can be thought that this distribution of crystal orientation may change the path of the crack sufficiently enough to dissipate energy and increase toughness. The ability for acetylated CNCs to self-assemble in organic media in stationary and shear states was studied in our previous work, agreeing with the self-assembly observed in the nanocomposites in the present study.

3.4. Crystallinity of Nanocomposite Films. PLA-CNC nanocomposite crystallinity was determined by DSC, and the results are shown in Figure 7. Neat PLA exhibited low crystallinity, which is likely due to the enantiomer composition, L (95%) and D (5%). It is observed that the addition of CNCs did not significantly affect PLA crystallinity, which is advantageous to the enhancement of toughness and elongation at break. However, a slight increase in crystallinity occurs for the DA composites, which were observed to be the least agglomerated and most oriented out of the 3 modifications studied in this work. DSC analysis also revealed a double melting peak for PLA which occurs at specific conditions of cooling and heating rates [45]. The double peaks have been attributed to a melting-recrystallization mechanism of PLA in which small and imperfect crystallites change into more stable crystals during the melting of the polymer [46].

3.5. Optical Properties. The study of the optical properties of the films is important for advanced and commercial applications. The transparency of the PLA-CNC-DA films, which also exhibited improved toughness, can be observed in Figure 8, showing significant optical transparency for the low concentration of CNCs.

Besides a good transparency, the nanocomposites with high CNC concentration also exhibited interesting optical properties when observed between crossed polars. Colored phases appeared as the thickness was increased by stacking

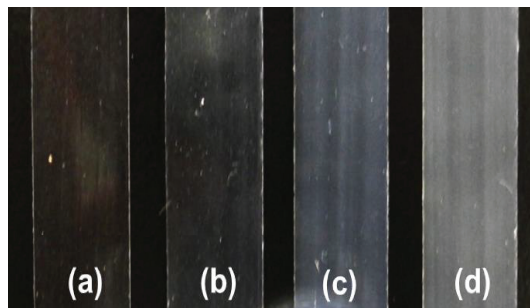


FIGURE 8: Example of the transparency of PLA-CNC-DA composites with CNC loads of (a) 1%, (b) 3%, (c) 5%, and (d) 10%.

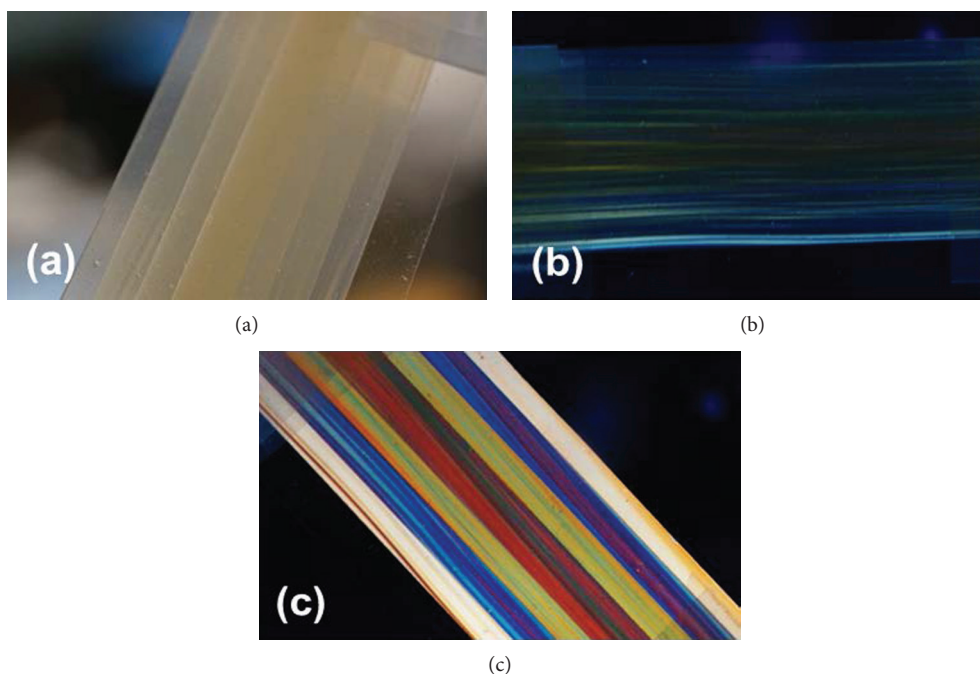


FIGURE 9: Photographs of four PLA-CNC(10%)-DA films that are stacked on top of one another with an offset such that the edges are one film thick and the center is four films thick. The stacked films are viewed (a) in unpolarized light, (b) between crossed polars at a 0° angle, and (c) between crossed polars at a 45° angle.

layers of the composite films (Figure 9). This behavior is believed to be the result of the self-assembly of CNCs within the films despite the agglomerations observed at high CNC concentrations. The colors are the result of high retardations that are dependent on both the thickness of the films (t) and the difference of the refractive index of the two crystallographic axes of the liquid crystal material ($n_2 - n_1$) or birefringence. The DA-modified films showed the most intense colors, visually demonstrating a higher birefringence and confirming once more the ability of DA to aid the formation of semiorganized structures. The birefringence can also be quantified using the Michel-Levy chart [47], which includes the colors obtained at a wide range of retardations (R). This chart can also be expressed by the following equation [48].

$$R = t \times |n_2 - n_1|. \quad (2)$$

Assuming that ($n_2 - n_1$) remains constant for a specific CNC concentration, it is possible to predict the retardations when the thickness is varied and, therefore, also predict the colors of the films. The nanocomposites with 5 and 10% CNCs were the only ones that showed colorful arrangements between crossed polars when the thickness was varied. These colors were matched with the colors in the Michel-Levy chart, and the retardations were read from the chart. Using (2), the birefringence ($n_2 - n_1$) was then determined to be 0.0017 ± 0.0001 for the PLA-CNC(10%)-DA films and 0.0008 ± 0.0001 for the PLA-CNC(5%)-DA films. For the PLA-CNC(10%)-UM and the PLA-CNC(10%)-CTAB composites, the birefringence values were 0.0015 ± 0.0002 and 0.0011 ± 0.0003 , respectively. These results have the same trend as the resulting mechanical properties and dispersibility of CNCs within the matrix as discussed earlier in the work, demonstrating that self-assembly occurs in spite of the agglomerations obtained at higher

concentrations. The birefringence values can be used for the prediction or targeting of certain colors by changing the thickness of the composites or the CNC concentration. These optical properties can have potential applications in areas such as decorative coating, security papers, and liquid crystal displays among others.

4. Conclusions

Surface-modified CNCs were added into PLA as reinforcement, resulting in enhanced mechanical and optical properties of extruded films. The toughness of the PLA composites was enhanced by 61% compared to that of neat PLA when using 1% of DA-modified CNCs without detriment to the tensile strength or modulus. As the concentration increased, toughness gradually decreased to very low values for the 10% loading. For unmodified and CTAB-modified CNCs, toughness decreased with concentration worsening the properties of PLA. The increase in toughness was attributed to a relatively good dispersion and good interfacial adhesion between the CNCs and the matrix. Tensile strength and modulus remained fairly similar compared to neat PLA, but as CNC concentration increased, these properties decreased more than 45% for the 10% CNC composites. The lack of surface charge on the surface of the CNCs may induce the formation of agglomerations at high concentrations preventing the development of a percolating network which has been previously shown to increase the tensile properties. Polarized light microscopy images of the CNC nanocomposites revealed the formation of oriented CNC, which provided interesting colors to the composites at high CNC loadings. It was shown that a better dispersion of CNCs results in a better organization in the composites, especially in the ones modified with DA. However, the degree of alignment was found to be relatively low with CNC orientation pointing at multiple directions around the extrusion line for the toughened composites, which has been attributed to the inherent spiral assembly of cellulose as reported in the literature [40]. The crystallinity of the nanocomposites was not increased by the addition of the CNCs, which also facilitated the toughening of the composites by the addition of the filler. Overall, this work demonstrated the ability to increase the toughness and optical properties under polarize light of PLA films without sacrificing good tensile properties by the addition of low percentage of acetylated CNCs functionalized with surfactants.

Data Availability

The experimental data used to support the findings of this study are included within the article and supporting information file.

Conflicts of Interest

The authors declare that they have no conflicts of interest.

Acknowledgments

This study was funded by the National Science Foundation (grant no. CMMI-1130825) and the NASA South Carolina Space Grant Consortium. We would also like to acknowledge Frederick Wewers for his collaboration in this work.

Supplementary Materials

Figure S1: representative stress-strain curves for 10 samples of (a) pure PLA, (b) PLA with 1 wt.% CNC without added surfactant, (c) PLA with 1.0 wt.% CNC and decylamine surfactant, and (d) PLA with 1.0 wt.% CNC and CTAB surfactant. Values for the tensile strength, tensile modulus, and toughness (energy at break) were determined for each curve and averaged to yield values in Figure 3. Figure S2: orientation of the polarizer, analyzer, and the first-order red filter (red slow direction) and colors observed when liquid crystals are oriented in the corresponding angles of rotation. Figure S3: polarized microscopy of PLA-CNC-UM films at different CNC loadings using a first-order red plate (5% and 10% lack of meaning when analyzed with the red plate due to the high retardations). Figure S4: polarized microscopy of PLA-CNC-DA films at different CNC loadings using a first-order red plate (5% and 10% lack of meaning when analyzed with the red plate due to the high retardations). Figure S5: polarized microscopy of PLA-CNC-DA films at different CNC loadings using a first-order red plate (5% and 10% lack of meaning when analyzed with the red plate due to the high retardations). Figure S6: PLA-CNC (5% and 10%) composite films with (a) unmodified CNCs; (b) DA-modified CNCs; and (c) CTAB-modified CNCs. Figure S7: low magnification polarized light microscopy of PLA-CNC(10%)-DA nanocomposites showing colored optical properties. (*Supplementary Materials*)

References

- [1] K. Madhavan Nampoothiri, N. R. Nair, and R. P. John, "An overview of the recent developments in polylactide (PLA) research," *Bioresource Technology*, vol. 101, no. 22, pp. 8493–8501, 2010.
- [2] Bioplastics, E, "Bioplastics facts and figures," [cited 2013 06/06/2013], 2013, <https://www.european-bioplastics.org/>.
- [3] X. Pang, X. Zhuang, Z. Tang, and X. Chen, "Polylactic acid (PLA): research, development and industrialization," *Biotechnology Journal*, vol. 5, no. 11, pp. 1125–1136, 2010.
- [4] R. M. Rasal, A. V. Janorkar, and D. E. Hirt, "Poly(lactic acid) modifications," *Progress in Polymer Science*, vol. 35, no. 3, pp. 338–356, 2010.
- [5] R. A. Auras, L. T. Lim, S. E. Selke, and H. Tsuji, *Poly (Lactic Acid): Synthesis, Structures, Properties, Processing, and Applications*, vol. 10, Wiley, 2011.
- [6] J. C. Bogaert and P. Coszach, "Poly(lactic acids): a potential solution to plastic waste dilemma," *Macromolecular Symposia*, vol. 153, no. 1, pp. 287–303, 2000.
- [7] E. T. H. Vink, K. R. Rábago, D. A. Glassner, and P. R. Gruber, "Applications of life cycle assessment to NatureWorks™ polylactide (PLA) production," *Polymer Degradation and Stability*, vol. 80, no. 3, pp. 403–419, 2003.

- [8] J. Ahmed and S. K. Varshney, "Polylactides—chemistry, properties and green packaging technology: a review," *International Journal of Food Properties*, vol. 14, no. 1, pp. 37–58, 2011.
- [9] H. Balakrishnan, A. Hassan, M. Imran, and M. U. Wahit, "Toughening of polylactic acid nanocomposites: a short review," *Polymer-Plastics Technology and Engineering*, vol. 51, no. 2, pp. 175–192, 2012.
- [10] M. Jamshidian, E. A. Tehrani, M. Imran, M. Jacquot, and S. Desobry, "Poly-lactic acid: production, applications, nanocomposites, and release studies," *Comprehensive Reviews in Food Science and Food Safety*, vol. 9, no. 5, pp. 552–571, 2010.
- [11] H. Liu and J. Zhang, "Research progress in toughening modification of poly(lactic acid)," *Journal of Polymer Science Part B: Polymer Physics*, vol. 49, no. 15, pp. 1051–1083, 2011.
- [12] S. Sinha Ray, "Polylactide-based bionanocomposites: a promising class of hybrid materials," *Accounts of Chemical Research*, vol. 45, no. 10, pp. 1710–1720, 2012.
- [13] E. C. Ramires and A. Dufresne, "A review of cellulose nanocrystals and nanocomposites," *Tappi Journal*, vol. 10, no. 4, pp. 9–16, 2011.
- [14] D. Bondeson and K. Oksman, "Dispersion and characteristics of surfactant modified cellulose whiskers nanocomposites," *Composite Interfaces*, vol. 14, no. 7–9, pp. 617–630, 2007.
- [15] E. Fortunati, I. Armentano, Q. Zhou et al., "Multifunctional bionanocomposite films of poly(lactic acid), cellulose nanocrystals and silver nanoparticles," *Carbohydrate Polymers*, vol. 87, no. 2, pp. 1596–1605, 2012.
- [16] J. K. Muiruri, S. Liu, W. S. Teo, J. Kong, and C. He, "Highly biodegradable and tough polylactic acid–cellulose nanocrystal composite," *ACS Sustainable Chemistry & Engineering*, vol. 5, no. 5, pp. 3929–3937, 2017.
- [17] Y. Habibi, L. A. Lucia, and O. J. Rojas, "Cellulose nanocrystals: chemistry, self-assembly, and applications," *Chemical Reviews*, vol. 110, no. 6, pp. 3479–3500, 2010.
- [18] A. Sturcova, G. R. Davies, and S. J. Eichhorn, "Elastic modulus and stress-transfer properties of tunicate cellulose whiskers," *Biomacromolecules*, vol. 6, no. 2, pp. 1055–1061, 2005.
- [19] R. J. Moon, A. Martini, J. Nairn, J. Simonsen, and J. Youngblood, "Cellulose nanomaterials review: structure, properties and nanocomposites," *Chemical Society Reviews*, vol. 40, no. 7, pp. 3941–3994, 2011.
- [20] B. Braun and J. R. Dorgan, "Single-step method for the isolation and surface functionalization of cellulosic nanowhiskers," *Biomacromolecules*, vol. 10, no. 2, pp. 334–341, 2009.
- [21] J. Kim, G. Montero, Y. Habibi et al., "Dispersion of cellulose crystallites by nonionic surfactants in a hydrophobic polymer matrix," *Polymer Engineering & Science*, vol. 49, no. 10, pp. 2054–2061, 2009.
- [22] R. Rusli, K. Shanmuganathan, S. J. Rowan, C. Weder, and S. J. Eichhorn, "Stress transfer in cellulose nanowhisker composites—influence of whisker aspect ratio and surface charge," *Biomacromolecules*, vol. 12, no. 4, pp. 1363–1369, 2011.
- [23] D. Y. Liu, X. W. Yuan, D. Bhattacharyya, and A. J. Easteal, "Characterisation of solution cast cellulose nanofibre – reinforced poly(lactic acid)," *Express Polymer Letters*, vol. 4, no. 1, pp. 26–31, 2010.
- [24] M. Grunert and W. T. Winter, "Nanocomposites of cellulose acetate butyrate reinforced with cellulose nanocrystals," *Journal of Polymers and the Environment*, vol. 10, no. 1/2, pp. 27–30, 2002.
- [25] S. J. Eichhorn, A. Dufresne, M. Aranguren et al., "Review: current international research into cellulose nanofibres and nanocomposites," *Journal of Materials Science*, vol. 45, no. 1, pp. 1–33, 2010.
- [26] X. Xu, F. Liu, L. Jiang, J. Y. Zhu, D. Haagenson, and D. P. Wiesenborn, "Cellulose nanocrystals vs. cellulose nanofibrils: a comparative study on their microstructures and effects as polymer reinforcing agents," *ACS Applied Materials & Interfaces*, vol. 5, no. 8, pp. 2999–3009, 2013.
- [27] A. Pei, Q. Zhou, and L. A. Berglund, "Functionalized cellulose nanocrystals as biobased nucleation agents in poly(L-lactide) (PLLA) – crystallization and mechanical property effects," *Composites Science and Technology*, vol. 70, no. 5, pp. 815–821, 2010.
- [28] R. K. Johnson, A. Zink-Sharp, and W. G. Glasser, "Preparation and characterization of hydrophobic derivatives of TEMPO-oxidized nanocelluloses," *Cellulose*, vol. 18, no. 6, pp. 1599–1609, 2011.
- [29] M. Roman and W. T. Winter, "Effect of sulfate groups from sulfuric acid hydrolysis on the thermal degradation behavior of bacterial cellulose," *Biomacromolecules*, vol. 5, no. 5, pp. 1671–1677, 2004.
- [30] D. Y. Kim, Y. Nishiyama, M. Wada, and S. Kuga, "High-yield carbonization of cellulose by sulfuric acid impregnation," *Cellulose*, vol. 8, no. 1, pp. 29–33, 2001.
- [31] K. M. Z. Hossain, I. Ahmed, A. J. Parsons et al., "Physicochemical and mechanical properties of nanocomposites prepared using cellulose nanowhiskers and poly(lactic acid)," *Journal of Materials Science*, vol. 47, no. 6, pp. 2675–2686, 2012.
- [32] P. Dhar, D. Tarafder, A. Kumar, and V. Katiyar, "Thermally recyclable polylactic acid/cellulose nanocrystal films through reactive extrusion process," *Polymer*, vol. 87, pp. 268–282, 2016.
- [33] M. R. Kamal and V. Khoshkava, "Effect of cellulose nanocrystals (CNC) on rheological and mechanical properties and crystallization behavior of PLA/CNC nanocomposites," *Carbohydrate Polymers*, vol. 123, pp. 105–114, 2015.
- [34] C. B. Ng, B. J. Ash, L. S. Schadler, and R. W. Siegel, "A study of the mechanical and permeability properties of nano- and micron-TiO₂ filled epoxy composites," *Advanced Composites Letters*, vol. 10, no. 3, pp. 101–111, 2001.
- [35] M. Bulota, A. H. Vesterinen, M. Hughes, and J. Seppälä, "Mechanical behavior, structure, and reinforcement processes of TEMPO-oxidized cellulose reinforced poly(lactic acid)," *Polymer Composites*, vol. 34, no. 2, pp. 173–179, 2013.
- [36] E. E. Urena-Benavides and C. L. Kitchens, "Cellulose nanocrystal reinforced alginate fibers—biomimicry meets polymer processing," *Molecular Crystals and Liquid Crystals*, vol. 556, no. 1, pp. 275–287, 2012.
- [37] M. Bulota, K. Kreitsmann, M. Hughes, and J. Paltakari, "Acetylated microfibrillated cellulose as a toughening agent in poly(lactic acid)," *Journal of Applied Polymer Science*, vol. 126, no. S1, pp. E449–E458, 2012.
- [38] S. T. Knauert, J. F. Douglas, and F. W. Starr, "The effect of nanoparticle shape on polymer-nanocomposite rheology and tensile strength," *Journal of Polymer Science Part B: Polymer Physics*, vol. 45, no. 14, pp. 1882–1897, 2007.

- [39] J. K. Kim and R. E. Robertson, "Toughening of thermoset polymers by rigid crystalline particles," *Journal of Materials Science*, vol. 27, no. 1, pp. 161–174, 1992.
- [40] E. E. Urena-Benavides and C. L. Kitchens, "Wide-angle X-ray diffraction of cellulose nanocrystal–alginate nanocomposite fibers," *Macromolecules*, vol. 44, no. 9, pp. 3478–3484, 2011.
- [41] J. Z. Liang and R. K. Y. Li, "Rubber toughening in polypropylene: a review," *Journal of Applied Polymer Science*, vol. 77, no. 2, pp. 409–417, 2000.
- [42] L. Tang and C. Weder, "Cellulose whisker/epoxy resin nanocomposites," *ACS Applied Materials & Interfaces*, vol. 2, no. 4, pp. 1073–1080, 2010.
- [43] E. E. Urena-Benavides, P. J. Brown, and C. L. Kitchens, "Effect of jet stretch and particle load on cellulose nanocrystal–alginate nanocomposite fibers," *Langmuir*, vol. 26, no. 17, pp. 14263–14270, 2010.
- [44] J. C. H. Affdl and J. L. Kardos, "The Halpin-Tsai equations: a review," *Polymer Engineering and Science*, vol. 16, no. 5, pp. 344–352, 1976.
- [45] M. Yasuniwa, S. Tsubakihara, Y. Sugimoto, and C. Nakafuku, "Thermal analysis of the double-melting behavior of poly(L-lactic acid)," *Journal of Polymer Science Part B: Polymer Physics*, vol. 42, no. 1, pp. 25–32, 2004.
- [46] Z. Tang, C. Zhang, X. Liu, and J. Zhu, "The crystallization behavior and mechanical properties of polylactic acid in the presence of a crystal nucleating agent," *Journal of Applied Polymer Science*, vol. 125, no. 2, pp. 1108–1115, 2012.
- [47] P. Robinson and M. Davidson, *Michel-Levy Interference Color Chart*, Nikon website, 2006, <http://www.microscopyu.com/articles/polarized/michel-levy.html>.
- [48] S. Robinson and P. Bradbury, *Qualitative Polarized Light Microscopy, Microscopy Handbooks*, vol. 9, Oxford University Press—Royal Microscopical Society, Oxford, UK, 1992.

Research Article

Structural, Optical, and Photocatalytic Activities of Ag-Doped and Mn-Doped ZnO Nanoparticles

Mengstu Etay Ashebir ¹, Gebrekidan Mebrahtu Tesfamariam,¹
Gebretinsae Yeabyo Nigusie ¹ and Tesfakiros Woldu Gebreab²

¹Department of Chemistry, College of Natural and Computational Sciences, Mekelle University, Mekelle, Ethiopia

²Department of Physics, College of Natural and Computational Sciences, Mekelle University, Mekelle, Ethiopia

Correspondence should be addressed to Mengstu Etay Ashebir; mengstuetay@gmail.com

Received 12 April 2018; Revised 26 June 2018; Accepted 24 July 2018; Published 3 September 2018

Academic Editor: Giuliana Magnacca

Copyright © 2018 Mengstu Etay Ashebir et al. This is an open access article distributed under the Creative Commons Attribution License, which permits unrestricted use, distribution, and reproduction in any medium, provided the original work is properly cited.

We report the photocatalytic activities of ZnO, Ag-doped ZnO, and Mn-doped ZnO nanoparticles (NPs). Ag-doped and Mn-doped ZnO samples were synthesized using a coprecipitation method and calcined at 600°C. XRD, SEM, EDX, and UV-vis spectroscopy techniques were employed for characterization of the synthesized samples. The photocatalytic activities of the samples were evaluated by measuring the photocatalytic decolorization of methyl violet with sunlight being the source of energy. XRD patterns of the samples confirmed the wurtzite structure without change which was indicative of the absence of Mn- and Ag-related secondary phases for the doped ZnO. The UV-vis spectra indicated the band gap energy of ZnO, Ag-doped ZnO, and Mn-doped ZnO to be 2.98, 2.80, and 2.64 eV, respectively. Photocatalytic decolorization of methyl violet for the synthesized samples was found to be favorable at a pH of 9.0, catalyst dose of 1 g/L, and initial dye concentration of 4.5×10^{-4} g/L. Mn-doped ZnO and Ag-doped ZnO photocatalytic decolorization efficiency was significantly higher than undoped ZnO. Incorporation of Mn and Ag enhanced the visible-light photocatalytic activity of ZnO; this could be due to the ability of these metals to increase the surface defects of ZnO which in turn shift their optical absorption towards the visible region.

1. Introduction

Currently, industrial effluents and household wastewater that are improperly disposed into the environment are becoming the major sources of residual dye pollutants [1]. Wastewater contaminated with residual dyes from textile industries, paper industries, and other industries are among the main sources of environmental pollutants in both developed and developing countries. Such industries produce a lot of organic contaminants including dyes such as methyl violet (MV) which is toxic as it can cause severe skin, respiratory, gastrointestinal tract, and eye irritations [2]. The toxic and potentially carcinogenic substances coming from these dyes cause severe environmental and health problems when they are released into the aquatic environment [3].

Numerous studies have been conducted to develop methods and technologies for the removal of residual dyes from wastewater which can be classified as physical,

biological, and chemical methods. Physical methods include membrane filtration, adsorption, and precipitation [4], biological methods include biodegradation processes to remove bacteria used for the degradation of soluble organic matter present in effluent, and chemical methods include photochemical decolorization, chlorination, and ozonation [5]. These conventional ways for treatment of wastewater, such as adsorption, chemical precipitation, separation, and coagulation which merely transfer dyes from one phase to another are not effective methods, because they bring secondary pollution.

Nowadays, the use of metal oxide nanoparticles for water treatment has gained special attention. This is due to their cost-effectiveness, stability, recyclability, and environmental friendliness as photocatalysts [6]. Surface area and surface defects play a significant role in enhancing the photocatalytic activities of metal oxides. The reason is that doping of metal oxides with metal and/or transition metals increases the

surface defects, affects the optical and electronic properties, and shifts the optical absorption towards the visible region [7].

ZnO has been known to be one of the desired NPs for photocatalytic degradation of inorganic and organic contaminants in various matrices. This is due to its high photosensitivity, harmlessness, low cost, and chemical stability [8, 9]. Most semiconductor photocatalysts like ZnO has a band gap energy in the range of the ultraviolet region, which is ≥ 3.2 eV [10]. Thus, semiconductors enhance photocatalysis with UV radiation. Unfortunately, the sunlight spectrum includes only about 5–7% of UV light [11]. This minimum amount of UV light in the sunlight spectrum has particularly ruled out the use of the natural source of light for photocatalytic decolorization of pollutants.

Methyl violet (MV) is a cationic dye which has an aromatic structure which is resistant to light and biological activity [2]. It has a variety of uses in the textile and leather industries, as well as in processing paper and pulp. The release of the dye to the environment causes toxicity problems. Long-term exposure to the dye causes mutagenic, carcinogenic, and allergic effects [12]. Thus, in this study, the photocatalytic decolorization of the MV dye has been investigated. In this paper, the synthesis of ZnO, Ag-doped ZnO, and Mn-doped ZnO NPs through the precipitation method and their photocatalytic decolorization activities using MV as a model have been reported.

2. Experiments

2.1. Materials. All chemicals used were analytical grade and used without further purification. These chemicals include zinc chloride (ZnCl_2 , Sigma-Aldrich), anhydrous manganese (II) chloride (MnCl_2 , Sigma-Aldrich), silver nitrate (AgNO_3 , Sigma-Aldrich), ammonia water (NH_4OH , Sigma-Aldrich), sodium hydroxide (NaOH , Sigma-Aldrich), ethanol ($\text{C}_2\text{H}_5\text{OH}$, 99.5%, Sigma-Aldrich), acetone, and distilled water.

2.2. Synthesis of ZnO, Ag-Doped ZnO, and Mn-Doped Nanoparticles. The ZnO nanoparticle was synthesized from ZnCl_2 through the precipitation method. 1 mol of ZnCl_2 was added to a beaker and dissolved in 100 mL of distilled water with continuous stirring. A 10% NaOH solution was added into the beaker dropwise until the pH became 12. During the addition of the NaOH solution, white precipitates were formed and finally, the sedimentation process was finished at pH 12. The precipitates were washed many times with deionized water and separated through a separatory funnel and centrifuged until free of impurities. The purified white precipitate was dried for 24 hours at 80°C . At this point, the white product did not show high crystallinity because it consisted of ZnO and $\text{Zn}(\text{OH})_2$. Then, it was calcined at 600°C for 3 hours, to allow for the complete removal of inorganic matter and to obtain highly crystallized ZnO NPs. The resulting precipitate was washed with ethanol and centrifuged (4000 rpm). The above procedure was repeated five times to remove unreacted ions. The synthesized NPs

were then used for further experimental exploration, adapted from [13] with some modifications.

To prepare Mn-doped ZnO NPs, 0.95 mol of ZnCl_2 and 0.05 mol of MnCl_2 were mixed in a beaker, and dissolved in 100 mL of distilled water with continuous stirring until the homogeneous solution was formed. 25–30% of aqueous ammonia was added slowly into the solution to get sedimentary products until the pH of solutions became 8.5. When the reaction of the precursors and ammonia was completed, the precipitate was collected via centrifugation from the solution. The precipitated products were washed with diethyl ether in the fume hood and then washed using 99.9% purity ethanol. As a final point, it was washed three times with deionized water and centrifuged. Finally, it was dried at 80°C for 24 h and calcined at 600°C for 2 h under normal atmospheric conditions, and nanoparticle products were obtained [13].

To prepare Ag-doped ZnO NPs, 0.95 mol of ZnCl_2 and 0.05 mol of AgNO_3 were mixed to 100 mL of distilled water; aqueous ammonia was added drop by drop until a pH of 7 was attained with continuous stirring for 30 min. The white gel produced was allowed to settle overnight. For the complete elimination of impurities, the precipitate formed was washed with deionized water and acetone followed by centrifugation at 3500 rpm. The precipitate was then kept in an oven at 80°C for 24 h to obtain a dry powder which was then subjected to calcination at 600°C for 2 h in a muffle furnace fitted with a PID temperature controller with the heating rate kept at $10^\circ\text{C min}^{-1}$ [14].

2.3. Characterization. X-ray diffraction (XRD) measurements of all the samples were carried out using the Shimadzu X-ray diffractometer with Cu-K α radiation ($\lambda = 1.5406 \text{ \AA}$) and a scan speed of 3.00 deg/min. The scanning electron microscopy (SEM) study was carried out by a JEOL JSM-5610 equipped with a BE detector scanning electron microscope. The energy dispersive X-ray (EDX) spectrum was recorded with the JEOL JSM-5610 SEM equipped with EDX. UV-vis spectra of the oxides were recorded employing a PerkinElmer Lambda 35 spectrometer used to estimate the absorbance edge which is operated at a wavelength range of 200–800 nm in diffuse reflectance mode. Spectra were recorded at room temperature, and the data were transformed through the Kubelka-Munk function [15].

2.4. Photocatalytic Testing. In laboratory scale, numerous methods for the heterogeneous photocatalytic decolorization of dyes have been investigated. In this work, the MV dye was selected as the model chemical for the evaluation of the photocatalytic efficiency of the silver- and manganese-doped ZnO NPs. The MV dye (molecular formula: $\text{C}_{24}\text{H}_{28}\text{N}_3\text{Cl}$, molecular weight: 407.99 g/mol) has an absorbance of $\lambda_{\text{max}} = 590 \text{ nm}$ (Figure 1). The MV was used as a model due to its frequent presence in industrial wastes and its health effects [2]. The photocatalytic experiments were carried out in a 500 mL capacity beaker reactor and the mixture of 1 g/L of ZnO, Ag-doped ZnO, and Mn-doped ZnO with $4.5 \times 10^{-4} \text{ M}$ MV dye were stirred in the dark for 30 min to allow adsorption/desorption equilibrium before irradiating [16]. The irradiation was then conducted

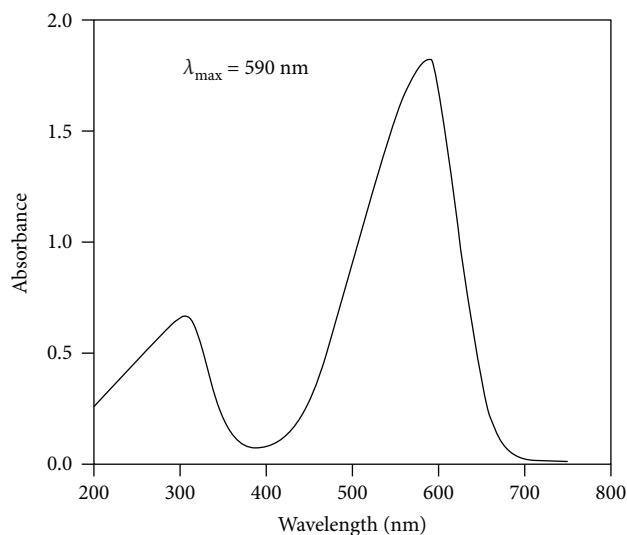


FIGURE 1: The absorbance spectrum of methyl violet.

using sunlight specifically on sunny days in between 10 AM and 2 PM, when the solar intensity fluctuations were minimal [17].

The progress of the photocatalytic decolorization of methyl violet was monitored by withdrawing 10 mL of the sample at 20 min intervals. The suspension was centrifuged at 3000 rpm for 5–7 min and filtered using 0.45 mm Whatman paper to remove the catalyst particles before measuring absorbance. The experiment was repeated with other concentrations and pH levels of the dye solution. The concentration of MV was determined by measuring the absorption intensity at the maximum absorbance wavelength (as measured using a UV-vis spectrophotometer), and percentage of decolorization was calculated from the following equation:

$$\% \text{decolorization} = A_0 - \frac{A_t}{A_0} \times 100, \quad (1)$$

where A_0 is absorbance of dye at initial stage and A_t is absorbance of dye at time “ t ”.

3. Results and Discussion

3.1. XRD Analysis. The X-ray diffraction patterns of ZnO, Mn-doped ZnO, and Ag-doped ZnO are shown in Figure 2. As shown in Figures 2(b) and 2(c), the diffraction patterns of Mn-doped ZnO and Ag-doped ZnO NPs are almost similar to the undoped ZnO NPs except for minor differences probably caused by the presence of tiny impurities of the Ag-doped and Mn-doped ZnO NPs as reported in the JCPDS file number 36-1451. For the Ag-doped ZnO, the existence of silver changed the relative intensity of the diffraction peaks at about 31.80° (100), 34.47° (002), 36.29° (101), 47.58° (102), 56.62° (200), 62.90° (112), 66.40° (103), 67.98° (110), 69.11° (201), and 76.99° (202) as displayed in Figure 2(b). The XRD of Ag-doped ZnO does not show peaks of metallic Ag at 38.21° (111), 44.41° (200), and so on (JCPDS03-092). This may be because of the low dosage of

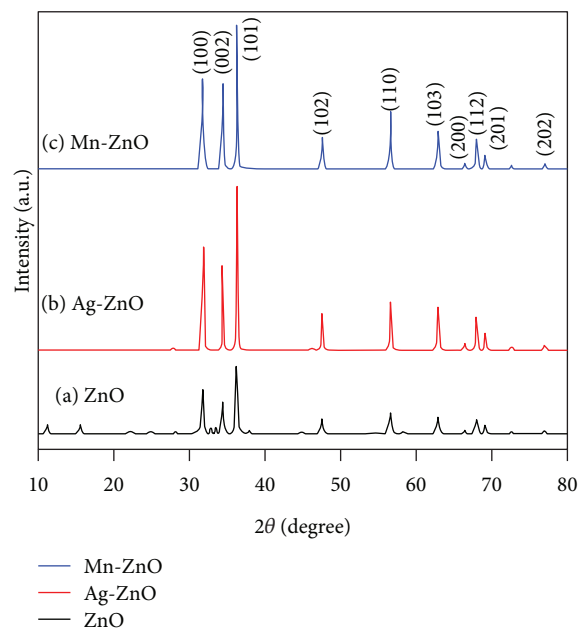


FIGURE 2: The XRD patterns of (a) ZnO, (b) Ag-doped ZnO, and (c) Mn-doped ZnO NPs at 600°C .

silver ions. It might also be due to the O vacancies that were produced from the lower charge of the silver ion-doped ZnO NPs compared with that produced from zinc ions and the formation of a deficiency in silver ion-doped ZnO nanoparticles [7].

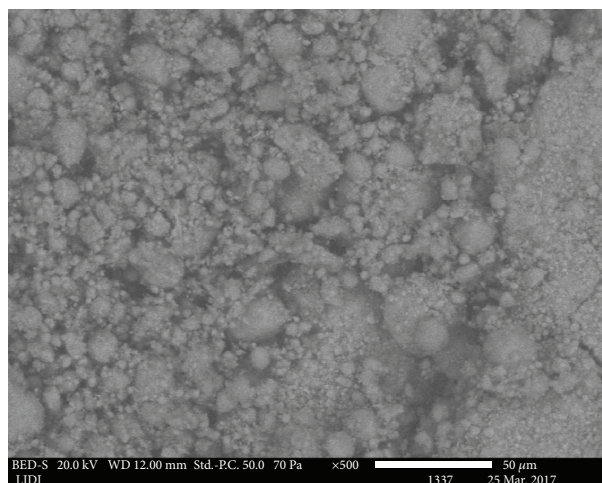
For the Mn-doped ZnO, the presence of manganese changed the relative intensity of the diffraction peaks at about 31.79° (100), 34.46° (002), 36.28° (101), 47.57° (102), 56.61° (110), 62.89° (103), 66.39° (200), 67.97° (112), 69.10° (201), and 76.97° (202) as displayed in Figure 2(c). Due to the difference in ionic radii between Zn^{2+} (0.72 \AA) and Mn^{2+} (0.80 \AA) [18], only a small extent of manganese would be incorporated in the ZnO lattice. This could improve the photocatalytic activity of ZnO, which was verified by the photocatalytic experiments using the MV model dye.

The sharp, definite line broadening of the diffraction peaks positioned at 2θ indicated that the samples are highly crystalline and the synthesized materials are in the nanometer range as it has been reported by others [18]. The crystalline domain size of the synthesized samples of ZnO, Ag-doped ZnO, and Mn-doped ZnO have been obtained from the half width of the full maximum (HWFMM) of the most intense peaks of the respective crystals using the Scherrer equation [19].

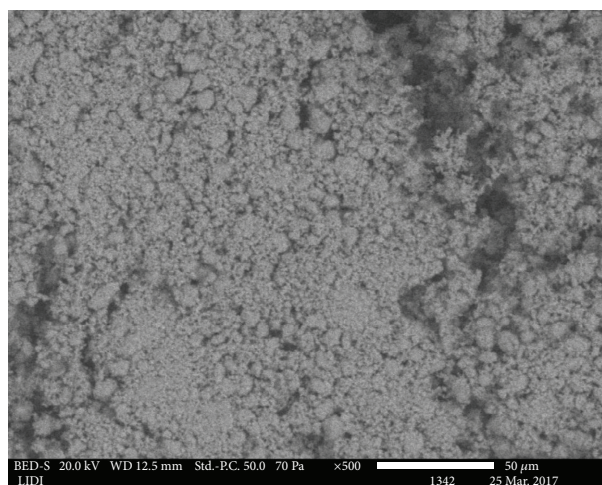
$$D = \frac{K\lambda}{\beta \cos \theta}, \quad (2)$$

where the constant K is the shape factor = 0.94, λ is the wavelength of X-rays (1.5406 for Cu-K α), θ is Bragg's angle, and β is the full width at half maximum.

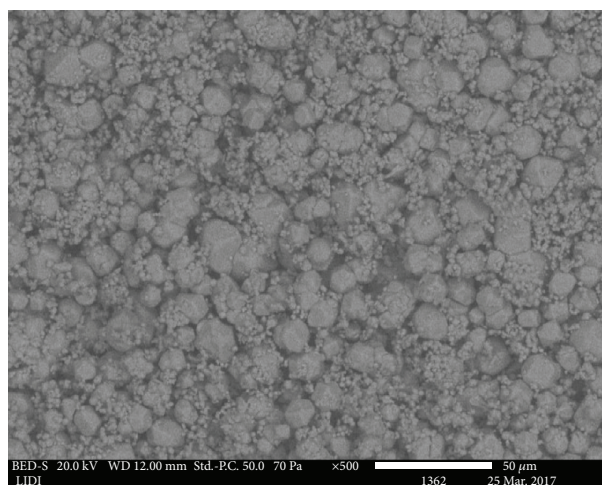
The crystalline domain size of ZnO, Mn-doped ZnO, and Ag-doped ZnO were found to be 31.78 nm , 49.88 nm , and 41.3 nm , respectively. The crystalline domain sizes of Ag-



(a)



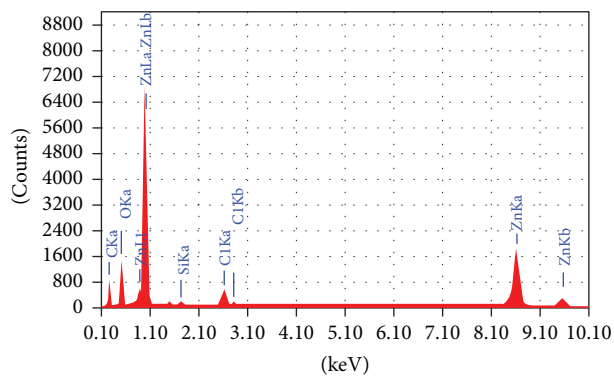
(b)



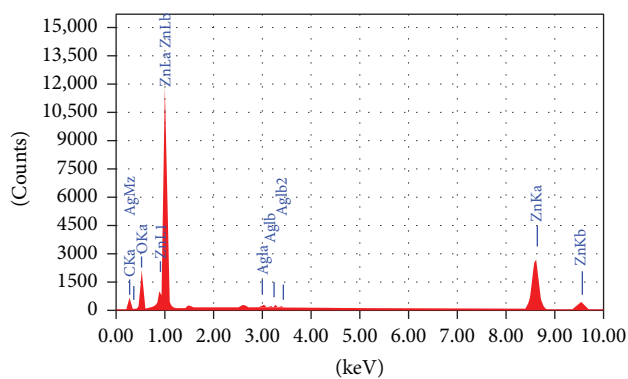
(c)

FIGURE 3: The SEM micrographs of (a) ZnO, (b) Ag-doped ZnO, and (c) Mn-doped ZnO NPs at 600°C.

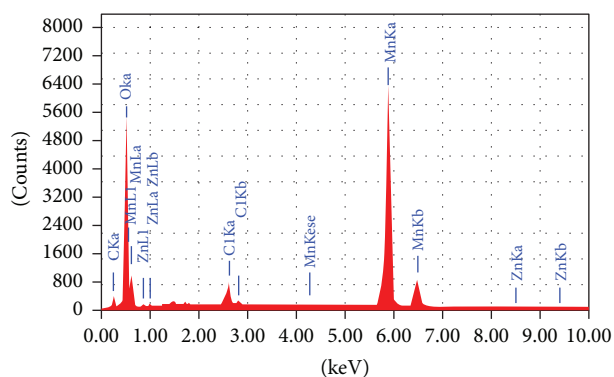
doped ZnO and Mn-doped ZnO are larger than ZnO, and this might be due to the anchoring of very small amounts of Ag and Mn at the surface of ZnO, or due to the segregation



(a)



(b)



(c)

FIGURE 4: EDX spectrum of (a) ZnO, (b) Ag-doped ZnO, and (c) Mn-doped ZnO.

of Ag and Mn ions in the boundaries of ZnO [20, 21], or due to the lesser solubility of Mn/Ag in ZnO as reported in [19].

3.2. SEM Analysis. The morphologies of ZnO, Ag-doped ZnO, and Mn-doped ZnO NPs calcined at 600°C are shown in Figure 3. From SEM micrographs, it is evident that the morphology of ZnO changes after doping with Mn and Ag. The SEM micrographs of Mn-doped ZnO and Ag-doped ZnO illustrate that the morphology is relatively ordered and show that the agglomerations of particles are much less in this method of preparation (Figures 3(b) and 3(c)) than in ZnO NPs. Mn and Ag might have disturbed the growth process resulting in the formation of uniformly distributed

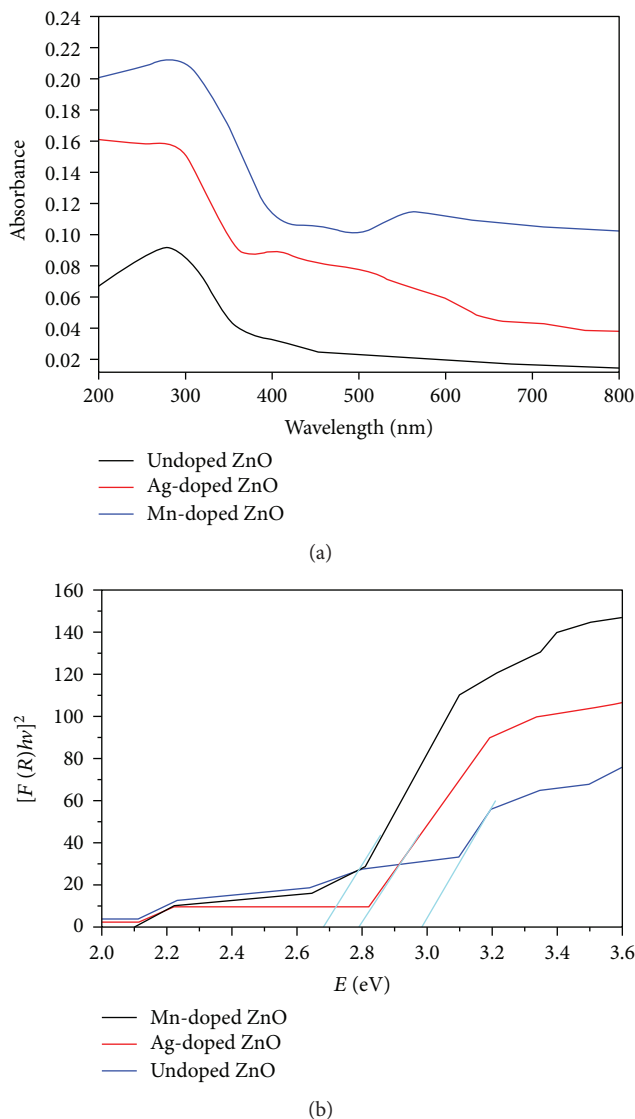


FIGURE 5: (a) UV-visible absorption spectra and (b) Kubelka-Munk function versus energy plots of ZnO, Ag-doped ZnO, and Mn-doped ZnO NPs at 600°C.

nanosized particles, giving a smooth surface morphology as reported in other studies [18].

Figures 4(a)–4(c) shows the EDX spectrum of ZnO, Ag-doped ZnO, and Mn-doped ZnO NPs. EDX analysis confirmed the presence of manganese and silver in ZnO crystal and some chlorine impurities.

3.3. Optical Analysis. Figure 5(a) shows the UV-visible absorption spectra for ZnO, Mn-doped ZnO, and Ag-doped ZnO NPs. The as-synthesized nanoparticles have a strong absorption maximum below 400 nm. The band gap energy of the nanoparticles is measured by the extrapolation of the linear portion of the graph between the modified Kubelka-Munk function $[F(R)/hv]^2$ versus photon energy ($h\nu$) [15] as presented in Figure 5(b). The band gap energy of ZnO (2.98 eV) is decreased for Ag-doped ZnO (2.80 eV)

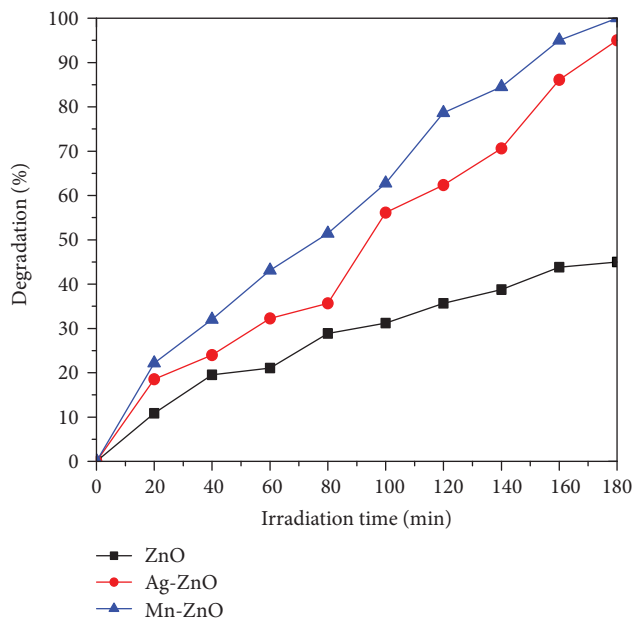


FIGURE 6: Photocatalytic decolorization of MV using ZnO, Ag-doped ZnO, and Mn-doped ZnO NPs under solar light.

and Mn-doped ZnO (2.64 eV). This clearly shows that the improvement of the visible-light absorption is attributed to the presence of metallic Ag and Mn elements that contributes to the narrowing of the band gap of ZnO extending its absorption edge to the visible region to harvesting more photons in the sunlight.

3.4. Photocatalytic Activities of ZnO, Ag-Doped ZnO, and Mn-Doped ZnO NPs. The decolorization percentage of the MV dye (4.5×10^{-4} M) after sunlight irradiation (conducted for 3 hours at a pH of 9.0) of its aqueous solution in the presence of the ZnO, Ag-doped ZnO, and Mn-doped ZnO photocatalysts (1 g/L each) was found to be 45%, 95%, and 100%, respectively (Figure 6). The photocatalytic activity of the ZnO nanoparticles increases by Ag and Mn doping. This might be due to an increase in surface area and oxygen defects [22]. The reaction between conduction band electrons and oxygen in the solution could generate the reactive oxygen species which are responsible for the decolorization [23].

The proposed mechanism of the synergetic effect of Ag-doped ZnO and Mn-doped ZnO NPs on the photocatalytic decolorization of MV has been shown in Figure 7. The valence band electrons in these NPs under sunlight with the photons of energy greater than or equal to ZnO band gap electrons can be excited to the conduction band producing an equal number of holes in the valence band, simultaneously. Because the conduction band energy level of ZnO NPs is higher than that of the intraband state of Ag-doped ZnO and Mn-doped ZnO NPs, electrons can flow from ZnO to Ag^+/Mn^{2+} NPs [24]. So, oxygen vacancy defects and Ag/Mn on the surface of ZnO NPs trap electrons and prevent the recombination of $e-h^+$ pairs [24]. Also, sunlight

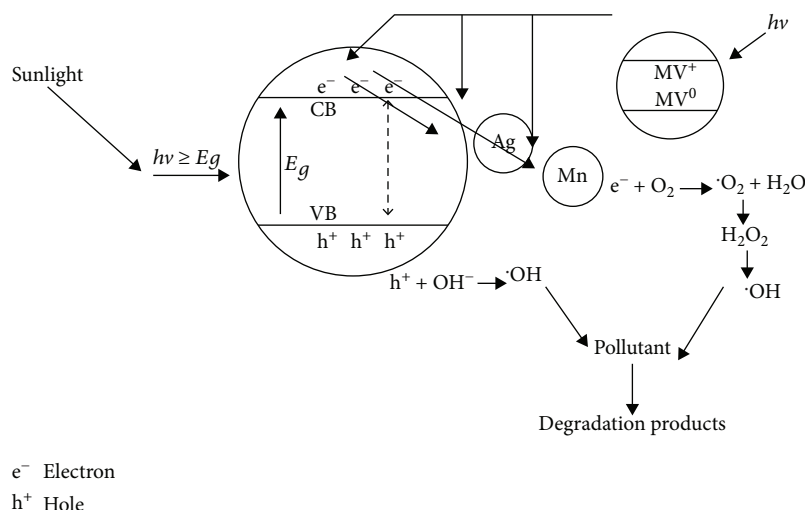


FIGURE 7: Proposed mechanism for Ag-doped ZnO and Mn-doped ZnO NPs on the photocatalytic decolorization of MV under sunlight.

excites the methyl violet dye molecules (MV^0 to MV^+). The MV molecules transfer electrons to the conduction band (CB) of ZnO (MV^+ to CB of ZnO) and the intraband state of Ag/Mn (MV^+ to Ag/Mn). Here, the intraband state of Mn is lower than Ag; this is why Mn-doped ZnO has a higher photocatalytic efficiency than Ag-doped ZnO.

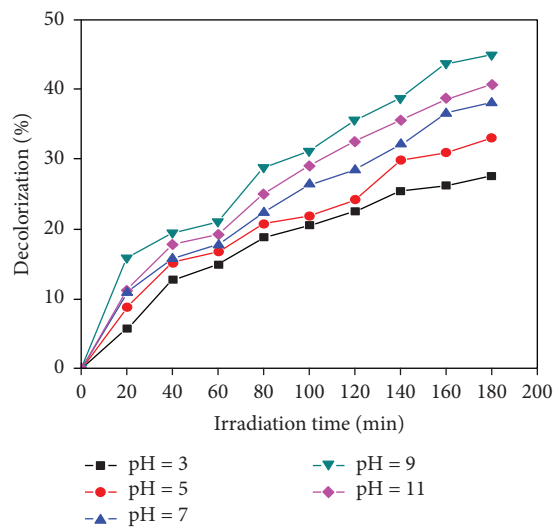
3.5. Influence of Parameters on the Photocatalytic Decolorization of Methyl Violet

3.5.1. Effect of pH. The role of pH value on the percentage of the photocatalytic decolorization was studied in the pH range of 3–11 at a constant dye concentration of 4.5×10^{-4} M and catalyst amount of 1.0 g/L with the irradiation time of 3 h plotted in Figures 8(a)–8(c). The influence of pH value on the photocatalytic process is the result of a surface charge of ZnO, Ag-doped ZnO, and Mn-doped ZnO and related with the cationic MV dye. The low initial reaction rates at the acidic pH values are due to the photodissolution of the photocatalysts [25]. Since MV is a type of cationic compound, the observed increase of the decolorization percentage at low alkali pH (7 to 9) can be attributed to the high hydroxylation of the catalyst surface. The concentrations of hydroxyl ions in the catalyst surface increased, and the photocatalytic decolorization percentage is improved. However, with a further increase of pH to a value of 11, the photocatalytic decolorization percentage of the MV dye becomes lower. Thus, at a high pH range, electrostatic attraction between the catalyst surface and the MV dye cations leads to a strong adsorption of the dye cations on the ZnO, Ag-doped ZnO, and Mn-doped ZnO NPs in good agreement with other studies [26]. At the high alkali level of pH 11, even though the electrostatic attraction is enhanced, the hydroxyl groups diminish simultaneously. The adsorption of H_2O molecules at the surface of the NPs is followed by the dissociation of OH^- groups, leading to coverage with chemically equivalent metal hydroxyl groups (M-OH) which in turn leads to the decline of photocatalytic decolorization [27]. The maximum photocatalytic decolorization percentage exhibited was at pH 9.0 (Figure 8). pH 9 was used for the next experiments

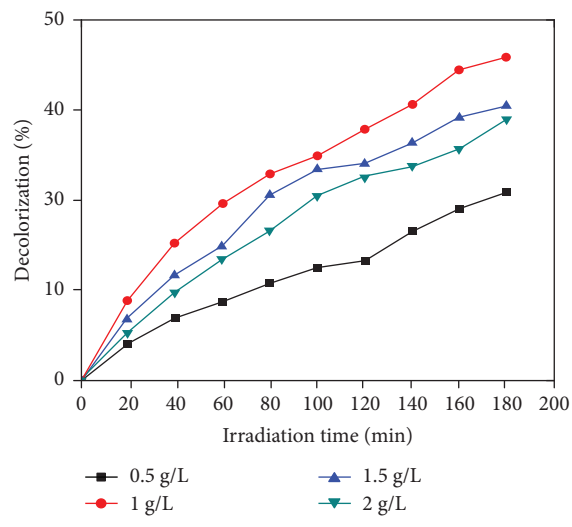
because concentrations of hydroxyl ions in the catalyst surface were increased and decolorization enhanced.

3.5.2. Effect of Catalyst Loading. The photocatalytic decolorization of MV with ZnO, Ag-doped ZnO, and Mn-doped ZnO under sunlight as shown in Figure 9 revealed that, initially, as catalyst loading increased from 0.5 g/L to 1.0 g/L, the photocatalytic decolorization percentage increases. The decolorization percentage exhibited a maximum at 1.0 g/L catalyst dosage because as catalyst loading increases, total active surface area increases; thus, more active sites on the catalyst surface are available and decolorization percentage is increased [28]. Thereafter, as the catalyst loading further increases (from 1 g/L to 2 g/L), the photocatalytic decolorization percentage starts to decrease. This is because of light scattering and screening effects [29]. The tendency of particle-particle interaction increases at a high concentration of catalysts, resulting in a decreasing surface area which is available for sunlight absorption. Finally, the photocatalytic decolorization percentage drops. Even though the number of active sites in solution increases with catalyst loading, a point emerged to be attained where light penetration is compromised due to excessive particle concentration [30]. The tradeoff between these two opposing phenomena results in an optimum catalyst loading for the photocatalytic reaction [31].

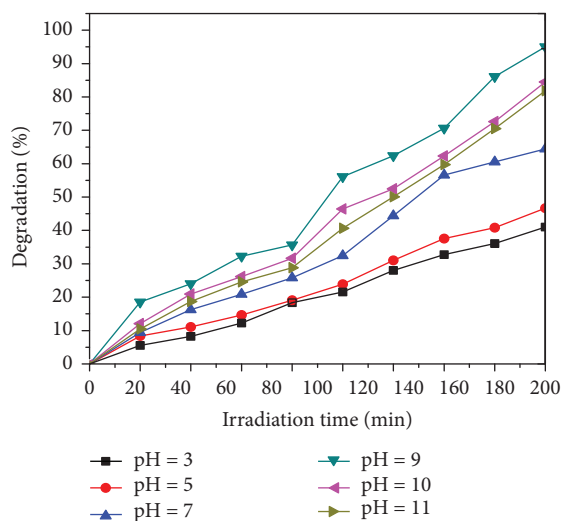
3.5.3. Effect of Dye Concentration. The photocatalytic decolorization of the MV was carried out by varying the initial dye concentrations from 4×10^{-4} M to 6×10^{-4} M in order to evaluate the proper amount of initial dye concentration. The results (Figures 10(a)–10(c)) revealed that the initial dye concentration influences the decolorization efficiency rigorously. Initially, as the concentration of the dye increased from 4×10^{-4} M to 4.5×10^{-4} M, the percentage of photocatalytic decolorization by the NPs also increased. However as the initial dye concentration exceeds 4.5×10^{-4} M, the decolorization percentage of the dye decreased sharply. This is due to the fact that a higher initial dye concentration prevents the solar radiation from reaching the catalyst surface (due to the



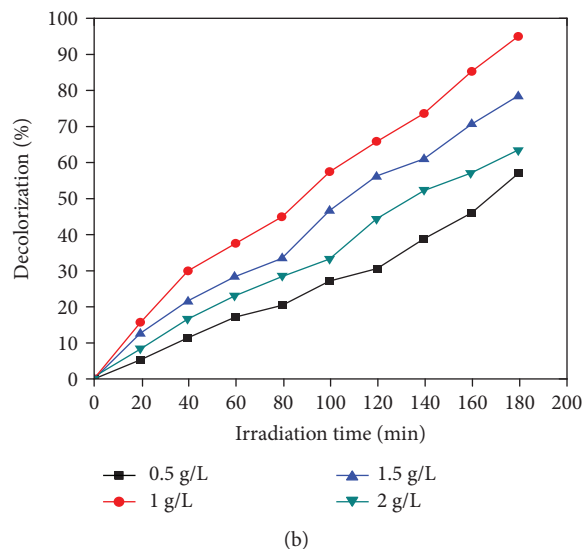
(a)



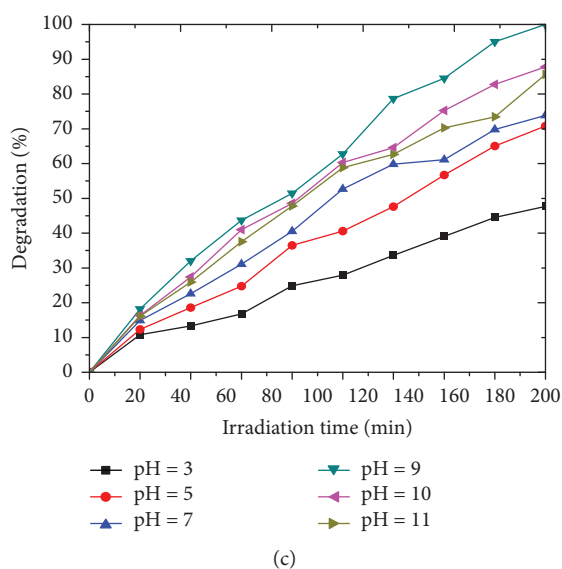
(a)



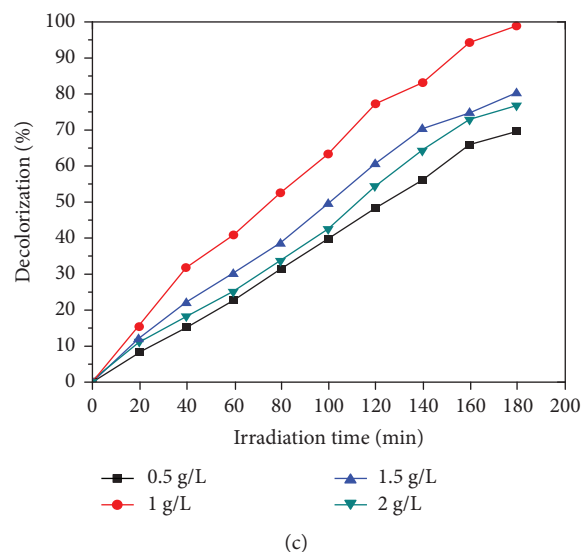
(b)



(b)



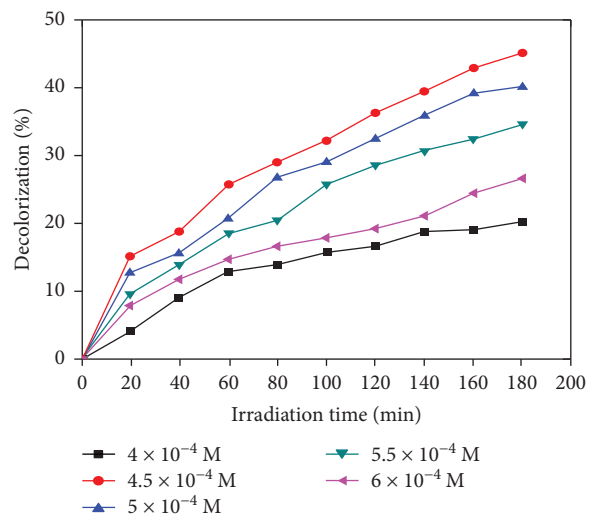
(c)



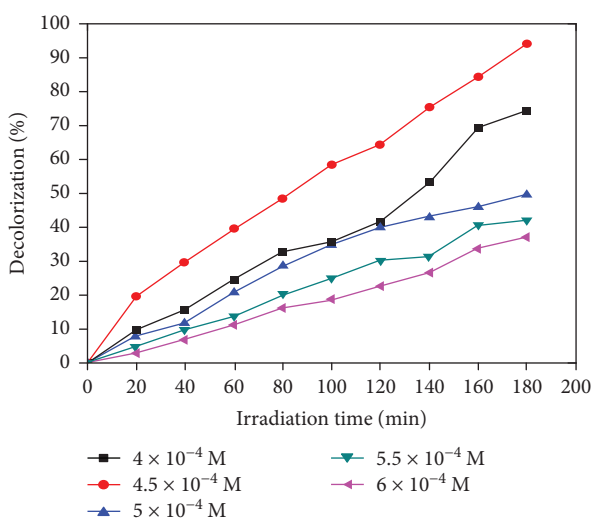
(c)

FIGURE 8: Effect of pH on decolorization of MV with (a) ZnO, (b) Ag-doped ZnO, and (c) Mn-doped ZnO NPs under sunlight.

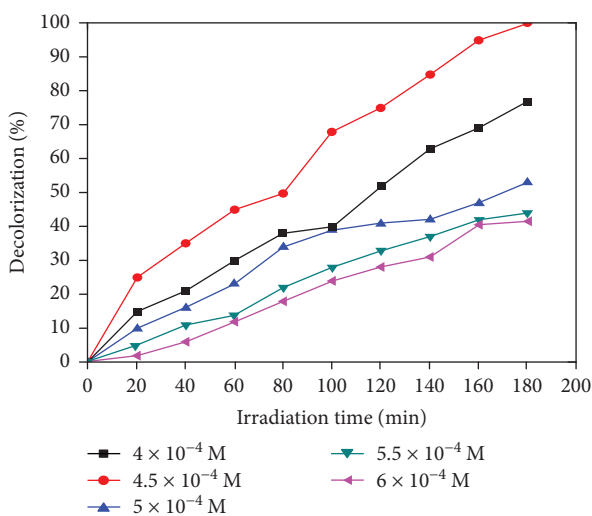
FIGURE 9: Effect of catalyst loading on the decolorization of MV with (a) ZnO, (b) Ag-doped ZnO, and (c) Mn-doped ZnO NPs under sunlight.



(a)



(b)



(c)

FIGURE 10: Effect of initial dye concentration on the photocatalytic decolorization of MV under solar light using (a) ZnO, (b) Ag-doped ZnO, and Mn-doped ZnO NPs.

increased path length) and thereby fewer photons reached the catalyst surface. This in turn reduces the production of hydroxyl radicals on the catalyst surface which again implies a reduced attack on the MV dye leading to lower decolorization efficiency [32].

4. Conclusion

In this study, ZnO NPs were synthesized using the precipitation method, and Ag-doped ZnO and Mn-doped ZnO NPs were synthesized using the coprecipitation method. XRD analysis showed that doping of Ag and Mn does not affect the crystal structure of ZnO. UV-vis spectroscopy study reveals that the incorporation of Ag and Mn does not increase the band gap of ZnO but rather decreases it. The EDX spectrum confirmed the presence of manganese and silver in ZnO crystal. Photocatalytic activities of Ag-doped ZnO and Mn-doped ZnO have a higher photocatalytic decolorization efficiency than ZnO. Doped ZnO NPs are promising photocatalysts for water and environmental detoxification.

Data Availability

The XRD, SEM/EDX, Uv-vis, and photocatalytic degradation data used to support the findings of this study are available from the corresponding author upon request.

Conflicts of Interest

The authors declare that they have no conflicts of interest.

Acknowledgments

The authors are especially grateful for the support from the NORAD project (CRPO/CNCS/MU-HU-NMBU/MSc/002/09) and grants from the Mekelle University.

References

- [1] Y. Hu and H. Cheng, "Application of stochastic models in identification and apportionment of heavy metal pollution sources in the surface soils of a large-scale region," *Environmental Science & Technology*, vol. 47, no. 8, pp. 3752–3760, 2013.
- [2] R. W. Sabnis, Ed., *Handbook of Biological Dyes and Stains: Synthesis and Industrial Applications*, John Wiley & Sons, Hoboken, NJ, USA, 2010.
- [3] B. S. Padhi, "Pollution due to synthetic dyes toxicity & carcinogenicity studies and remediation," *International Journal of Environmental Sciences*, vol. 3, no. 3, p. 940, 2012.
- [4] E. Forgacs, T. Cserhati, and G. Oros, "Removal of synthetic dyes from wastewaters: a review," *Environment International*, vol. 30, no. 7, pp. 953–971, 2004.
- [5] Q. Wan, T. H. Wang, and J. C. Zhao, "Enhanced photocatalytic activity of ZnO nanotetrapods," *Applied Physics Letters*, vol. 87, no. 8, article 083105, 2005.
- [6] S. Bhattacharya, I. Saha, A. Mukhopadhyay, D. Chattopadhyay, U. C. Ghosh, and D. Chatterjee, "The role of nanotechnology in water treatment and purification: potential applications and implications," *International Journal of Chemical Science and Technology*, vol. 3, no. 3, pp. 59–64, 2013.

- [7] R. Wang, J. H. Xin, Y. Yang, H. Liu, L. Xu, and J. Hu, "The characteristics and photocatalytic activities of silver-doped ZnO nanocrystallites," *Applied Surface Science*, vol. 227, no. 1–4, pp. 312–317, 2004.
- [8] C. Xu, L. Cao, G. Su et al., "Preparation of ZnO/Cu₂O compound photocatalyst and application in treating organic dyes," *Journal of Hazardous Materials*, vol. 176, no. 1–3, pp. 807–813, 2010.
- [9] M. M. Rashad, A. A. Ismail, I. Osama, I. A. Ibrahim, and A. H. T. Kandil, "Photocatalytic decomposition of dyes using ZnO doped SnO₂ nanoparticles prepared by solvothermal method," *Arabian Journal of Chemistry*, vol. 7, no. 1, pp. 71–77, 2014.
- [10] N. Elamin and A. Elsanousi, "Synthesis of ZnO nanostructures and their photocatalytic activity," *Journal of Applied and Industrial Sciences*, vol. 1, no. 1, pp. 32–35, 2013.
- [11] R. Ullah and J. Dutta, "Photocatalytic degradation of organic dyes with manganese-doped ZnO nanoparticles," *Journal of Hazardous Materials*, vol. 156, no. 1–3, pp. 194–200, 2008.
- [12] M. Joshi, R. Bansal, and R. Purwar, *Color Removal from Textile Effluents*, 2004.
- [13] D. Jung, "Syntheses and characterizations of transition metal-doped ZnO," *Solid State Sciences*, vol. 12, no. 4, pp. 466–470, 2010.
- [14] C. Karunakaran, V. Rajeswari, and P. Gomathisankar, "Enhanced photocatalytic and antibacterial activities of sol-gel synthesized ZnO and Ag-ZnO," *Materials Science in Semiconductor Processing*, vol. 14, no. 2, pp. 133–138, 2011.
- [15] S. Cimitan, S. Albonetti, L. Forni, F. Peri, and D. Lazzari, "Solvothermal synthesis and properties control of doped ZnO nanoparticles," *Journal of Colloid and Interface Science*, vol. 329, no. 1, pp. 73–80, 2009.
- [16] S. Yang, Y. Xu, Y. Huang et al., "Photocatalytic degradation of methyl violet with TiSiW₁₂O₄₀/TiO₂," *International Journal of Photoenergy*, vol. 2013, Article ID 191340, 5 pages, 2013.
- [17] Y. Jiang, Y. Sun, H. Liu, F. Zhu, and H. Yin, "Solar photocatalytic decolorization of C.I. Basic Blue 41 in an aqueous suspension of TiO₂-ZnO," *Dyes and Pigments*, vol. 78, no. 1, pp. 77–83, 2008.
- [18] R. Chauhan, A. Kumar, and R. P. Chaudhary, "Photocatalytic studies of silver doped ZnO nanoparticles synthesized by chemical precipitation method," *Journal of Sol-Gel Science and Technology*, vol. 63, no. 3, pp. 546–553, 2012.
- [19] K. Rekha, M. Nirmala, M. G. Nair, and A. Anukaliani, "Structural, optical, photocatalytic and antibacterial activity of zinc oxide and manganese doped zinc oxide nanoparticles," *Physica B: Condensed Matter*, vol. 405, no. 15, pp. 3180–3185, 2010.
- [20] K. Dhanshree and T. Elangovan, "Synthesis and characterization of ZnO and Mn-doped ZnO nanoparticles," *International Journal of Science and Research*, vol. 4, no. 11, pp. 1816–1820, 2015.
- [21] X. Zhou, S. Ge, D. Yao, Zuo, and Y. Xiao, "Preparation, magnetic and optical properties of ZnO and ZnO: Co rods prepared by wet chemical method," *Journal of Alloys and Compounds*, vol. 463, no. 1–2, pp. L9–L11, 2008.
- [22] S. M. Hosseini, I. A. Sarsari, P. Kameli, and H. Salamati, "Effect of Ag doping on structural, optical, and photocatalytic properties of ZnO nanoparticles," *Journal of Alloys and Compounds*, vol. 640, pp. 408–415, 2015.
- [23] P. Amornpitoksuk, S. Suwanboon, S. Sangkanu, A. Sukhoom, N. Muensit, and J. Baltrusaitis, "Synthesis, characterization, photocatalytic and antibacterial activities of Ag-doped ZnO powders modified with a diblock copolymer," *Powder Technology*, vol. 219, pp. 158–164, 2012.
- [24] T. Chen, Y. Zheng, J. Lin, and G. Chen, "Study on the photocatalytic degradation of methyl orange in water using Ag/ZnO as catalyst by liquid chromatography electrospray ionization ion-trap mass spectrometry," *Journal of the American Society for Mass Spectrometry*, vol. 19, no. 7, pp. 997–1003, 2008.
- [25] K. Vignesh, A. Suganthi, M. Rajarajan, and S. A. Sara, "Photocatalytic activity of AgI sensitized ZnO nanoparticles under visible light irradiation," *Powder Technology*, vol. 224, pp. 331–337, 2012.
- [26] J. Z. Kong, A. D. Li, X. Y. Li et al., "Photo-degradation of methylene blue using Ta-doped ZnO nanoparticle," *Journal of Solid State Chemistry*, vol. 183, no. 6, pp. 1359–1364, 2010.
- [27] M. M. Uddin, M. A. Hasnat, A. J. F. Samed, and R. K. Majumdar, "Influence of TiO₂ and ZnO photocatalysts on adsorption and degradation behaviour of erythrosine," *Dyes and Pigments*, vol. 75, no. 1, pp. 207–212, 2007.
- [28] M. S. T. Gonçalves, A. M. F. Oliveira-Campos, E. M. M. S. Pinto, P. M. S. Plasência, and M. J. R. P. Queiroz, "Photochemical treatment of solutions of azo dyes containing TiO₂," *Chemosphere*, vol. 39, no. 5, pp. 781–786, 1999.
- [29] N. Daneshvar, D. Salari, and A. R. Khataee, "Photocatalytic degradation of azo dye acid red 14 in water on ZnO as an alternative catalyst to TiO₂," *Journal of Photochemistry and Photobiology A: Chemistry*, vol. 162, no. 2–3, pp. 317–322, 2004.
- [30] N. Vela, G. Pérez-Lucas, J. Fenoll, and S. Navarro, "Recent overview on the abatement of pesticide residues in water by photocatalytic treatment using TiO₂," in *Application of Titanium Dioxide*, InTech, 2017.
- [31] A. Akyol, H. C. Yatmaz, and M. Bayramoglu, "Photocatalytic decolorization of Remazol Red RR in aqueous ZnO suspensions," *Applied Catalysis B: Environmental*, vol. 54, no. 1, pp. 19–24, 2004.
- [32] G. Thennarasu and A. Sivasamy, "Enhanced visible photocatalytic activity of cotton ball like nano structured Cu doped ZnO for the degradation of organic pollutant," *Ecotoxicology and Environmental Safety*, vol. 134, Part 2, pp. 412–420, 2016.

Research Article

Fabrication of Bifunctional TiO₂/POM Microspheres Using a Layer-by-Layer Method and Photocatalytic Activity for Methyl Orange Degradation

Ping Niu ¹, Dunqing Wang,¹ Aili Wang,¹ Yuhua Liang,² and Xinfang Wang¹

¹College of Chemistry and Chemical Engineering, Dezhou University, Dezhou 253023, China

²Department of Dermatology, Dezhou People's Hospital of Shandong Province, Dezhou 253023, China

Correspondence should be addressed to Ping Niu; np68@sina.com

Received 7 February 2018; Revised 7 May 2018; Accepted 22 May 2018; Published 7 June 2018

Academic Editor: Giuliana Magnacca

Copyright © 2018 Ping Niu et al. This is an open access article distributed under the Creative Commons Attribution License, which permits unrestricted use, distribution, and reproduction in any medium, provided the original work is properly cited.

Bifunctional films of Keggin-type polyoxometalates H₃PW₁₂O₄₀ (PW₁₂), H₄SiW₁₂O₄₀ (SiW₁₂), H₃PMo₁₂O₄₀ (PMo₁₂), and TiO₂ were successfully built on Fe₃O₄@SiO₂ microspheres using a layer-by-layer method. The characterization by field emission scan electronic microscopy (FESEM) and energy dispersive X-ray spectroscopy (EDX) shows that TiO₂ nanoparticles and polyoxometalate (POM) anions are successfully assembled. The photodegradation of methyl orange (MO) was used to test the photocatalytic efficiency of magnetic catalysts under UV irradiation. For MO decomposition, multilayer films that combine PW₁₂ and SiW₁₂ with TiO₂ show high efficiency, which can be attributed to the synergistic effect between POMs and TiO₂. The degradation of the model contaminant was also systematically checked under different conditions such as bilayer number deposited on magnetic microspheres, catalyst concentration, inorganic oxidants, and salts. The oxidation process of MO follows an apparent first-order reaction. Furthermore, the composite catalysts deposited on Fe₃O₄@SiO₂ magnetic microspheres can be conveniently, quickly, and efficiently separated by an external magnet from a solution.

1. Introduction

The production and use of synthetic dyes contribute to a massive pollution problem as a result of their high toxicity, slow biodegradation, and potential carcinogenicity [1]. To solve environmental problems caused by dye pollutants, various advanced methods have been adopted. Among these methods, photocatalytic oxidization technology has attracted growing interest on account of its energy saving, highly efficient, nonselective, and environmentally friendly characteristics. Its origin can date back to the 70s of the previous century in the field of wastewater treatment [2]. During the past decades, the nanostructured TiO₂ photocatalyst aroused much interest [3]. However, the fast recombination of photogenerated electrons and holes results in a decrease of photocatalytic efficiency and restricts the practical application of TiO₂.

In contrast to TiO₂, polyoxometalates (POMs) are often used as homogeneous photocatalysts in recent years [4, 5].

POMs are easily soluble in water and difficult to recycle from the reaction system for reuse. In order to overcome these shortcomings, heterogeneous catalysts containing POMs have been prepared by immobilizing POMs on solid supports such as functional microspheres [6–8], indium-tin oxide (ITO) [9], glassy carbon electrode [9, 10], and quartz slides [9, 11].

In recent years, significant attention was focused on the functional thin films containing POMs prepared by a layer-by-layer (LbL) self-assembly method. These films have potential applications in the fields of photoelectrochemistry [12, 13], photocatalysis [7, 14–16], electrocatalysis [17, 18], photochromism [18], sensors [9, 19], and electrochromism [18, 20]. Compared with films assembled by single building blocks, composite films are employed for high performance. Sun et al. [12] reported that the incorporation of CdS nanoparticles into Dawson-type polyoxometalate (P₂W₁₈) films improved remarkably the photocurrent response and power conversion efficiency. Novais et al. [17] found that

the $\{MG/Co(PW_9)_2\}_n$ multilayer films exhibited excellent electrocatalytic performance for nitrite and iodate reduction with very low detection limits. $(PW_{12}-TH)_n$ multilayer films deposited on the magnetic substrate of $Fe_3O_4@SiO_2$ microspheres showed a better ability in terms of photocatalytic activity, stability, and reusability than quartz slides [7]. In particular, films can be efficiently separated by a magnet. The Bi_2O_3 nanoparticles assembled into $[SiW_9V_3O_{40}]^{7-}$ endowed the films with specific properties. This film has a tendency toward electrocatalytic L-cysteine and nitrite as well as enhanced electrochromic and photochromic properties [18]. Moreover, the multifunctional films $(PV_6Mo_6/MV)_n$ ($PV_6Mo_6 = (NH_4)_5H_4PV_6Mo_6O_{40} \cdot 6H_2O$, $MV =$ methyl violet) exhibited electrochemical activity for the reduction of NO_2^- , BrO_3^- , and ClO_3^- and remarkable antibacterial properties toward *Escherichia coli* [21]. However, less attention was paid to the photocatalytic performance of $(TiO_2/POM)_n$ composite films coated on $Fe_3O_4@SiO_2$ magnetic microspheres.

In this work, $(TiO_2/POM)_n$ composite films with magnetic and photocatalytic performance were deposited on $Fe_3O_4@SiO_2$ core-shell microspheres by the LbL method. MO was used as the model pollutant to investigate the photocatalytic properties of bifunctional films. The influence of bilayer number deposited on magnetic microspheres, catalyst concentration, inorganic oxidants, and salts on the degradation of the methyl orange solution was studied in detail.

2. Experiments

2.1. Materials. The Fe_3O_4 magnetic microspheres were synthesized following the procedure reported by Sun et al. [22]. Silica-coated magnetic microspheres were prepared through the sol-gel method [7]. Titanium dioxide (TiO_2) colloids were prepared according to literature [23]. $H_3PW_{12}O_{40} \cdot xH_2O$ (PW_{12}), $H_4SiW_{12}O_{40} \cdot xH_2O$ (SiW_{12}), and $H_3PMo_{12}O_{40} \cdot xH_2O$ (PMo_{12}) were obtained from Sinopharm Chemical Reagent Co. Ltd, China. Methyl orange was purchased from Jining Chemical Engineering Research Institute. Commercial polyelectrolytes, poly(sodium 4-styrenesulfonate) (PSS, Mw ~ 70,000) and poly(allylamine hydrochloride) (PAH, Mw ~ 70,000) were obtained from Sigma-Aldrich Inc., USA. Perchloric acid was purchased from Shanghai Jinlu Chemical Co. Ltd, China. Sodium chloride and sodium sulfate were provided by Tianjin Kemiou Chemical Reagent Co. Ltd. Potassium chlorate, potassium bromate, and potassium iodate were obtained from Tianjin Kemiou Chemical Reagent Co. Ltd. Magnesium chloride, aluminium chloride, and sodium hydrogen phosphate were supplied by Aladdin Chemistry Co. Ltd. All reagents were used as received.

2.2. Buildup of $(TiO_2/POM)_n$ Composite Films on Magnetic Microspheres. In order to prepare $(TiO_2/POM)_n$ composite films, 0.2 g $Fe_3O_4@SiO_2$ core-shell microspheres were first immersed in a poly(allylamine hydrochloride) (PAH) and poly(sodium 4-styrenesulfonate) (PSS) aqueous solution for 15 min to gain a surface with uniform charge. Then, the powders were magnetically separated and washed three times with pH 2.0 $HClO_4$ aqueous solution. The concentration of PAH and PSS aqueous solution was fixed as 2.0 g/L

containing 0.5 mol/L NaCl. The photocatalytic $(TiO_2/POM)_n$ ($POMs = PW_{12}$, SiW_{12} , and PMo_{12} ; n is the number of TiO_2 - PW_{12} bilayers) films on magnetic microspheres were formed by alternative immersion in positively charged TiO_2 (10 g/L, pH ~ 2.0) and negatively charged POM solution (3 mmol/L). The assembly time was limited to 15 min to ensure the saturation adsorption of each component. Rinsing by $HClO_4$ aqueous solution with a pH of 2.0 for three times was conducted after each deposition cycle. The $Fe_3O_4@SiO_2$ microspheres coated with the desired deposition number of TiO_2 and POMs were finally obtained. Then, the obtained catalysts were dried overnight at 60 °C before further use. For comparison, $(PSS/TiO_2)_{10}$ and $(PAH/PW_{12})_{10}$ composite films on $Fe_3O_4@SiO_2$ magnetic microspheres were deposited in a similar way.

2.3. Characterization of Magnetic Microspheres. The morphology of magnetic microspheres was monitored using a field emission scanning electron microscope (FESEM, model: JSM-6700F, JEOL, Japan) with an accelerating voltage of 10 kV. The Fourier-transform infrared spectra of the products were recorded on a TR200 spectrometer (Thermo Electron Corporation). The chemical element of magnetic microspheres was detected by energy dispersive X-ray spectroscopy (EDX, model: Oxford X-Max 51-XMX1004, Oxford Instruments Co. Ltd., England). The magnetic property was measured on a MPMS (SQUID)-XL (Quantum Design) vibrating sample magnetometer at 300 K.

2.4. Evaluation of Photocatalytic Activity. The XPA-system photochemical reactor purchased from Xujiang Electromechanical Plant was used to conduct photocatalytic experiments. The photoreactor was equipped with a 300 W medium-pressure mercury lamp with a main emission wavelength of 365 nm. The lamp was horizontally arranged and surrounded by a quartz jacket in which cooling water was circulated to avoid overheating. There was a 20 cm distance between the light source and dye solution. A given amount of catalysts and 50 mL of methyl orange solution were placed in a 100 mL glass beaker thermostated using a water jacket. The temperature of the dye solution was controlled at $28 \pm 1^\circ C$ by adjusting the flow of cooling water. The reaction was performed at MO initial concentrations of 10 mg/L with the pH value of the solution at about 2.0 adjusted by $HClO_4$. In the experiments, the catalyst concentration was fixed at 2 g/L except for a few runs to evaluate the effects of the catalyst concentration and inorganic oxidants. In order to establish the adsorption-desorption equilibrium between the MO molecule and the catalysts' surface, the suspension was ultrasonically dispersed for 30 min in the dark. The photocatalytic decontamination of MO started after the mercury lamp became stable. At given intervals, a certain amount of the reaction solution was taken out and separated. The residual dyes were analyzed by a Shimadzu UV-2450 UV-vis spectrophotometer. The removal rate can be estimated by the following formula:

$$\text{Removal rate (\%)} = \frac{A_0 - A}{A_0} \times 100, \quad (1)$$

where A_0 is the original absorbance of the MO solution at the maximum absorption wavelength ($\lambda_{\max} = 507 \text{ nm}$), and A is the residual absorbance of MO after UV-light irradiation.

3. Results and Discussion

3.1. Characterization of Magnetic Microspheres. The surface morphology of magnetic microspheres was examined by FESEM. It is clearly visible from Figure 1 that the Fe_3O_4 microspheres modified by the hydrolyzation of tetraethyl orthosilicate exhibit a typical spherical form, and the average particle sizes are determined to be 150–200 nm. The shape of the magnetic microspheres has no prominent change when TiO_2 colloidal nanoparticles and PW_{12} nanoclusters assembled alternately on the outer surface of $\text{Fe}_3\text{O}_4@ \text{SiO}_2$ microspheres. It also shows that magnetic microspheres are aggregated to a certain extent because of the magnetic dipolar interaction among the particles. Moreover, the composition of magnetic photocatalysts was also confirmed by EDX spectroscopy (Figure 1(c)). EDX analysis reveals the presence of Ti, O, W, P, and Fe on the surfaces of $\text{Fe}_3\text{O}_4@ \text{SiO}_2$ magnetic microspheres. This proves the successful assembly of TiO_2 nanoparticles and polyoxometalate (POM) anions on the surface of $\text{Fe}_3\text{O}_4@ \text{SiO}_2$ microspheres. Meanwhile, a dramatic Pt peak can be seen. Pt comes from the plated platinum used to increase the conductivity of sample.

The assembly process of magnetic microspheres was monitored by FT-IR spectra. The results are shown in Figure 2. The band that appeared at 584 cm^{-1} is assigned to the vibration of the Fe-O bond for Fe_3O_4 particles. After coating a SiO_2 shell by the sol-gel method, three obvious bands at 1100 cm^{-1} , 798 cm^{-1} , and 469 cm^{-1} are assigned to the symmetric and antisymmetric stretching vibration of the Si-O bond. After an alternative deposition of TiO_2 and PW_{12} multilayer films through the LbL method, the intensity of the Fe-O and Si-O bands decreases. This phenomenon is ascribed to the effective screening of TiO_2 and PW_{12} multilayer films on Fe-O and Si-O bands. Meanwhile, the new bands at 960 cm^{-1} , 895 cm^{-1} , and 804 cm^{-1} appear, which associate with typical Keggin skeletal vibration bands for PW_{12} . This is consistent with the previous report [14]. However, the stretching vibration of the P-O bond at 1080 cm^{-1} is covered by a strong peak of the Si-O bond. The FT-IR spectrum of $\text{Fe}_3\text{O}_4@ \text{SiO}_2@ (\text{TiO}_2/\text{PW}_{12})_{10}$ microspheres indicates that the Keggin structure of PW_{12} still remains intact.

Figure 3(a) shows the magnetization of Fe_3O_4 , $\text{Fe}_3\text{O}_4@ \text{SiO}_2$, and $\text{Fe}_3\text{O}_4@ \text{SiO}_2@ (\text{TiO}_2/\text{PW}_{12})_{10}$ microspheres as a function of an applied magnetic field, which was measured by a vibrating sample magnetometer at 300 K. The samples all exhibit a superparamagnetic characteristic. The magnetizations of samples increase with the increase of the applied magnetic field and nearly reach saturation with saturation magnetization (Ms) values of 48.5, 15.8, and 6.0 emu/g, respectively. Compared to $\text{Fe}_3\text{O}_4@ \text{SiO}_2$ microspheres, the Ms values of composite photocatalysts slightly decrease. This is ascribed to the deposition of $(\text{TiO}_2/\text{PW}_{12})_{10}$ on core-shell $\text{Fe}_3\text{O}_4@ \text{SiO}_2$. Figure 3(b) illustrates the magnetic separation of $\text{Fe}_3\text{O}_4@ \text{SiO}_2@ (\text{TiO}_2/\text{PW}_{12})_{10}$ microspheres from the aqueous suspension. The photocatalysts possess a strong

magnetic response under an external magnetic field due to the existence of an Fe_3O_4 core. They can be easily removed from the MO solution after photodegradation by an external magnet. Then, a nearly colorless solution is obtained (see Figure 3(b)). The strong magnetic response of photocatalysts ensures their convenient, fast, and efficient separation from the reaction media for reuse.

3.2. Photocatalytic Activity of Magnetic Microspheres. In the photocatalytic procedure, methyl orange (MO) was used as the model organic molecule to evaluate the photocatalytic activity of composite films assembled on $\text{Fe}_3\text{O}_4@ \text{SiO}_2$ magnetic microspheres. The photocatalytic activity of samples toward azo dye MO is shown in Figure 4. In the dark, the degradation of MO is hardly observed even though magnetic films are presented. Only 13.30% of MO can be degraded by direct photolysis after UV-light irradiation for 100 min. After being exposed at the same time, the removal rates of MO in the presence of $(\text{TiO}_2/\text{PW}_{12})_{10}$, $(\text{TiO}_2/\text{PSS})_{10}$, and $(\text{PAH}/\text{PW}_{12})_{10}$ composite films deposited on $\text{Fe}_3\text{O}_4@ \text{SiO}_2$ microspheres are 83.91%, 28.66%, and 16.44%, respectively. The fast disappearance of MO in the presence of the $\text{Fe}_3\text{O}_4@ \text{SiO}_2@ (\text{TiO}_2/\text{PW}_{12})_{10}$ photocatalyst owes to the synergistic effect of TiO_2 and PW_{12} . Since photogenerated electrons can be transferred from the TiO_2 conduction band to the empty orbit of tungstophosphate acid, quantum efficiency can be improved. Accordingly, reactive oxygen species (ROs) are easy to generate through the reaction of electrons and holes with hydroxyl ion, adsorbed water, and oxygen. These ROs and active holes are without selectivity and can completely oxidize a MO molecule to CO_2 , H_2O , and inorganic salts. However, without the synergistic effect, the fast recombination of photoinduced holes and electrons cannot be avoided in pure TiO_2 or PW_{12} films, which leads to the decrease in photocatalytic efficiency.

Moreover, the photocatalytic efficiency of $\text{Fe}_3\text{O}_4@ \text{SiO}_2@ (\text{TiO}_2/\text{SiW}_{12})_{10}$ and $\text{Fe}_3\text{O}_4@ \text{SiO}_2@ (\text{TiO}_2/\text{PMo}_{12})_{10}$ magnetic films was also examined for comparison with $\text{Fe}_3\text{O}_4@ \text{SiO}_2@ (\text{TiO}_2/\text{PW}_{12})_{10}$. Under the same experimental conditions, the photodegradation of MO by the abovementioned films reaches 62.07% and 13.55%, respectively. These results shown in Figure 5 indicate that $(\text{TiO}_2/\text{PW}_{12})_{10}$ and $(\text{TiO}_2/\text{SiW}_{12})_{10}$ composite films deposited on $\text{Fe}_3\text{O}_4@ \text{SiO}_2$ can lead to effective degradation of MO. In particular, a higher efficiency can be obtained from $(\text{TiO}_2/\text{PW}_{12})_{10}$ films. However, the photocatalytic activity of $\text{Fe}_3\text{O}_4@ \text{SiO}_2@ (\text{TiO}_2/\text{PMo}_{12})_{10}$ magnetic microspheres is very low. This is because the reoxidization of reduced PMo_{12} is very difficult.

The effect of $(\text{TiO}_2/\text{PW}_{12})$ bilayer number coated on magnetic microspheres on MO decoloration was also investigated. As shown in Figure 6, the removal rate is increased significantly by increasing the $(\text{TiO}_2/\text{PW}_{12})_n$ bilayer number. After UV-light irradiation for 100 min, the degradation efficiency of MO with 2, 4, 6, 8, and 10 bilayers is 30.46%, 41.14%, 69.75%, 78.79%, and 83.91%, respectively. The highest degradation rate is obtained when the bilayer number of $(\text{TiO}_2/\text{PW}_{12})_n$ grows to 10. This study reveals that the photocatalytic activity strongly depends on the bilayer number of $(\text{TiO}_2/\text{PW}_{12})_n$ films. The increase of photocatalytic efficiency

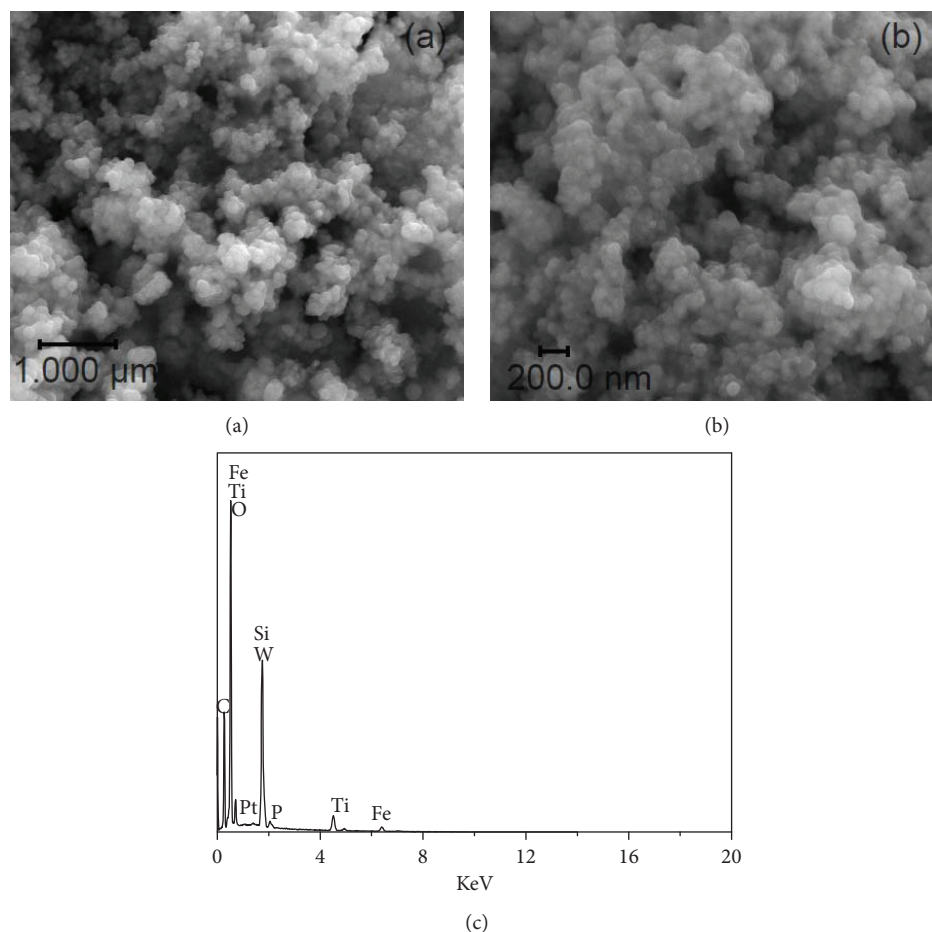


FIGURE 1: FESEM image of (a) $\text{Fe}_3\text{O}_4@SiO_2$ core-shell microspheres and (b) $\text{Fe}_3\text{O}_4@SiO_2@(TiO_2/PW_{12})_{10}$ microspheres. (c) EDX spectrum of $\text{Fe}_3\text{O}_4@SiO_2$ microspheres coated with a $(TiO_2/PW_{12})_{10}$ film.

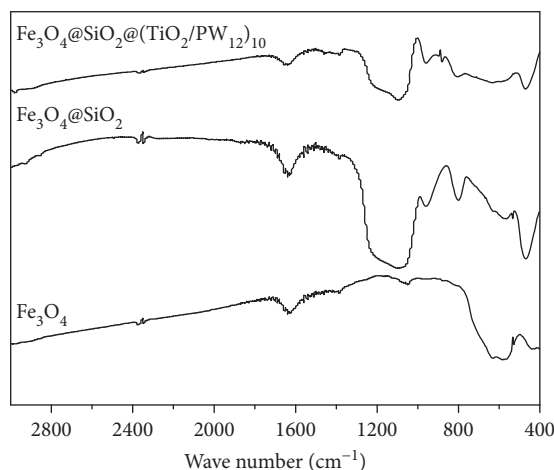


FIGURE 2: FT-IR spectra of Fe_3O_4 particles, $\text{Fe}_3\text{O}_4@SiO_2$ microspheres, and $\text{Fe}_3\text{O}_4@SiO_2@(TiO_2/PW_{12})_{10}$ microspheres.

is attributed to more TiO_2 and PW_{12} nanoparticles effectively deposited on $\text{Fe}_3\text{O}_4@SiO_2$ core-shell microspheres. It should be noted that $\text{Fe}_3\text{O}_4@SiO_2$ microspheres have no photocatalytic activity. Thus, the reason why $(TiO_2/PW_{12})_{10}$ magnetic microspheres have a higher photocatalytic efficiency is that

the contents of TiO_2 and PW_{12} in $(TiO_2/PW_{12})_{10}$ are higher than in other catalysts.

Figure 7 compares the photodegradation of MO under various concentrations of $\text{Fe}_3\text{O}_4@SiO_2$ microspheres coated with $(TiO_2/PW_{12})_{10}$ films. The catalyst concentration was selected as 0.2, 0.4, 0.8, 1.4, and 2.0 g/L. It is observed that the degradation rate increases gradually with the growth of the catalyst concentration. In the presence of $(TiO_2/PW_{12})_{10}$ magnetic microspheres, the degradation efficiency of MO with 0.2 g/L of the catalyst is 69.37% after UV-light irradiation for 100 min. When the concentration of the catalyst is 2.0 g/L, $(TiO_2/PW_{12})_{10}$ magnetic microspheres exhibit the excellent degradation capability for MO and around 83.91% of MO molecules are removed. The inset shows the plot of the rate constant (k) versus a sample concentration. It is indicated that the photocatalytic efficiency increased with the catalyst concentration and the optimal concentration was 2.0 g/L. The enhancement of photocatalytic efficiency is mainly relevant to the increase of catalyst concentration, which generates massive active sites. Thus, high efficiency can be obtained when more catalysts are added.

The photocatalytic efficiency of MO by $(TiO_2/PW_{12})_{10}$ films coated on $\text{Fe}_3\text{O}_4@SiO_2$ microspheres was enhanced when halate was introduced. The comparative results with

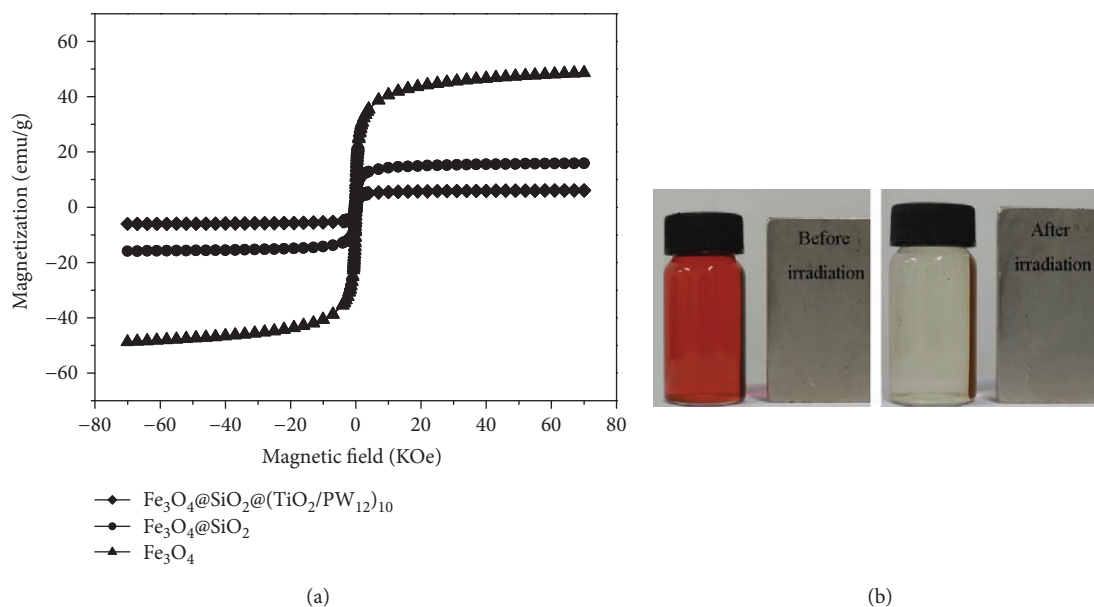


FIGURE 3: (a) The magnetic hysteresis loops of different samples. (b) Photograph of photocatalysts collected by an external magnet.

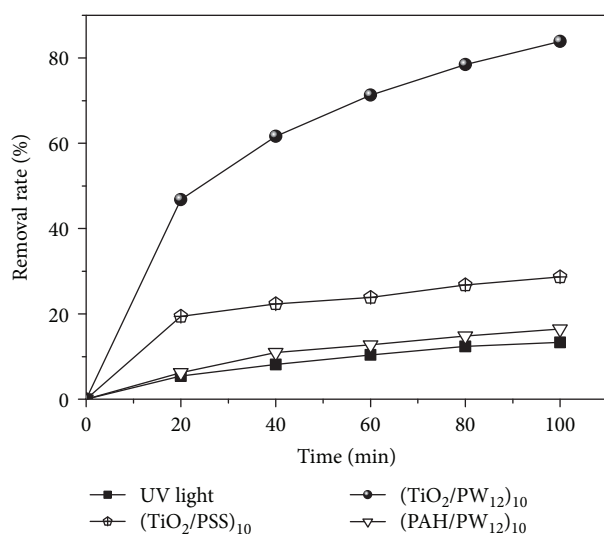


FIGURE 4: The photocatalytic degradation of methyl orange by different catalysts deposited on $\text{Fe}_3\text{O}_4@SiO_2$.

different halate concentrations are shown in Figure 8. It displays a highly positive role in MO degradation due to the addition of halate. The highest degradation rate of 97.32% is obtained at 1 mM BrO_3^- after 40 min of irradiation. Without BrO_3^- , only 52.51% of the MO removal rate is attained within the same amount of time. The enhanced removal rate by the addition of KIO_3 , KBrO_3 , and KClO_3 may be attributed to the fact that all of them can act as electron acceptors in the aqueous solution, thus inhibiting electron-hole recombination on the catalysts' surface. The efficiency of BrO_3^- is always higher than that of IO_3^- and ClO_3^- . This is probably related to the higher redox potential of BrO_3^- , which easily reacts with the conduction band electron [24]. The degradation by IO_3^- is accelerated straightforward by the extra

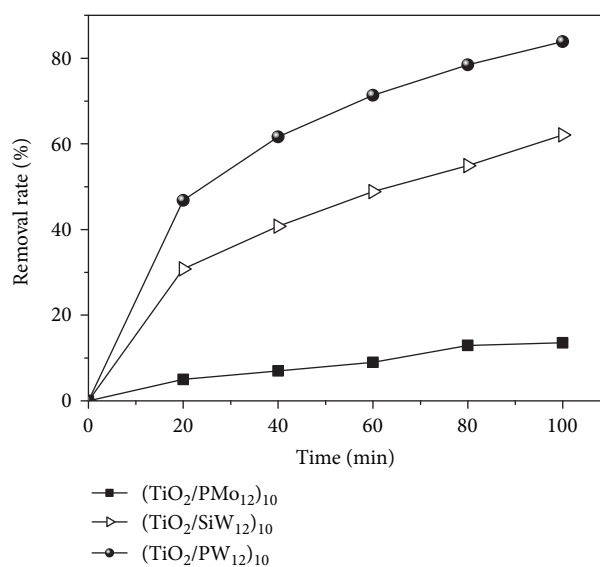


FIGURE 5: Effect of POM type on MO removal by $\text{Fe}_3\text{O}_4@SiO_2$ microspheres coated with $(TiO_2/POM)_{10}$ films.

radicals such as $\text{IO}_2\cdot$ and $\text{HIO}_3\cdot$. However, the effect of I^- as the end product of reduction should not be overlooked. The accumulated I^- can result in a significant deterioration of the MO degradation rate [25].

To determine the effect of inorganic salts which always coexists with dye wastewater on the degradation process, different experiments were carried out. Figure 9 shows the results when inorganic salts such as NaCl , MgCl_2 , AlCl_3 , Na_2SO_4 , and Na_2HPO_4 were added. These salts play different roles in the process of MO photocatalytic degradation. The results shown in Figure 9 reveal that metal chloride has a significant accelerating effect on MO degradation. AlCl_3 illustrates the highest photocatalytic efficiency, and the removal

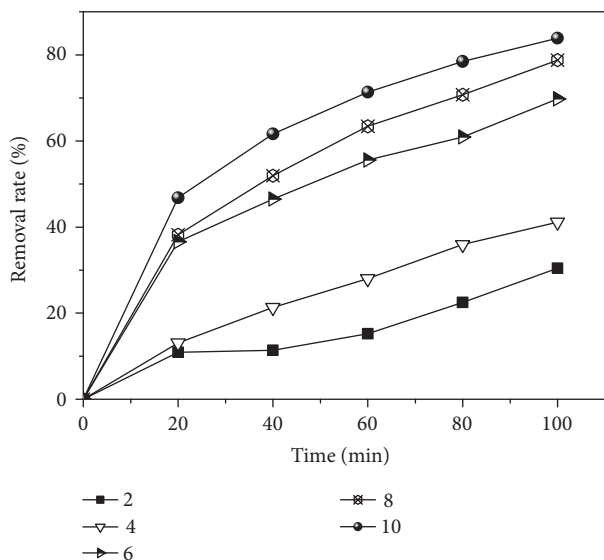


FIGURE 6: The effect of $(\text{TiO}_2/\text{PW}_{12})_n$ bilayer number deposited on $\text{Fe}_3\text{O}_4@/\text{SiO}_2$ microspheres on MO degradation.

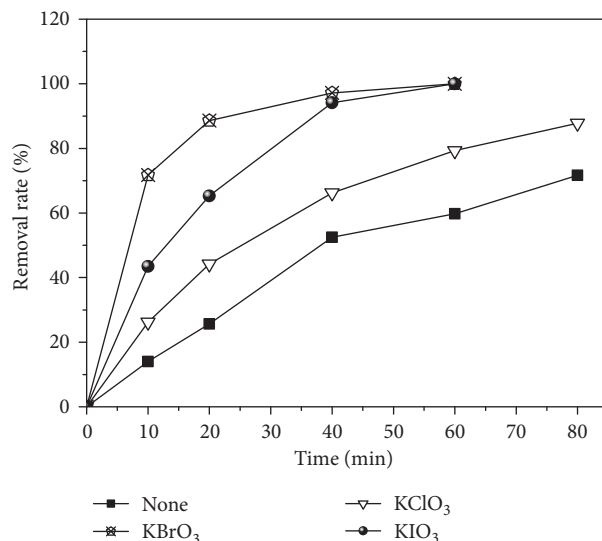


FIGURE 8: Effect of KClO_3 , KBrO_3 , and KIO_3 (1 mM) on MO degradation by $(\text{TiO}_2/\text{PW}_{12})_{10}$ films coated on $\text{Fe}_3\text{O}_4@/\text{SiO}_2$ microspheres (catalyst concentration: 0.4 g/L).

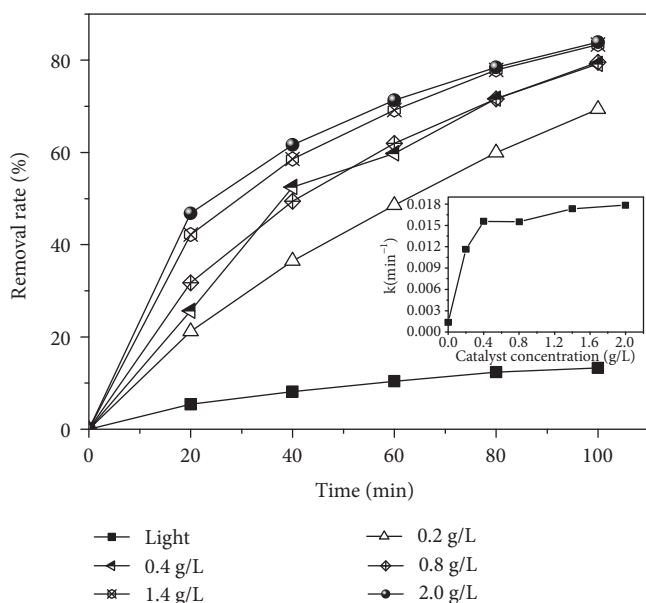


FIGURE 7: Effect of catalyst concentration on MO degradation by $\text{Fe}_3\text{O}_4@/\text{SiO}_2@(\text{TiO}_2/\text{PW}_{12})_{10}$ magnetic microspheres.

rate reaches 97.32% after being irradiated for 60 min. Na_2SO_4 has no obvious impact on MO removal. However, the addition of Na_2HPO_4 results in a great decrease in the MO degradation rate, which is less than 11.45% after UV-light irradiation for 100 min. The presence of Cl^- ions which leads to the reduction of photocatalytic efficiency has been stated by many previous reports [26–29]. The photocatalytic activity inhibits by Cl^- anion mainly attributed to competitive adsorption between Cl^- and pollutant. However, the positive effect of chloride was achieved in our experiments. This enhancement should be attributed to the efficient formation of chlorine and dichloride anion radicals by scavenging holes

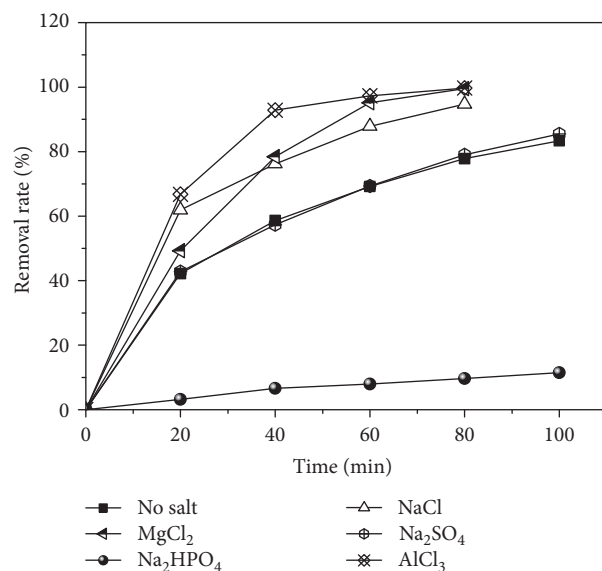


FIGURE 9: Removal efficiency of MO at different inorganic salts by $\text{Fe}_3\text{O}_4@/\text{SiO}_2@(\text{TiO}_2/\text{PW}_{12})_{10}$ films.

and $\cdot\text{OH}$. This process promotes the separation of photo-generated electron-hole pairs [26]. In addition, the higher efficiency of AlCl_3 may be related to the charge density δ of the metal cation calculated through the ionic radii. The higher charge density of the metal cation favors the photocatalytic degradation of MO by inhibiting recombination of the intermolecular relaxation of dye molecules with electrons [30]. The decrease of the removal rate by Na_2HPO_4 is due to the addition of Na_2HPO_4 which results in a pH increase of the MO solution. At high pH, $\text{H}_3\text{PW}_{12}\text{O}_{40}$ will be decomposed [15].

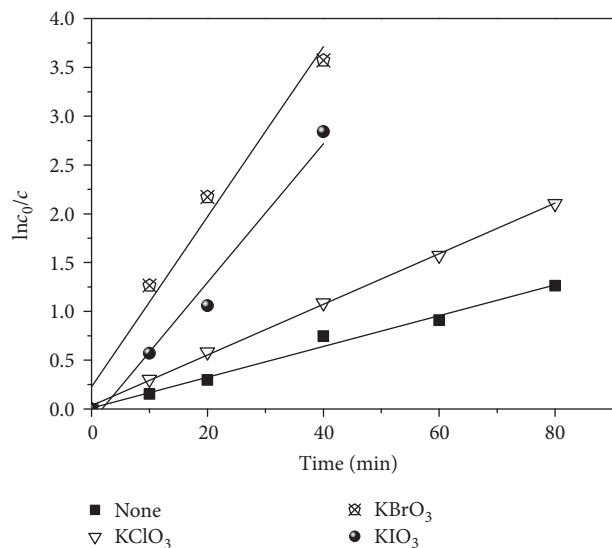


FIGURE 10: Reaction kinetic study of MO photodegradation under KClO_3 , KBrO_3 , and KIO_3 .

The reaction kinetics of MO photodegradation in the presence of halate by $\text{Fe}_3\text{O}_4@\text{SiO}_2@(\text{TiO}_2/\text{PW}_{12})_{10}$ films were investigated. It can be found in Figure 10 that the plots of $\ln c_0/c$ (where c_0 stands for the initial concentration and c is the residual concentration at time t) versus the reaction time yields straight lines. It indicates that the photodecomposition of the diluted MO solution follows apparent first-order kinetics. The first-order rate constants (k) shown in Table 1 were determined from the regression curves of $\ln c_0/c$ versus the reaction time. The constants are 0.01578 min^{-1} without halate, 0.02592 min^{-1} for KClO_3 , 0.08717 min^{-1} for KBrO_3 , and 0.07117 min^{-1} for KIO_3 . The rate constant increases along with the addition of halate, and the greatest rate constant reaches by 1 mM BrO_3^- . It also confirms that photocatalytic efficiency is enhanced, which ascribes to the effective reception of photogenerated electrons.

4. Conclusions

Photocatalytic $(\text{TiO}_2/\text{POM})_n$ film coated on magnetic $\text{Fe}_3\text{O}_4@\text{SiO}_2$ microspheres were prepared based on the electrostatic LbL method. Degradation of methyl orange under UV irradiation was investigated to compare their photocatalytic activity. The presence of PW_{12} and SiW_{12} leads to the effective degradation of MO due to the synergistic effect by combining POMs with TiO_2 . However, the reoxidization of reduced PMo_{12} is very difficult, which causes the decline of the catalysts' effectiveness. The degradation of methyl orange is significantly enhanced by increasing the bilayer number and catalyst concentration. The combination with inorganic oxidants enhances significantly the photodecoloration rate of the dye. It is found that 97.32% of MO is removed after 40 min of irradiation by the addition of KBrO_3 . Analyses on the primary role of inorganic salts demonstrate that the photocatalytic efficiency increases drastically by metal chloride, but strongly decreases by Na_2HPO_4 . The degradation reactions of MO follow pseudo first-order kinetics. It is found

TABLE 1: The rate constants (k) and linear correlation coefficients (R^2) for MO degradation in the presence of halate.

| Halate | k/min^{-1} | R^2 |
|-----------------|---------------------|--------|
| None | 0.01578 | 0.9852 |
| KClO_3 | 0.02592 | 0.9989 |
| KBrO_3 | 0.08717 | 0.9691 |
| KIO_3 | 0.07117 | 0.9709 |

that the use of magnetic support guarantees a photocatalyst with facile, clean, fast, and efficient separation.

Data Availability

The data used to support the findings of this study are available from the corresponding author upon request.

Conflicts of Interest

The authors declare that they have no conflicts of interest.

Acknowledgments

This work was financially supported by the National Natural Science Foundation of Shandong Province Combination Research Projects (ZR2013BL001, ZR2015BL032, and ZR2014BL001).

References

- [1] J. Deng, S. F. Feng, X. Y. Ma et al., "Heterogeneous degradation of Orange II with peroxymonosulfate activated by ordered mesoporous MnFe_2O_4 ," *Separation and Purification Technology*, vol. 167, pp. 181–189, 2016.
- [2] A. R. Khataee and M. B. Kasiri, "Photocatalytic degradation of organic dyes in the presence of nanostructured titanium dioxide: influence of the chemical structure of dyes," *Journal of Molecular Catalysis A: Chemical*, vol. 328, no. 1–2, pp. 8–26, 2010.
- [3] P. A. K. Reddy, P. V. L. Reddy, E. Kwon, K. H. Kim, T. Akter, and S. Kalagar, "Recent advances in photocatalytic treatment of pollutants in aqueous media," *Environment International*, vol. 91, pp. 94–103, 2016.
- [4] A. Mylonas and E. Papaconstantinou, "On the mechanism of photocatalytic degradation of chlorinated phenols to CO_2 and HCl by polyoxometalates," *Journal of Photochemistry and Photobiology A: Chemistry*, vol. 94, no. 1, pp. 77–82, 1996.
- [5] A. Hiskia, A. Mylonas, and E. Papaconstantinou, "Comparison of the photoredox properties of polyoxometallates and semi-conducting particles," *Chemical Society Reviews*, vol. 30, no. 1, pp. 62–69, 2001.
- [6] Z. Yang, S. Y. Gao, H. F. Li, and R. Cao, "Synthesis and visible light photocatalytic properties of polyoxometalate-thionine composite films immobilized on porous TiO_2 microspheres," *Journal of Colloid and Interface Science*, vol. 375, pp. 172–179, 2012.
- [7] H. F. Li, S. Y. Gao, M. N. Cao, and R. Cao, "Self-assembly of polyoxometalate-thionine multilayer films on magnetic microspheres as photocatalyst for methyl orange degradation

- under visible light irradiation," *Journal of Colloid and Interface Science*, vol. 394, pp. 434–440, 2013.
- [8] X. Yang, H. Zhao, J. F. Feng, Y. N. Chen, S. Y. Gao, and R. Cao, "Visible-light-driven selective oxidation of alcohols using a dye-sensitized TiO₂-polyoxometalate catalyst," *Journal of Catalysis*, vol. 351, pp. 59–66, 2017.
- [9] L. H. Gao, J. F. Zhang, H. L. Wang, X. Y. Lin, J. M. Qi, and K. Z. Wang, "Effects of elemental composition variations of Keggin polyoxometalates on photocurrent generation of their layer-by-layer self-assembled films with a hemicyanine dye," *Electrochimica Acta*, vol. 166, pp. 215–222, 2015.
- [10] L. Zhang, S. B. Li, Z. F. Zhang, L. C. Tan, H. J. Pang, and H. Y. Ma, "Facile fabrication of reduced graphene oxide and Keggin-type polyoxometalates nanocomposite film for high performance electrocatalytic oxidation of nitrite," *Journal of Electroanalytical Chemistry*, vol. 807, pp. 97–103, 2017.
- [11] S. Y. Gao, D. M. Pan, and R. Cao, "Layer-by-layer self-assembly polytungstogermanate multilayer films and their photocatalytic properties under sunlight irradiation," *Journal of Colloid and Interface Science*, vol. 358, no. 2, pp. 593–597, 2011.
- [12] Z. X. Sun, F. Y. Li, L. Xu, S. P. Liu, M. L. Zhao, and B. B. Xu, "Effects of Dawson-type tungstophosphate on photoelectrochemical responses of cadmium sulfide composite film," *The Journal of Physical Chemistry C*, vol. 116, no. 10, pp. 6420–6426, 2012.
- [13] W. Yang, L. H. Gao, and K. Z. Wang, "Photoelectric properties of polyoxometalate-based thin films—recent advances and future perspective," *Polyhedron*, vol. 82, pp. 80–87, 2014.
- [14] A. Nakajima, T. Koike, S. Yanagida, T. Isobe, Y. Kameshima, and K. Okada, "Preparation and photocatalytic activity of [PW_xMo_{12-x}O₄₀]³⁻/TiO₂ hybrid film composites," *Applied Catalysis A: General*, vol. 385, no. 1–2, pp. 130–135, 2010.
- [15] P. Niu and J. C. Hao, "Efficient degradation of organic dyes by titanium dioxide-silicotungstic acid nanocomposite films: influence of inorganic salts and surfactants," *Colloids and Surfaces A: Physicochemical and Engineering Aspects*, vol. 443, pp. 501–507, 2014.
- [16] C. H. Sui, C. Wang, Z. Y. Wang et al., "Different coating on electrospun nanofiber via layer-by-layer self-assembly for their photocatalytic activities," *Colloids and Surfaces A: Physicochemical and Engineering Aspects*, vol. 529, pp. 425–433, 2017.
- [17] H. C. Novais, D. M. Fernandes, and C. Freire, "Hybrid methyl green/cobalt-polyoxotungstate nanostructured films: self-assembly, electrochemical and electrocatalytic properties," *Applied Surface Science*, vol. 347, pp. 40–47, 2015.
- [18] C. X. Li, K. P. H. Y. M. O'halloran, and S. L. Shi, "Multifunctional multilayer films containing polyoxometalates and bismuth oxide nanoparticles," *The Journal of Physical Chemistry B*, vol. 113, no. 23, pp. 8043–8048, 2009.
- [19] L. Zhang, L. Ning, Z. F. Zhang et al., "Fabrication and electrochemical determination of L-cysteine of a composite film based on V-substituted polyoxometalates and Au@2Ag core-shell nanoparticles," *Sensors and Actuators B: Chemical*, vol. 221, pp. 28–36, 2015.
- [20] S. P. Liu and X. S. Qu, "Construction of nanocomposite film of Dawson-type polyoxometalate and TiO₂ nanowires for electrochromic applications," *Applied Surface Science*, vol. 412, pp. 189–195, 2017.
- [21] X. Yua, C. Y. Chen, J. Peng et al., "Antibacterial-active multilayer films composed of polyoxometalate and methyl violet: fabrication, characterization and properties," *Thin Solid Films*, vol. 571, pp. 69–74, 2014.
- [22] H. W. Sun, J. H. Yu, P. J. Gong, D. M. Xu, C. F. Zhang, and S. D. Yao, "Novel core-shell magnetic nanogels synthesized in an emulsion-free aqueous system under UV irradiation for targeted radiopharmaceutical applications," *Journal of Magnetism and Magnetic Materials*, vol. 294, no. 3, pp. 273–280, 2005.
- [23] D. G. Shchukin, J. H. Schattka, M. Antonietti, and R. A. Caruso, "Photocatalytic properties of porous metal oxide networks formed by nanoparticle infiltration in a polymer gel template," *The Journal of Physical Chemistry B*, vol. 107, no. 4, pp. 952–957, 2003.
- [24] K. Selvam, M. Muruganandham, I. Muthuvel, and M. Swaminathan, "The influence of inorganic oxidants and metal ions on semiconductor sensitized photodegradation of 4-fluorophenol," *Chemical Engineering Journal*, vol. 128, no. 1, pp. 51–57, 2007.
- [25] D. Zhang, Y. Q. Zhang, H. Y. Ma, H. Yan, and Y. B. Song, "Fabrication of a 12-tungstophosphate and cadmium oxide composite film and its properties," *Materials Chemistry and Physics*, vol. 144, no. 3, pp. 369–376, 2014.
- [26] D. E. Santiago, J. Araña, O. González-Díaz et al., "Effect of inorganic ions on the photocatalytic treatment of agro-industrial wastewaters containing imazalil," *Applied Catalysis B: Environmental*, vol. 156–157, pp. 284–292, 2014.
- [27] Y. C. Dong, J. L. Chen, C. H. Li, and H. X. Zhu, "Decoloration of three azo dyes in water by photocatalysis of Fe (III)-oxalate complexes/H₂O₂ in the presence of inorganic salts," *Dyes and Pigments*, vol. 73, no. 2, pp. 261–268, 2007.
- [28] M. Muruganandham and M. Swaminathan, "Photochemical oxidation of reactive azo dye with UV-H₂O₂ process," *Dyes and Pigments*, vol. 62, no. 3, pp. 269–275, 2004.
- [29] M. Muthukumar and N. Selvakumar, "Studies on the effect of inorganic salts on decolouration of acid dye effluents by ozonation," *Dyes and Pigments*, vol. 62, no. 3, pp. 221–228, 2004.
- [30] M. Makita and A. Harata, "Photocatalytic decolorization of rhodamine B dye as a model of dissolved organic compounds: influence of dissolved inorganic chloride salts in seawater of the Sea of Japan," *Chemical Engineering and Processing: Process Intensification*, vol. 47, no. 5, pp. 859–863, 2008.